Open-Wheel Aerodynamics: Effects of Tyre Deformation and Internal Flow

SPROT, ADAM,JOSEPH

How to cite:

SPROT, ADAM,JOSEPH (2013) *Open-Wheel Aerodynamics: Effects of Tyre Deformation and Internal Flow*, Durham theses, Durham University. Available at Durham E-Theses Online: http://etheses.dur.ac.uk/7292/

Open-Wheel Aerodynamics:
Effects of Tyre Deformation and Internal Flow

by

Adam Joseph Sprot
of Collingwood College

Supervised by
Dr D. B. Sims-Williams,
Dr R. G. Dominy

Durham University
School of Engineering
and Computing Sciences

Submitted in conformity with the requirements
for the degree of Doctor of Philosophy

To Dad

Kevin John Sprot

1958 - 2012

Abstract

Competitive performance of an F1 race car relies upon a well designed and highly developed aerodynamic system. In order to achieve this, total understanding of the downstream wake of exposed rotating wheels is essential. Components such as bargeboards and indeed much of the front wing are developed to provide pressure gradients and vortex structures to influence the wheel wake, ensuring high energy mass-flow to the sensitive leading edge of the underfloor and eventually the rear wing.

Wind tunnel testing of model-scale deformable tyres has become a common occurrence in F1 in recent years although there is a significant lack of available literature, academic or otherwise, as to their use. This work has studied in detail the aerodynamic consequences which occur from the varying sidewall bulge and contact patch region making use of several techniques. These include scanning rotating tyre profiles under load, static contact patch size measurements, five-hole pressure probe wake measurements, particle image velocimetry (PIV) and load-cell drag measurements. CFD simulations utilising two industrial codes have also been performed to support the experimental work. Coordinates representing tyre profiles under a range of on-track conditions are available for other researchers to use as a basis for CFD studies.

The work presented here includes a full range of representative on-track axle heights which far exceed the more conservative range usually tested in an industrial setting for longevity reasons. The most sensitive parameters for aerodynamic testing of wheels have been identified. For development of a full car, in decreasing order of priority, the following must be correctly matched to the realistic scenario: axle height, yaw condition (without glycerol - often used to reduce friction at the expense of a compromised tyre profile), camber angle, detailed internals, high inflation pressure, through-hub flow rate and least significantly the rotation of the internal brake rotor.

The study of through-hub flows revealed that the external aerodynamic effect of the brake scoop inlet varies significantly with the amount of internal restriction. The pumping effect of the brake rotor was measured to be negligible compared to the restrictive effect of its internal passages and that leads to an effect known as inlet spillage with a negative cooling drag trend, whereby the drag of the wheel assembly decreases with increased through-hub flow.

Declaration

The material contained within this thesis has not previously been submitted for a degree at Durham University or any other university. The research reported within this thesis has been conducted by the author unless indicated otherwise.

Copyright Notice

Acknowledgements

I would like to extend my sincerest gratitude to both of my supervisors: Dr David Sims-Williams and Dr Robert Dominy. It is with their teaching, support, guidance and encouraged independence that I have been able to achieve so many things over the past three years, not limited to (although exemplified by) the work contained within this very document.

I would also like to acknowledge all other members of staff in the School of Engineering and Computing Sciences who had an involvement; offering either their technical support or useful conversations, or both, over time. In particular I would like to thank Mr Ian Hutchinson (Electronics Workshop) for helping out on many occasions, especially for the times when it was not necessarily within his domain and Mr Colin Wintrip (Mechanical Workshop) for being so supportive and forthcoming with advice with regards to the design and production of components used in the experimental work. Additional thanks to Mr Gary Parker (Thermo/Fluids Lab Technician) not only for his assistance with the lab equipment, inclusive of the wind tunnel, but also for his wealth of knowledge outside of the research topic which has been absorbed over the years.

I am extremely grateful for the two years of funding awarded by the School of Engineering and Computing Sciences, without which, this most-certainly would not have developed into the scale of work presented here.

I would like to thank Mike Johnson for his unrelenting advice and support in the seamless operation of the Linux-based mini-cluster from which almost half of the results in this thesis originated.

Thanks to the following postgraduate students from the department, for the countless invaluable discussions and at times, motivation, throughout: Kieran Massey, Fred Hamlin, Nicholas Oettle, Mike Wilson and Oliver Mankowski.

Thanks to the following colleagues from my summer postgraduate internship for stepping up my knowledge, experience and perspective both in and out of the research topic which undoubtedly benefited my final year immeasurably: Simon Phillips, Simon Belcher, Andy Morgan, Andy Chilton,

Andy Cusdin and Dominic Turner. In addition, to my current colleagues for the same reason during the final stages of writing up: Davide Felappi, Michael Hart, Chris Harley, Rob van den Heijkant and Laurence Kenworthy.

Thanks to Mr Ian Lawson, Mr Guy Wilks and Mr Dave Glynn (of Karting North East) for their generous offer of part-time employment as part-time circuit manager which enabled me to survive financially throughout my self-funded first year and allowed me to gain experience and skills in a very different setting to the academic world.

Last, and most of all, thanks to my family for being there not just over the past three years, but always. Thanks to my parents Kevin and Lynda who have always encouraged me to follow my dreams and went out of their way to enable me to get to where I am today, among so many other things; to my grandparents Doreen and Robert for generously paying my tuition for the first year; and to my sister and brother-in-law, Anna and Alisdair, for always providing moments of well needed respite from such a relentless endeavour.

Contents

List of Figures

List of Tables

List of Abbreviations

Abbreviation	**Definition**
ASD	Amplitude Squared Density
$\overline{ASD}$	Mean Amplitude Squared Density
CAD	Computer Aided Design
CCD	Charge Coupled Device
CFD	Computational Fluid Dynamics
CoM	Centre of Mass
DSW	Durham Software for Windtunnels
F1	Formula 1
FEA	Finite Element Analysis
FEM	Finite Element Method
FIA	Federation Internationale de l'Automobile (Governing Body)
HFN	Hub Flow Number
$\mathrm{HFN_c}$	Corrected Hub Flow Number
KERS	Kinetic Energy Recovery System
LDA	Laser Doppler Anemometry
LES	Large Eddy Simulations
MGP	Moving Ground Plane
MRF	Moving Reference Frame
PIV	Particle Image Velocimetry
RANS	Reynolds-Averaged Navier-Stokes
RKE	Realisable k-epsilon
RPM	Revolutions per Minute
URANS	Unsteady Reynolds-Averaged Navier-Stokes
VLES	Very Large Eddy Simulations
VR	Variable Resolution

List of Symbols

Symbol	**Definition**
D	Nominal Diameter of Wheel (0.32m)
L	Length
R	Radius
h	Height of Laser Scanner (from MGP)
l	Characteristic Length
y	Distance of Object to Laser Scanner (corrected)
y^+	Non-Dimensionalised Characteristic Wall Length/Distance
A_s	Reference Area of Scoop
A_f	Projected Total Frontal Area
$U; u$	Local Velocity
v	Wheel Peripheral Velocity
$U_{ref}; U_\infty$	Reference / Freestream Velocity
$U_b; U_{belt}$	Belt Peripheral Velocity
$U_{hub,CFD}$	Hub Velocity from CFD
$U_{duct,CFD}$	Scoop Velocity from CFD
f	Frequency (Shedding)
μ	Dynamic Viscosity
ρ	Density
σ	Standard Deviation
P_{Dyn}; q_0	Dynamic Pressure
P_{tot}	Total/Stagnation Pressure
$\dot{m}_0$	Freestream Mass-Flow Rate
$\dot{m}_6$	Exit Mass-Flow Rate
$Re = \frac{\rho l U}{\mu}$	Reynolds Number
α	Ratio of Peripheral Speed of Wheel to Freestream
α_s	Slip Angle
β	Yaw Angle
θ_c	Camber Angle
$\theta_{crosswind}$	Crosswind Angle
θ_L	Lase Incidence Angle (to MGP)

Symbol	**Definition**
$D_{cooling}$	Cooling Drag Force
D_{inlet}	Drag Force of the Scoop Inlet
D_{ram}	Ram Drag Force
D_{spill}	Spillage Drag Force
D_{ub}	Underbody Drag Force
F_D, F_{drag}	Drag Force
$F_L; F_{lift}$	Lift Force
F_x	x-component of Driving Force
$C_{D,RAM}$	Coefficient of Ram Drag
$C_D = \frac{F_D}{\frac{1}{2}\rho A U_{ref}^2}$	Drag Coefficient
$C_{D,Experimental}$	Experimentally Measured Coefficient of Drag
C_D^{axial}	Coefficient of Drag Perpendicular to the Axle
C_D^{body}	Coefficient of Drag for the Vehicle Body (Not Including Wheels)
$C_D^{wheel\&housing}$	Coefficient of Drag for the Exposed Vehicle Wheel Housing and Wheel
$C_{D,combined}$	Combined Coefficient of Drag (Multiple Components)
C_{side}	Coefficient of Side Force
$C_L = \frac{F_L}{\frac{1}{2}\rho A U_{ref}^2}$	Coefficient of Drag
$C_{t,inlet}$	Thrust-Recovery Coefficient for Inlet
$P_0 - P_4$	Pressure values for each hole of the 5-hole probe
$Cp_0; Cp_T$	Coefficient of Stagnation / Total Pressure
$Cp; Cp_s$	Static Pressure Coefficient
Cp_{Dyn}	Dynamic Pressure Coefficient
Cp_{Pitch}	Pitch Coefficient
Cp_{Yaw}	Yaw Coefficient

Chapter 1

Introduction

This thesis aspires to contribute towards a field of vehicle aerodynamics which currently suffers a significant gap in research. Specifically, the focus of this work concentrates on the region in and around the front wheel assembly of a Formula One (F1) car. It is no secret that the winning potential of a modern F1 car is dominated by its aerodynamic performance and as such the field is very much shrouded in secrecy and great complexity.

This first chapter of the thesis portrays the motivation behind the work by putting into context the importance of the front wheel aerodynamic flow-field in relation to the whole race car. A literature review is presented which draws upon the sporadic yet significant published works within this field. The aims, objectives and scope of the investigations undertaken in this work are then clearly defined.

Due to what is now a generous array of tools available to aerodynamicists, the experimental wind tunnel chapters have been isolated from those of the computational fluid dynamics (CFD) simulations. The findings are then drawn together in a single summary of discussions chapter. Finally, future work has been recommended to further the depth and understanding of this field.

1.1 Context and Motivation - The Aerodynamics of F1 Cars

1.1.1 The Requirement for Aerodynamics

It is a mechanical fact, as discussed by Smith [1], for example, that the greater the reaction force acting upon a wheel, the higher the level of lateral acceleration the tyre can withstand. This allows higher cornering velocities and in principle, shorter lap times through better traction and braking. Hence, although aerodynamic efficiency is an important factor (downforce-to-drag ratio), the endeavour to achieve higher downforce levels on a component-by-component basis will almost always supersede any drag penalty. As a result, the drag of an F1 car is particularly high, in the region of $C_D \geq 0.8$ compared to that of a conventional production car with $C_D \sim 0.3$ (Katz [2]).

The aerodynamic behaviour of an F1 car is built upon a highly complex and sensitive system of vortices and pressure gradients. The ultimate aim, on the most basic level, is based around the concept that higher mass-flow leads to lowered static pressures and therefore suction acting normal to any interacting surface. By exploiting this principal on underside surfaces wherever possible, the net aerodynamic lift on an F1 car becomes largely negative, commonly referred to as ‘downforce’.

The most obvious contribution for an F1 car’s downforce generation is in the form of wing assemblies. There are two main assemblies, one at the front and one at the rear. Between the two, they contribute around half of the total downforce of an F1 car. The aggressiveness of the aerofoil sections and the vortex features generated from the wing (and smaller ancillary wing) tips contribute to a large wake and high drag level, albeit producing large levels of downforce.

The most efficient downforce originates from accelerating air without taking large quantities of energy out of it. This allows for more potential to be exploited as the air traverses to the rear of the car as well as allowing vortical structures to remain strong, stable and long-lived. The primary method of producing efficient downforce is to rely upon ground-effect and ground interaction. The ground clearance of an F1 car is of the order of millimetres which means the fluid-accessible cross-sectional area under the floor is much smaller than that of the total projected frontal area of the car. Providing that favourable inlet and outlet conditions are established, air will accelerate to high local velocities thus achieving a significant low-pressure region under the car.

1.1.2 Wheel Wake Control and Variable Operating Conditions

The open-wheeled nature of some racing series, such as F1, is dictated by the rules and regulations of the sport. This is believed by many to protect the history, the heritage and the technical challenge [3] [4] [5]. The collection of bluff-bodies (objects dominated by leading edge or blunt-base separation) comprising an F1 car, such as the typical example in Figure 1.1, leads to many cumulative interacting wake structures, constituting the overall flow-field of the car. These result in low stagnation pressures, and possible energy losses, which in turn result in high drag forces.

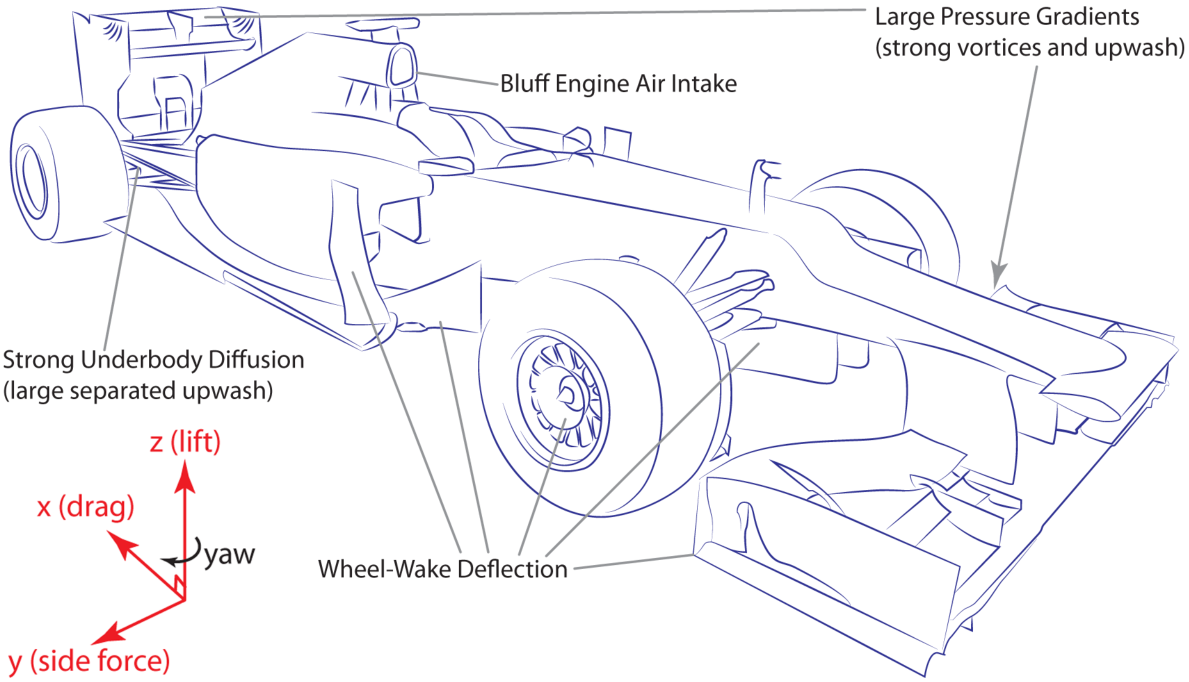

Figure 1.1: *A typical example of a current F1 car with key flow features highlighted. The standard (SAE) axes of experimentation are defined.*

Typically, aircraft, with the exception of take-off and landing, are designed and optimised with respect to operating for long periods within one medium at a set velocity under very specific conditions. Race cars, however, have the solid non-static ground (relatively) as a constant influence. They are also required to have high performance over a much larger range of velocities, albeit lower in magnitude. Because of this large operation window, geometrical changes can become quite significant. Geometrical changes can be brought about by elastic or spring deformations in the tyres and the suspension respectively due to pitch and roll changes when on track. Since the vehicle underfloor is of the order of millimetres from the ground, these effects can significantly affect the balance and aerodynamic design of the car.

In addition to the obvious boost in straight-line speed and acceleration, there still exists a genuine advantage in reducing drag. The aggressive nature of the rear wing is often adjusted to achieve a target drag level specific to an individual race circuit, often with wasted potential downforce levels left in reserve. Tracks such as 'Monza' in Italy, and the 'Circuit Gilles Villeneuve' in Canada, are both high-speed circuits which require lower drag levels for a short lap time than the tight and twisting streets of Monte Carlo, for example. Therefore reducing the drag contribution from bluff body components, such as the wheels, which do not provide useful downforce, allows aerodynamicists to run more aggressive rear wings in order to achieve greater net downforce for the same target drag penalty. It is a reported fact by Dominy [6] that the exposed rotating wheels of an F1 car can contribute between thirty-five and fifty percent of the overall drag of the vehicle.

As a consequence of the above, significant time and resources are spent either counteracting or controlling the wake of an F1 tyre. Components on the front wing can be designed to provide outwash or small vortex structures to change the upstream flow-field and therefore facilitate further alteration of the downstream wake. Through-hub flow to cool the brakes also provides outwash and barge-boards, deflectors and vertical sidepod wings are all designed to push the low-energy air, sometimes referred to as 'dirty air', away from the sensitive downstream components of the car (Figure 1.1). The sidepods, cooling inlets and the highly sensitive leading edge of the underfloor are the key areas of concern. Without deflecting or moulding the flow-field of the front wheels, an F1 car would severely lose any possible competitive advantage.

The wheel assemblies comprise dynamic systems. These do not only change off the track, but as a result of interactions with the track, inertia and forces resulting from being driven on the limit of adhesion. Given the delicate balance of an F1 car at any instantaneous point in time, it is imperative to understand what geometrical changes take place, particularly in the sidewalls and contact patch of the tyre and therefore establish a way of modelling this for future car development. Due to recent budget limitations and regulations set by the governing body, the primary development test bed for F1 is in model-scale wind tunnel testing. This is often supported by CFD simulations as a concept development methodology. Very little on-track development now takes place which is why it is becoming increasingly important to hone modelling techniques.

Dominy & Dominy [7] produced a mathematical model to quantify the aerodynamic and chassis changes in terms of lap times, straight line speed and cornering attitude. Such ability to predict the performance of an F1 car prior to taking it to a track is the priceless tool that most teams strive to obtain and refine. Since the Lotus ground-effect cars of the late 1970's, F1 teams have significantly increased their focus on aerodynamic research and development. Among many others, Dominy & Dominy [7], and later by Dominy [6], provide a clear overview of the aerodynamic influences present on grand prix cars of the time in much more detail than will be discussed here. With the exception of sliding skirts, used at the time to seal the underfloor to prevent outwash in order to increase underbody mass flow, the fundamental aerodynamic processes which take place on modern F1 cars are no different.

Similarly, Velenis and Tsiotras [8] performed a study based on cornering techniques to refine their mathematical lap time simulator. Their approach was based upon the understanding that the most unpredictable element of a race car will always be the driver. Even considering two drivers performing at their peak performance, making no mistakes, they may employ two very different techniques to negotiate the same corners yet produce similar overall lap times. The common styles investigated analytically were path optimisation for either minimum time or maximum exit velocity. The latter is typical of rally driving but also circuit racing when two or more slow-speed corners are in close proximity to each other. By taking more time through the first corner and maximising corner exit velocity of the second onto a long straight, a shorter overall lap time can be produced.

Mathematical simulation of an overall system is an extensive field in its own right and will not be discussed here any further. However, the results and conclusions from studies such as those in this thesis should provide a comprehensive list of the finer details and greatest sensitivities to on-track variables which can sometimes be overlooked when simplifying the simulation process.

1.1.3 Motivation for Aerodynamic Research

It is a necessity as much as a desire to achieve total understanding of the flow-field effects around a front wheel assembly. By studying the wheel flow in isolation from complex suspension geometry and front wing elements, the nature of the flow at key areas of the assembly can be identified. Notably, the perimeter of the contact patch, the sidewalls, the upper shoulders, the internal geometries and internal flow all hold a high level of interest. Therefore, this work will adopt an isolated configuration. The ultimate aim of testing and optimisation is in finding the greatest sensitivities and therefore exploiting areas which offer superior development over financial outlay. This is the basis and the motivation for this thesis.

1.2 Literature Review

1.2.1 On-Track Tyre Deformation and Setup Parameters

There are several on-track conditions under which a tyre will experience changes to its shape and characteristics. This thesis has been written with these geometrical changes in mind and endeavours to investigate the aerodynamic influence of such dynamic variables as well as design variables such as steering angle, toe, caster, camber and axle height, which all play a vital role in the mechanical aspect of the car's design and performance. This section will briefly outline the most significant of these parameters to contextualise their importance from a mechanical perspective, hence how they influence the tyre's behaviour under its most sensitive condition, whilst cornering.

The stresses that a racing or even production vehicle tyre experiences result in extreme movements of the basic structure. Because of the multi-layer construction, shown in Figure 1.2, it is difficult to obtain an analytical model of the tyre deformation even using FEA methodologies (Yang & Olatunbosun [9]).

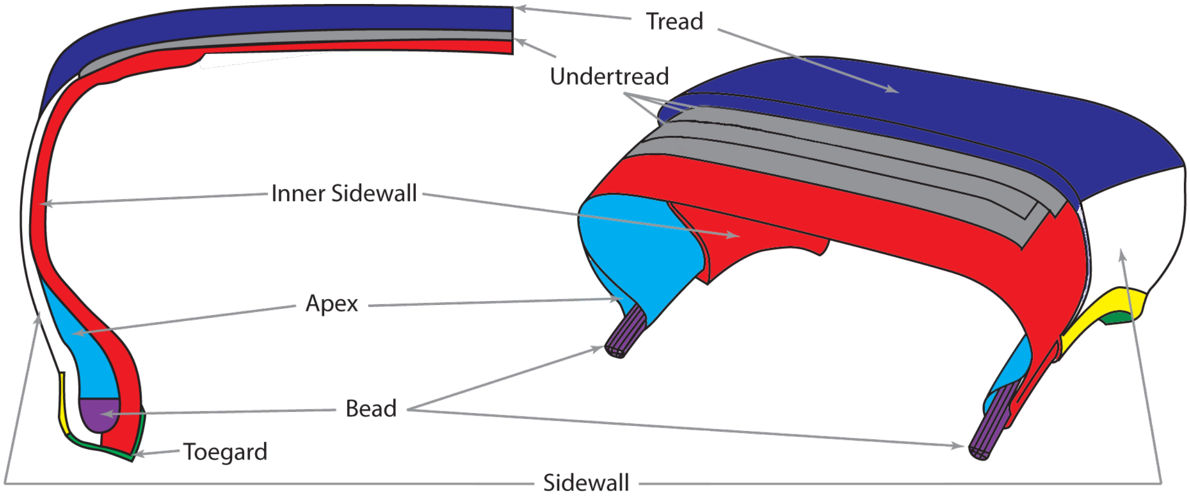

Figure 1.2: *Combined figures (after Yang & Olatunbosun [9]) showing the multi-layer construction of a generic tyre.*

Clark [10] provided a mathematical analysis of the behaviour of a tyre under load, although the finite element methods applied by Yang & Olatunbosun [9], Ridha & Theves [11] and Ghoreishy [12] are more modern methods of simulating deformation. Sabey & Lupton [13] performed an investigation into the photography of tyre contact patches under various loading conditions. These early works combine the two main features of tyre deformation: contact patch shape and sidewall profile shape.

Ridha & Theves [11] presented the difference between a stationary and rotating wheel with a pneumatic tyre under a 'free-spin' test. The differences can be seen in Figure 1.3. There exists an extreme straightening of the sidewall from the centrifugal force under rotation. This becomes an issue when conditions are set statically in the wind tunnel and data are measured under rotation assuming that the pneumatic tyres in the testing facility are designed to mimic their real-world counterparts.

The straightening of the sidewall due to high-speed rotation has two opposing effects. The top of the tyre has no constraints such as the road to hinder the movement of the tread and as such extends as seen in the Figure 1.3. The underside, however, opposes the straightening and results in either a rise in axle height or a bulge in the sidewall of the tyre. In most instances both can be present. This means the profile of the tyre is not axially symmetric.

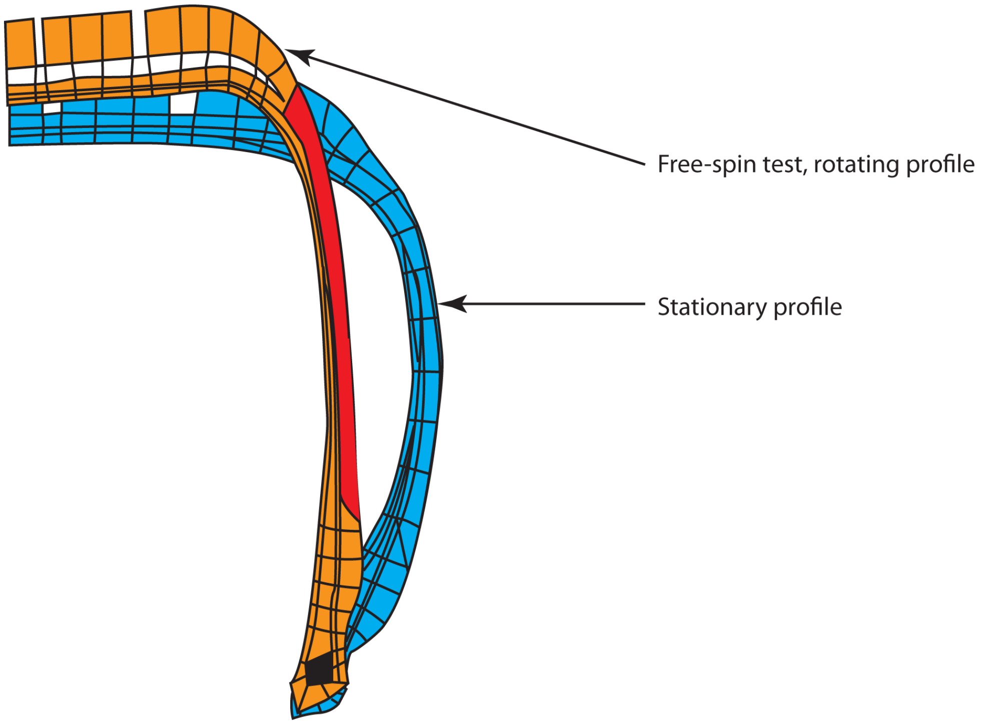

Figure 1.3: *Differences between observed stationary and rotating tyre profiles (Ridha & Theves [11]).*

It is important to realise that the cord angles in the undertread, for example, can lead to significant changes in the behaviour of a tyre between different manufacturers and even models. Nevertheless, global trends should be universal. As such, attempts have been made in the literature to measure the deformation of a tyre under rotation by means of an ultra-sonic sensor placed inside the tyre, mounted on the rim as in the case of Mágori et al. [14] or a Hall-effect sensor using a highly sensitive AlGaAs/GaAs position sensor as with Brandt et al. [15]. The latter cases were, however, only measurements of the radial distance from the rim to the tread and no detailed information regarding the real-time rotating cross-sectional profile were provided.

The deformation of a tyre is also exaggerated under cornering conditions and there is little available data, presumably due to the aforementioned tyre specific characteristics, to describe the processes taking place in the tyre under these conditions. This is as much an issue in the field of aerodynamics as with vehicle dynamics.

Each F1 team is provided with model-scale pneumatic wind tunnel tyres by the official tyre supplier every year. These are designed to deform in the same way as the full-size equivalent but with a much reduced vertical loading requirement and provide a much lower level of lateral grip. The data provided by the tyre manufacturers to accompany the yearly allocation of scale model deformable tyres comprise a loaded radius equation, sidewall profiles for certain loads (although these rarely match test conditions in terms of the severity of deformation level) and an FEM model to produce CFD and vehicle dynamics simulations based upon this behaviour.

1.2.2 Geometrical Parameters of Racing Wheels

1.2.2.1 Slip

For high-performance driving, the high friction forces between the road and the tyre's contact patch, coupled with the deformable elasticity of the rubber on the tread result in the tyre resisting the steering angle applied by the driver and results in a side-force. This in turn results in a twisting moment of the contact patch due to variations in the local side-force. Slip is the angle between the direction of travel of the moving vehicle (and road, in static-car moving-ground studies), with respect to the steering angle.

At normal road speeds, with low values of centrifugal force, cars follow a clearly defined trajectory determined by the steering angle associated with an Ackerman steering geometry. This is discussed well by Smith [1] and Dixon [16], among many others. Because there is a low level of lateral acceleration and the tyres are not at or near their limit of grip, the wheels can be described as simply rolling about their axle and the tread exhibits approximately the same shape as a static tyre all around the circumference. There is a minimal slip angle developed.

Figure 1.4 illustrates how the resistance of the contact patch to the turning moment on the wheel results in a twisting effect in the tread. As a general rule, the contact patch rubber will follow the trajectory of the car whilst the wheel will be turned in excess of this path.

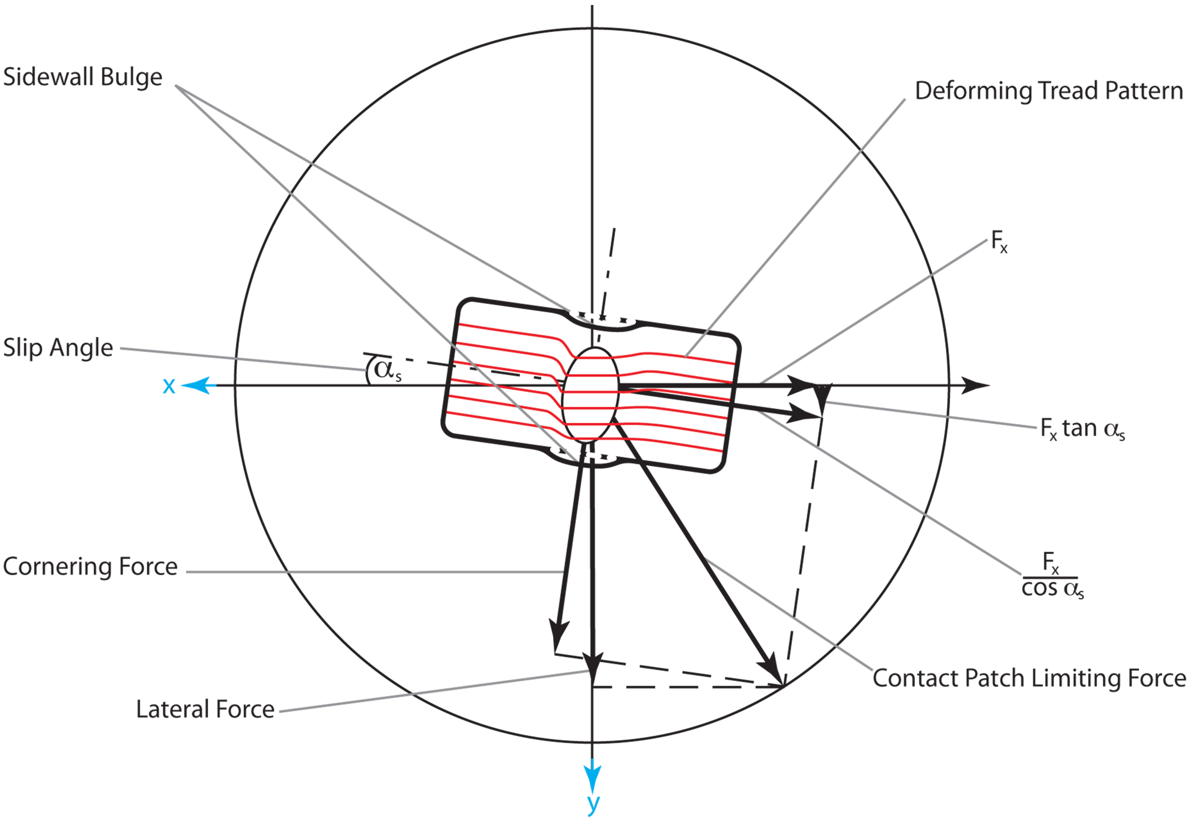

Figure 1.4: *The forces on a slipping tyre. Combined figures from Smith [1] and Dominy & Dominy [7] with tread deformation and cornering thrust vectors highlighted.*

A tyre has a characteristic limit of slip angle whereby the tyre will begin to understeer or oversteer depending on whether this happens first on the front or rear wheels respectively. Further beyond this the car will lose grip entirely. Figure 1.5 illustrates this varying lateral coefficient of friction, and therefore the force trend against slip angle. Also highlighted on this figure is the breakaway point for each tyre. The trend shows that the higher performance tyre has a less stable plateau before a sudden loss of grip. A longer, more forgiving plateau is often engineered into tyres, whereby, although no further force develops with increasing slip angle, the driver is less likely to suffer by turning beyond this point.

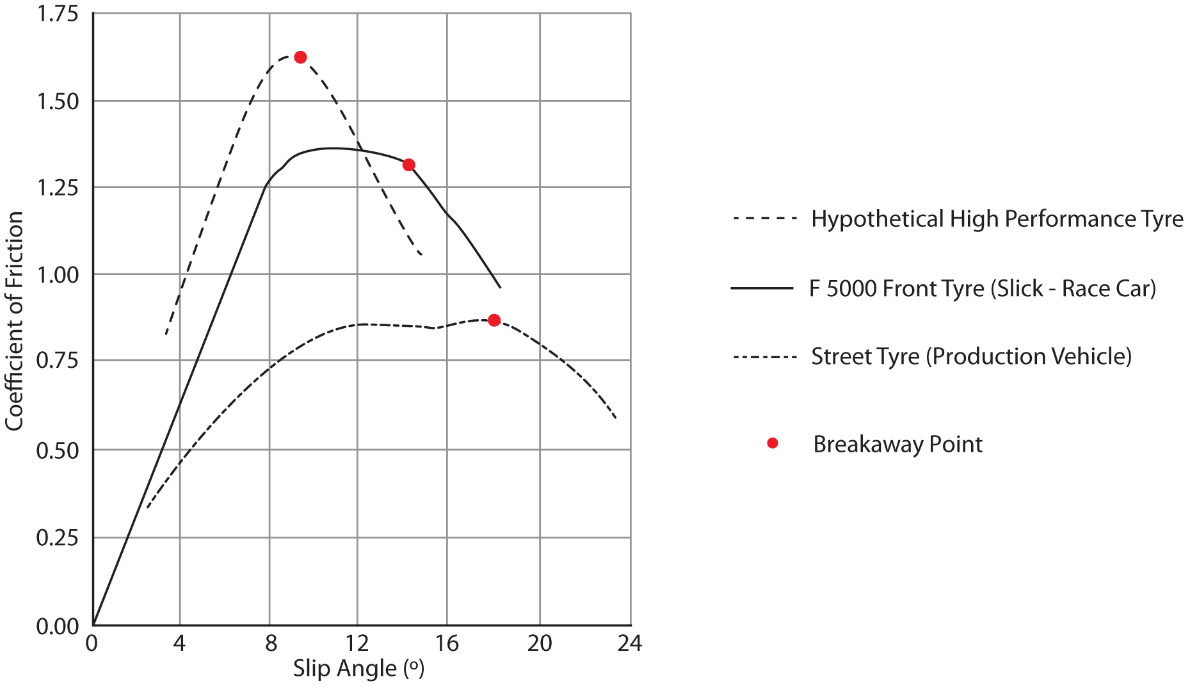

Figure 1.5: *Typical coefficient of friction vs. slip angle characteristics (modified from Smith [1]).*

Although the magnitudes are expected to be different for a modern-day tyre, the trends are known to be the same and it is also known that modern-day F1 tyres generally do not observe greater than 8° of slip before breakaway.

1.2.2.2 Neutral Steer

Neutral steer describes a condition whereby a car is rotating about its centre-of-mass (CoM) as well as that CoM being projected stably around the corner radius. Specifically, it is the condition where all four wheels each have an equal degree of slip. This is inherently unstable due to suspension geometries containing springs and dampers which are constantly moving, thus effecting a weight-transfer. This causes a sudden drop off towards understeer or oversteer.

In F1, and many other racing series, the drive force is applied to the contact patches of the rear wheels and therefore any slip angle applied to the rear wheels will increase due to the drive thrust emphasising the contact patch twist. This can be observed by an increased turning thrust for that wheel or in the case of F1 with limited-slip differentials, the whole rear of the car.

Since the highest demand for aerodynamic loading is during cornering conditions, simulating the effect of aerodynamic yaw is one of the most important things to include in component testing. This is discussed further in Section 1.2.3.

1.2.2.3 Camber

Observing an F1 car from the front, the wheels appear to be at an angle to the vertical plane. Negative camber is shown in Figure 1.6. This is the most commonly used setup, and defines the angle in question.

Under straight line conditions, the camber parameter dictates that the wheel is not necessarily utilising the full potential of the contact patch. It will also exhibit a cone-like frontal view. A cone rolling about its axis will always precess around its apex. Negative camber ensures that the outside wheel on a corner, which has higher loading due to dive and roll, will have an additional cornering thrust compared to that purely of the steering angle. In addition, due to the friction with the road, there is a moment which tries to straighten the tyre and eliminate the camber effect. There are many suspension geometries which prevent this change of camber from happening and they can be reviewed in most vehicle dynamics texts such as Smith [1] and Dixon [16]. As a result of the resistance from the suspension geometry

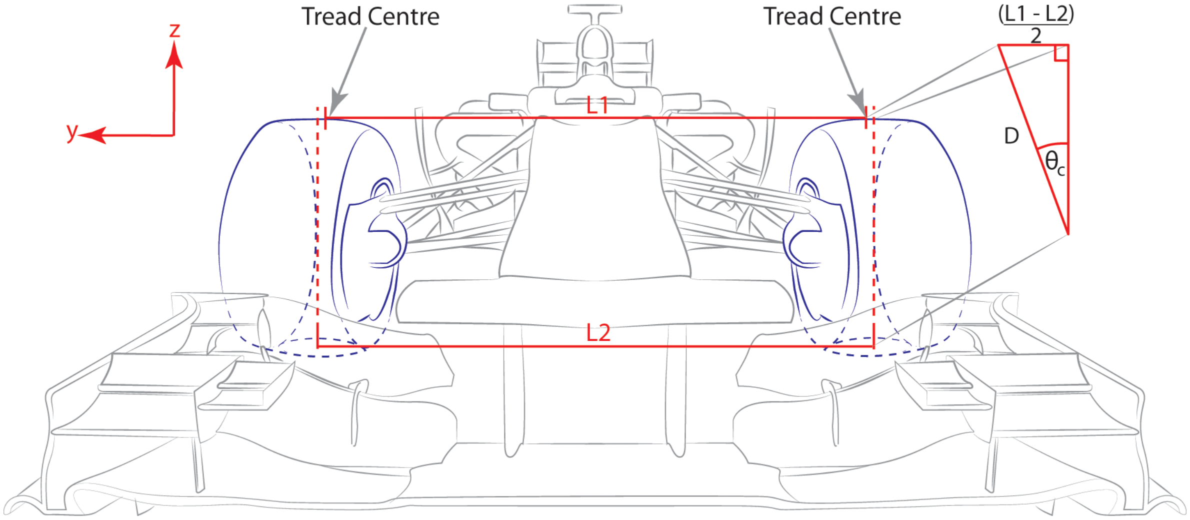

Figure 1.6: *Definition of wheel camber angle based on front track measurements.*

maintaining a constant camber angle, the contact patch of the tyre is deformed and dragged inboard (as in Figure 1.4) and ensures the entire contact patch is being utilised when it is needed most.

The above arguments can be seen in the data presented in Figure 1.7 in which the performances with positive and negative camber are presented. As a result, camber, although responsible for high and uneven tyre wear, provides improved mechanical characteristics and will therefore always be used.

As a result, this typical range of values is fairly significant and accounts for a geometrical discrepancy from the usual straight-up and straight-ahead test cases employed by the majority of aerodynamic testing. Because camber is always present at non-trivial angles, in the case of the front wheels of a racing car, the aerodynamic performance of a vertical tyre is not necessarily a sufficient testing methodology. Camber has been attempted to be modelled with rigid tyres for wind tunnel testing in the literature and will be discussed further in Section 1.2.6. This has been achieved by using a conical tyre which presents an artificial pressure gradient in plan-view and also accounts for an exaggerated angle to the road for the upper tread as illustrated in Figure 1.8.

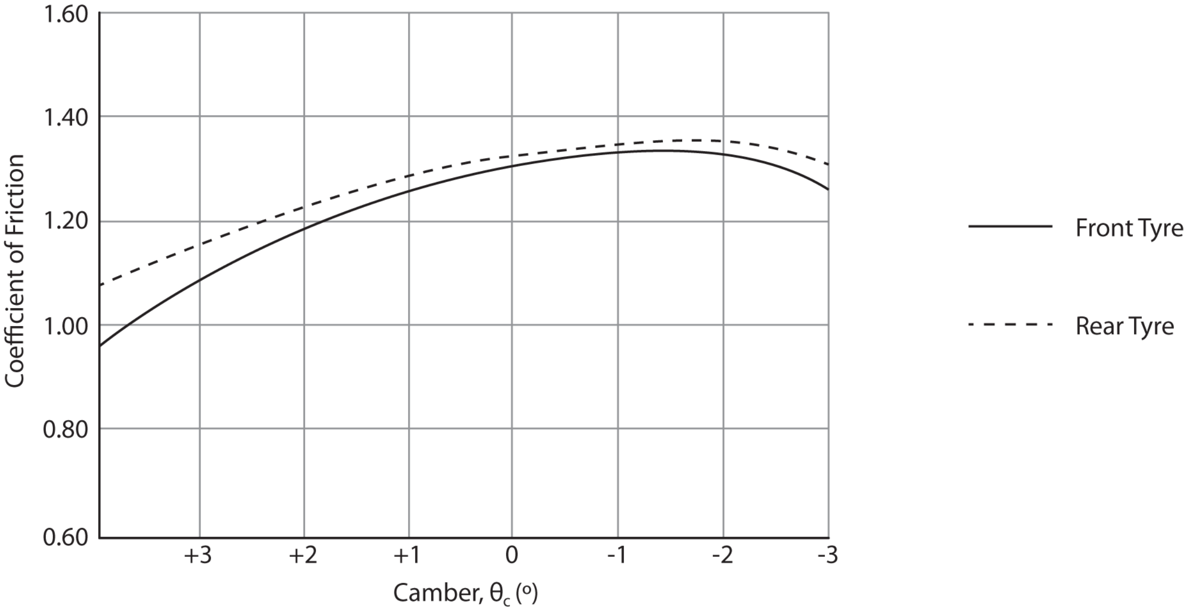

Figure 1.7: *Typical coefficient of friction vs. camber angle characteristics (modified from Smith [1]).*

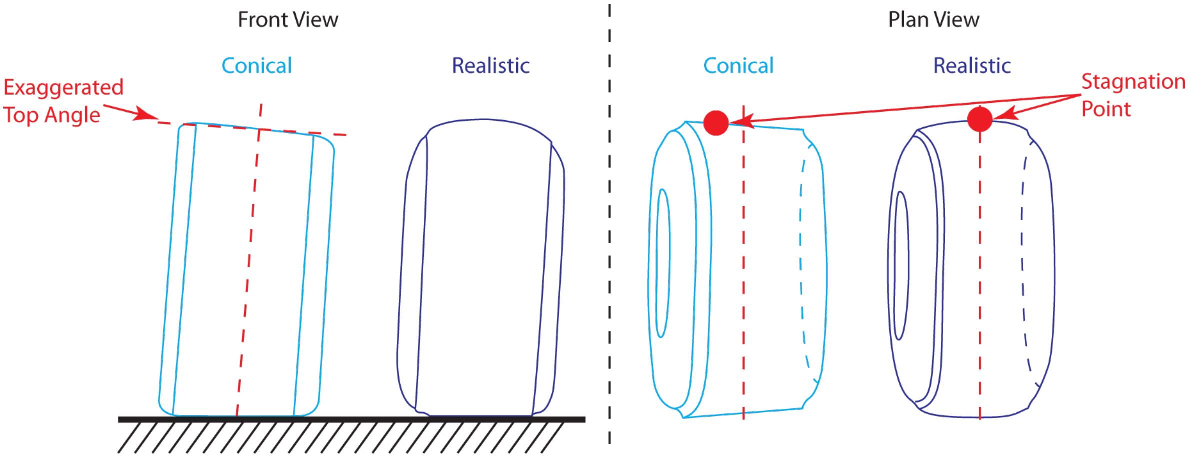

Figure 1.8: *Front and plan projections of rigid conical wind tunnel tyres compared to realistic geometry. The exaggerated camber of the upper tread and artificial outboard stagnation point are highlighted.*

1.2.2.4 Toe

Toe is another geometric setup parameter which is usually associated with stability and not necessarily in improving cornering ability. 'Toe-out' is the typical setup for front wheels of a modern F1 car, with angles of only a few tenths of a degree. This is where the trailing edges of the wheel pair are closer than the leading edges. By doing this by a small amount, small changes in steering angle become ineffective for a cornering thrust. This is useful for high-speed cars such as those in F1 in order to have stability at the end-of-straight leading into braking zone condition. In addition, the inside wheel on a corner when toeing out describes a tighter steering angle than the outside which is appropriate for the relative cornering radii experienced on slow corners. For high-speed larger radii corners the inboard tyre becomes unloaded due to roll. Therefore, the discrepancy between the steering angles, which is extreme for larger cornering radii, become inconsequential.

The constant deflection that toe provides describes an aerodynamic yaw situation. Although a small geometrical change, it is proposed that this will affect the symmetry of the contact patch vortices (see Section 1.2.6) and therefore alter the overall flow-field sufficiently to be noticeable in force measurements and downstream car development.

It can be argued that testing race cars and associated components purely in a straight line is not adequate to describe the forces at work. The aerodynamic sensitivities to the above parameters to-date have not been very well understood, modelled or even approached in some cases. It is therefore crucial to understand the wind and road direction relative to the car's motion, under the above circumstances to ensure correct modelling in a wind tunnel or CFD environment.

1.2.3 Aerodynamic Yaw, Crosswind and Steer Applicable to Race Cars

Yaw is defined as a rotation about the (vertical) z-axis, as defined in Figure 1.1. For vehicle aerodynamics, there is a need to define a distinction between two types of angular flow, yaw and crosswind. Crosswinds are gusts of natural ambient wind with an angular component relative to the vehicle trajectory. In a straight line there is no yaw effect but there may be crosswinds present. The freestream direction for ground-based vehicles is also the direction of the translational motion of the vehicle. Therefore, the relative road motion matches the freestream and the yaw angle is defined between the centreline of the car and the direction of travel (and freestream in the absence of wind). Figure 1.9 illustrates these defining principles.

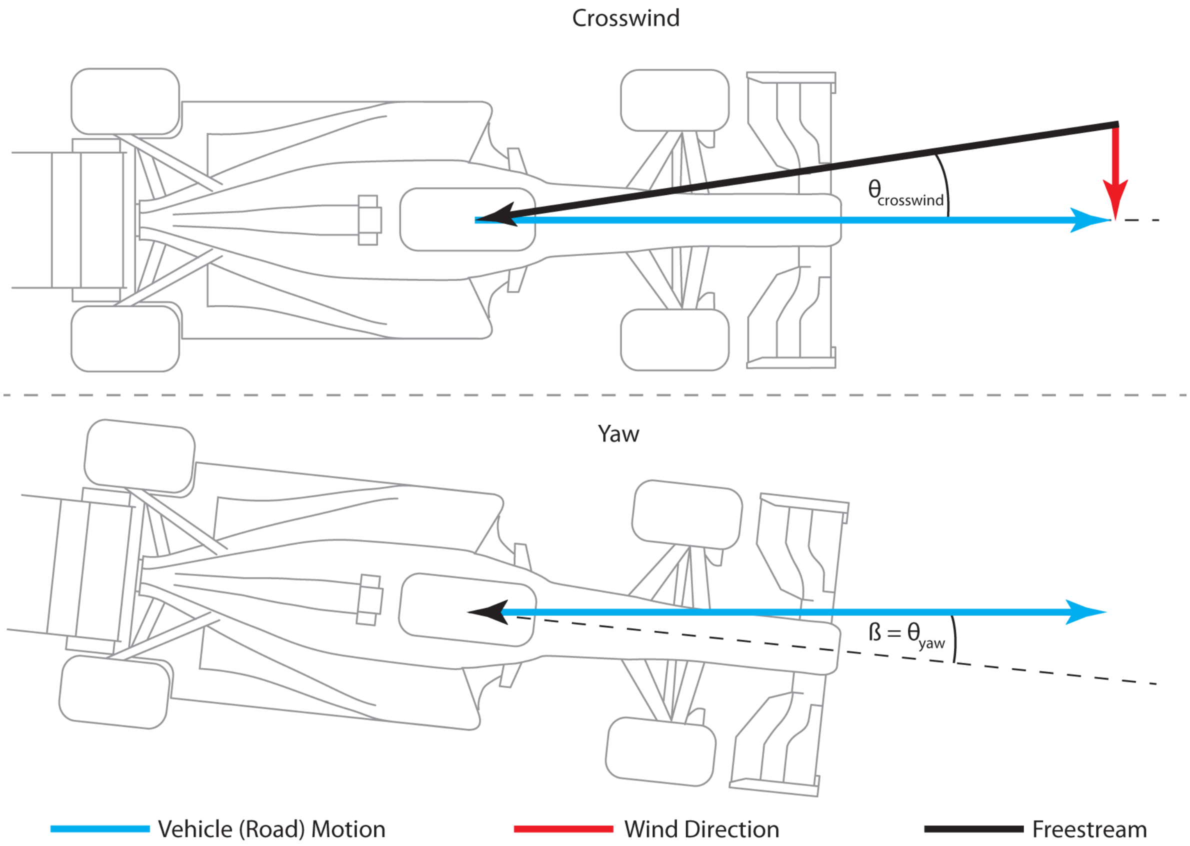

Figure 1.9: *The definition of crosswind (angle of ambient wind influenced freestream against vehicle direction) and yaw (angle of freestream (here simplified to purely vehicle direction without the influence of ambient wind) against car centreline).*

In a neutral steer situation the above scenario describes a car which rotates about its centre-of-mass (CoM) as well as the CoM moving in an arc around the corner. The instantaneous tangential direction of the CoM is therefore the vector of the road movement relative to the car. Because of this rotation about the CoM, the front and rear of the car observe very subtly different yaw conditions at the same instantaneous point in time. Although for racing cars this effect is expected to be small due to the relatively slow rate of turn around the CoM compared to the overall car peripheral velocity. The dynamics of this cornering scenario are outlined in Bastow [17].

From these definitions, a cornering scenario (Figure 1.10) can be explained in more depth. The rotation about the CoM is relative to the freestream or road direction and is therefore a yaw, not a crosswind. In addition to this, the front wheels, which provide the cornering thrust, have an additional angular component. This angle is the slip angle and the wheels observe additional aerodynamic yaw characteristics, therefore relative to the freestream and the road. Hence the total steering angle, relative to the car centreline, is the local vehicle yaw angle plus the front wheel slip angle.

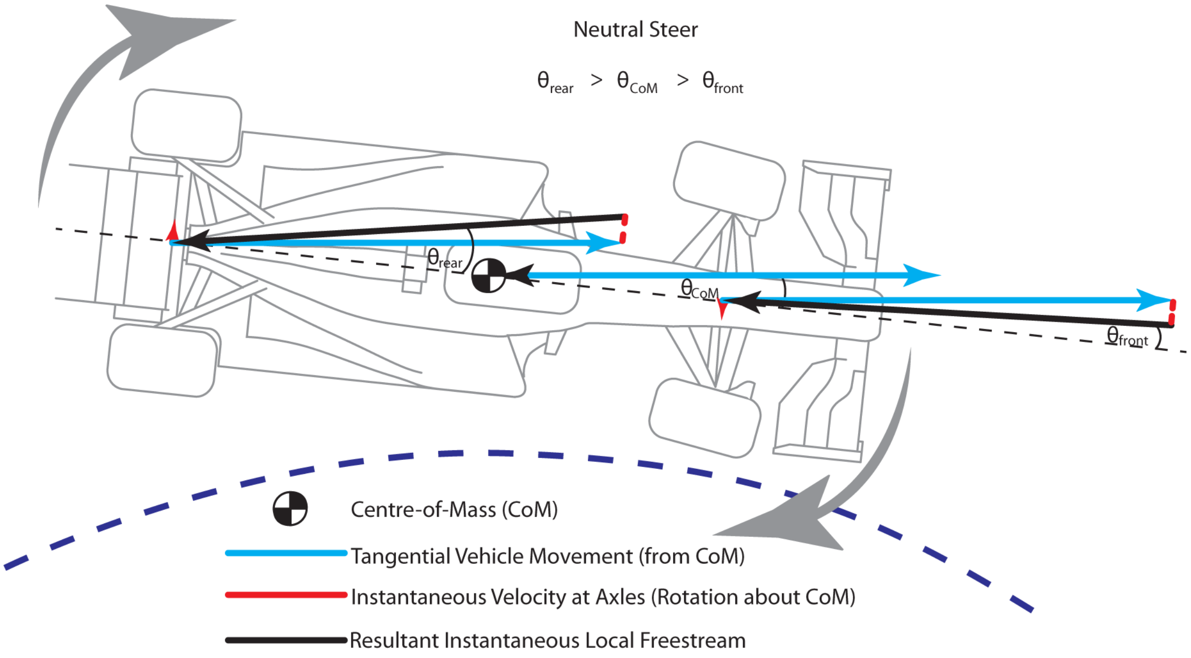

Figure 1.10: *A steady-state 'neutral steer' scenario showing the instantaneous wind directions.*

Arguably, there is more time to be gained in slow-speed corners than fast ones as proportionally more time is spent per lap in these and carrying higher exit velocities also benefits the straight-line speed following the corner.

1.2.4 Historical Studies of Wheel Aerodynamics

In motorsport, the general design philosophy is to engineer components which perform as many tasks as possible, thus reducing part-count, therefore weight and overall complexity. This ensures better performance and reliability respectively. Parts are also generally shaped with aerodynamic considerations in mind.

The wheels are one component which can neither be made to perform another task, nor directly moulded to perform an aerodynamic function. Essentially, they are designed for one purpose only, to ensure maximum traction for the four contact patches and are the only method by which the car can transfer its extreme forces to the ground. As a result, the first published studies into the flow-field characteristics of exposed rotating wheels emerged in the late 1960s, almost two decades after the inaugural 1950 season of Formula One [18]. Due to several limitations and simplifications or assumptions made during these early studies, they do not all conform to the modern accepted method of aerodynamic testing. For this reason, they are presented here in their own section for completeness.

1.2.4.1 Circular Cylinder Flow-Field

Circular cylinders are a specific type of bluff body which have been investigated in great depth in both two and three dimensions, initially with end-plates simulating an infinite aspect ratio.

Shedding vortices are a well documented phenomenon for suspended cylinders in a freestream. These occur when the air passing over the body combines in the separation region forming a base pressure and a regular periodic vortex structure in the wake of the object. This effect is particularly well known in the case of construction of cooling towers and bridges, for example in Bearman [19]. Park & Lee [20] [21] are two examples of recent hot-wire anemometer, flow visualisation and PIV studies into the effects of cylinder flow. However, as with many PIV studies in the literature, the Reynolds number is very low at Re = 7,500 but their work has particular relevance to wheel flows. They observed that changes to the tip shape, known as the ‘free-end’, despite the long aspect ratio, had significant effects on the local flow-field and shedding frequencies. This is an important observation for this work, as the shape of the sidewall of a tyre can be likened to this ‘free-end’ and for a significantly smaller aspect ratio, end-effects are known to be more dominant as discussed by Massey [22].

Free-end effects entrain onto the central cylinder flow and reduce or eliminate the regular shedding vortices [3] [23]. What is left, is the unsteady wake structure which is characteristic of such a small aspect ratio. The air cannot flow underneath the cylinder in the case of a wheel in contact with the ground. This lack of air feeding the lower wake inhibits the production of a regular vortex street. Fackrell [23] inferred similarities between cylinder flow-fields and flat-plate studies by Fail et al. [24] which show the presence of shedding vortices down to aspect ratios of one half. The current FIA regulations for F1 [25] dictate that the front wheel aspect ratio must be 0.54[1], comparable to this observation. Therefore, this gives reasonable grounding to assume there will be some element of transient unsteady flow in the wake, even if not related exactly to the shedding frequency associated with a cylinder in free air.

In addition to circular cylinder studies, there exists bluff body research in the context of vehicle aerodynamics. The studies by Bearman & Zdravkovich [26], Bearman [19] and Cooper [27] provide a transition study between the basic bluff body shape and that of a wheel or vehicle.

Cooper [27] focused on bluff body aerodynamics as applied to vehicles. This extensive review encompasses wheel rotation and ground simulation, unsteadiness and turbulent onset wind conditions and wind tunnel blockage corrections. These were subsequently applied to several case studies including an open-wheeled race car. An extensive mathematical model was presented which attempted to model the wind-averaged drag coefficient for a commercial vehicle.

Bearman & Zdravkovich [26] is a frequently cited study of the flow around a circular cylinder near a plane boundary. This work is fundamental to that of Cogotti [28] performed a few years later, and is discussed in Section 1.2.4.3. However, as the cylinder used in the case of Bearman & Zdravkovich spanned the width of the test section it exhibited no free-end effects. It is also worth noting that the plate boundary used was allowed to grow a thick boundary layer of approximately 0.8 diameters which would significantly affect the flow-field. Bearman & Zdravkovich presented base pressure measurements for varying ground clearances and inferred higher drag for cases where air was allowed to pass underneath the wheel, either entirely or partially. This has been identified as being particularly relevant for this work for camber studies where the outboard side of the wheel can be known to unload in

---

[1] Maximum width of 355mm with a maximum diameter of 660mm.

a straight-line condition. Their review of circular cylinder aerodynamics is particularly comprehensive and calls regularly upon potential flow (or 'imaging') theory for the case of a bluff body near a wall. This describes the effect of vortex shedding at various clearances and the dependence on the 'mirror' body in the downstream wake.

The interested reader in such fundamental background is directed to their work and to the later review by Bearman [19]. The latter is particularly applicable to wheels and vehicle aerodynamics as opposed to fundamental bluff body theory.

1.2.4.2 The Magnus Effect

The Magnus effect, as discussed by any fundamental fluid dynamics text such as by Massey [22], is harnessed in many applications of aerodynamics. Various examples include incorporating a rotating cylinder into the leading edge of an aerofoil (Clarke [29]) in order to increase the stall angle of the wing, or as an alternative to wings entirely (Swanson [30]). The effect has been very important in military history and many sports to explain curving ball movements. The Magnus force is dependent upon the rotational angular velocity, the translational velocity of the object and the size of the object.

For the case of a cylinder rotating forwards, as is the case for a wheel, the lower pressure forms below the cylinder and therefore downforce is generated. However, despite being historically one of the prime arguments for flow-fields of rotating cylinders the effect is of limited use in terms of explaining wheel aerodynamics due to the fact that as soon as the cylinder, or wheel, comes into contact with the ground, air can no longer pass underneath the object the effect no longer occurs. The air is instead forced over the wheel and forms a lower pressure on the upper surface, resulting in time-averaged lift.

1.2.4.3 The First Wheel Aerodynamics Studies

Initial investigations into the aerodynamic properties of wheels were in relation to a suspended aeroplane wheel which was neither rotating nor in ground contact. The relevance of freestream studies to road vehicles is questionable and the work of Clark [10] was the first to make steps towards investigating ground contact. This work was, however, mainly based on the theoretical and mathematical background of the interaction with the ground from a mechanical perspective and no significant aerodynamic experimental observations were made until those of Morelli [31].

Morelli's work was the first significant study of wheel aerodynamics although it is well documented that simplifications made in the experimental procedure led to erroneous conclusions. A load-cell or mechanical force balance measurement of lift for a rotating wheel includes a reaction force with the ground which is known to vary and is therefore indeterminate (Mears [3], Whitbread [5], Fackrell [23], Hinson [32] and McManus & Zhang [33]). It is a contentious issue as to whether separating this varying reaction force from the load-cell measurement gives a reliable measurement of lift. Due to this, Morelli's plan was to lower the tyre into a recess cut out of the stationary floor. This ensured a rectangular contact patch shape and allowed the use of load-cells to take measurements. Figure 1.11 shows this experimental setup.

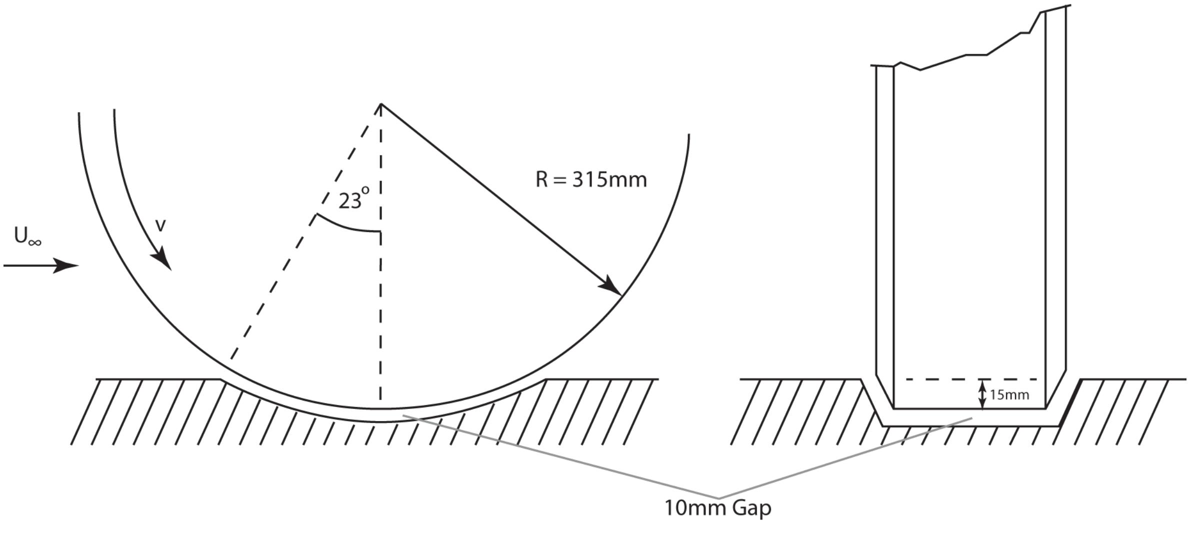

Figure 1.11: *Schematic of the experimental method applied by Morelli [31]. Illustrating the concept of the wheel suspended in a floor recess to allow load-cell lift measurements.*

The issue with this methodology arises from the gap which appeared underneath the tyre. Indirectly, this allowed a venturi effect to dominate the results as the accelerated air underneath the tyre caused a low pressure. This resulted in negative lift conclusions. As significant as this was at the time, being consistent with the predictions of the Magnus effect, the conclusion was quickly dismissed, at first by Stapleford and Carr [34] discussed in more detail below.

In addition to having the gap below the wheel, there was no moving ground plane which is now accepted as necessary for wind tunnel testing of rotating wheels. Without the moving ground plane, the airflow of a moving body cannot be effectively simulated. The airflow entering the wind tunnel builds up a boundary layer and this boundary layer creates a non-uniform velocity profile at the surface, and most importantly, at the contact patch of the tyre. Bleeding off the boundary layer using suction and simulating ground movement with a moving ground plane allows this non-uniform velocity profile to be minimised. Section 1.2.5.1 discusses in detail some of the relevant studies on this topic.

Stapleford and Carr [34] investigated the aerodynamic effect of a wheel on a full vehicle. Their work used the same methodology as Morelli [31] but they sealed the gap between the tyre and ground with strips of paper (so as not to transmit force in the process). They concluded that the time-averaged positive lift and drag forces were decreased by the rotation of the wheel. In addition to their simple but effective flow visualisation experiment shown in Figure 1.12, they investigated the surface pressure distribution. Their conclusions observed early separation and gradual introduction into turbulence in the rotating wheel case. Without the presence of the sudden large reduction in pressure, as seen in the stationary wheel case, it is accepted that the rotating case produces lower drag forces. The fact that the airflow is attached for less of the upper surface implies a lower lift force.

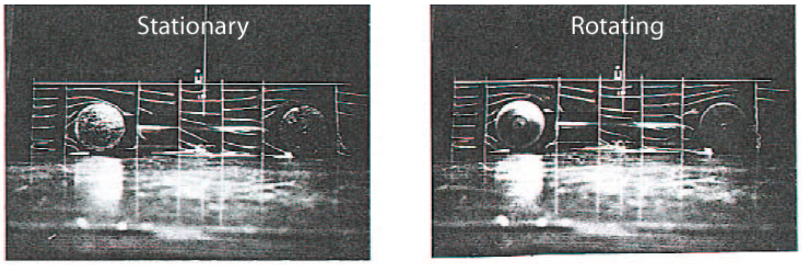

Figure 1.12: *Photograph of the flow visualisation experiment by Stapleford and Carr [34] showing the earlier separation of a rotating wheel (right) compared to that of a stationary wheel (left).*

Cogotti [28] followed the work of Stapleford & Carr and Morelli by investigating the pressure distribution over a rotating wheel at varying ground clearances. This proved the concept of the venturi effect influencing the results of Morelli and combined with the Magnus effect in ground proximity (for larger clearances) resulted in negative lift. Figure 1.13 illustrates the pressure distribution for varying clearances and confirms the understanding of the source of Morelli's data.

Cogotti's experimental procedure was similar to that of Stapleford and Carr [34] as there was no moving ground plane. The wheels were rotated using an AC motor mounted only 250mm from the full sized wheel. The gap underneath the tyre was filled with a solid foam block. The fact the motor housing was in such close proximity to the wheel would have influenced the results significantly, however, and this fact was self-confessed in the publication.

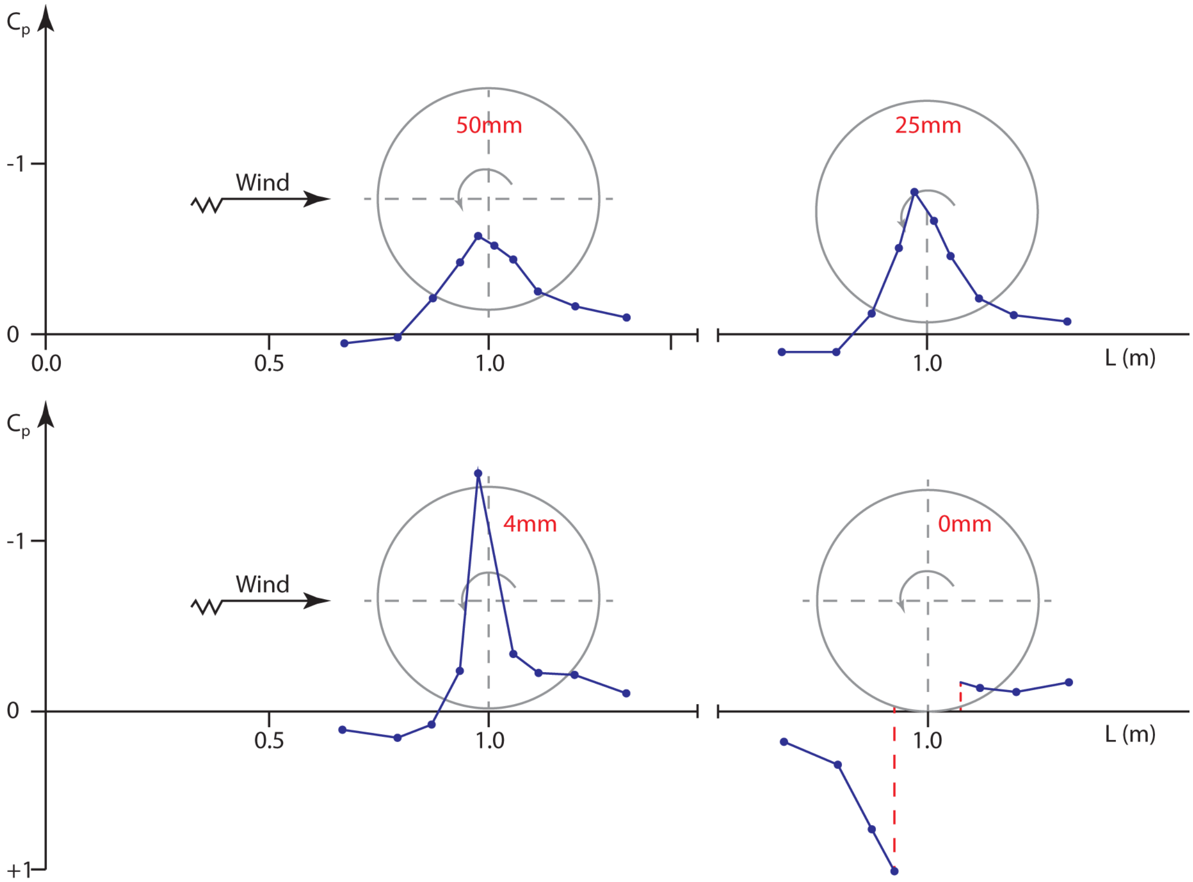

Figure 1.13: *The pressure distribution around a rotating wheel with varying ground clearance (modified after Cogotti [28]).*

Cogotti's results proved to be fairly conclusive and showed that for standard non-faired rims, the effect of rotating a wheel reduced the drag by around 4% and the lift by around 34%.

Cogotti also presented results of an investigation into yaw angles although these were only for the case of a stationary wheel. What was observed was a sinusoidal relationship between the drag coefficient and the yaw angle with a peak around ±15° and a minimum at 0° and 30°. This observation, however, could be skewed by the method of measuring drag, given the drag force is measured perpendicular to the axle. Given the above discussion of slip angles (Section 1.2.1), the axle drag is not necessarily in the same direction as the drag vector of the vehicle.

1.2.5 Closed-Wheel Aerodynamics

Unlike the scope of this work, which investigates the aerodynamic characteristics of open-wheeled formulae, there has been a more focused interest in the literature in observing the flow-field effects due to the presence of wheel housings. This is primarily for production vehicle appeal, in terms of sales figures and increased perception of quality relating to aeroacoustics and soiling, as covered by Regert & Lajos [35] and Gaylard & Duncan [36].

The enclosed wheel cases will be addressed here, for completeness, and the following section will describe in more depth the work that has been carried out in isolated open-wheeled experiments.

The conclusions reached by Stapleford and Carr [34] not only provided a description of the testing parameters which must be observed for wheel testing, but also the trends in the drag and lift forces between stationary and rotating cases. It has been noted by several authors that the presence of a wheel arch or housing complicates this flow significantly. Bearman et al. [37], Wiedemann [38] and Mercker et al. [39] all agree with the drag trends of Stapleford & Carr [34]. Axon et al. [40], however, describes a reversed trend whereby drag increases in a wheel housing with wheel rotation. Therefore, there is evidently a sensitivity when studying the effect of the moving ground simulation affecting both the magnitude and trends of forces in addition to the general flow-field.

A typical enclosed flow-field describes a significant outwash (negative y-direction) behind the wheel. The presence of a wheel and wheel housing, compared to a shrouded vehicle design (i.e. without wheel aerodynamic influence), is shown to be responsible for a significant drag increase. Wickern et al. [41] described the Audi A3's wheels and wheel arches as being responsible for 30% of the total drag of the vehicle. Regert et al. [42] and Elofsson & Bannister [43], who will both be discussed later in this section, also commented on this significant observation. The latter work describes the contribution as being around ΔC_D = 0.07 - 0.08 ($\sim$ 25%) and produced a mathematical model of the contribution towards the drag, shown by

$$C_D^{total} = C_D^{body} + \Delta C_D^{wheel\&housing} \tag{1.1}$$

and

$$C_D^{wheel\&housing} = \Delta C_D^{direct} + \Delta C_D^{bodyinterference} \tag{1.2}$$

1.2.5.1 Ground Simulation

For production cars, even in the present day, it is common practice to test a full-scale vehicle inside a wind tunnel with static wheels and little or no ground simulation. Wiedemann [38] investigated the importance of ground simulation, summarising the comparative force measurements using different techniques used to remove the boundary layer established upstream of the test vehicle. Figure 1.14 shows how the drag coefficient can change by as much as 8% depending on which ground simulation technique is adopted for the case of rotating or stationary wheels with varied cooing flows through the radiator. The full-width moving ground plane or belt is described as the most realistic condition given this provides both wheel rotation as well as removing boundary layer conditions due to the no-slip condition of the moving floor. Bearman et al. [37] goes as far as stating "It has been our experience that unless particular attention is paid to obtaining a uniform flow, any influence of the floor movement on vehicle aerodynamics can be masked". This statement emphasises the necessity to have efficient boundary layer suction as well as the moving ground condition.

This is particularly relevant for racing cars due to a ground clearance of less than 0.01L (where L is the length of the vehicle). Production vehicles approach much larger ground clearances of 0.05L making the simulation of the ground a contentious topic for discussion. Elofsson & Bannister [43]

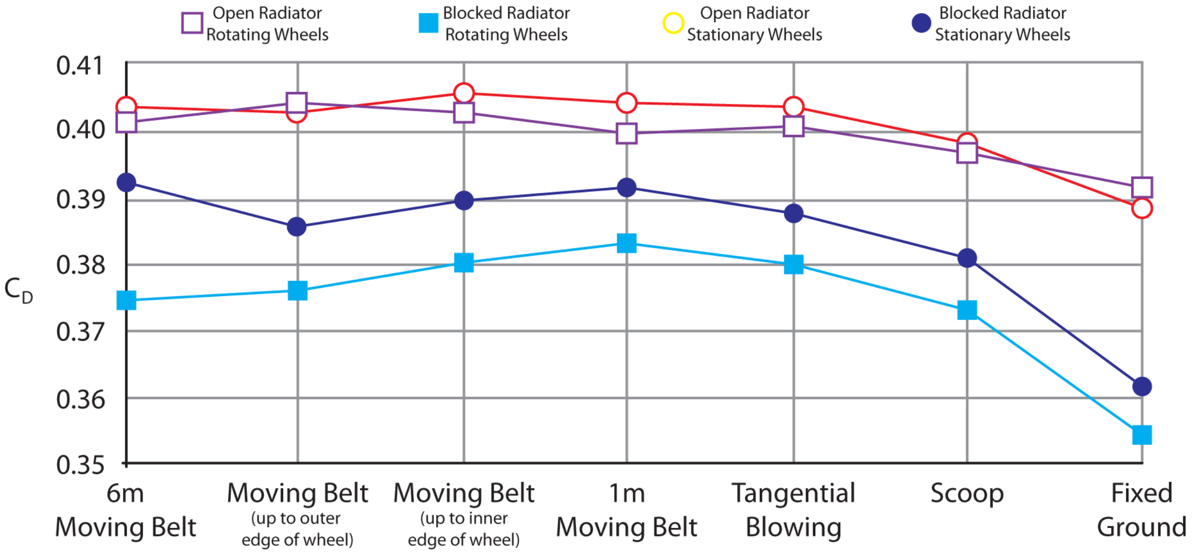

Figure 1.14: *AfterWiedemann [38] (modified) showing the sensitivity of a model vehicle on the ground simulation technique, with and without engine cooling internal-flow.*

illustrated that the reduced momentum losses present in the turbulent wind tunnel boundary layer can be responsible, in the case of a wheel in a wheel arch, for producing a higher dynamic head incident on the wheel therefore higher measured drag. Likewise, the momentum losses present can influence the measurements of the wake leading to false drag estimates using the wake integration method, as discussed by Bearman et al. [37] and Wiedemann [38].

Other techniques outlined by Bearman et al. [37] are not too dissimilar to the aforementioned case. However, the roller method of rotating the wheels clearly provides some form of discrepancy. This is possibly due to the local contact patch crosswind flow in the case of front wheels which will be discussed later. It is conclusive, however, that the lack of a moving ground such as using a scoop, tangential blowing or nothing at all, provides completely different results from a full ground simulation. The discrepancy between the values given here suggests that “this might mean that if the test engineer is using classic ground simulation in a wind tunnel, he will make the aerodynamics worse on the strength of the measurement data for the car” (Bearman et al. [37]). That is indeed the case for production vehicles but even more so for competition cars. The effectiveness of a rear wing on a 2.5 litre competition touring car is shown to have a reversed performance trend when ground simulation methodology changes [37].

1.2.5.2 Local Contact Patch Flow Angularity (Closed Wheel)

Wiedemann [38] also observed flow angularity for the contact patches of the wheels. The term 'yaw' needs to be interpreted with care, particularly in wheel studies where both yaw and local crosswind can be present. To reiterate, yaw is an angular difference between the vehicle's motion, which is represented by the vector of the ground plane movement, and the vehicle's centreline. Crosswind is where the freestream is at an angular incidence to both the vehicle and the road motion (the vehicle's trajectory). In the case of the local flow around a front wheel for straight-ahead studies, the motion of the road is aligned with the vehicle centreline but the deviation of the onset flow to the wheels is angular to both of those. This is, therefore, a crosswind by definition although it is commonly generally referred to as yaw. The local flow angularity is also discussed in Regert & Lajos [35] [42]. Wiedemann observed that the closing of the radiator duct causes a reduced front wheel yaw angle, from around 4° to around 3.5°. This was due to a reduced mass-flow exiting the engine bay through the wheel arch.

In a racing environment, yaw or crosswind angles will never be as large as 20° under controllable conditions. Figure 1.15, after Cooper [27] describes the probability of observing certain yaw angles at a range of velocities. Low-speed corners are more susceptible to high aerodynamic yaw angles and therefore, since a larger proportion of time is spent in the slower corners than the faster ones, the performance of a race car is arguably significantly improved over the course of a lap by reducing its sensitivity to yaw angles. This figure was produced based upon the reduction of the significance of non-longitudinal wind directions and was therefore intended as a crosswind study. The application to high-speed cornering scenarios is taken to have the same behaviour, again, due to the higher longitudinal vehicle speed reducing the influence of any yawed onset flow.

The work of Regert & Lajos [42] characterises the effect of the contact patch crosswind flow in the case of an enclosed wheel. Therefore the onset flow of an enclosed wheel is non-uniform. One could argue that the onset flow of an exposed racing wheel is also non-uniform due to the upstream components such as the front wing. As a result, care must be taken when interpreting results from a uniform wind tunnel test in terms of appreciating the requirement to understand the isolated pressure gradients and flow-field behaviour with local changes, but not necessarily defining the absolute flow-field of a real-world application.

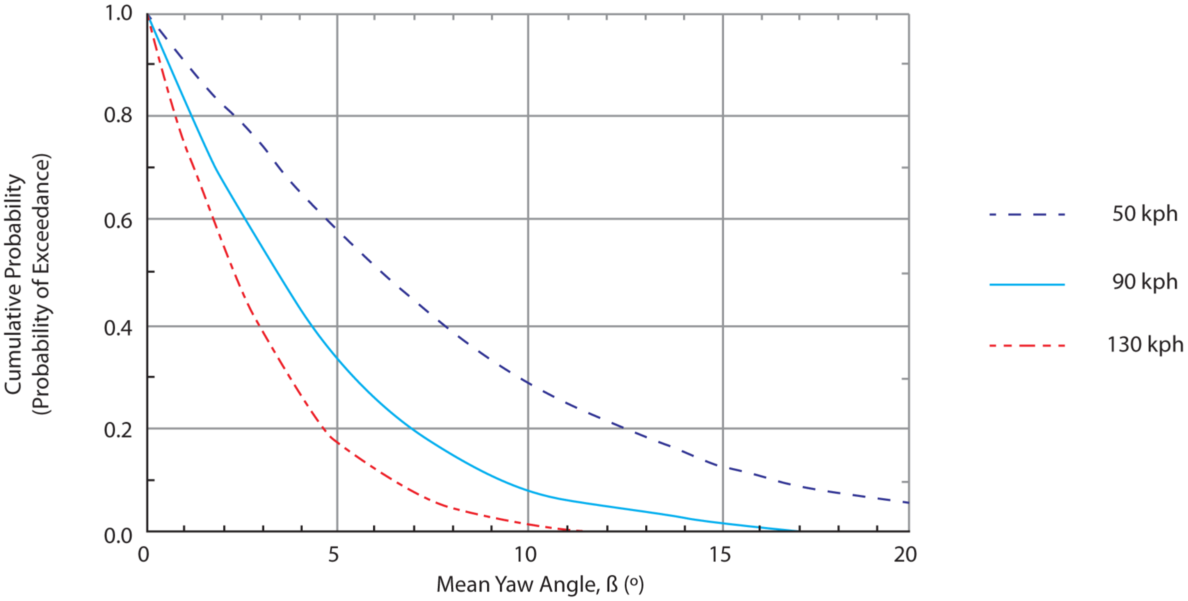

Figure 1.15: *After Cooper [27], illustrating the cumulative probability (or instantaneous probability of exceedance) of yaw angles at varying velocities.*

1.2.5.3 Global Flow-Field (Closed Wheel)

An unsteady CFD simulation (URANS) of a simplified car model, taking many design principles from the standardised Ahmed body [44], but containing a wheel housing, was tested by Regert & Lajos [42]. This evaluated the wake depending on the length of the body and again, the effects of wheel rotation. By varying the length of the fore-body, the flow angularity was noted to change significantly. For a single wheel diameter length fore-body, a contact patch 'yaw' angle of 9.18° was observed. This reduced to 7.50° for two diameter fore-body and for an 'infinite' fore-body, this reduced further to 2.85°.

A vortex skeleton method was used as a method of visualising the vortex structures emanating from the wheel housing. A series of wheel-specific vortices were identified and discussed in relation to the fore-body length. The dominant vortices form on the inboard shoulders and contact patch of the tyre and are extracted from the wheel housing with only one strong vortex continuing beneath the vehicle. By changing parameters of the wheel housing design, the strength of these inboard vortices as well as their directionality was severely affected.

These structures have a significant effect on drag, due to high-loss low-pressure cores; and lift, due to their low-pressure cores acting underneath the floor of the vehicle, combined with their high rotational stability preventing cross-flows, which may reduce underbody cross-flows.

For production vehicles, vehicle soiling, particularly in and around the wheel arches severely affects the customer's perception of the quality of a vehicle [36]. Therefore, significant effort is made to control or add to these structures in order to address these issues depending on the prime function of the vehicle.

The force measurements by Regert & Lajos [35] exposed another sensitive area when investigating the distance between the axle and the base of the vehicle. For the case of a front wheel where the distance to the base would be very large, in fact much larger than tested by Regert & Lajos [35], it is suggested that the drag would be higher than that of a rear wheel. The lift, on the other hand, would be considerably lower. All of the force measurements were confirmed by equivalent changes in base pressure.

A significant asymmetry was noted in the flow-field dominated by large outwash regions behind the tyre. A large separation on the outboard side of the wheel was noted, very likely due to the local contact patch angular flow. Outboard hub-side recirculating regions were identified at ground level.

Axon et al. [40] investigated both experimentally and computationally the effect of the ground condition on the flow around a wheel in a wheel housing. The geometry used was a non-symmetric design with narrow aspect ratio wheels and a narrow housing and body. This will have reduced the crosswind effect of the contact patch as described above but is also of significantly different design to those normally tested. Indeed, their conclusion was a reversal of the trend usually observed between a stationary and a rotating case.

The total drag was noted to have increased by rotating the wheel by $\Delta C_D = 0.012$ and 0.019 for experimental and CFD methods respectively. Similarly the wheel specific component of this was reported to have increased by $\Delta C_D = 0.027$ and 0.022 for the same conditions. The CFD and experimental methodologies therefore seem in good agreement with each other suggesting geometrical effects are responsible for the reversed trend.

The conclusion is consistent with Elofsson & Bannister's [43] work showing that the reduction of the drag on the front wheel, due to the rotation, can be masked by the incurred losses from downstream effects in the wake and vortex structure changes. This effect can be further explained by one of the mechanisms described by Wiedemann [38] as being responsible for a significant proportion of the drag reduction. This is the effect of flow straightening due to the moving ground plane, reducing the front flow angularity. With this angularity minimised to begin with, the effect of adding a moving ground plane and wheel rotation will be less significant and can be dominated by the downstream losses.

Elofsson & Bannister [43], aside from presenting a clear and concise review of enclosed wheel and ground simulation aerodynamics, presented experimental evidence of only 40% of the change in front wheel force to be present in the vehicle's base pressure profile. By this, the prediction of the local force change by integrating the pressure of the wake at the rearmost point of the vehicle (the base pressure) was only 40% of the change actually observed. This was obtained using an array of static pressure spades and 14-hole probe survey at 'Pininfarina', Torino and the 'Volvo' wind tunnel in Gothenberg. The force change from rotation of the rear wheels, however, was fully represented by the base pressure profile. This is logical, given the rear wheels are closer to the base of the vehicle and therefore there is a much smaller distance for the wake to be dissipated, re-energised by other components or washed out of the vehicle's cross-section altogether before reaching the base.

Dimitriou et al. [45] investigated the pressure distribution over the wheel surface (more in Section 1.2.6). The angular resolution of surface pressure measurements was 0.72° and the data were downloaded using an Ethernet cable at the end of each run. The work paid particular attention to the comparison between isolated wheels and enclosed wheels. The investigation included a 50% scale BMW Z4 sports car for which they investigated the effect of placing the wheel in a housing and the effects of wheel fairings and wheel spoilers. The tested wheel was of aluminium construction and had four grooves simulating a tread pattern with a built-in 2° of camber, therefore conical in plan-view.

The presence of the grooves was described as being responsible for the reduced 'jetting' effect observed. Jetting is a flow-field phenomenon characteristic of rotating wheels in ground contact and is driven by the interaction of shear-layers on the forward rotating cylindrical bluff body with the longitudinally moving ground plane. This concept is covered in much more detail in the isolated wheel section.

The reduced jetting is noteworthy since the grooves in the ‘full wet’ tyres used in F1 today are each known to displace 60 litres of water every second at top speed [46]. In drier conditions, air will follow these paths and significantly change the flow-field.

The rear jetting (jetting effect behind the contact patch) was, however, still observed. The suction peak in reference to the grooved and slick tyre respectively were said to be due to the accelerated air in the former case and a ‘suction cup’ in the latter.

The wheel housing covered around 80% of the frontal area of the tyre and highlighted some interesting effects including trapped recirculation bubbles of air between the housing and the tyre. These contributed towards consistency with other reports [34] [37] [38] [39], large drag coefficient for the enclosed case. Despite this, introducing the wheel housing was reported to have reduced the drag by a significant 50% and introducing a wheel spoiler (sometimes referred to as an ‘air dam’) just in front reduced it by a further 35%. The former is largely inconsistent with the above reports although the use of a full and detailed model car, coupled with such low ground clearance compared to the majority of the above tests, may be responsible for such a trend. Aerodynamic lift, measured using an under-belt load-cell [47], had a similar reduction whereby introducing the housing alone dropped this value by a significant 75%. Although concerns can be raised at the presence of load-cell data used for lift.

1.2.6 Isolated Open-Wheel Aerodynamics

The study of isolated wheel aerodynamics is one which is becoming increasingly more established. Advanced studies are now being performed to include partially deformable tyres, complete hub assemblies and surrounding geometry. Due to this reason, this section will summarise the most significant published results and will review those most applicable to the advanced study to be undertaken in this work.

1.2.6.1 Fackrell's Jetting Phenomenon

The work of Fackrell [23] is the most cited in the field of rotating wheel aerodynamics and his thesis led to some important conclusions and predictions. He investigated six different wheels of aluminium construction comprising two subsets of different sidewall shoulder profiles in complete ground contact within the supercritical fluid flow regime. He postulated that there should exist a large peak followed by a trough in the static pressure distribution around the treadline at the contact patch (Figure 1.16). His experimental work comprised a set of pressure tappings distributed across half of the tread of each wheel which were each attached via slip rings to a common data logger situated on the axis of rotation to eliminate centrifugal effects. The data were not interpreted in real time and were extracted subsequent to the experimental procedure. The resolution of the experiment was 0.5°, compared to the 30° sampling period of Stapleford & Carr [34].

His findings (Figure 1.16) confirmed the positive peak which displayed pressure coefficients in excess of unity. A pictorial description of this concept shown in Figure 1.17 shows the local analytical flow-field and shear-layer behaviour at the tyre's surface. By deconstructing the suggested processes involved, it is clear to see that viscous effects created by the intersecting shear-layers at the frontal contact patch create this high pressure coefficient. In essence, work is being done on the air by the moving parts, referred to as "Fackrell's jetting phenomenon" in various publications. Fackrell & Harvey [48] published a brief paper which focused on this jetting concept while a second paper focused on the aerodynamics of tread patterns and illustrated a situation whereby introducing grooves or a simple tread pattern into the wheel would introduce some of the low underside pressure concepts observed by Morelli [31], Stapleford & Carr [34] and Cogotti [28].

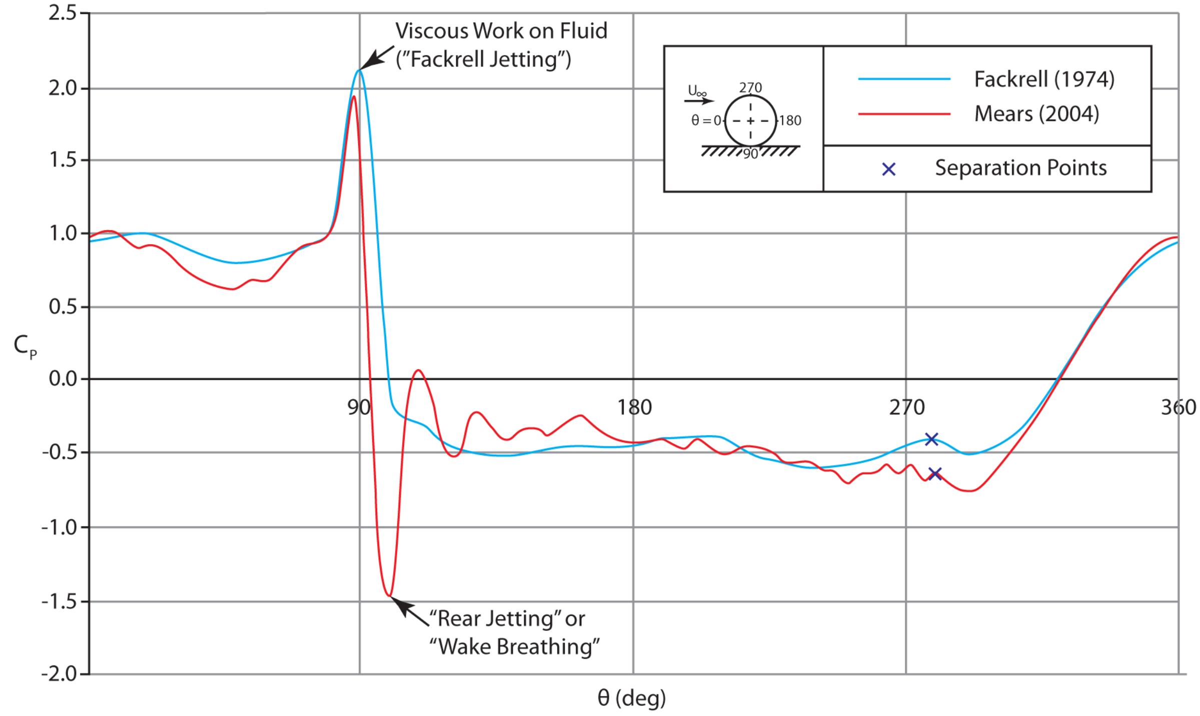

Figure 1.16: *Pressure distribution of a rotating wheel (Mears [3] and Fackrell [23]).*

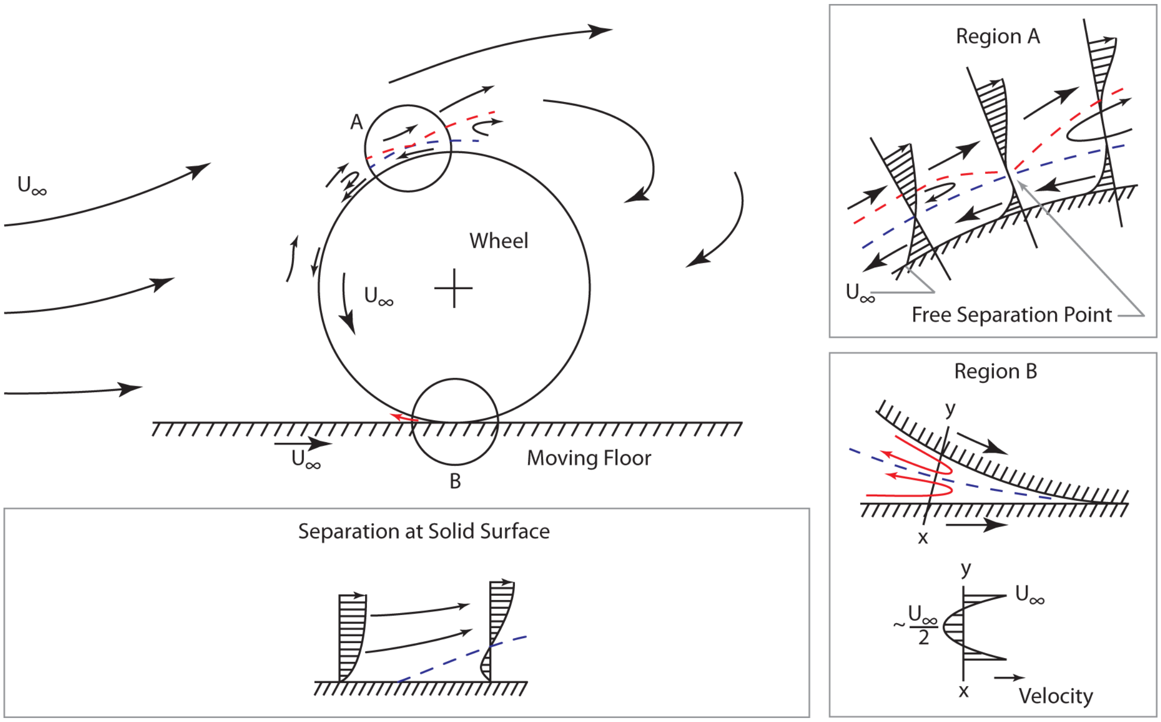

Figure 1.17: *The separation point and jetting flow of a rotating wheel, after Fackrell [23] (modified).*

Axon et al. [40] also observed the strong jetting effect for a wheel in a wheel housing and concluded that the presence of the jetting phenomenon appears to be independent of wheel geometry.

Fackrell's pressure distribution in particular has been one of the most significantly cited results in the field, demonstrating many properties of a rotating wheel at speed. It is possible to identify the point at which the airflow separates and this is commonly found to be around 280-290° where this angular convention is defined in Figure 1.16. Fackrell also predicted a negative peak shortly after the contact patch although he was not able to detect it experimentally. However, it was subsequently identified by other researchers including Hinson [32] and Mears [3] (Mears et al. [49] [50] [51]).

1.2.6.2 Aerodynamic Effect of Aspect Ratio

As many theoretical flow-field studies have been performed on high aspect ratio, infinite span two-dimensional circular cross sections, there is scope for understanding the effect of lowering the aspect ratio of the cylinder. Figure 1.18 shows Fackrell's combined work of several authors illustrating the effect of varying aspect ratios on the drag coefficient.

The drag coefficient is reassuringly observed to tend towards the two-dimensional solution with increasing aspect ratio. This was explained by Fail, Lawford & Eyre [24] in such a way that increasing aspect ratio produces a lower base pressure behind the object.

However, due to the free-end effects of a non two-dimensional system, the airflow around the sidewalls of the tyre is therefore significant and is discussed by Fackrell [23].

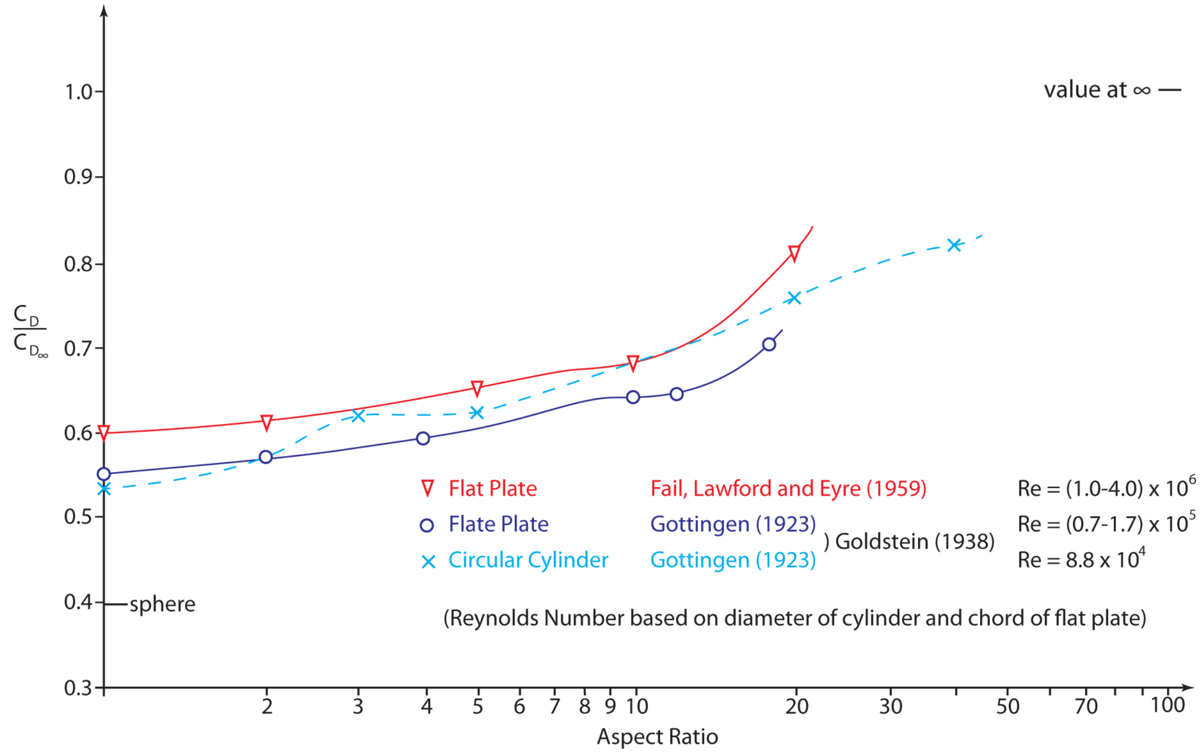

Figure 1.18: *After Fackrell [23], showing the combined work of others in the study of comparing the effect of aspect ratio on the drag coefficients.*

1.2.6.3 Effect of Fluid Flow Regime

Many published works refer to the necessity of running simulations in the supercritical (transient) flow regime so that the flow is fundamentally the same as the real-world scenario in terms of the location of transition to turbulence. For racing cars this corresponds to $Re = 4 \times 10^5$ to around $Re = 4 \times 10^6$ (using the wheel diameter as the characteristic length). The well known Reynolds number, the ratio between inertial and viscous forces of a fluid flow, is defined by

$$R_e = \frac{\rho U l}{\mu}. \tag{1.3}$$

For half-scale model testing achieving airspeeds of twice those on-track (required to match the Reynolds number) is not feasible in automotive wind tunnel testing. However, in the case of air passing over a rotating wheel, the supercritical regime Reynolds number is achievable as it spans nearly two magnitudes and the full range of racing car speeds is well encompassed by this region.

1.2.6.4 Effect of Peripheral Velocity (Rotational Frequency)

Clarke [29] summarised his own studies together with those of Swanson [30] and Tanaka & Nagano in order to validate the important principle that air flows around a rotating suspended cylinder can be classified into two regions as depicted in figures 1.19 and 1.20.

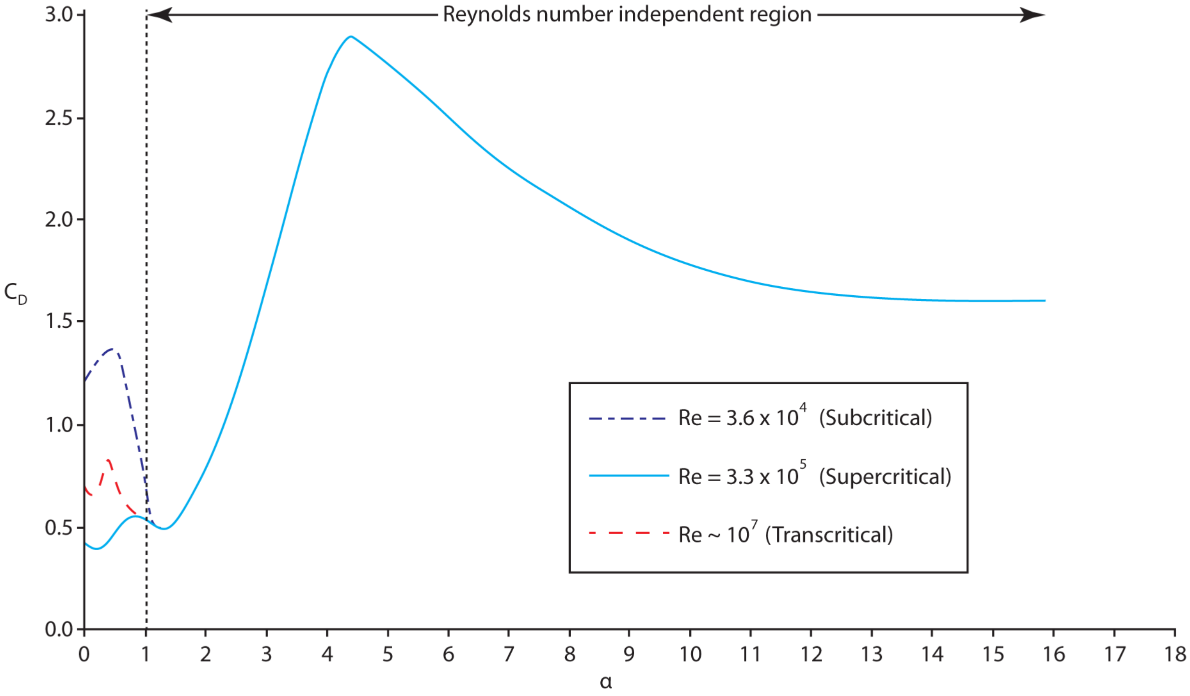

Figure 1.19: *Drag coefficient for a rotating cylinder illustrating three distinct regions below* $\alpha = 1$ *which converge to produce one single flow-field. After Clarke [29], in turn illustrating Swanson's data [30].*

The first region, where the peripheral speed of rotation is less than that of the freestream ($\alpha < 1$), is a highly Reynolds number dependent region whereby one can have completely different wake structures, drag and lift forces depending on whether the test subject is in the subcritical, supercritical or much higher transcritical region. However, once the ratio between the rotational velocity of the cylinder matches that of the freestream velocity ($\alpha = 1$) the aerodynamic coefficients converge in order to produce what is assumed to be a unified flow-field. Fackrell [23] also presented similar results in his thesis but they were not as conclusive. He combined the results of others to produce a similar figure to figures 1.19 and 1.20. Although a full convergence was not found at $\alpha = 1$, this could be explained by different aspect ratios being used between the sources. Despite this, the trend shows the results beginning to converge which strengthens Clarke's concept.

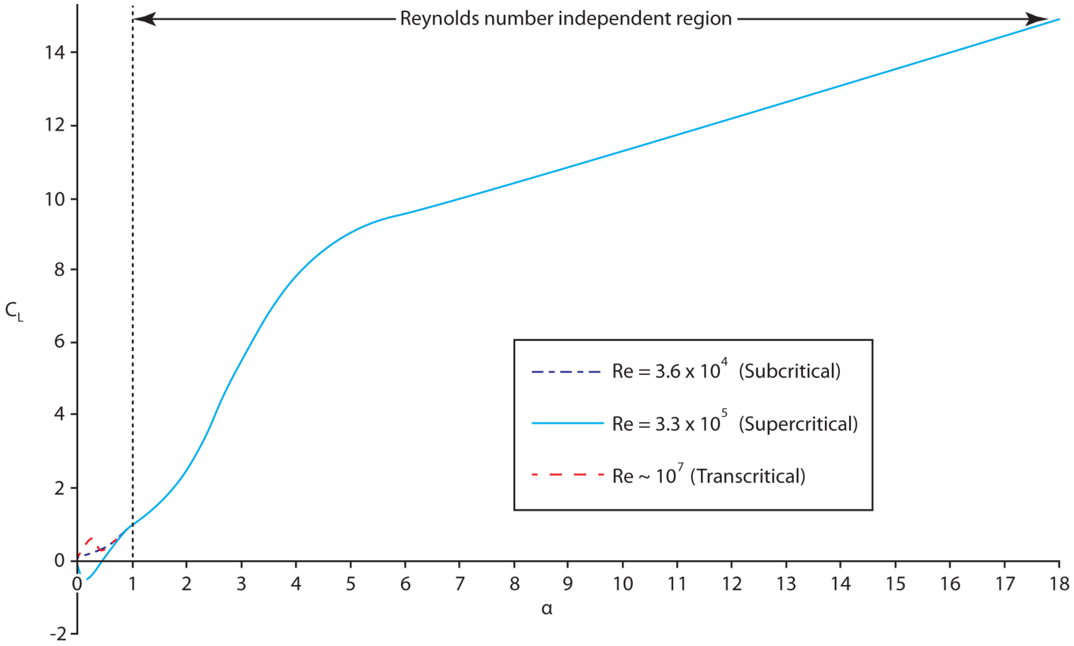

Figure 1.20: *Lift coefficient for a rotating cylinder illustrating three distinct regions below* $\alpha = 1$ *which converge to produce one single flow-field. After Clarke [29], in turn illustrating Swanson's data [30].*

In the absence of slip the wheels rotate at the same peripheral speed as the freestream. It is essential when setting up any experiment to ensure this is the case. It is, however, a test parameter very easily overlooked as in the case of Purvis [52], for example.

1.2.6.5 Global Flow-Field (Isolated Wheel)

Kellar et al. [4] published a study focusing on drag measurements, low Reynolds number smoke visualisation and CFD of a full front-right quarter of an F1 car. This comprised bodywork, suspension (faired and non-faired) and most significantly, a front wing with changeable end-plates. The scope was very broad for a single publication. Some compromises were made in experimentation such as performing CFD and low Reynolds number simulations on a stationary wheel. There was also a hinted presence of a clearance of the wheel, relative to the ground plane.

The authors emphasised that F1 flow-fields are dominated by strong vortical flows, particularly from the contact patch, upper shoulders and front wing end-plates. The force measurements performed in a 2m^2 wind tunnel with a velocity of 38.5ms^{-1} show the performance of a stationary versus rotating wheel with and without suspension shrouding, with and without front wing and so on. Their results conclude relatively large differences for all of the geometrical cases, including a significant reduction of wheel drag in the case with a front wing. However, every case tested shows a rotating wheel drag larger than that of a stationary wheel. The authors claim good correlation with results published by Fackrell & Harvey [48] although this trend is in fact the inverse of their conclusions from isolated experiments.

The static pressure distribution is often considered as being the best methodology for determining the aerodynamic lift of a rotating wheel. Various methods have been employed since Fackrell's on-board data system. Uawithya [53] and Mowatt [54] utilised a bank of infra-red transmitters and receivers to avoid the noisy and oversized slip-ring technique that can be used to read pressures in real-time. Hinson [32] incorporated a Scanivalve pressure measurement system situated directly inside the wheel and measured radial static pressure distributions via a radio telemetry system. Investigations were carried out on both stationary and rotating wheels with varying angular resolution and varying models. Since it has already been established that stationary flow-fields are of little consequence to a realistic simulation, they will not be discussed any further here.

Hinson's experiments took place in a very large working section in excess of 4m^2 with a Reynolds number between Re = (3.5 - 9.6) × 10^6 complete with full moving ground plane. The rigid tyre was of the type consistent with the dry weather F1 tyres of a decade ago, complete with longitudinal grooves in the tread which reduce the contact patch area. This tyre also included a 3mm thick rubber tread around the circumference in order to establish a more correct contact patch condition. The nature of deformable tyres is discussed in Section 1.2.7.

The tyre incorporated surface static pressure tappings on the tread and confirmed the pressure distribution of Fackrell (Figure 1.16). Hinson's observed pressure peak, however, showed unusual characteristics. At low Reynolds numbers the peak jumped to a pressure coefficient of $Cp > 25$ compared to Fackrell's, which was an order of magnitude smaller than this, and commented to be more feasible. In addition to this, concern was raised by both Mears [3] and Whitbread [5] regarding the reference pressure being taken inside the non-sealed wheel within the test section. This would lead to a presumed incorrect absolute pressure values being recorded.

It was concluded that the excessive peak was not due to flow-field effects, but instead this was described as being due to a "sudden compression of air contained in the tube to the transducer as the rubber coating on the tread surface was squashed by the contact with the ground plane". Higher Reynolds numbers led to reduced loading of the contact patch, hence, this effect was reduced.

The prime focus of Mears' work [3] was on a radio telemetry system which allowed the data to be recorded in real time via a radio signal to a nearby computer, similar to Hinson and Whitbread. Figure 1.21 shows this radio telemetry system inside the specially made hub assembly with a go-kart tyre acting as a rigid tyre (high inflation pressure). The high resolution of this methodology allowed Mears [3] and Mears et al. [49] [50] [51] to produce the pressure distribution that is shown alongside that of Fackrell [23] in Figure 1.16. This not only confirmed the presence of the negative peak which was nervously concluded by Hinson [32], but matched almost perfectly the remaining distribution of pressure found by Fackrell's original work. This negative pressure peak illustrates the concept of 'rear jetting' which is behind the line of contact. The different shoulder profiles and aspect ratios are almost certainly responsible for the small discrepancies in the pressure distribution plots.

The PIV data published by Mears et al. [51] and in more detail in Mears [3] show an overhead interrogation in order to analyse the jetting phenomena. It was suggested that the rear jetting of the tyre was potentially responsible for reduced drag although this was not verified. They explained this concept as 'wake-breathing'. The rotating wheel case exhibits a downwash area behind the tyre of just over a quarter of the freestream velocity. For a stationary wheel, the air was significantly directed around the wheel sidewalls as well as moving over the top surface. This shows a disturbance in the flow either side of the wheel whereas the rotating case shows the opposite trend with the majority of the separation over the tread, leaving the sidewall air relatively freestream orientated.

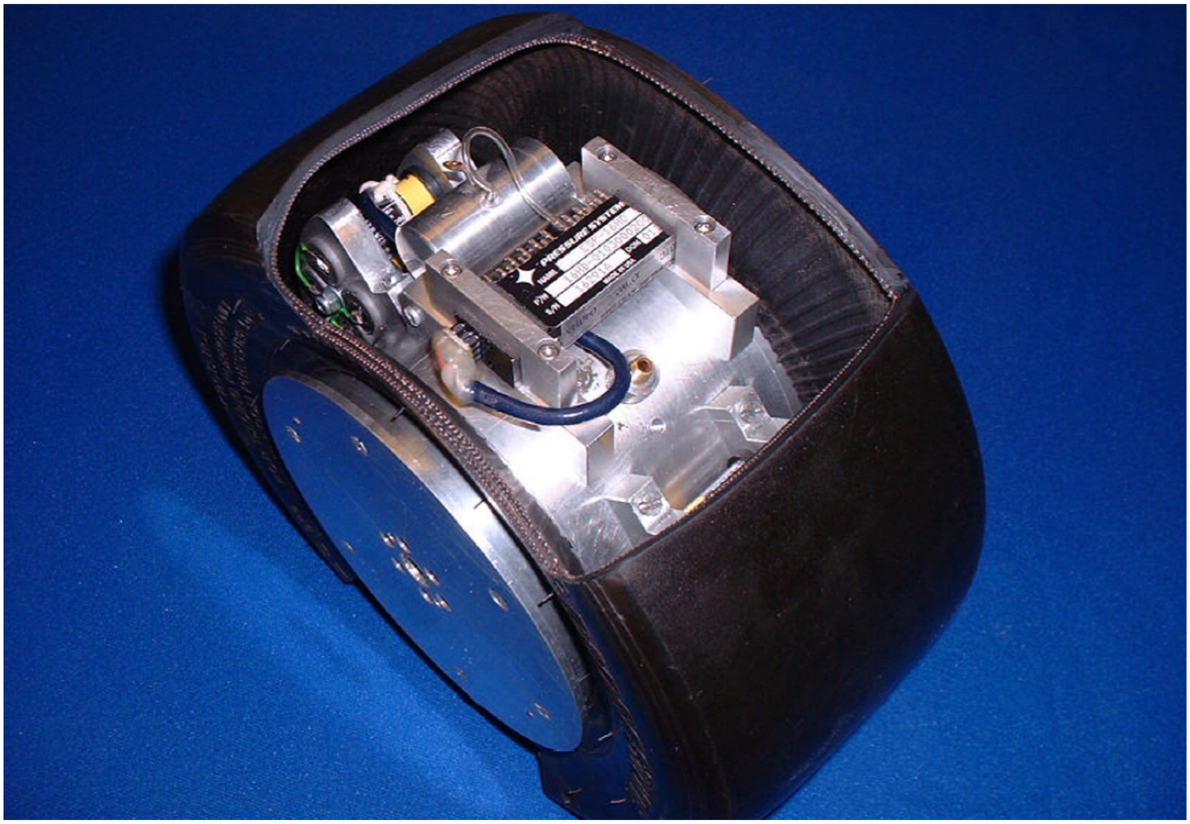

Figure 1.21: *Photograph of the Durham University Radio Telemetry System as used by Mears [3] and Mears et al. [49] [50] [51].*

1.2.6.6 Effect of Yaw and Camber

A camber investigation was carried out by Hinson [32] with a ±2.5° camber range. The conclusion was that air on the outboard side of the tread of the wheel, with respect to the camber, was always lower pressure than the inboard side. This would be consistent with the results of Cogotti [28] whereby the effect of air accelerating underneath an incomplete seal can be quantified.

Whitbread [5] performed a direct extension of Hinson's work [32] and addressed an issue with the temperature fluctuation sensitivity of the transducers used in Hinson's experiments. Although the reference pressure issue was mentioned, no details were provided regarding the solution to this problem.

Whitbread presented camber and yaw angle effects on the drag measurements of the wheel and can be seen in figures 1.22 and 1.23 respectively. As expected for yaw, an increase in drag is observed and

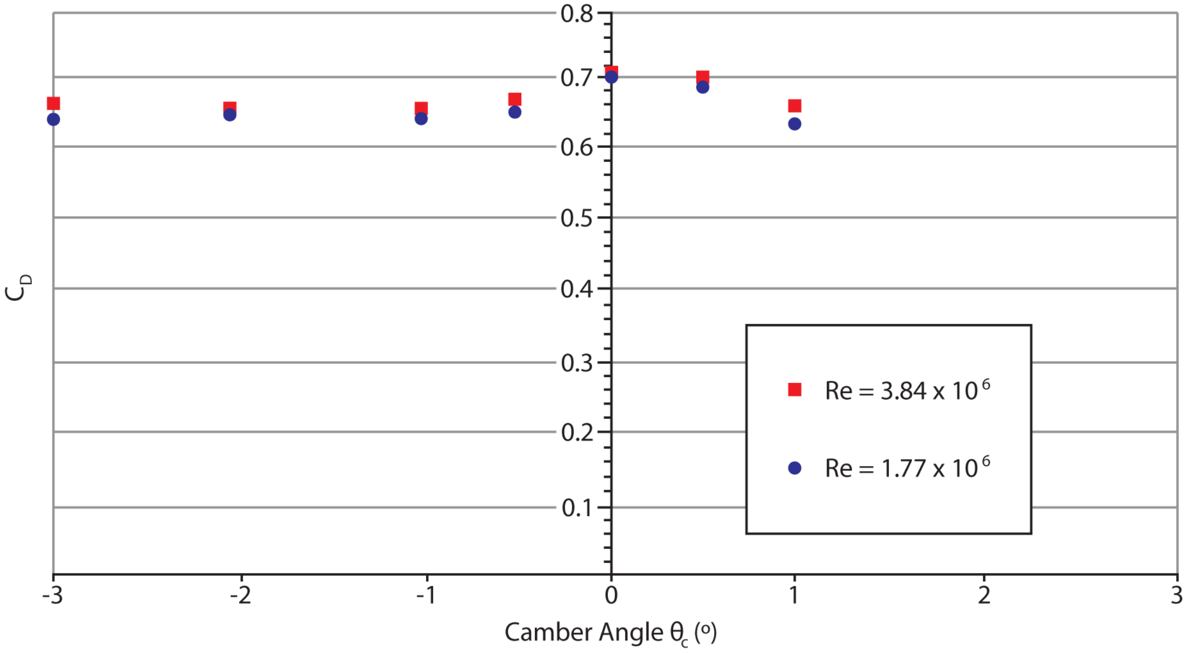

Figure 1.22: *Camber measurements taken by Whitbread [5] at positive and negative camber for two Reynolds numbers.*

consistent with that of Cogotti [28]. Angles of up to 20° were tested although this has already been discussed as being excessive for high-speed environments.

The drag for increasing camber angle, positive or negative, shows an initial sharp reduction followed by a levelling off then a slight increase. A description of the mechanisms taking place was not really offered in the work. The conclusion is less easy to interpret than in the case of yaw without more direct flow-field measurements. However, arguably by allowing higher stagnation pressure air to pass underneath the outboard side of the wheel, this would result in an increased base pressure which would account for the reduction in drag. From the same argument though, stronger vortices could be expected from the inboard sidewall which may increase the size of the wake. Given the number of complex flow structures on an isolated wheel, it is not possible to infer any further without additional data. One reason the inboard structures may have not had an influence on this measurement is due to the fact that the sidewalls were not deformable. In fact, a camber study was also reported to be carried out on the rigid wheel, which would imply an incomplete contact patch was present for some of the test conditions.

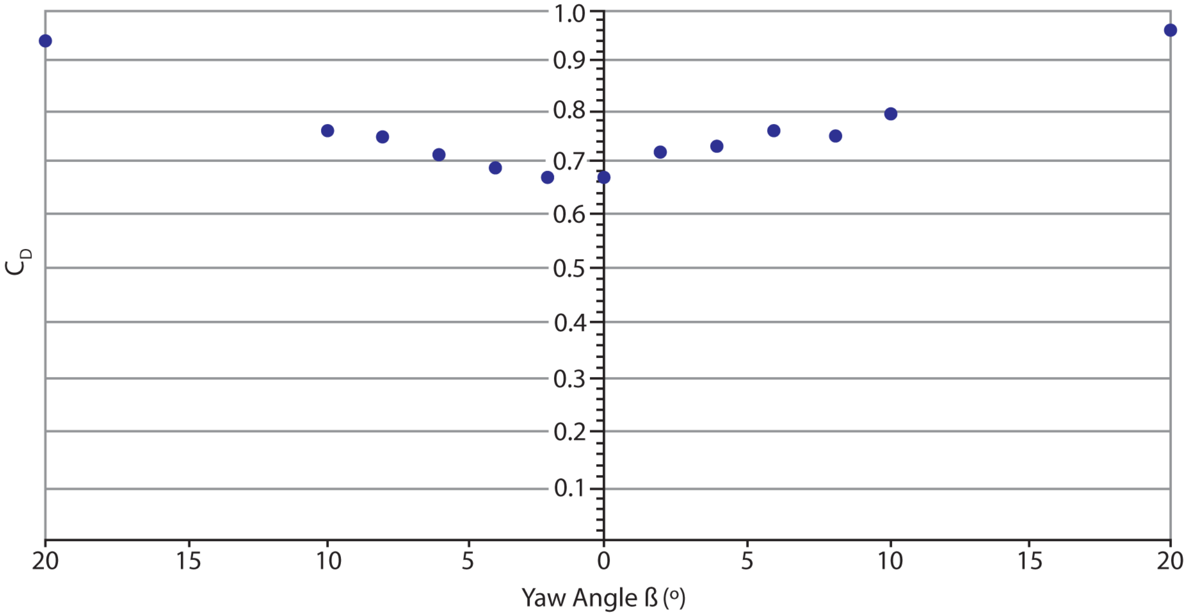

Figure 1.23: *Yaw measurements taken by Whitbread [5] at positive and negative yaw.*

The experimental work of Knowles was split into two phases relating to the aerodynamics of a 40% 'Champ Car' wheel and to those of an F1 car. The flow-field was essentially exactly as illustrated by Mears et al. [51] although important results due to the camber were noted, not least the increase in drag coefficient of around 12% for a 4° camber case compared to having no camber. This is an interesting observation as Whitbread's camber results, which suggested the opposite trend, did not extend to this range. It was also noted that the lower vortices were made less intense and that for cambered wheels the entrainment of the upper and lower vortices was less obvious.

1.2.7 Aerodynamics of Deformable Tyres

The technology surrounding fully deformable model-scale tyres provides many additional complications and, as such, has only recently emerged as a viable option even in F1. Rigid wheels have historically been used for scaled aerodynamic experiments, usually of carbon-fibre construction or machined from aluminium. This ensures durability and longevity of the test equipment as neither the wheel nor moving ground plane, if applied, exhibit signs of high wear as vertical loads are minimal.

The use of a rigid tyre, however, insists a non-cylindrical conical geometry in order to test camber (as presented in Figure 1.8). Aside from the fundamental aerodynamic issues previously discussed, the range of cambers which can be tested is limited to the exact conical angle built into the tyre. Effects of sidewall bulge and contact patch shape are also neglected by this method. A curved sidewall bulge can be designed into the inboard side of the wheel although this is subsequently exhibited around the entire sidewall and not just at the contact patch. Likewise, the contact 'patch' becomes a 'line' of contact. This will ensure a sealed gap, providing there are no vibrations or imbalance in the rotating system causing it to jump off the surface of the road. Arguably though, this sealed area is much less progressive than in the case of an elliptical contact patch seen in real rubber tyres. This much harsher geometry could lead to changes in the jetting vectors and vortices emanating from the contact patch. In addition, any vibrations in the system will lead to a complete leak from front to rear of the contact line changing the aerodynamic signature of the wheel entirely.

Many investigations have adopted rotating rigid wheels as the process of manufacturing such a wheel is quite accessible. Deformable tyres require some level of vertical load to create the realistic non circumferentially uniform sidewall deformation and correct contact patch shape. Some publications have attempted to overcome the latter by applying either a rubber or foam layer to the tread of the tyre in the case of Wäschle [55], Hinson [32], Whitbread [5] and Purvis [52].

Wäschle et al. [55] performed a flow-field study which used a deformable tread simulation. The tyre was constructed from fibreglass and had a bonded tape of foam rubber wrapped around the contact area to simulate a deformable tread. This deformable tread was able to compress by 1.5mm. This allowed a half-way solution to allow a proper contact patch to be modelled, but not the correct sidewall deformation. The method of interrogation was with a three-dimensional LDA system. The wind speed of the test was sufficiently high at 45ms^{-1} and the wheel was a one third scale F1 wheel. There was also a brake disc (rotor) included in the assembly. Their investigation, however, was mainly focused on validating CFD simulations and not the flow-field itself. The strong downwash was observed in the stationary case as with Mears et al. [51]. The vortex centres were predicted to be much lower than they were measured in every combination of simulations.

Saddlington et al. [56] set out to determine a unified theory of flow-field development based on their own experimentation and the work of others. By using a 50% scale F1 wheel in ground contact in association with LDA measurement techniques they determined their definitive version of the developing flow-field of the rotating wheel. Figure 1.24 shows the theories they based their experiments on and their additions below. Their general conclusions were that the central region and ground vortex 'lobes' form an inverted 'T' shaped wake. They blamed the presence of the support sting for the asymmetrical nature of the wake and this verifies the conclusions of Knowles. The ground lobes in this case were formed forward of the axle and combined with the upper lobes which were termed to have 'rolled off' the upper shoulders. Further downstream there was no evidence of the upper vortices and the flow was dominated by the lower vortices which were getting wider, something which Purvis [52] also observed.

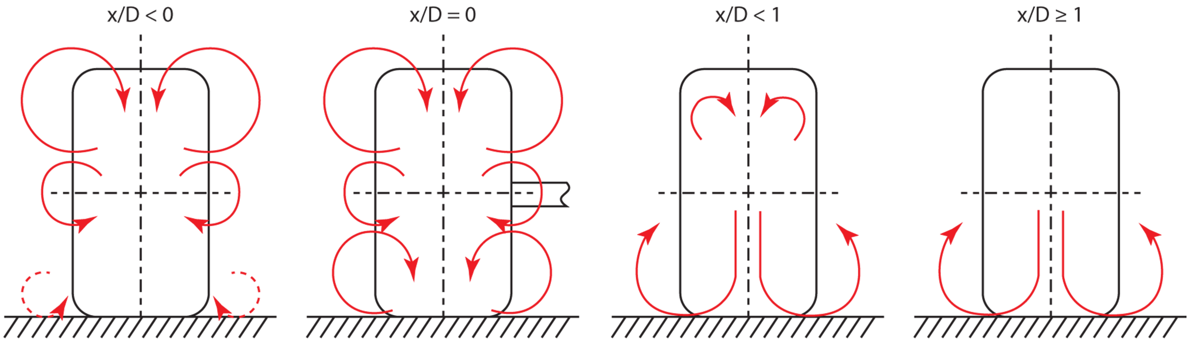

(a) After Cogotti (1983)

(b) After Mercker and Berneburg (1992)

(c) Saddlington et al. (2007)

(d) Saddlington et al. (2007)

Figure 1.24: *The suggested flow-field formation (after Saddlington et al. [56]) of an isolated wheel.*

The most recent studies into wheel aerodynamics are those of Axerio et al. [57]. Their work involves the study of a 60% F1 tyre which is reported to be deformable. The main purpose of their work was to compare experimental work with two CFD codes, those being LES and RANS. The understated flow-field investigation involves the use of PIV.

Their results show that the near wake of the tyre is dominated by two large counter-rotating vortices as with all of the above experimental conclusions. The inboard vortex is reported to be larger again, due to influence from the sting. A periodic oscillation of the vortex centres was observed. The oscillation of these structures is quite strong and there are reported to be approximately ten vortex-centre turnovers in the space of one wheel diameter downstream of the axle. Whether the oscillation is due to interrogation methods or typical of a deformable tyre is not clear. However, it is a very understated conclusion which should be added to the flow-field descriptions built up by the above works.

Wickern [41] is reported to have stated quite boldly that correct simulation of tyre contact patches is not important and that the difference in drag between a tyre with full or reduced load is negligible for a single rotating wheel within a wheel housing [43]. However, Purvis' results [52] are displayed in Figure 1.25 and show the size of the wake, and fundamentally drag, increasing with the contact patch width. This effect is more prominent further downstream.

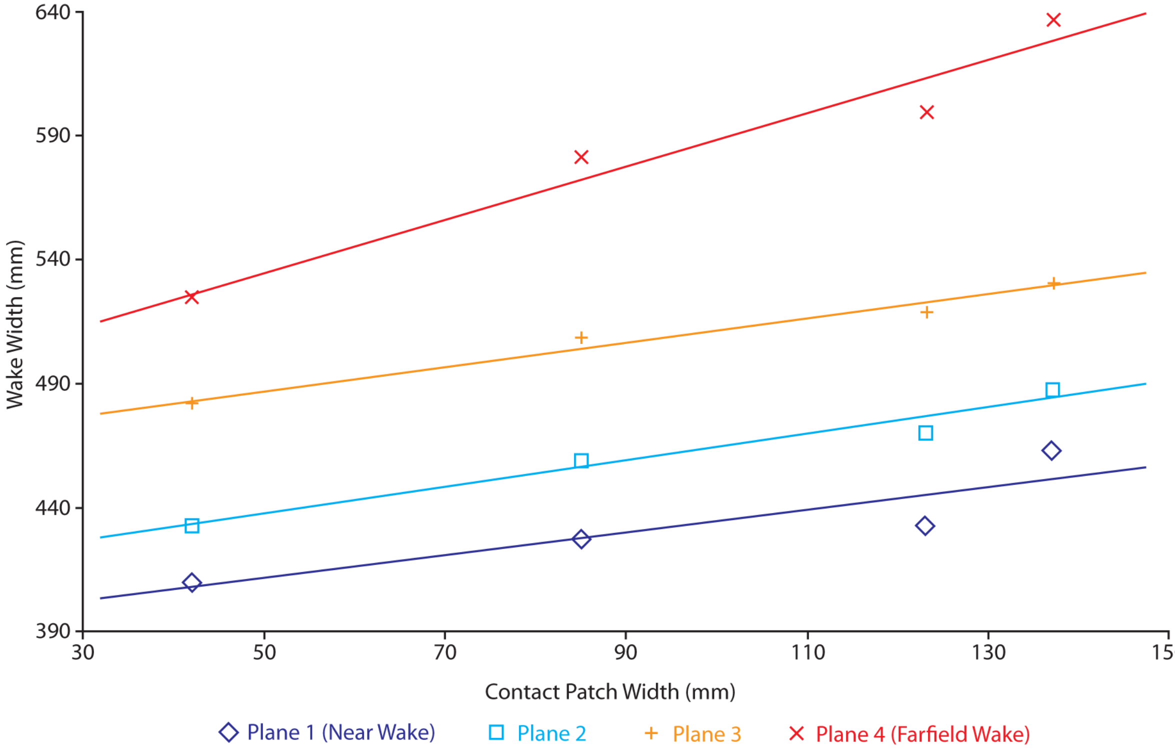

Figure 1.25: *Experimental results from Purvis [52] showing the increase of the width of the wake with the measured contact patch width at various measurement planes in the downstream wake.*

Full-scale testing often utilises real tyres due to the ease of application and availability. However, they are rarely investigated for their sensitivities to the aerodynamic flow-field. There is recent evidence in the literature of an investigation by Landstrom et al. [58] whereby the extent of tyre deformations and their global effect on a production car were observed. This was investigated from a global car scope.

In the current era of budget racing, as imposed by the rules and regulations of F1, the only full-scale testing that tends to occur is by those of automotive manufacturers for production vehicles. They are unlikely to be as concerned by high-speed cornering deflections of the tread and sidewalls and therefore the fact there is little available work in the literature until recently is not surprising.

The only work to date to notably use a fully deformable scale tyre was that of Axerio et al. [57]. The characteristics of the use of such a new technology were, however, unreported. Instead, the tyre was simply used as a tool to compare wind tunnel tests with those of Large Eddy Simulation (LES) against standard steady RANS CFD.

Given the sensitivity in the rubber deformation and range of variables such as vertical load, axle height, tyre inflation pressure, hysteresis, temperature fluctuations and so forth, there are a lot of unknowns in the usage of such a young technology. These have not been quantified in any published works and as such there is little to base experimental work on when using similar tyres.

1.2.8 Aerodynamic Cooling and Internal Flow Structures

The brake rotor of an F1 car is typically of carbon construction and operates in the window of 677K (400°C) to around 1277K (1000°C). Operation below or above this window results in either insufficient brake performance or extreme wear and degradation respectively. This information is available in depth from most of the brake material manufacturers including 'Brembo' [65] and 'Hitco' [66]. Many detailed articles, although not published in an accredited academic setting, relating to braking system operation are available on the internet [67]. The technical detail is sufficient for any interested reader and indeed for many avenues of research in such a fast-paced and secretive business, this is often the only source that is available to an audience external to the industry.

Brake rotors (or discs as they are often known), all operate by the same principal in design. By turning kinetic energy into heat they produce an opposing torque to slow the car down. The carbon material in its carefully layered construction allows a large heat capacity which in turn allows huge braking potential from high speeds. Braking decelerations of up to 6.08g have been recorded [65] taking the car from 312kph to a mere 62kph in 3.1 seconds, over a distance of only 125m. This equates to a kinetic energy loss of around 22.2kJ, although not all of this energy is lost through the brake rotors. A considerable retarding force is present from the high drag of the vehicle, KERS harvesting components and engine compression when off throttle. Nevertheless, a significant proportion of this energy is converted into heat which is stored in the car's brake rotors. Associated with this, are large temperature peaks. Once the rotor is at a high temperature, the ability to convert and absorb a similar amount of energy again is limited or impossible. The rotor therefore needs to lose this energy before it can be effective again. Taking air from close-to the axis of rotation, by the use of fins and ventilation in the rotating geometry, the rotor acts as a centrifugal pump and this movement of air cools the rotor by forced convection, allowing it to remain in the intended temperature window.

McPhee & Johnson [68] investigated both the heat transfer effectiveness and internal flow-field behaviour of such a brake rotor. The former investigation was performed by means of a transient convective flow study, utilising K-type thermocouples positioned radially along one of the vents. An assumption was made that there were negligible radiative heat transfer rates due to the low temperatures and an asbestos disc preventing conduction to the hub geometry. The flow-field study was performed by means of clear plastic windows in the brake rotor with simplified internal geometry designed for use with a PIV system. Figure 1.26 shows the 37-fin rotor used in their experiments. From experience, and epitomised by the work of Charlesworth [69], the use of clear windows so close to the camera's focal point results in significant distortion of the flow-field vector magnitudes, although general flow behaviour can be detected.

The conditions tested comprised rotational speeds of 342, 684 and 1025rpm, and 583K against room temperature. A full-scale F1 wheel and therefore brake rotor, travelling at around 70ms^{-1} (mid-straight speed) would be expected to observe wheel rotational speeds of 2089rpm[1], twice that of the highest tested speed in their case. In addition, some circuits allow much higher speeds to be obtained, up to 2,850rpm for example at 'Monza', Italy.

---

[1] Based on full-scale wheel diameter of 640mm.

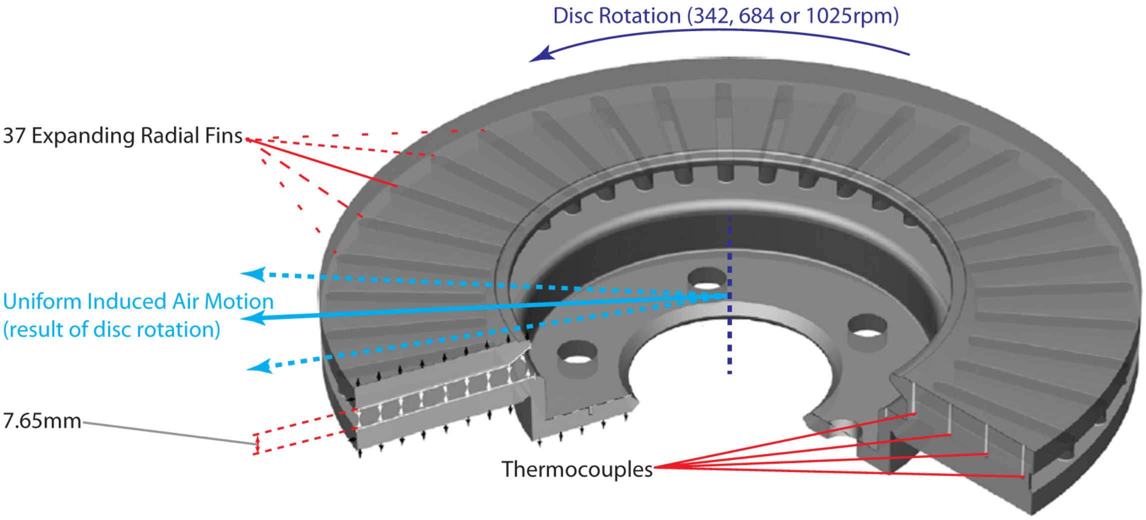

Figure 1.26: *A simple brake rotor, after McPhee & Johnson [68] (modified) illustrating their experimental apparatus.*

The cooling flow exit velocity, which is highly rotational frequency dependent, is expected to be very low even for high peripheral rotor-speeds. This means the flow regime may be close to the sensitive transient regions for pipe flows, the approximation applied to the cooling channels in the rotor.

Table 1.1 shows a summary of Reynolds numbers calculated from their experiments including PIV measured velocities, using the vent height as characteristic length, analogous to a pipe diameter. For idealised pipe flow conditions, as have been applied here, the transition to the critical flow regime is around Re = 2,000, and to supercritical at around 4,000 (Massey [22]).

Table 1.1: *Reynolds numbers corresponding to the range of experiments carried out by McPhee & Johnson [68] illustrating the sensitivity for through-vent airflows to transition.*

Disc Temp. (K)	Nominal RPM	F1 Vehicle Velocity (ms^{-1})	Cooling Flow (ms^{-1})	Re
583	342	11.5	1.6	247
	684	22.9	3.4	525
	1,025	34.3	4.6	710
	2,089 (Not Tested)	70.0	6.5	1,003
	2,850 (Not Tested)	95.5	7.3	1,134
300	342	11.5	1.6	717
	684	22.9	3.4	1,523
	1,025	34.3	4.6	2,061
	2,089 (Not Tested)	70.0	6.5	2,910
	2,850 (Not Tested)	95.5	7.3	3,289

Of course the condition of inlet flow turbulence intensity, imperfections in the pipe due to lack of circular cross-section and the shortness of pipe will largely affect these regime boundaries. Nevertheless, it is evident from the hot rotor experiments, that should the speeds be the same as observed in the colder PIV experiments, the flow condition is always in the laminar sub-critical regime.

The same cannot be said for the cold rotor experiments (used for PIV measurements). Here, the first two rotational speeds are within this sub-critical regime, although much closer to the critical crossover and indeed at their fastest speed and extrapolated velocities from their data points, there is a crossover to the critical regime even under idealised conditions.

This is an interesting observation for testing of brake cooling flows as a separate issue. In the case of McPhee & Johnson [68], their hot and cold rotor experiments based on their published data will almost definitely have been under different conditions. How much this affects their measured volumetric flow rates is unclear but their measured velocities under the two different temperature conditions will produce different cooling characteristics due to the sensitivity of the flow regimes. Although the cooling was measured directly via thermocouples, any relationship to through-rotor flow-field is to be taken with consideration. The above investigation was an extension of the previous study carried out by Johnson et al. [70] using the same geometry.

This poses the question as to whether wind tunnel tests of internal geometries within F1 are performing as they are intended to. The performance of the brake rotor can be seen as being either a restrictive hindrance or a pumping aid. Therefore knowing the exact volumetric flow rate and the condition of the flow travelling through the rotor is vital to ensure small-scale experimental accuracy. This is a question which is intended to be answered by this work.

This argument is applicable to F1 despite the fact their rotors are known to operate at temperatures much higher than those tested by McPhee & Johnson [68]. The Reynolds number is expected to change slightly as a result of higher temperatures but due to much more sophisticated designs and with the addition of a ram air intake duct, the cooling velocity will be higher and this will bring the Reynolds numbers well within this sensitive region. It may even be postulated that the flow regime of a brake rotor cooling flow does indeed pass through the entire critical region between the slowest corners and the fastest straights of the same circuit.

Parish & MacManus [71] combined the above studies to perform a miniature five-hole pressure probe (1.5mm head diameter) and hot wire anemometry study of a rotor geometry with differing internal geometries. Of those tested were straight and curved fin designs with varying fin counts. It was concluded that although the mass-flow rates were reduced for larger fin counts, the flow conditions may suit heat transfer requirements better than their apparent superior designs. All experiments were, however, performed on a cold rotor. Detailed turbulence information was presented and a much more realistic rotational speed than McPhee & Johnson was attained (2,250rpm). Small changes to the flow were noted, particularly at the slower peripheral speeds, which may suggest there is some weight to the above hypothesis relating to changing flow regimes over the range of the operating speeds. These changes were, however, subtle. Generally they considered little difference between the peripheral speeds, except of course for the absolute velocities of the cooling passages which were described as increasing linearly with peripheral rotor speed.

1.2.9 External Effects of Through-Hub Flow

In terms of the method by which the rotor is fed air and likewise the way in which the air expelled is exhausted from the hub there is little available in the literature. All modern F1 cars essentially feed the rotor with air from the inboard side via a brake cooling duct or scoop and then the hot air expels from the outboard side through the spokes. Figure 1.27 explains the principle of a modern brake rotor.

The brake rotor, caliper, upright and stub-axle are all one tightly packaged assembly with a carbon-fibre outer shell. It is important to note that there is no rotating axle with this method. Both the brake rotor and rim have bearings and three locating pins protruding from the inner diameter of the rotor interlock with a ring of holes in the rim's inboard side. This simple stub-axle principle should transfer well into a wind tunnel testing environment.

Knowles [59] and Knowles et al. [60] [61] investigated the flow-field of a wheel using LDA and CFD. Through-hub flows due to the absence of the sting were reported. Hetherington et al. [62] [63] and in more detail in Hetherington [64] describe the sensitivities to model wind tunnel experiments due to the presence of support stings.

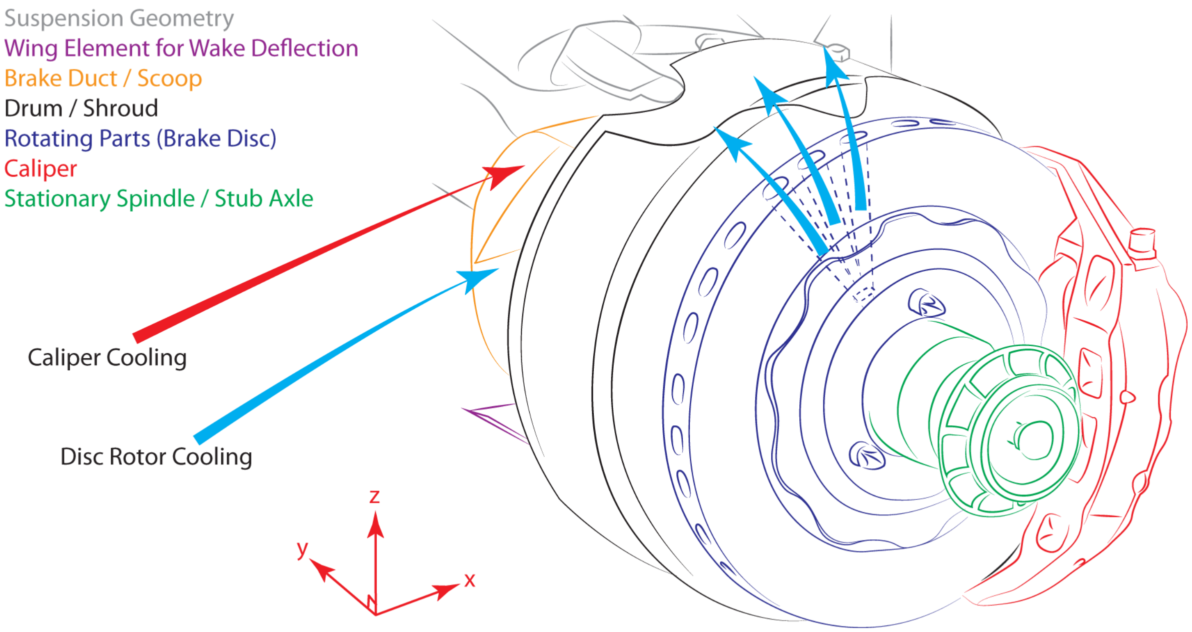

Figure 1.27: *Line drawing of a typical front brake assembly highlighting the brake cooling channels and components of the hub.*

Morelli [31] observed that there might be an external influence from through-hub flows. By applying a wheel fairing, he reported a reduction in drag of 22%. Unfortunately, this conclusion is taken with some consideration of his methodology as already covered. Through-hub flows were regarded by Fackrell & Harvey [72] as insignificant for wide wheels (higher aspect ratios) as the recess into the hub would be a large separation bubble and would play little part in the overall flow-field. Their comments, however, neglected to consider brake cooling requirements on the onset flow of real-world applications.

Cogotti [28] also investigated this effect. The effect of fairing the rims by introducing a flush cover reduced the drag by 16% in the rotating case and 9% in the stationary case. The lift was affected only by a negligible amount. This reduction in drag by introducing a fairing illustrates the importance of through-hub flows and suggests circulating air attached to the rim influences the flow-field and trailing wake. The fact that there still exists an appreciable decrease in the drag for the stationary wheel illustrates that the effect cannot be entirely attributed to the rotating air attached to the rim. This instead could be due to preventing the separation area from occurring in the outer centre of the wheel.

It is generally considered that the exit flow of a cooling duct or passage is responsible for the majority of the pressure loss or induced drag. Depending upon the way that the low energy air is reintroduced into the freestream, the effect of the internal flow can have a dramatic effect on the global flow-field. Indeed, part of Williams' equation,

$$\frac{\Delta D_{cooling}}{q_0 A_f} = \frac{\dot{m}_0 u_o}{q_0 A_f} + \frac{\Delta D_{spill}}{q_0 A_f} - \frac{(\dot{m}_6 u_6 cos\alpha - \Delta D_{ub})}{q_0 A_f}, \tag{1.4}$$

described an exit flow thrust-recovery coefficient which has been negated for this investigation due to the assumption of high loss due to the 'chopping' by the spokes and the exit directionality being perpendicular to the freestream. Dimitriou et al. [45] reported the presence of a flush hub-cover as being responsible for a drag reduction of 9% and a lift reduction of 16%. The latter of which was measured using an underfloor load-cell as mentioned in Section 1.2.5 and is therefore a little controversial. However, the conclusion is consistent with expectation. The concept of the spillage drag term will be discussed later.

There was, for a short time, a popular design direction in F1 whereby outboard wheel fairings were used in order to improve the aerodynamic effect of the wheels on the overall flow-field. Typically these comprised complete discs with holes cut out, or a section removed, as shown in Figure 1.28 (centre). The presumption is that the control of the exit airflow allows the reintroduction of the cooling flow into a more favourable section of the wake. In addition to this, by restricting the size of the exit orifice, the velocity of the reintroduced air will be much higher resulting in a lower outboard pressure which helps to divert the wheel wake away from vital downstream components. Minto [73] investigated these fairings and the positioning of the exit. The results are summarised in Figure 1.29 and his CFD findings confirmed the above presumption.

A general reduction in drag can be observed for the presence of the outboard fairing in all instances. However, the two locations, facing down and rearwards are the most promising resulting in a maximum drag saving of 12.2% compared with the case of no fairing at all. Given these fairings are no longer legal in F1, although geometries which are part of the rim itself have been explored (see Figure 1.28 (right)), they will not be investigated in depth in this thesis due to their diminished relevance.

Figure 1.28: *Left: Standard rim, spokes only with glowing brake rotor. Centre: Rim fairing characteristic of the 2008 and 2009 F1 season. Right: A post 2009 wheel cover ban solution incorporating the "fairing" into the rim itself.*

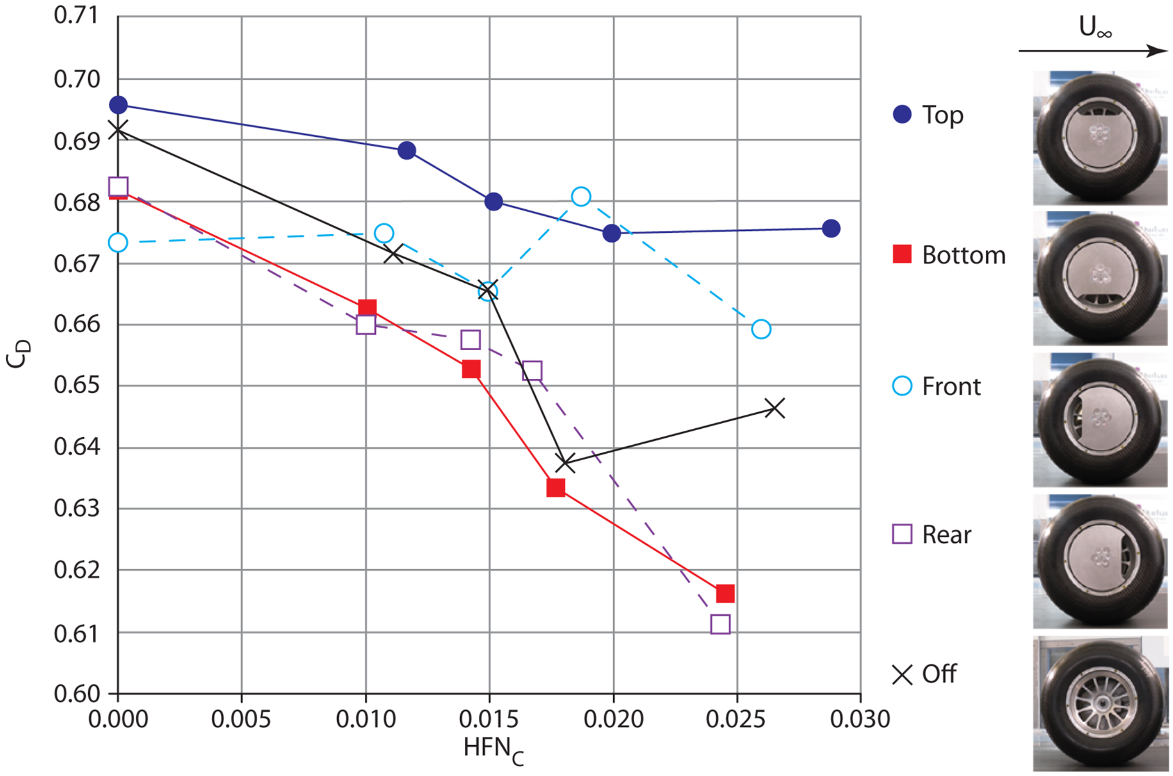

Figure 1.29: *Drag coefficient against corrected hub-flow number for varying positions of the exit orifice for outboard rim fairings, after Minto [73].*

1.2.10 Inlet Flow Conditions

Minto [73] investigated the effect of through-hub flow on the external flow-field for an isolated wheel and was the precursor to this work, subsequently combined with some of the early results from this thesis, in Sprot et al. [74]. His work investigated the drag penalty for varying levels of through-hub flow as well as briefly investigating the outboard wheel fairings used in the 2008 and 2009 F1 seasons. He measured a significant reduction in drag penalty for increasing levels of through-hub flow. This is contrary to the common effect of reduced drag by closing off radiator ducts on most production vehicles. This is discussed by Hucho [76] and Wiedemann [38] for example. The conventional thought process dictates a situation whereby the lack of highly restricted air travelling through the internals of the car reduces the drag induced by it.

Previous studies of through-body flows such as those by Barnard [75], who investigated the effect of axial momentum loss and focused on detailed work on the exit design for an internal cooling flow; and Seddon et al. [77], who characterised the crucial stages of a cooling system whereby pre-entry streamtube momentum is lost. Oler et al. [78], Gilliéron & Chometon [79] and Williams et al. [80] investigated the whole cooling system from a cooling drag and flow-field perspective. Work on cooling flows tends to be analytical, as modelling internal body flows in a wind tunnel is a difficult task. Therefore, the ability to predict accurately the performance of a system on paper and simplify experimental tests is a desirable outcome. This is the motivation for the aforementioned authors among many others.

A non-dimensional term, known as hub-flow number (HFN) [73], which is essentially volumetric flux ratio, is defined by

$$HFN = \frac{A_s U_s}{A_f U_\infty}. \tag{1.5}$$

For the case of Minto [73], this hub-flow number was varied by placing fine wire meshes between the brake scoop and the inboard side of the drum. This ensured that the brake scoop did not turn into a solid bluff body and allowed a restriction to take place at the inlet for the hub.

Minto documented an issue whereby even with a fully sealed duct, an intake velocity was measured. This was due to the geometry of the brake scoop allowing air to flow in and spill over the sides further downstream of the pitot-static probe's tip. As a result, a correction was applied based upon CFD studies. This correction is defined by

$$HFN_c = \frac{U_{hub,CFD}}{U_{duct,CFD}} \left(HFN - HFN_{closed,probe} \right). \tag{1.6}$$

The reduction in drag was postulated to be due to an effect described by Williams [81] called 'inlet spillage drag'. By introducing a blockage into the cooling duct, or engine bay of a vehicle, the back-pressure forms a restriction which effectively causes the flow to 'spill' out causing a local separation at the leading edge. This separation contributes to a drag penalty at low HFNs which is not present at high HFNs. The hypothesis is that this force is dominant compared to the delta between the maximum and minimum HFN drag forces and therefore reverses the conventional theory and produces a negative cooling drag trend.

Williams [81] declared a mathematical model which describes the overall drag for a system involving a through-body flow. This was expressed in Equation 1.4 for which the terms are defined in the nomenclature at the beginning of this document. This principle has also been illustrated in graphically Figure 1.30.

This equation comprises three components for an Ahmed model [44] style experimental model. The first of which is the standard ram drag from the cooling inlet, the second term describes the contribution from the HFN dependent spillage effect and the third component is associated with underbody recovery effects which reduce the drag penalty. The final term is not relevant in the case of a wheel study as there is no controlled expansion or recovery of the cooling flow. The flow exits after a turn of 90° and therefore all axial momentum is lost. He went further to describe the particular development of the spillage drag term. This is defined by

$$D_{spill} = \left(1 - c_{t,inlet}\right) q_0 A_s \left(1 - \frac{U_s}{U_{ref}}\right)^2. \tag{1.7}$$

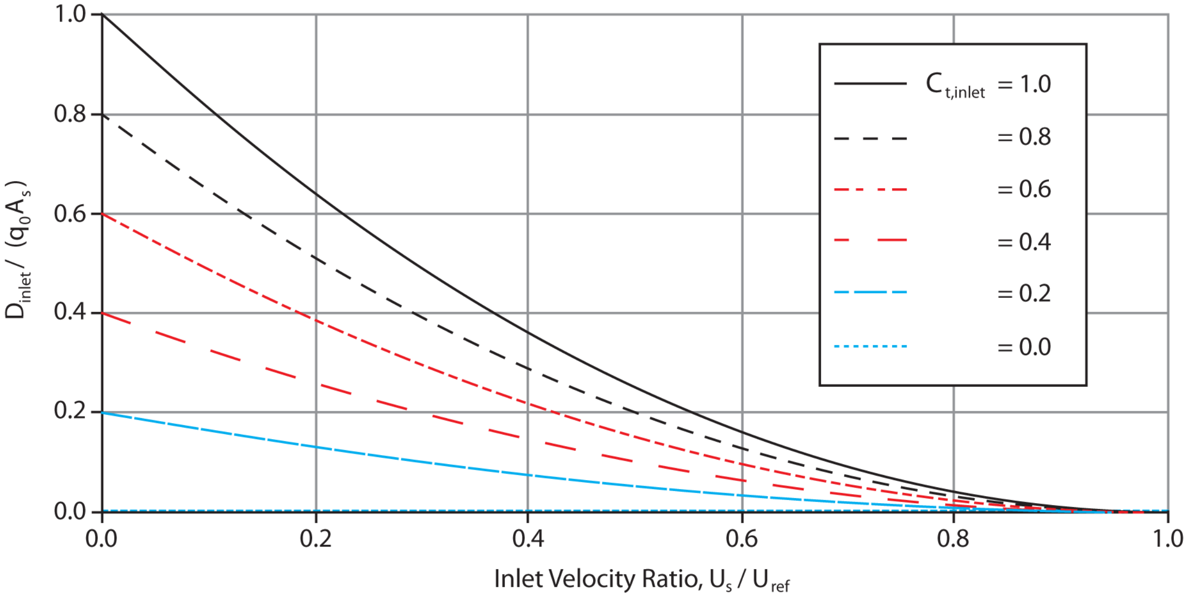

Figure 1.30: *Graphical representation of the inlet drag based on inlet thrust-recovery coefficient as per Williams' equation [81] (Equation 1.4).*

This drag term is defined in terms of a thrust-recovery coefficient in order to be consistent with the aforementioned third component of the complete model. Therefore if $c_{t,inlet}$ is unity, there is no spillage effect and therefore no spillage drag penalty. Conversely, if this is zero, the full and maximum spillage drag penalty is present. This is an empirically measured quantity.

It is this that Minto described as being responsible for the negative cooling drag but made no attempt to quantify this. In the interest of making any investigation into the effect of varying through-hub flow on the overall flow-field, this shall be tackled first.

1.3 Summary of Literature Review

From the above review it can be seen that the consequences of the flow-field for a modern-day F1 front wheel assembly are far from trivial. The flow-field itself is considerably more detailed and sensitive than it would first appear and the downstream development of the wake amplifies any small changes made locally. The development of a full F1 car depends highly upon the correct modelling of the front wheel wake.

It has been established, early in the literature, that the testing of a wheel in a wind tunnel requires both rotation and full ground contact to be ensured as the flow-field changes dramatically without either of these parameters. Indeed, with the former, an effect known as 'Fackrell jetting' is well documented and this contributes to vortex structures which are not present for a stationary wheel. The drag and lift of a rotating wheel are known to be lower than those of a stationary wheel and in association with appropriate ground simulation techniques, a viable experiment can be undertaken.

The front tyre, specifically, experiences several physical processes when accelerating, braking, cornering and reacting to pitch, roll, dive and increasing vertical loading with speed of an F1 car. The cornering condition is one which is of particular interest as developing a car which is insensitive to yaw angles is an attractive proposition to an aerodynamicist. Additionally, the steering input from the driver contributes a 'slip' angle, which provides a lateral thrust that in turn, mechanically initiates cornering. Slip, is responsible for an additional yaw component of the wheel and aerodynamic studies of yaw are, to-date, sparse in numbers

Several mechanical and geometrical modifications are often applied to a wheel assembly of a race car to improve the tyre's interaction with the ground. Since this is the primary function of a wheel and tyre, this is an unavoidable geometrical condition and therefore parameters such as toe and camber should not be ignored.

The above paragraphs describe situations that influence the shape of the tyre, either as a global effect as in the case of off-track setup parameters, or local changes as a result of reactions to on-track geometry changes or inertia. As such, the shape of a tyre under operation can only be correctly simulated using deformable materials. This process employs relatively new technology in the case of model-scale tyres. The effect of parameters such as the contact patch shape and size, axle height, sidewall profile and non-circumferentially symmetric geometry to the aerodynamic flow-field are all unknowns.

In addition to the geometrical changes of a wheel in operation, there are also several internal flow features which to-date have not been investigated from a global flow-field perspective. The effect of through-hub flow, used primarily for brake cooling as well as developing outwash for wake management, has a significant effect on the flow-field and forces of the wheel. The presence of a brake rotor (disc) is often overlooked in experimentation and the intricacies of through-hub flow are not well appreciated.

1.4 Scope and Objectives

The above sections have described a field which is not regularly or widely reported in the public domain, neither is it usually explored in full depth in an industrial environment due to resource restrictions and project time limits. It would be grossly oversimplifying the approach of F1 teams by describing their efforts as trial-and-error but their ultimate goal is to make an entire system work better than the opposition's contender. This means that isolated studies to determine the exact nature of the flow-field and aerodynamic sensitivities to on-track variations are limited if not completely unachievable. This is even more true of lower formulae such as GP2, Formula 3 and so on. This thesis intends to plug that gap for one particularly crucial area of interest for open-wheeled formulae, the front wheel assembly.

This work investigates the effect of the detailed geometry changes likely to be seen in all open-wheeled racing formulae. Isolated wheel experimentation performed in both wind tunnel and computational (CFD) environments allows the sensitivity to detailed setup parameters of the wheel to be identified in terms of aerodynamic forces and flow-field detail. This also enables the understanding of the local aerodynamic effects on the wake due to geometry changes of the tyre and its assembly under differing racing conditions.

The objectives for this thesis, from an aerodynamic perspective are:

Deformable Tyres:

- Identify the exact nature of geometrical changes to the sidewalls under varying load conditions.
- Determine the significance of their effects on the aerodynamic flow-field and force measurements.
- Use a deformable tyre to study the properties of yaw (steer, slip and toe) and camber.

Through-Hub Flow:

- Identify the external flow-field influences from through-hub flows.
- Experiment with scoop/brake duct inlet conditions.
- Determine the necessity for detailed internal geometry in model-scale testing.

Chapter 2

Methodology - Wind Tunnel

2.1 Apparatus

2.1.1 Wind Tunnel

The Durham University 2m^2 wind tunnel was used in all of the experimental research undertaken in this thesis. The tunnel is of the open-jet and open-return type with a test section aspect ratio of 3:2 complete with full width moving ground plane (MGP), platen suction and upstream boundary layer suction. More details of the layout and characteristics of the tunnel can be found in extensive detail in Sims-Williams & Dominy [82] [83]. Figure 2.1 shows the salient features of the tunnel. The test section is located within a large plenum chamber (not featured in the figure).

The rigid tyre, with older specifications than the deformable tyre, had a characteristic frontal area of 0.0592m^2 equating to a blockage of 2.96% with an additional 0.70% from the scoop and sting. The wheels used in the experimentation, discussed later in detail, both had a diameter of 0.32m and as such the tests performed had a Reynolds number of $\mathrm{Re} = 4.80 \times 10^5$. This value is implanted well within the supercritical regime. The importance of operating within this region was outlined in Chapter 1.

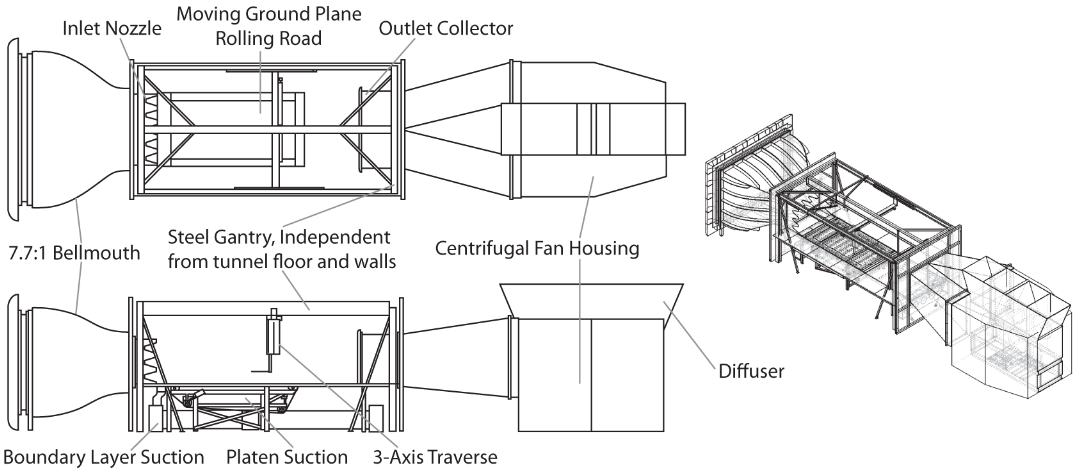

Figure 2.1: *Plan, side and isometric projections of the Durham University 2m^2 wind tunnel highlighting some of the salient features.*

For the deformable tyre which has the more recent specification narrower tread and therefore lower aspect ratio than the older generation tyres, the blockage ranged between 2.77% and 2.71% (0.0554m^2 and 0.0544^2 respectively) depending upon the level of deformation. Again, with an additional 0.70% from the influence of the scoop and support sting.

Given the low levels of blockage from both experimental configurations, especially for an open-jet wind tunnel which is considered more forgiving of blockage, traditional blockage corrections were not applied as it was considered that the jet widening and local overspeeding effects would be negligible. Cooper [27] showed the range of blockages required for correction. The procedures and corrections that are traditionally applied, when required, are outlined in Johnson [84] and Barlow [85].

The wind tunnel is fitted with a three-axis traverse system which can access points in the wake of the wheel from the axle rearwards. The primary usage of this traverse system is for pressure probe measurement but it can be used to mount other instruments to perform any function desired, as outlined in Section 2.2.7.

All aerodynamic tests were performed with the MGP in operation matching the freestream velocity (each measured within 0.1ms^{-1}). For mechanical tares and geometrical measurements, a range between 0 and 25 ms^{-1} was explored.

2.1.2 Rigid Tyre

The rigid tyre used in the through-hub flow investigations was modified from the grooved style tyre (Figure 2.2). The wheel was constructed from carbon fibre and was originally part of a full-car 50% scale model of a Jaguar R5 - Red Bull RB1 crossover. The front-left wheel and its wheels-off sting were taken from this model and utilised in isolation. More detail regarding the sting, adapted to be run inboard, as opposed to outboard, can be found in Section 2.1.4.

The tread of the tyre was filled with Nakiplast modelling wax since treaded dry weather tyres are no longer relevant in the light of current racing regulations. In addition, the entire wheel was sprayed with matt black paint to prevent laser-glare to assist close-range PIV measurements.

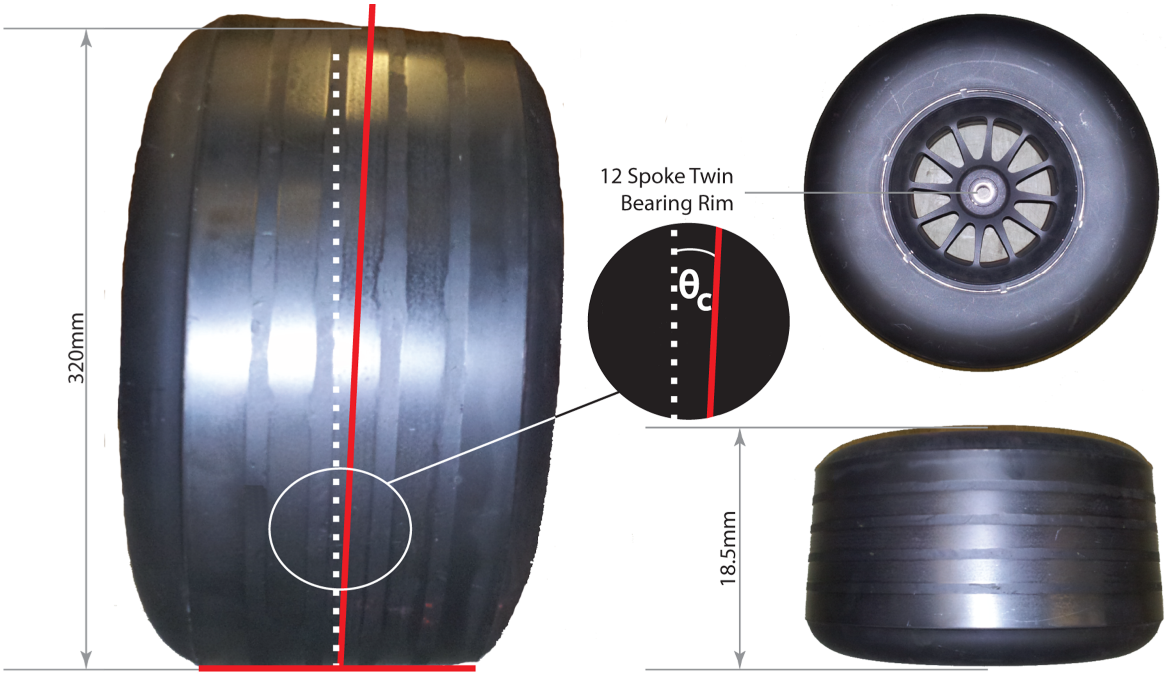

Figure 2.2: *Photographs with dimensions of the 50% scale carbon fibre rigid tyre.*

The twelve-spoked rim was constructed from aluminium and matched the style still used by Red Bull Racing, albeit now with only ten spokes. The tyre was conical with a built-in camber angle of -3.5°. It had an aspect ratio of 0.58 with a centreline diameter of 0.32m. The wheel ran with a peripheral speed of 25ms^{-1} without any vibrations, visible or otherwise detectable by the load-cell.

2.1.3 Deformable Tyre

The deformable tyre used for the majority of the wind tunnel investigations, and for the geometry baseline for CFD experimentation, was of the specification introduced in 2010 (the same dimensions as are currently enforced by the technical regulations of the sport in 2012 [25]). It was manufactured by the F1 tyre constructor of the time. The wheel was, again, a 50% scale wind tunnel model and the spoke pattern matched exactly that of the rigid tyre outlined in the previous section. The rim-diameter was identical and the only appreciable difference was the reduced aspect ratio with the narrower tread width. This resulted in an aspect ratio of 0.53, again with a wheel diameter of 0.32m. The latter dimension, however, is less easy to define with the deformable nature of the tyre causing variable 'ballooning' due to inflation pressure, and deformation due to vertical load. The aforementioned value has been used as the nominal wheel diameter for non-dimensional properties and defining positions within the flow-field.

The tyre was of slick type and was designed by the manufacturer to match exactly the deformations seen under specific vertical loading on the full-size wheel. The tyre itself had a stiff reinforced sidewall, as with the real tyre construction, although it is not known if it had the same layering construction as the full-size tyre. The intention of the tyre is to match the deformation characteristic of its full-size counterpart. The contact patch was a thin layer of rubber which did not have much support but was designed to give the correct shape and size of contact patch, again, with a certain vertical loading. Figure 2.3 shows the tyre used.

The inflation pressure of such a tyre is relatively low in order to allow deformations at low levels of vertical loading. The exact pressures used by the F1 teams are considered confidential information and as such they were neither disclosed nor available in open literature. Preliminary testing with the tyre showed that an inflation pressure of 3.0psi (0.21bar or 20.7kPa) was seen as the maximum inflation pressure possible to achieve end-of-straight levels of deformation within reasonable levels of vertical loading in a wind tunnel environment. Section 2.1.6 contains all of the details for method of deformation application as well as the axle heights tested and the corresponding vertical loading with each inflation pressure.

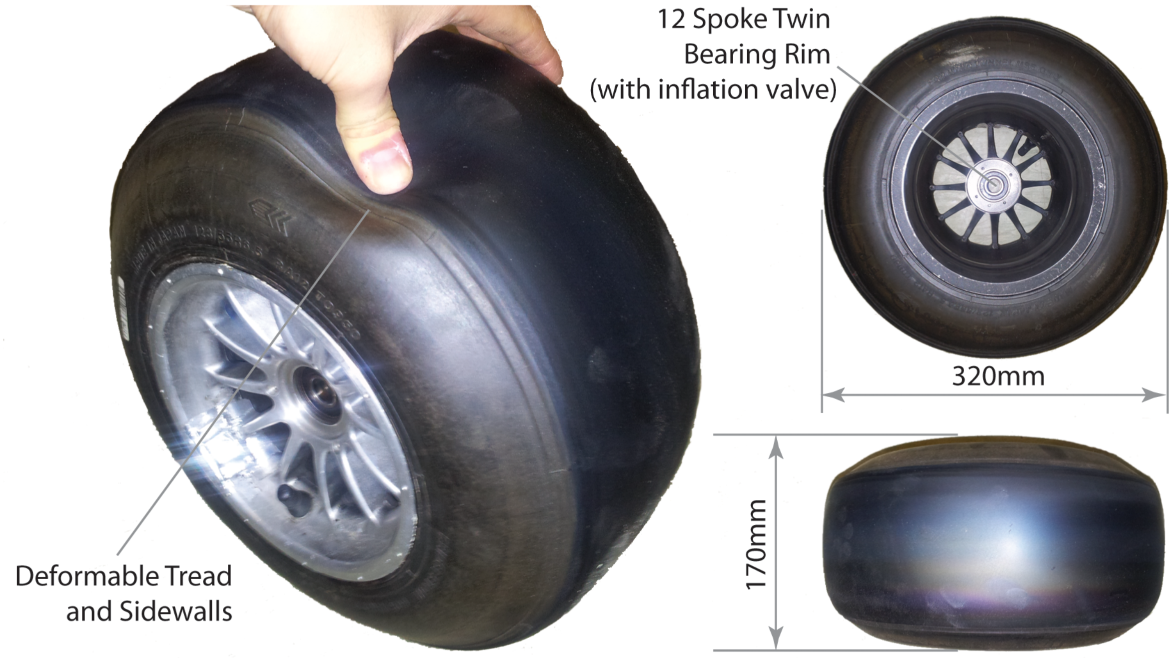

Figure 2.3: *Photographs with dimensions of the 50% scale fully deformable tyre.*

The deformable technology presents complications in experimentation compared with the rigid tyre. Firstly, there can exist a large vibration whilst 'spinning up'. These resonances are due to an imbalance in the wheel which can be cured by the traditional method of adding weights to the rim at a specific point. For this work, the positioning was determined by observing the oscillating measurements from the drag load-cell and synchronising these with a once-per-revolution datum measurement. Once the vibration was minimised it became apparent that resting the tyre on the road for long periods led to an irregular shape and therefore further vibration. Therefore, the practicalities of testing a deformable tyre in a wind tunnel are significantly more complex when compared with the testing of a rigid tyre. The question to be answered is: How sensitive is the aerodynamic flow-field to the geometrical changes and therefore is the extra setup and increased requirement for maintenance justified?

To maximise the longevity of the tyre in an F1 wind tunnel, the teams use glycerol on their rolling road systems. A fine coating provides a much lower coefficient of friction and causes a lower wear rate of the belt and the tyre, especially at yaw. However, this reduces the effectiveness of the sidewall deformation at yaw and, again, it is postulated that the requirement to use glycerol negates much of the benefit brought about by using the deformable tyre.

The majority of tests were performed in this instance without glycerol, to mimic the true deformation of the tyre. A collection of tests was performed at the end of experimentation with glycerol to scan the tyre profile and compare with the true case. This test was performed at the end of experimentation as glycerol embeds itself in the fibres of the rolling road belt and the coefficient of friction would therefore have been inconsistent for any subsequent testing.

2.1.4 Sting and Hub Geometry

The support strut was mounted to the inboard side of the wheel, as is the case with race car suspension geometry, in order to allow camber tests to be performed with a shorter support strut to reduce flexibility as well as providing minimal disruption to the spoke-exit airflow for through-hub flow investigation. As a result, the base of the sting had to be modified to provide the positive incline allowing the -3.5° of camber for the rigid wheel. The resulting sting was as shown in Figure 2.4.

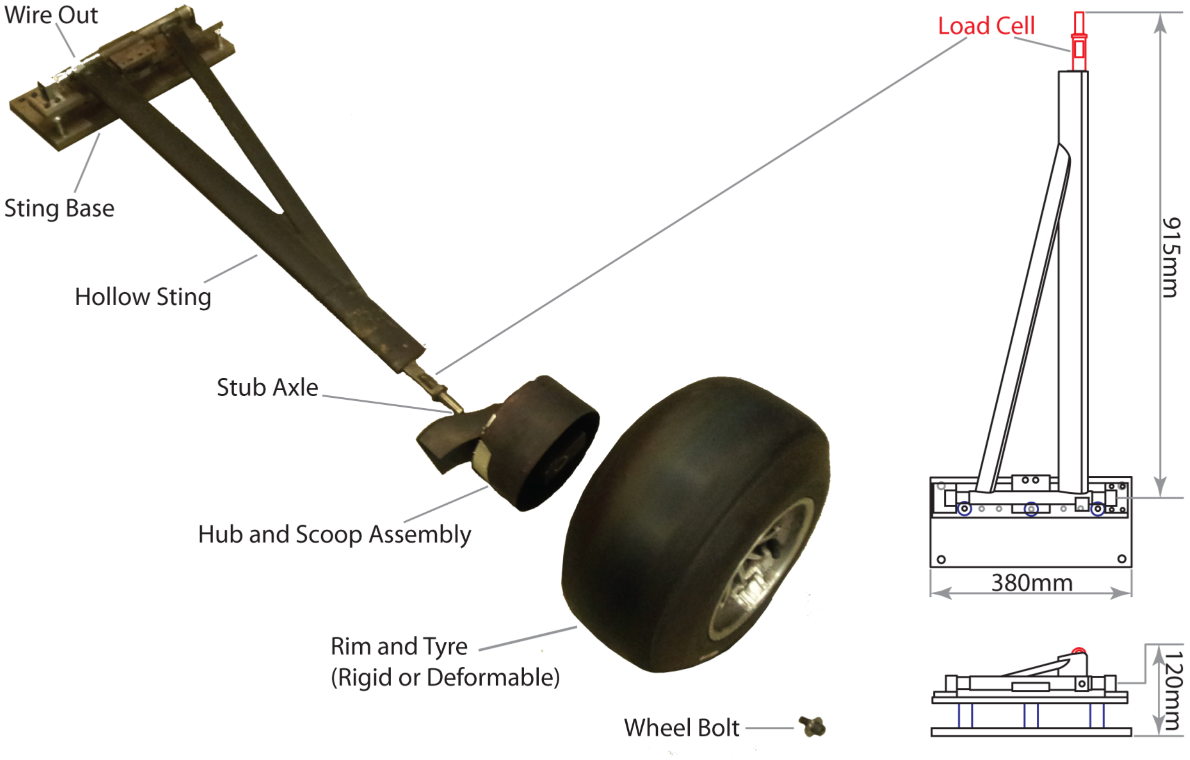

Figure 2.4: *Isolated wheel support sting with integrated load-cell used in the wind tunnel experimentation.*

The sting was of steel construction and hollow in order to allow data cables to be fed through it. It had good resistance to bending moments and relatively small deflection was observed even at high levels of vertical load. The end of the sting comprised a recess and four slots which received a purpose-built drag load-cell which had a stub-axle machined onto the live end. The wheels as described above both had a twin bearing system allowing free running on the stub-axle. The stub-axle had a threaded bore which accepted a specially designed wheel bolt, essentially comprising a washer and cap-head bolt together, in order to secure the wheel.

The hub itself was a simplified version of the real car wheel internals for the wind tunnel tests. It comprised a central block, machined from aluminium which was tightly clamped between the inner wheel bearing washer and the end of the load-cell. Onto this block was mounted the inboard circular plate, again made from aluminium, which was 156mm in diameter, leaving a 2mm gap around the perimeter to the rim. A drum was mounted to this inboard circular plate which mimicked the carbon-fibre shroud discussed in Section 1.2.8 and specifically in Figure 1.27. The shroud was constructed from rapid prototyping resin and was cylindrical, contrary to the rim profile which tapered and therefore reduced the aforementioned gap between the rim and the hub.

The brake duct, which was defined as a scoop type with having an open internal wall, was mounted to the inboard plate to complete the hub assembly. This is summarised in Figure 2.5

2.1.5 Brake Scoop and Through-Hub Flow Control

The brake duct, or ‘scoop’ as the specific type is commonly termed, was produced by rapid prototyping techniques and modelled from precise surface measurements taken from the one on the full-car 50% model. A pitot-static tube was produced, also from rapid prototyping materials, and assembled into the scoop in order to measure the inlet velocity and therefore through-hub flow at the most forward part of the duct. This design and manufacturing process was done as part of Minto’s [73] investigations and can be found in more detail in his report.

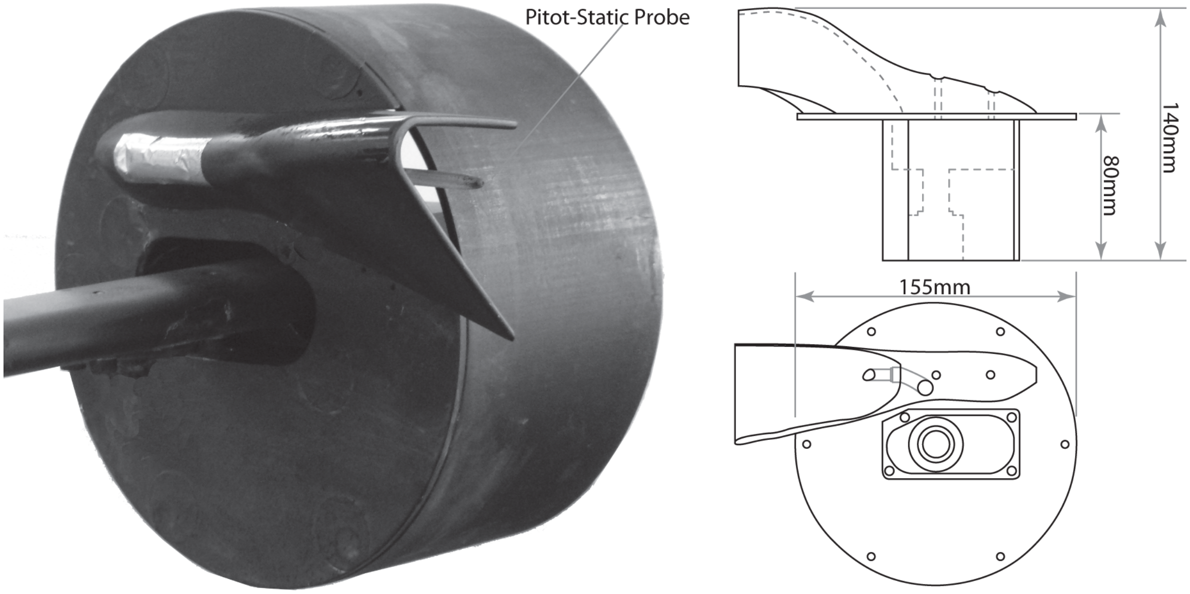

Figure 2.5: *Summary photograph and schematic of the hub and scoop geometry.*

Five different through-hub flow rates were tested comprising fully-open and fully-closed interfaces, a single mesh screen (as Minto [73]), two meshes and three meshes to fill in the range. The resultant hub-flow range was relatively evenly spaced allowing a good representation of the possible flow-rates through the wheel due to the restriction of the centrifugal brake rotor and cooling fins.

The meshes were placed between the scoop and the inboard disc in order to minimise direct influence on the external aerodynamic flow features. Each time the scoop was removed to fit a mesh it was ensured that the angle of incidence when refitted was parallel to that of the ground plane. The local flow direction around the wheel is known to vary. It was considered from Minto's findings [73] that the local velocity vector at the inlet of the scoop was indeed with that of the freestream. Therefore, this was a viable parameter to adhere to. In the case of a real F1 car, the brake ducts are generally at a negative angle of incidence, pointing down, due to the fact that the local velocity at the duct inlet is largely dominated by a strongly accelerated upwash from the front wing. In the absence of the front wing in the test section, realigning the duct with the freestream was appropriate.

Additional modifications were applied to the wind tunnel model of the scoop in order to try to understand the flow-field phenomena observed. These included boundary layer trips, 5mm in height (in order to induce separation at that point, rather than just to encourage transition of the boundary layer) and Nakiplast modelling wax fairings to the leading edges. The exact geometries are presented in the results section in Chapter 3.

2.1.6 Application of Deformation

The deformable tyre's deformation level could be controlled by three inter-linked variables: the axle height, tyre inflation pressure and vertical loading. Tyre inflation pressure and vertical loading both determined the axle height, which was considered to be the most direct variable to describe deformation levels. By changing the tyre inflation pressure, a different vertical loading was required to achieve the target axle height. Vertical loading is known to change constantly on-track and tyre inflation pressure is also known to fluctuate, either through design or reaction to external heat sources, friction and constant deformation of the tyre structure. The axle height is a non-manufacturer specific parameter. This means, because all teams are adhering to the same set of rules and regulations, which dictate physical geometrical sizes, leaving maximum downforce levels, aero-balance and tyre inflation pressure as free variables, the axle height was considered as the most generic variable to determine a level of deformation which would yield trends regardless of team or even formula.

The method by which deformation was applied in this set of experiments was to make use of the wheels-off sting. A 6mm thick steel arm was extended beyond the pivot point, outside of the jet, whereby a pneumatic cylinder applied an upwards force which could be adjusted via an air-pressure regulator. This translated to a downward vertical load on the tyre and hence a controllable and repeatable deformation. Figure 2.6 shows this layout.

The axle height was set statically, making use of the average value taken with a vernier calliper from the ground plane to the sting on the inboard side, and from the ground to the centre of the wheel-nut on the outboard side. This accounted for any camber changes and meant the nominal axle height set was the mid-axle height from the ground plane.

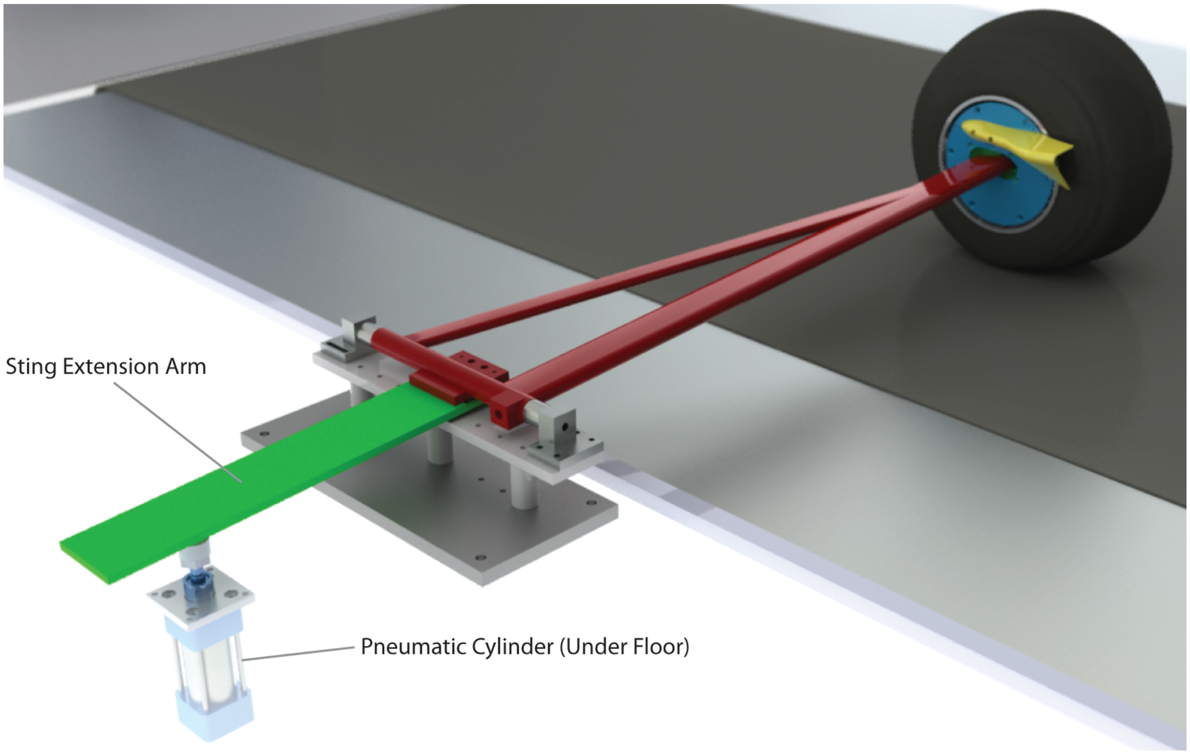

Figure 2.6: *Illustration of the method by which vertical load (hence tyre deformation) was applied.*

As with the results of Ridha & Theves [11], covered in Section 1.2.1, there was a notable axle rise brought about by the extending and straightening of the sidewall of the tyre under rotation. Given the sidewall of the tyre was weak to begin with, in order to achieve realistic deformation levels with minimal loading, this effect was significant. Therefore static axle heights were set lower than required for the test condition in order to take into account the axle-rise due to rotation. This means the nominal axle height quoted on all results is in fact the axle height of the rotating test condition and not necessarily the static axle height set before the experiment. There did not appear to be any pattern to this axle rise and therefore measurements were taken carefully for each test condition individually. These were measured by placing a Baumer laser distance meter with a range of 30-130mm to the sting and measuring the change of the distance from the sting-mounted sensor to the floor. These values are presented in Table 2.1.

As aerodynamic downforce increases with a velocity-squared relationship, the tyre's vertical loading constantly changes on-track. As a result, due to a constant nominal inflation pressure, the axle height changes with the downforce level. This factor is difficult to predict as the deformation of a tyre is known to be non-linear (see Yang & Olatunbosun [9], Section 1.2.1). A set of representative model-scale axle heights for the purpose of this investigation are presented in Table 2.1. The four axle heights presented, in decreasing order, represent slow-corner exit, early-straight, mid-straight (or high-speed corner) and end-of-straight conditions respectively.

Table 2.1 also shows the nominal loading required in order to achieve each of the target axle heights. These were calculated by extrapolating pressure on the cylinder bore to the axle. F1 teams run wheels-on models (wheels attached to the on-car suspension as opposed to wheels-off stings, the latter of which removes the wheel influence on the overall car load but introduces extra blockage) which severely limit the method by which they can apply vertical loading in the wind tunnel. As the teams' typical methodology of applying deformation is to purely rely upon a heavy wheel made of a bronze alloy, or made from machined aluminium with steel or tungsten weights bolted radially to the outside of the rim, it can be seen that only the very first test condition on the table can feasibly be achieved using this tyre. Although suited well to the slow-corner condition, whereby arguably most lap time can be gained, there is still a large range of loadings which go untested and since the floor of the model-scale vehicle moves by a similar magnitude in a typical range of aerodynamic tests (in order to represent a variety of on-track ride heights and cornering conditions), it is easy to see that there could exist a large aerodynamic sensitivity in the reaction to the wake at these different axle heights.

Table 2.1: *Range of tyre inflation pressures and axle heights tested (model-scale) with associated nominal loading. Values below the red line are not feasible to test in a day-to-day wind tunnel environment (as is the case of F1 teams).*

Tyre Pressure (psi / bar / kPa)	Mid-Rim Axle Height (mm - Model Scale)	Nominal Load (N)	Rotational Axle Rise (mm - Model Scale)
0.5 / 0.03 / 3.4	159	46	2.8
	156	127	2.1
	153	191	3.3
	150	240	2.9
2.0 / 0.14 / 13.8	159	127	1.6
	155	191	1.5
	153	240	2.0
	150	280	2.0
3.0 / 0.21 / 20.7	159	175	1.7
	155	240	1.8
	153	289	1.8
	150	334	2.6

The tyre developed resonances at different inflation pressures. This can be seen in section 2.2.1. These resonances are highly sensitive to vertical loading. As such, changing the tyre inflation pressure changed the axle height at which the resonance occurred. In the case of 3.4kPa, the 155mm case could not be tested because this fell exactly on a resonant load. Instead, 156mm was tested for this early-straight speed condition.

2.1.7 Yaw and Camber Experimentation

To enable yaw experimentation, the four mounting holes, as in Figure 2.4, were replicated in the tunnel floor at three discrete angles of -5°, 0° and +5°. To test each angle of yaw, the assembly was simply unbolted and replaced in the required location. This described a pivot point about the pneumatic cylinder tip which ensured deformation could be applied consistently independent of yaw angle. This allowed a solid mount with no backlash or unwanted movements which would change the yaw angle during experimentation.

The method of applying deformation altered the camber angle slightly, from -3.2° to -3.4° from low to high axle heights respectively. This was replicated in CFD work reported in more detail in Chapter 4. For the purposes of studies of deformation, this effect was not taken into account for the experimental setup although it has been considered in the analysis of results.

For the camber range studies, the camber angle was set by varying the height of the pivot bar, again as defined by Figure 2.4, as well as the vertical loading. The three cylindrical spacers in the schematic were replaced with four threaded rods, using the available mounting holes already in the sting, and the displacement from the ground to the upper platform containing the pivot bar was adjusted by flanged nuts above and below.

In order to maintain the axle height as well as set a camber angle, a fine balance of pivot bar height and vertical loading had to be chosen empirically for a fixed nominal inflation pressure. These are presented in Figure 2.7. This ensured the characteristic deformation was unaltered between cases (axle height parameter) and the only changing variable was the camber angle, measured with a digital inclinometer capable of measuring to one hundredth of a degree, placed flush against the rim at two points one directly above the other. The range extended from 0.0° to -4.0° (negative only as this is generally all that is used on a race car due to the mechanical benefits discussed in the Chapter 1), a fairly extreme camber angle reported to be used on one occasion during the 2011 F1 season, allegedly responsible for tyre blistering at the Belgian Grand Prix [86]. Because of this, and the fact it is similar in size to the built-in camber of the rigid wheel, it was considered as a good limit for the tested range. Incremental steps of 0.5° were used and drag measurements were taken for all values. For flow-field experimentation, only 0.0°, 2.0° and 4.0° were measured to show any progressive changes in the flow-field.

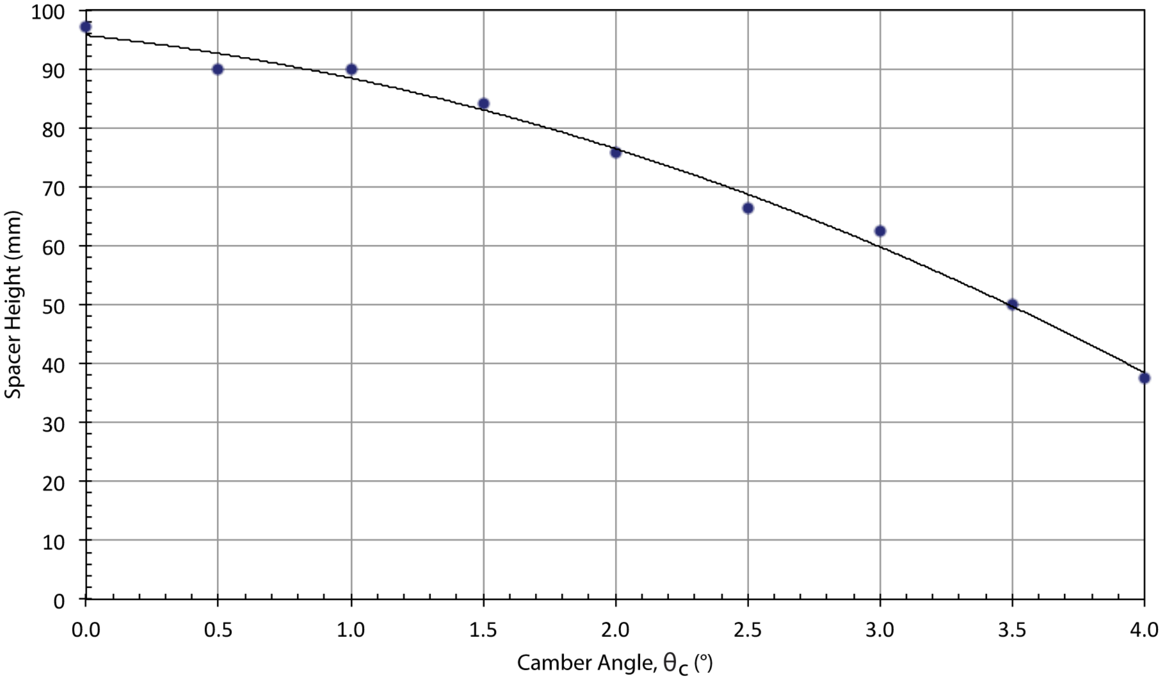

Figure 2.7: *Sting pivot bar spacer height vs. camber angle.*

2.2 Measurement Techniques

2.2.1 Load-Cell Force Measurements

Load-cell drag force measurements are often the most useful for quickly identifying changes to flow structures (indirectly). Although not quantifiable in terms of exact flow-field characteristics, they can be used to determine the overall performance of a component and infer the size of the wake, and hence, the behaviour of the average base-pressure. As mentioned in the literature review, load-cell measurements are generally used only for drag measurements in isolated wheel aerodynamics studies, as lift is difficult to resolve from the varying reaction force, especially with a deformable tyre.

The load-cell was of a typical strain gauge Wheatstone bridge construction and situated at the end of the sting as described earlier. A calibration was performed by applying known masses, measured within a tenth of a gram using independent pre-calibrated scales, to the live side of the cell and the output voltage was recorded to six decimal places using a NI-DAQmx data logger by National Instruments. The calibration can be found in Appendix A. The circuit was amplified in a low-noise environment and the voltages were recorded using in-house written software which was part of the 'Durham Software for Windtunnels' (DSW) suite. The final recorded voltage measurements for a static load, measured at 500Hz for 8,192 samples, were found to have an uncertainty [87] of what equates to 0.008N. This value equates to an experimental uncertainty of $C_D \pm 0.0004$, less than half a 'count' of drag, built into the measuring technique. It is worth emphasising that the load-cell measures a drag force perpendicular to the axle and not always the freestream. This is accounted for in any data analysis.

Once the sensitivity of the device had been found, the offset or 'tare' was required at the start of every run. This was achieved for both tyres by taking a measurement of drag at the tunnel and belt speeds shown in Table 2.2. These values were all taken at a 500Hz sampling frequency for 4096 samples in the case of the rigid tyre experiments and 800Hz with 8192 samples for the deformable tyre experiments. For the rigid wheel, the low-speed trundle (wind-off: Run 2) was deducted from the main test (Run 4) in order to account for the aerodynamic effects induced by the high-speed rotation of the wheel and road whilst still deducting mechanical drag forces. This is common practice in both the literature [23] and in F1. However, for the deformable tyre, a non-constant mechanical drag was noted. Figure 2.8 shows the incrementing wind-off mechanical drag-force over the whole range of velocities.

Table 2.2: *Range of wind and belt speeds used for load-cell measurements.*

Run Ref.	U_{ref} (ms^{-1})	U_{belt} (ms^{-1})	Description
1	0	0	Load-Cell Zero Offset
2	0	1	Low-Speed Trundle (Bearing Drag)
3	0	25	High-Speed Trundle (Rotation Induced Flow-Field)
4	25	25	Main Test Run
5	25	0	Stationary Wheel

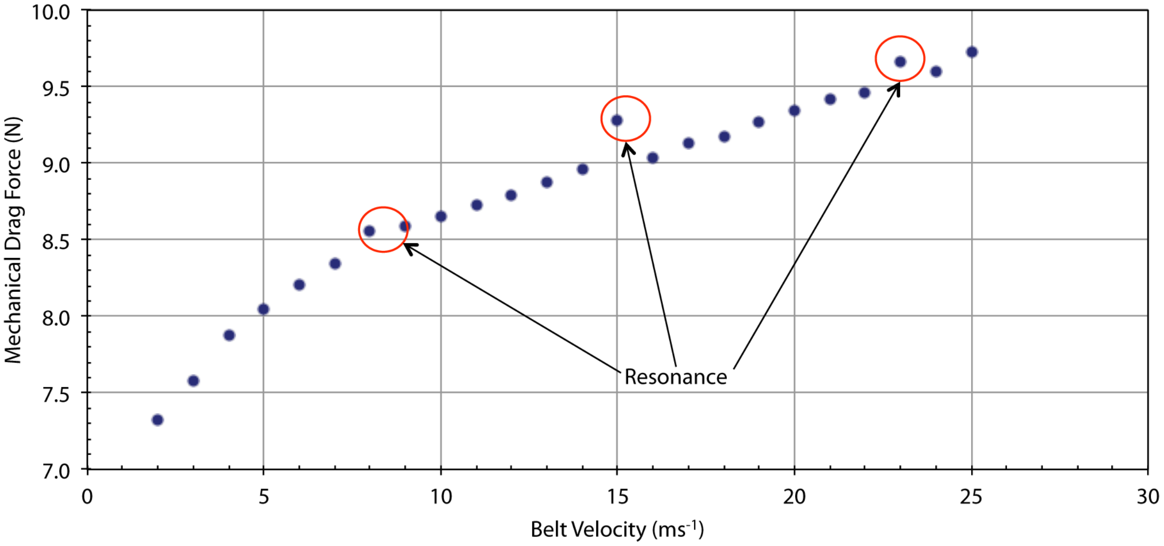

Figure 2.8: *Rotational speed-dependent mechanical drag force on the deformable tyre at 150mm axle height with an inflation pressure of 20.7kPa.*

The non-constant mechanical force can be identified over the first part of the velocity range. After which, a velocity-squared component was observed which explains the induced flow-field. However, this occurred very late at around $23ms^{-1}$ upwards. Deforming a tyre takes energy out of the system and this can be quantified as a drag force and explains why the mechanical force is not constant after a certain low-speed value. To begin with, the force increases steeply and linearly, including the non-resolvable bearing drag and the initial hysteresis in the rubber. As the rotational velocity increases, the axle height rises slightly (reducing the tyre deformation), unloading the system, and the inertia of the system also contributes to a smaller gradient. There are several points where a resonance occurs with the tyre (Figure 2.8). This was taken into account when choosing velocities in order to prevent the resonance from impacting on the test values in Table 2.2.

As a consequence of the above, the high-speed trundle (wind-off: Run 3) was used for the deformable tyre's tare. This meant that some of the rotation induced aerodynamic forces ('windage') were removed from the final result. However, using the low-speed tare, as in the case of the rigid tyre, would have led to false trends because of the non-constant mechanical drag.

2.2.2 Pressure Transducers

The pressure transducers utilised in this investigation were amplified pressure transducers produced by Sensor Technics (HCLA12X5DB). They had an operating pressure between 0.0mbar and 12.5mbar (1.25kPa) and a very high proof pressure of 250mbar (25kPa). For the application used here, the largest change in pressure was predicted using the expected dynamic pressure (q). For tunnel velocities in the 2m^2 tunnel, pressure differences of no more than 750Pa ($\sim 2q$) were to be expected meaning these were well suited for the application. Because the transducer chips were amplified, voltages in the range of (0.0-5.0)V were a typical output range without the need for external electronics. Amplified transducers also provide the added benefit of having a lower susceptibility to noise and interference. Banks of five transducers had been packaged in-house and hence each box could be used for five-hole probe measurements. The five-hole probe transducer banks all used a common atmospheric reference pressure. Banks of two had also been assembled for use with pitot-static probes.

In the case of the latter, the stagnation (or 'total') gauge pressure was measured independently and the second transistor measured the dynamic pressure by connecting the stagnation pressure to one terminal and the static pressure to the other. This way, the dynamic pressure to be used in velocity calculations and for non-dimensionalising was measured directly and not a result of post-processing. If the static pressure was required, it could be determined by deducting the dynamic from the stagnation pressure.

The voltages were transmitted through a single large bundled cable into a breakout box which filtered the channels for common interference before feeding into the NI-DAQmx data logger (as used in the load-cell measurements). The transducers were all calibrated individually in-house by applying known pressures created by connecting two micro-manometers together. One micro-manometer was used to apply a pressure (by adjusting the height of the reservoir bottle) which could be measured accurately using the other. The same pressure differential was fed into the pressure transducer and the output voltage logged for the production of the individual calibration. This calibration file was compatible with the DSW suite used for the analysis of all pressure data.

2.2.3 Five-Hole Pressure Probe

In order to measure the flow-field characteristics of the wake, one of Durham University's in-house designed and manufactured five-hole pneumatic pressure probes was used. The tip was of a specially designed geometry and was manufactured using rapid prototyping with a layer resolution of 16μm. Due to the relatively short lifespan of rapid prototyped products left untreated, which in this instance had to be the case, the rest of the body was constructed from an aluminium tube with the same outside diameter as the head. The hypodermic plumbing was contained within the tube and the pipes were held in place using a rapid prototyped end-stop. The probe can be seen in Figure 2.9. A design of this nature allows fast turnaround of production as well as a high accuracy tip. The probe was used here as a steady-state probe although it can be used for transient studies in conjunction with a transfer-function correction (as in Sims-Williams & Dominy [91] and Oettle et al. [88] [89] [90], for example).

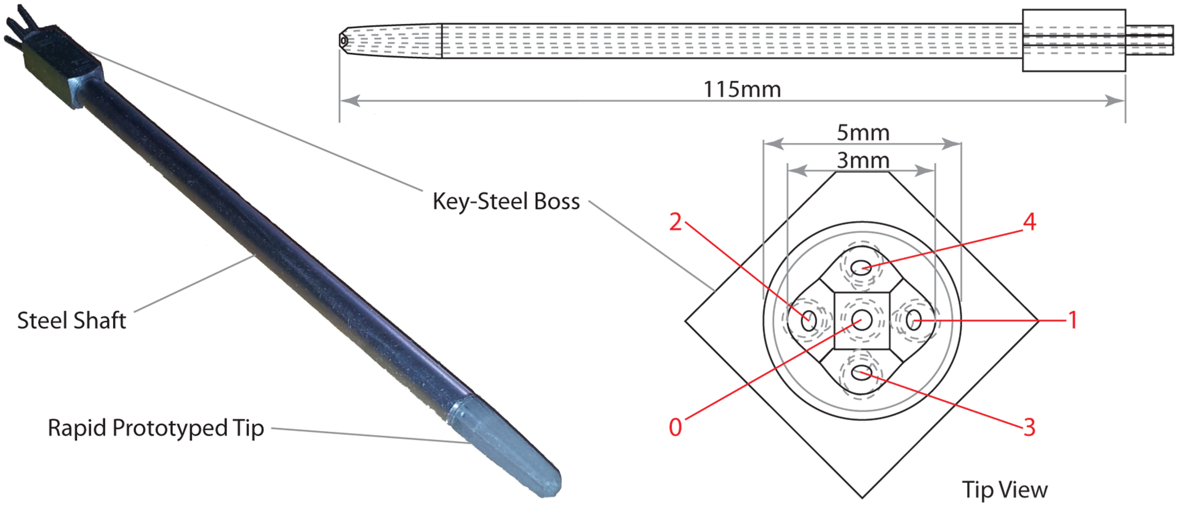

Figure 2.9: *Photograph and schematic of the Durham University five-hole pressure probe.*

The first hole is located on the tip which is a small square plane perpendicular to the probe's axial direction. The four holes around this tip, in a diamond configuration at 45° to the tip plane work together to allow flow angularity to be detected. The equations used to obtain coefficients of yaw and pitch, as well as the stagnation and dynamic pressure coefficients respectively are defined by

$$C_{yaw} = \frac{P_1 - P_2}{P_0 - \left(\frac{P_1+P_2+P_3+P_4}{4}\right)}, \tag{2.1}$$

$$C_{pitch} = \frac{P_3 - P_4}{P_0 - \left(\frac{P_1+P_2+P_3+P_4}{4}\right)}, \tag{2.2}$$

$$Cp_0 = \frac{P_0 - P_{tot}}{P_0 - \left(\frac{P_1+P_2+P_3+P_4}{4}\right)} \tag{2.3}$$

and

$$Cp_{Dyn} = \frac{P_0 - \left(\frac{P_1+P_2+P_3+P_4}{4}\right)}{P_{Dyn}}, \tag{2.4}$$

with pressures based upon the numbering in red in Figure 2.9.

As a result these non-dimensionalised parameters can be plotted in a graph of real yaw and pitch and when populated with enough points, form a calibration file (Appendix A). The probe was individually calibrated using a dedicated calibration facility. This comprised a nozzle which was 102mm (4in) in diameter connected to a fan via a long diffuser. The flow speed was measured using upstream and downstream-of-nozzle static pressures and this was pre-calibrated with pitot-static tube velocity measurements. Therefore, the exact velocity exiting the nozzle was known and by placing the probe tip in the centre of this nozzle, at a range of known angles of pitch and yaw set by a rotating traversing stage, a calibration file was populated.

Measurements in the wind tunnel could therefore be treated by an inverse process. By creating pitch and yaw coefficients from the individually measured pressures for each hole, the result could be interpolated to give an exact pitch and yaw angle of the flow at that discrete point.

The advantage a five-hole pressure probe brings is in its large amount of velocity and pressure data for such a simple design and operation principle. They are commonly used within the aerodynamic wind tunnel testing field and Sims-Williams & Dominy [91] and Bryer & Pankhurst [92] both provide good reviews of the use of these devices.

The probe had a range of ±45° in both pitch and yaw (although calibrated between ±60°). This is typical of a five-hole probe. However, this means that areas of high flow-angularity and areas of reversed flow could not be resolved. The general wake structure outside of these regions could be obtained, however, and for regions of reversed flow and local-wake, other techniques had to be used.

2.2.4 Particle Image Velocimetry (PIV)

Particle image velocimetry (PIV) is a non-intrusive technique enabling the visualisation of a flow-field. It is not restricted by reverse flow regions and as such provides valuable information regarding the direction and magnitude of the velocity of the entire fluid flow. Since a large concentration of the work in this thesis was in relation to obtaining successful PIV measurements within a large working section, it will be discussed in detail here.

Unlike point-by-point laser doppler anemometry (LDA), or the five-hole pressure probe, an entire image plane can be captured in only a few seconds. The setup of such a system, however, is much more laborious and time-consuming than the other technologies. It also only provides velocity magnitudes and vectors with no direct information relating to the pressures and hence losses within the system.

The principle of operation is that a high-intensity laser beam is fired from a dual headed pulsed laser. In this instance, a 120mJ Nd:YAG laser manufactured by New Wave Research [94] was used. The airflow is seeded with fine particles which are entrained in the fluid flow and the illuminated particles from the double laser flash are detected with the cameras. The images are then processed electronically via cross-correlation and velocity vector plots are produced. Riethmuller [95] published a lecture series which describes PIV in further detail than will be discussed here.

2.2.4.1 Seeding

The flow was seeded using a 40 nozzle seeder by ILATEC [93] which holds a reservoir of Di(2-ethylhexyl) Sebacate (DEHS). This fluid is atomised by the nozzles, fed by compressed air, and dispersed as a ‘fog’ or ‘smoke’ into the flow. The particle size is reported to be of the order of one micron for this seeder. This ensures a small enough particle to entrain onto the fluid correctly, without buoyancy effects affecting the path, but with large enough size to be detectable by at least two pixels in the camera field-of-view. The importance of this is discussed in Section 2.2.4.8.

The seeder was connected to a purpose designed smoke-rake which is summarised in Figure 2.10. This comprised four copper pipes with 2mm diameter holes drilled at 15mm apart to allow high-density seeding in areas of interest and 25mm spacing for low-density seeding around all other areas. Seeding intensity was controlled via the inlet air-pressure for the seeder and by temporary sealing of unwanted holes in the smoke-rake. It was important to balance the level of seeding as excessive smoke in the flow can cause a weakening of the image (due to distortion from smoke not in the laser plane) and also as the image can lose the distinct peaks and troughs necessary for cross-correlation.

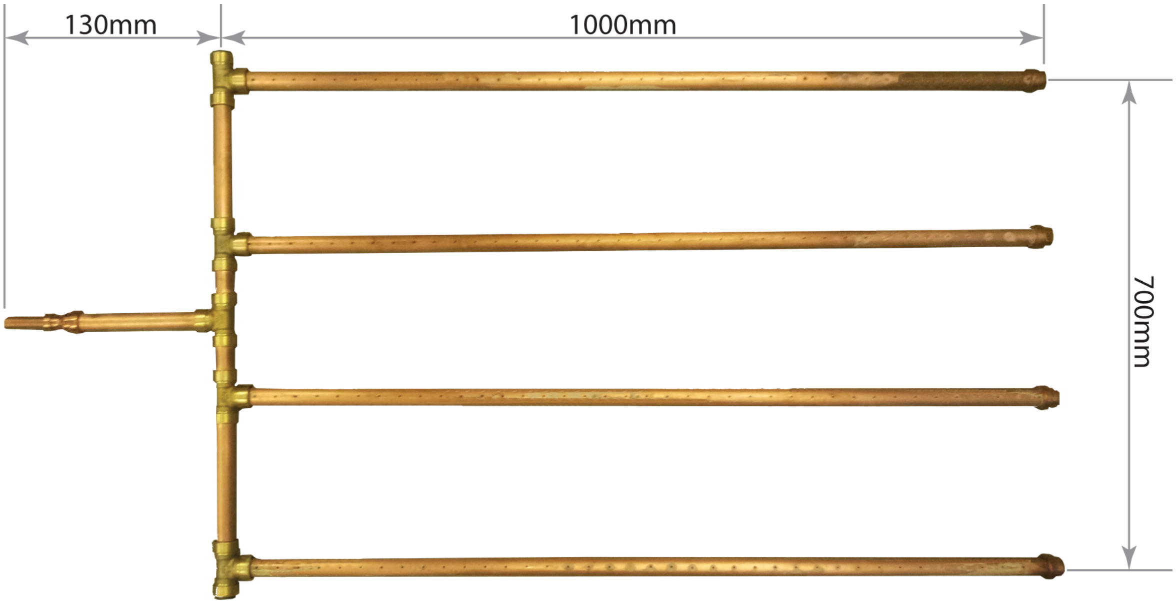

Figure 2.10: *Photograph and important dimensions of the purpose-built PIV seeding rake.*

2.2.4.2 The Laser

A Nd:YAG laser is a high-powered crystalline solid-state laser which is optically pumped via a high-intensity flash-lamp. The instantaneous photon energy from the flash lamp produces a phenomenon called ‘population inversion’ whereby electrons in the Nd:YAG crystal are promoted to a high energy state. These electrons naturally collapse down to the ground energy state either directly or in multiple steps. The resulting energy is emitted via photons, particles of light with discrete energy. The discrete wavelength depends upon how many of the discrete energy levels each electron fell in one go. These photons are subsequently made to reflect and resonate in an optical cavity producing a cascade of photons each with the same wavelength.

In the case of a pulsed laser there is a mirror at both ends which have a very low transmittance value (the amount of light that can penetrate the mirror and be either absorbed or transmitted through) and an exit aperture adjacent to one of them. In order to determine whether the light is to resonate and ‘charge up’ or to fire, a Q-switch (birefringent Pockel’s cell), which has two available discrete refractive indices can be controlled externally via an electric field which is fast-acting and therefore well suited to PIV. Changing the refractive index electronically allows the laser to be fired instantaneously for short bursts.

The laser used in this investigation produced a high-intensity 120mJ beam, visibly green of wavelength $\lambda = 532nm$. The subsidiary wavelengths were either not in the visible spectrum, not powerful enough to be visible or were filtered out by the camera at the detection stage.

As two images are required of the order of microseconds apart, to detect particle movement but not allow signal drop-out (see Section2.2.4.7) two optical-cavities are needed as the laser would not have enough time to charge up for the second flash. This is why the dual-head laser was used in this application. More information on Nd:YAG lasers can be found in Silfvast [96] among many other books on laser fundamentals.

2.2.4.3 Beam Delivery

A common technique for beam delivery is via an articulated arm which has multiple mirrors and articulated pivoting elbow sections. This allows multiple degrees of freedom and therefore delivery of the beam to any desired location. The fact that there are so many mirrors, however, leads to many cascading losses. For the through-hub flow experiments in this research (those on the rigid tyre), an articulating arm manufactured by ILA [93] was used. This layout can be seen in Figure 2.11. It had a length of 1.6m when fully deployed and had an 8kg counterweight used to keep the system balanced and to provide a damping effect when the arm was placed in the flow-field. It comprised seven 45°

steering mirrors at each of the joints plus one at the base-block to which it was mounted, each with a two-axis adjustment. However, over the length scales required in the wind tunnel, the aforementioned losses were occasionally too high to the point where particles were not visible. Typically, mirrors used in this sort of application have a reflectance of in the region of 95-98% [97] and as a result the final beam was only around two-thirds the intensity of the initial beam.

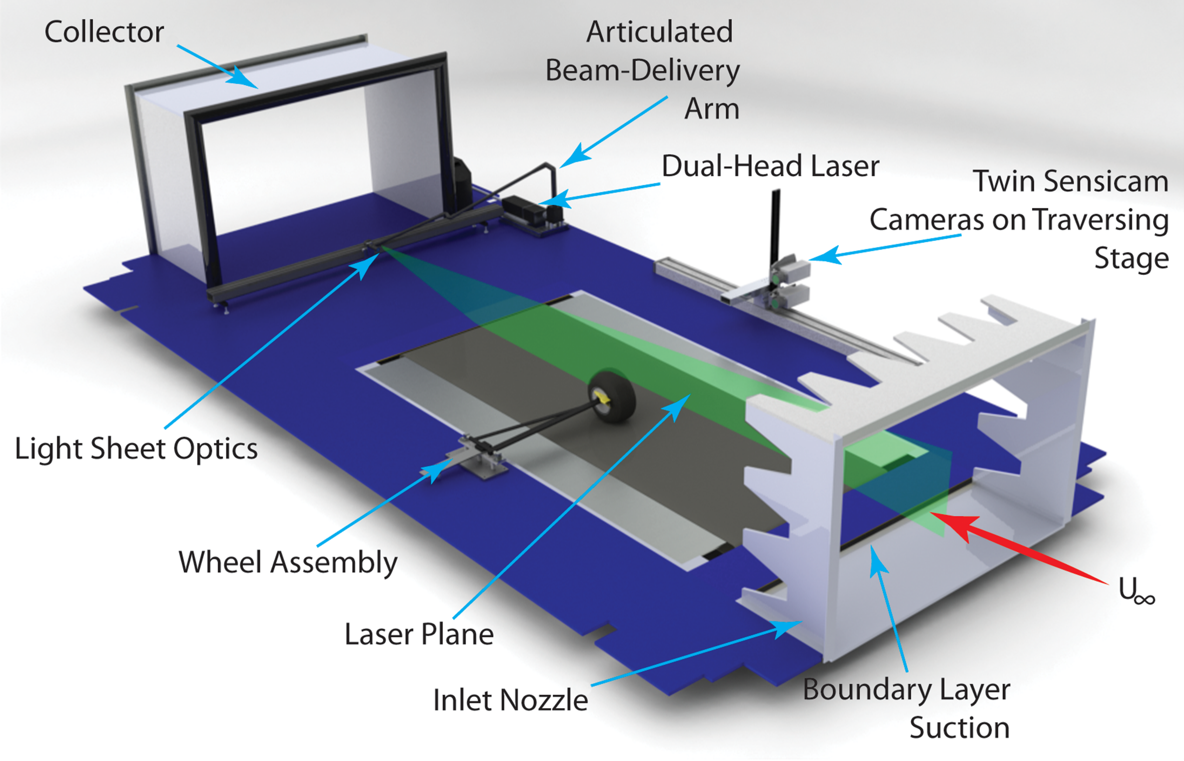

Figure 2.11: *CAD image representing the general layout of PIV equipment in the Durham University $2m^2$ Wind Tunnel.*

To counter this effect, deformable tyre PIV comparisons were undertaken without the articulated arm, instead mounting the laser body directly in the freestream. This was placed over ten wheel diameters (10D) downstream from the wheel and measurements were initially only taken as far as 1.8D downstream of the axle, and then refined to 1.2D once the size of the recirculation zone was known. The blockage introduced by the laser body was of the order of 1.4% near the collector. This resulted in a direct beam to light-sheet optics configuration which allowed the full intensity of the beam to be utilised in the PIV. This allowed particles that were previously invisible or faint to become vivid and usable. This configuration has since been applied in the work of Howell et al. [98] when investigating base-cavities for drag reduction of commercial vehicles in the same wind tunnel.

To improve the system further, a lower blockage configuration was designed and constructed. The Durham University PIV Periscope was designed as part of this work. Essentially, a slot was cut into the floor of the wind tunnel which allowed a cylinder to protrude, of the same dimensions as the initial stage of the articulated arm. A 90° bend was machined which allowed a high-quality high-reflectance mirror (98%) to be mounted onto a rapid prototyped cap. Figure 2.12 shows the summary of the design.

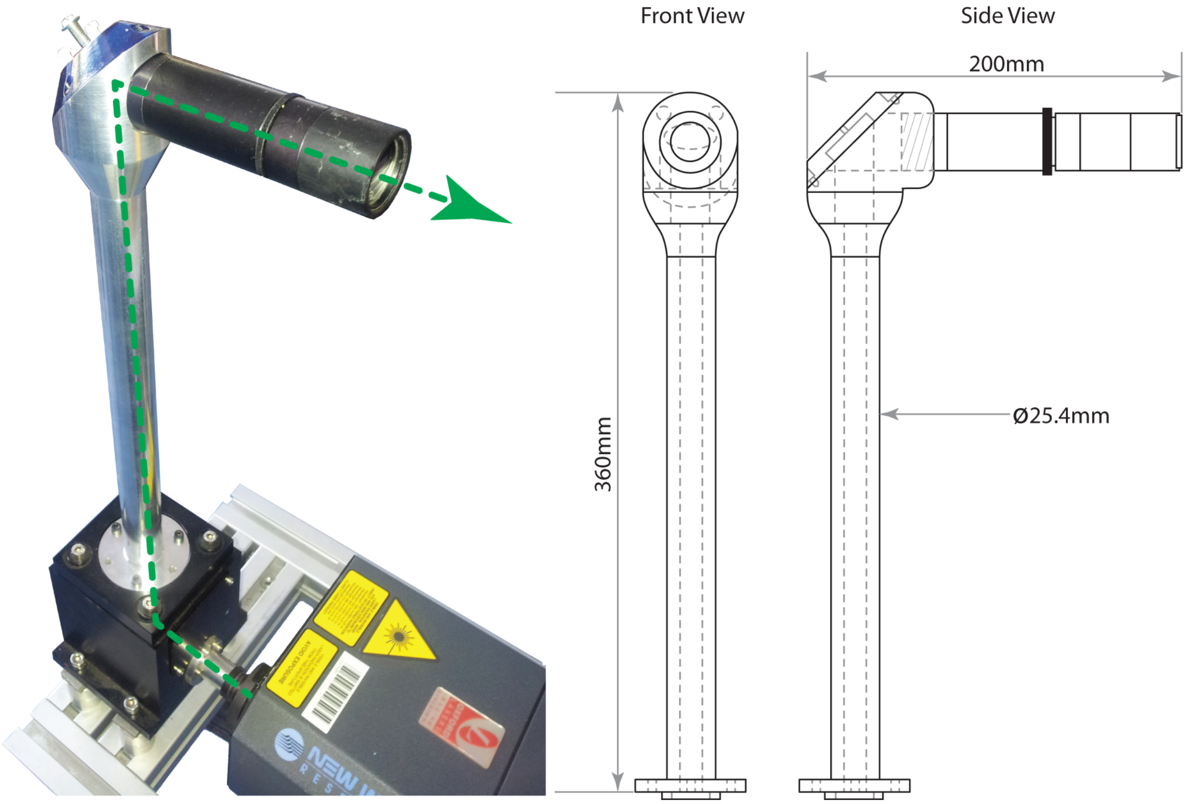

Figure 2.12: *Photograph and schematic of Durham University PIV Periscope designed for high-intensity beam delivery and minimal test-section blockage.*

This design was utilised for the yaw and camber studies. Although overall the images produced post-filtering vector field validity (see Section 2.2.4.8) in excess of 90% irrespective of which of the previous two techniques were applied, the periscope allowed a blockage of only 0.2% and delivered a beam within 95% of the overall intensity capacity of the beam. Although the laser-body-only technique provided 100% of the intensity, it was at a much higher price from an aerodynamic perspective. The laser body also had to be sealed in an impervious bag to prevent the seeding fluid from contaminating the laser internals, making it appear only as a short term solution.

2.2.4.4 Light-Sheet Optics

Once the laser beams were in the test section, tightly focused, coincident and co-linear, a set of light-sheet optics were used, essentially comprising a focusing lens followed by a cylindrical lens in order to disperse the sheet into a very thin diverging plane. Adjustment of the distance between the focusing and cylindrical lenses led to changes in the focal point of the sheet and the divergence angle could be controlled by moving or clipping the cylindrical lens. It was important to keep the beam from diverging too much otherwise laser intensity was wasted in the interrogation region. It was also important to have the focal point at or near (Section 2.2.4.8) the area of interest in order to have highly visible particles.

2.2.4.5 Cameras

The images were obtained by a pair of Sensicam cameras, each with a Peltier-cooled CCD which was 1280 × 1024 pixels in size. The cameras were grey-scale and could obtain 12-bit images allowing high fidelity in shading. This allowed precise representations of the particles in the flow to be captured in the images. In addition, a single narrow-band filter was applied after the lens in order to filter out all but the 532nm light transmitted by the laser. Of course, this frequency exists in natural light and long exposures led to ambient features being included in the frame. These did not move relative to the accompanying image, however, so they did not cause a problem in the cross-correlation process.

Two cameras were utilised in order to double the size of the image frame. The total instantaneous capture measured 180×350mm. In addition to this, the cameras were placed on a one-dimensional traversing stage which could be moved allowing the cameras to remain focused on the laser plane but allowing further detail of the wake to be obtained. There was a cross-over of around 15mm.

Three different plane orientations were available for flow-field studies. The first is the longitudinal plane (x-z) which describes the vertical centreline of the wheel. This was the most commonly used as the image quality was high and recirculation lobes could be identified as well as allowing useful comparisons with probe work of other authors. Similarly, the horizontal planes (x-y) allowed a similar quality of image. In the longitudinal plane, the laser was downstream (in the airflow) and the cameras were to the side out of the air flow. This meant that there was less likely to be a vibration in the images. For horizontal planes, the cameras were mounted to a structural beam in isolation of the test section (Sims-Williams & Dominy [82] [83]) with the laser in the same location as for the longitudinal planes.

Crossplanes (y-z) often show extremely interesting flow-features but are regularly and consistently captured with five-hole pressure probes. In addition, when performing PIV measurements in this orientation, the majority of the flow direction is out-of-plane leading to a lot of signal drop-out (Section 2.2.4.8). Crossplane measurements were taken for the rigid wheel but this was deemed as being no more useful than the five-hole pressure probe measurements. As a result, the crossplanes for deformable studies, yaw and camber were obtained solely using the probe.

The cameras were mounted on a Scheimpflug mounting which allowed focusing onto a plane which was not parallel to the CCD. By allowing the lens to be on a flexible mount, the camera could be pivoted to focus on the plane. Figure 2.13 describes this pictorially.

This apparatus was only used subtly in cases where the distance from the camera to the laser plane was limited or where there was a detrimental high-intensity laser reflection into the path of the camera. Backscatter radiation is also of higher intensity than perpendicular scatter. Therefore positioning the cameras downstream, looking upstream, focused on the laser plane with the Scheimpflug apparatus was occasionally utilised (as in Figure 2.13). The spatial calibration feature of the software allowed for a perspective mapping of points.

2.2.4.6 Calibration

For the purpose of the analysis stage, a calibration image had to be captured. A combination of the calibration field for spatial reference combined with the image separation time (see Section 2.2.4.7) allowed pixel movements per image pair to be converted into a velocity vector. This was achieved by a grid of points 1mm in diameter, spaced 10mm apart, with every 100mm being denoted by a large

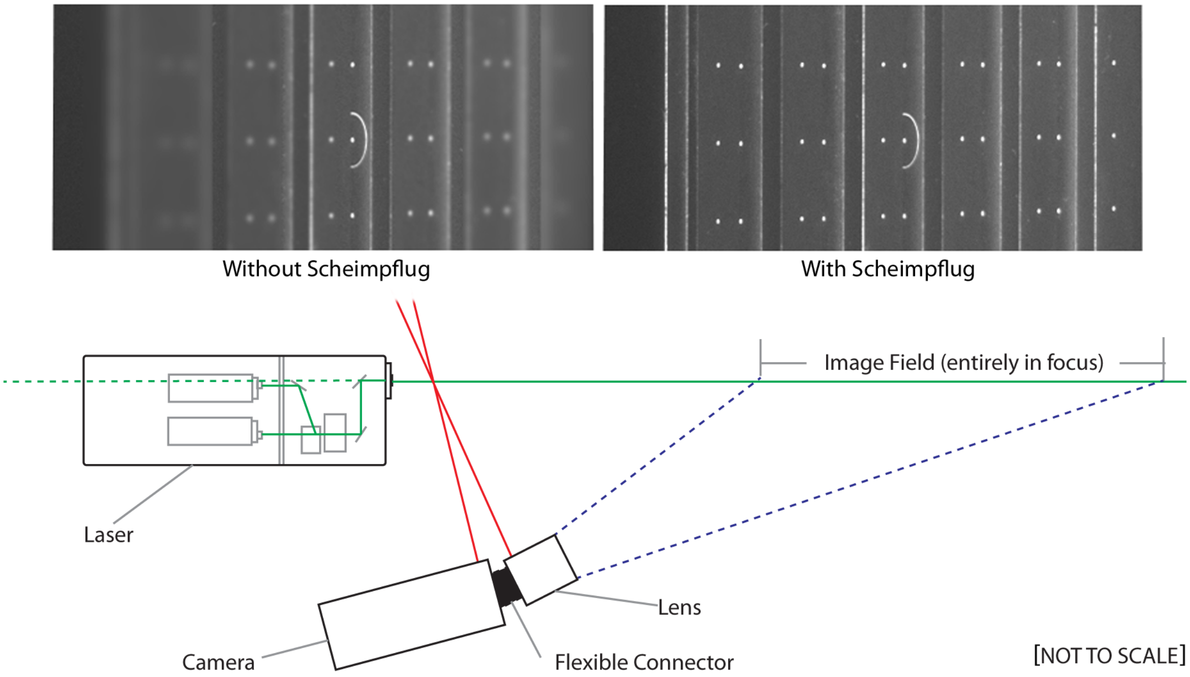

Figure 2.13: *Illustration of the concept of Scheimpflug focusing apparatus. Allowing the planes of the lens and the CCD to intercept on the image plane produces an image with a fully in-focus interrogation zone.*

circle of diameter 8mm with a central cross. This could be detected by the software when applying the calibration grid allowing it to ‘snap’ to the photographed points. A calibration image had to be taken for all camera and laser positions although in the case where a traversing stage was used, repeat images were not taken when revisiting points.

2.2.4.7 Timing and Synchronisation

The successful implementation of PIV requires careful tuning of the timing and synchronisation of the above equipment. The frequency of the laser flashes or image pairs (pulse frequency), the timing between the two laser flashes and hence the image separation (pulse distance), the intensity or charge time of the lasers (pulse energy), the camera pulse separation (camera width), laser and camera delays and camera exposure time are all parameters which must be controlled. These can be seen pictorially in Figure 2.14

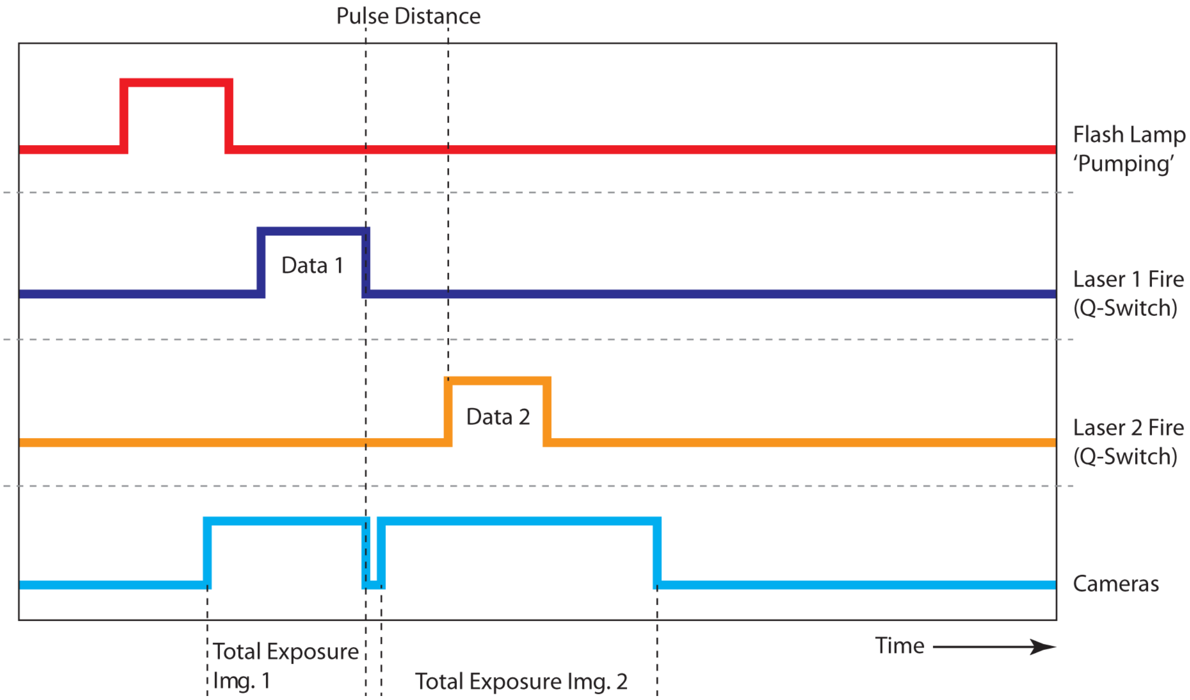

Figure 2.14: *Illustration of the timings and equipment synchronisation for PIV.*

The PIV synchroniser made by ILA [93] was used in this instance and controlled manually rather than by software interface. It was found that more light intensity could be found by manually adjusting the settings as opposed to using the pre-defined laser-strength parameters in the software. The pulse energy setting was adjusted to 185μs which allowed maximum light intensity to be achieved. Charging for longer than this resulted in either no further gain or a reduction in light intensity in extreme cases.

The pulse distance or image pair separation was the most sensitive parameter. It was important to set this parameter in order to obtain a significant movement of particles between the images, thus reducing uncertainty in displaced measurements, but at the same time reducing the likelihood of something called 'signal drop-out'. This is where particles captured by the first image move out-of-plane before the second image is captured. This means that there are a different set of particles to compare in the second instance and the correlation is poor. This parameter was measured empirically as being optimised around 20-30μs, for an image width of around 300mm with a freestream velocity of 25ms^{-1}. Although this only resulted in a 2-3 pixel movement between frames, this was enough to prevent pixel-locking (described in detail in Section 2.2.4.8) and was sufficient to allow velocities to be tracked without pixel-locking dominating (see next section).

The delays were set to zero and the camera width (triggering separation) was calculated automatically by the synchroniser's firmware. The remaining parameter, pulse frequency, was set at 4Hz as higher frequencies resulted occasionally in misfires and unusable 'dead image pairs' whereas lower frequencies extended the test period.

Each test case for the through-hub flow investigations comprised 250 image pairs, and for the deformable tyre and camber studies 400 image pairs were recorded and processed as in the following sections. It was important to collect a high number of image pairs as possible in order to obtain high averaging quality. Some previous studies overlook this and choose significantly fewer pairs. Newnham [99], however, recorded 1,002 image pairs for each variation on the standardised Ahmed geometry. However, that study involved an attempt to observe unsteadiness rather than just time-averaging. Thivolle-Cazat & Gilliéron used 200 image pairs for an isolated against enclosed wheel study. As a result, the values chosen here were made to intersect those referenced.

2.2.4.8 PIV Analysis : Cross-Correlation

Cross-correlation is the process by which PIV images are analysed. Each resulting vector field is comprised of two images called an image pair. These image pairs are compared with each other in the cross-correlation process. This is achieved by keeping one image static and breaking up the other into a grid of 'windows'. The operator can determine the size of these windows and the amount by which they can move when being compared. The process involves the movement of the window over the image below and a two-dimensional Fourier analysis of the peaks and troughs of the greyscale image, caused by the white particles on a black background, results in a correlation distribution which shows the most likely displacement of the fluid-flow at that position. In order for this to work, there must be discrete particles to produce a strong correlation. Otherwise the field is dominated by a noisy distribution and this can yield erroneous vector directions or sizes larger or smaller than the correct value by several magnitudes. These are dealt with in the post-processing, however, better results are obtained from a more accurate first stage cross-correlation. For more depth on the process of cross-correlation, and indeed the whole PIV procedure, the reader is referred to Riethmuller's published lecture series [95].

The software used in this investigation was VidPIV 4.0g by ILA [93]. The window sizes for cross-correlation were defined as being 64×64 pixel squares with a maximum separation of 32 pixels in the case of the through-hub flow studies and 32×32 pixel windows with a separation of 16 pixels for deformation, yaw and camber studies. In all cases, the grids presented in the wind tunnel results chapter (Chapter 3) were of a courser nature chosen to match the 15mm × 15mm grid taken by the five-hole pressure probe measurements. The finer resolution in the case of the 32 pixel windows, however, provided slightly more subtle flow detail than that of the 64 pixel window although more difficult to achieve.

It was found in the case of low laser intensity that defocusing the laser from the image field helped to increase the scattering angle of the particles. This is because the laser plane was in the process of diverging or converging and therefore increased the range of onset angles. This process resulted in the imaged particle sizes being larger and helped to prevent something called ‘pixel-locking’. This was where the particles were only of the order of one pixel in size and therefore the cross-correlation algorithm could only predict discrete velocity magnitudes and directions. Having particles larger than one pixel allowed a Gaussian distribution rather than a square peak to represent the particle and therefore sub-pixel movements could be identified.

The defocusing technique was not ideal as the laser intensity suffered but a study comparing an image plane 300mm wide with the focus line vertically in the centre, and then 150mm offset from this produced a particle size increase from an average of 2.2 ± 0.1 pixels to 2.9 ± 0.1 pixels. This took the particle size from the critical two-pixel diameter to being comfortably in the Gaussian range. With an increase of laser intensity through the methods described in Section 2.2.4.3 the two techniques provided sub-pixel detection and high vector validity.

2.2.4.9 PIV Analysis : Post-Processing

Once vector fields had been produced, the process of filtering took place. A two-stage filtering process was applied. Initially, a ‘window-filter’ was applied whereby the processed vector fields were analysed and plotted in a scatter-plot. By selecting an area to define which vectors were valid and which were not, or specifically, which were feasible and which were not, the erroneous vectors were omitted from the final output.

After a window-filter a local-filter was applied. This process investigated each individual vector and compared it with its nearest neighbours and the average velocity field. If the vector turned out to be considerably larger in magnitude or opposing in direction, where a shear-layer was not obvious, it was labelled as invalid.

The result was a vector field with typically between 90-98% valid vectors. In the event that the count was lower than this range, the test was repeated after either an adjustment to the seeding or refocusing of the cameras and laser optics.

There exists an option at this stage to apply an interpolation or adaptive cross-correlation. The former simply fills in the invalid vectors with mathematically viable vectors. The latter re-applies the cross-correlation algorithm but instead of moving the sample window in random directions horizontally and vertically, it is moved in the direction of the first-stage vector. This generally improves the measurement magnitude of the vector but not the overall flow-field description. Instead, for this investigation, the filtered vector fields were exported and run through a selective averaging program written for this purpose and subsequently added to the DSW suite. This computer code read in all of the image pairs and averaged only the valid vectors. In all cases, there were at least several frames which could contribute valid vectors for every grid point. This ensured that the final velocity field was constructed of only valid vectors of varying uncertainty. The results by this method are considered more informative than any where interpolation had been applied.

Because the cameras had been placed on a traversing stage and two cameras were utilised in order to increase the image field size, the vector fields needed to be stitched together in order to provide the final output. This was achieved by loading the files into Tecplot 360 [101]. This graphing software had many in-built fluid-dynamics specific features but for this application it was used to load the vector fields in with their absolute coordinates. A single file with a clean arranged grid of desired resolution from the input PIV measurements was then produced.

2.2.4.10 Additional Features of PIV

The PIV system was used in standard two-dimensional orientation although three-dimensional stereoscopic functionality was available. In the case of stereoscopic work, the cameras are arranged either side of the laser plane and the Scheimpflug apperatus is employed for its intended purpose. However, the data obtained by such stereoscopic work is not much more useful than the two-dimensional planes obtained as most of the flow-field characteristics are captured within a two-dimensional plane. The setup time is also considerably longer in the case of stereoscopic, therefore allowing fewer interrogation planes in a given test time. More planes were considered to be more beneficial towards understanding the changes in the flow-field with geometry than using the full stereoscopic functionality.

Additional techniques such as phase-locking, as used by Brizzi et al. [102] and McPhee & Johnson [68] allow the user to sample only a pre-defined moment in the flow-field, in the case of moving geometry. The former example studied a 40% rotating wheel assembly enclosed in a wheel housing and the latter is the already much talked about through-disc brake cooling study. For the purpose of this thesis, phase-locking was not considered a useful concept in the wind tunnel environment as global flow-fields, time-averaged forces and any unsteadiness could be detected by other means. PIV in this instance was used solely as a visual aid to help to better understand the flow physics involved.

2.2.5 Surface Flow-Visualisation Oil

Surface flow-visualisation oil is a very useful technique for examining a local flow-field. Areas of separation, recirculation, reattachment, high vortical-flow and general flow direction can all be easily identified from such a study. For this investigation, the technique involved the use of an orange UV-reactive powder mixed with kerosene (often paraffin) in order to produce a very low viscosity liquid. Coating the brake scoop evenly allowed the flow-field characteristics to be determined. By running wind-on for around five to ten minutes the kerosene was allowed to evaporate, during which time the mixture entrained onto the surface airflow. Thus, evidence of the surface flow was left behind in the form of varying concentrations of the powder, now attached to the surface. Examination using a UV light allowed very subtle details to be identified and photographed for later analysis. To accentuate the results, small black ink dots were placed on the surface in different zones of interest using a hypodermic needle and the experiment was run again. This provides a contrast to allow the strength of features to be visualised as well as the directionality.

2.2.6 Contact Patch Measurements

In order to measure the contact patch size a very simple but effective method was applied. By applying a cross to the slick tyre's tread in the x and y directions (with the circumference and perpendicular to that respectively) and using transferable ink, the contact patch length and width could be copied to paper and therefore measured exactly. As this could not be done under rotation, a static equivalent had to be applied. This was achieved by setting the axle height equal to exactly the run-time value and not the usual pre-rotation value (due to centrifugal reaction force leading to axle rise as already discussed).

2.2.7 Tyre Profile Scanning

As described in the literature review and the preliminary work described in the above deformable tyre apparatus section (Section 2.1.3), the profile of a tyre when rotating is noticeably different to that of a static tyre. As a consequence, a method of measuring the sidewall shapes at run-time was necessary.

Utilising the wind tunnel's existing three-axis traverse system, which could be controlled within an accuracy of 0.1mm, a laser distance meter was able to be driven around the wheel whilst it was rotating in-order to obtain the exact shape of the target profile. Figure 2.15 shows the principle used.

Two Baumer laser distance measuring sensors as described for the axle-rise quantification above (Section 2.1.3) were used for this arrangement. Specifically of type OADM 20I4460 with a range of 30-130mm. The first was targeted purely at a reference plate attached to the inboard hub disc, therefore measuring a flat reference with inclination equal to the camber angle of the wheel. The second laser measured the sidewall profile and was angled downwards by 8° in order to allow the laser

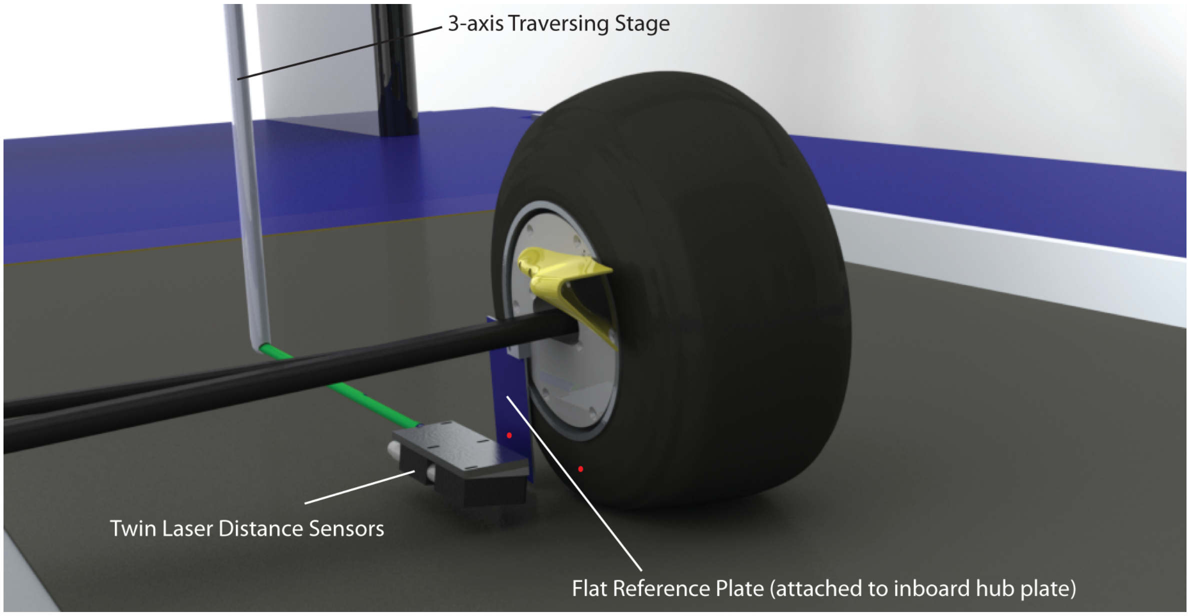

Figure 2.15: *Illustration of the principle used to measure the real-time sidewall profile of a fully deformable wind tunnel tyre using a twin laser distance sensor system.*

to observe the contact patch. Without this angularity, the lowest point that could be measured would be half the width of the laser unit, in this case 10mm. Since the contact patch and lowest regions of the profile were of the most interest, this was not an acceptable loss of data.

The laser sensors were checked for accuracy on a curved matt black rubber surface against the more traditionally used reflective planar surface (Appendix A). The average delta of the sensor on the curved rubber differed by 0.8mm compared to the same test on a reflective white surface. This was in addition to the inherent 0.3mm laser repeatability. Although this uncertainty of the order of 1mm appears large, the changes observed between cases were far in excess of this value, making this less significant.

As a result of the angle of incidence in order to view the full contact patch region, the raw measurements had to be converted into absolute measurements before they could be plotted or used for CAD reference points to put into CFD simulations. The correction is defined by

$$\Delta y = (L2 - L1)\, cos\theta_L - htan\theta_c \tag{2.5}$$

and is illustrated in Figure 2.16.

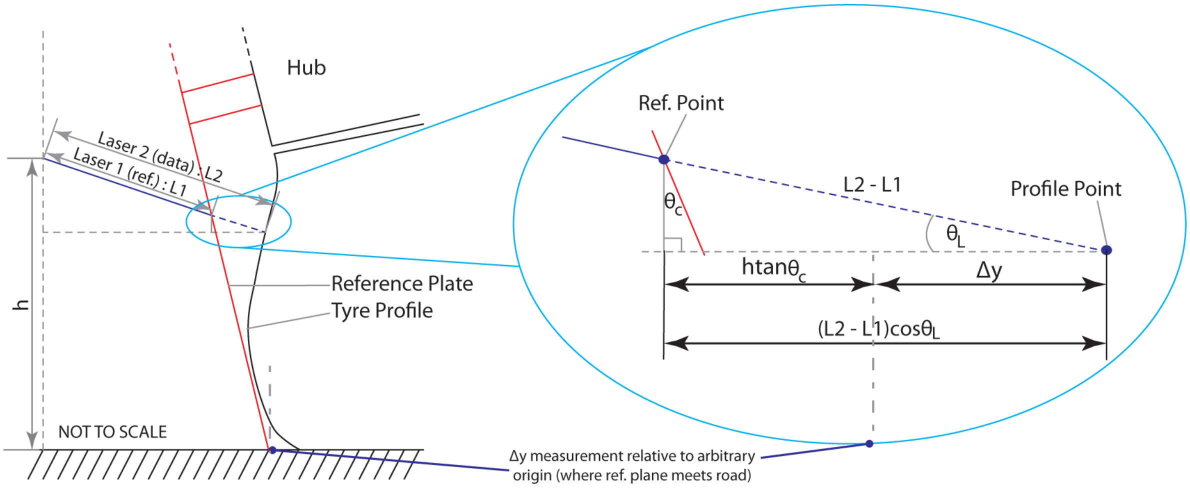

Figure 2.16: *Pictorial representation of the angles involved in the tyre profile scanning methodology. Equation 2.5 builds on the definitions in this figure.*

In the process of measuring the flat reference plate, an accurate description of the point-by-point movements and vibrations in the wheel system could be corrected for. By comparing the measured reference measurements with the expected inclination, a point-by-point offset was able to be deducted from the profile measurement in order to cancel out the unwanted movements. This resulted in a smoothed profile which was due to the change of physical geometrical shape and not due to any periodic or noisy features, as minor as they may have been.

The sidewalls were measured separately and given absolute coordinates in a CAD package based upon their connection with known points, in particular, the edges of the rim which could be placed and rotated by axle height and camber angle respectively. The profile of the centreline cut-through of the tyre was obtained, measuring the lower inboard and outboard contact patches, the upper inboard and outboard shoulders and in addition to this, the inboard and outboard rear middle at axle height (horizontal slice). It was assumed for the CAD that the rear and front horizontal sections would be identical and therefore the rear measurements were duplicated for the front slice to create a loft pattern. More information on the CAD model used for CFD is available in Chapter 4.

Chapter 3

Results and Discussion - Wind Tunnel

The purpose of this chapter is to present the experimental results obtained using the wind tunnel methodologies outlined in Chapter 2. The individual details, motivation for the experiments and a detailed breakdown of the figures are all presented here. For a more global discussion of the results the reader is directed to Chapter 6 which draws together the findings from the experimental wind tunnel and CFD results chapters in order to extract the finer details and conclusions from the data.

3.1 Rigid Tyre - Through-Hub Flow

Experimental data were taken for the rigid tyre with standard brake scoop and simplified internal geometry as described in detail in the previous chapter. The wheel was aligned at zero yaw and a built in camber angle of -3.5°. In order to assess the aerodynamic effects of varying the through-hub flow, load-cell measurements were first recorded for a spread of hub-flow numbers ranging from fully closed to fully open ducting. From this, the behaviour of the flow-field could be suggested.

The significance of this study is in relation to brake cooling flows. The level of restriction from the cooling components changes the amount of lateral mass-flow introduced into the system. The effect of this on the wake and the local components, including the brake duct, is the focus of this section.

3.1.1 Baseline Scoop

3.1.1.1 Drag Force Measurements

The drag forces were measured using the brake scoop in its standard baseline condition and they are presented in Figure 3.1. The maximum hub-flow rate corresponds to around 92% of the freestream velocity. This is determined by the velocity recorded in the open-sided scoop and as described in the first chapter, does not equate to the in-hub velocity. The hub-flow number (HFN) was corrected (HFN_c) using Equation 1.6 using a CFD correction ratio (as defined in Chapter 1) of 0.689 (the ratio between average through-hub velocity and that at the probe location from the Fluent simulations in Chapter 4). This results in a true through-hub velocity of 63% of the freestream value.

It is clear from Figure 3.1 that there are multiple functions combining to form the drag trend. This infers multiple flow features, each with differing levels of influence under varying circumstances. A traditional through-body flow would be expected to have its minimum drag condition with a fully blocked intake. This is due to the removal of high-loss ducting, cooling passages and quite often non-axial exit conditions. Instead what has been observed is a steep reduction in drag with increasing

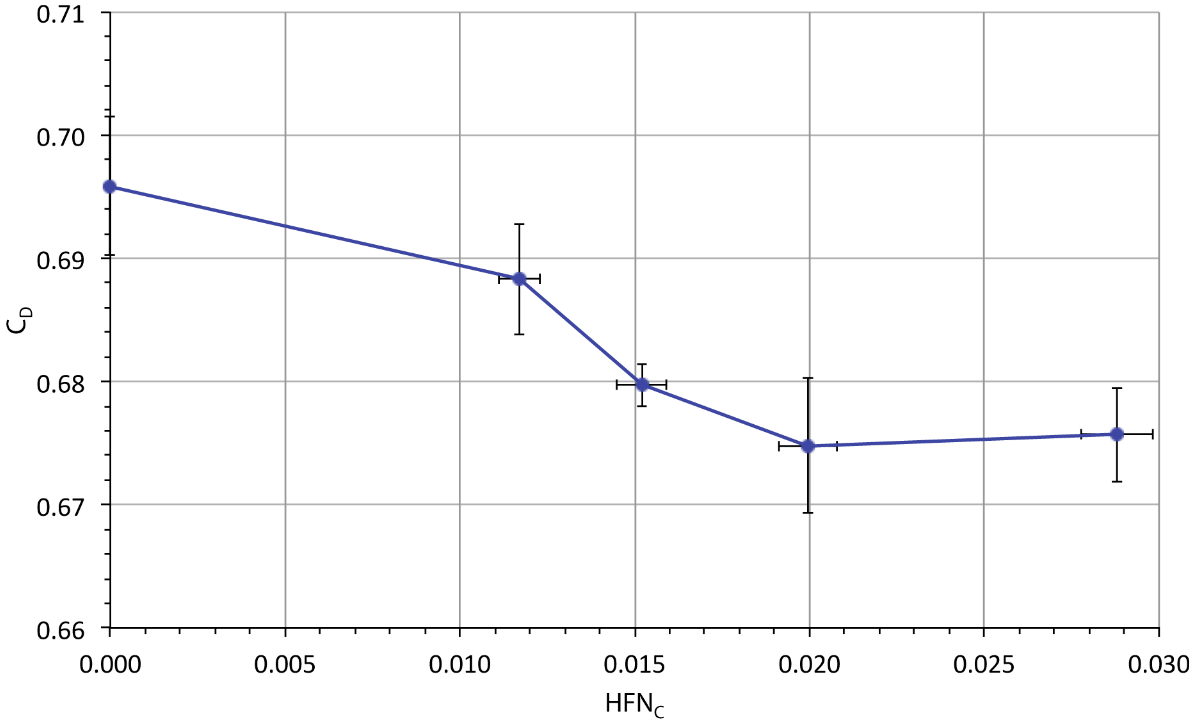

Figure 3.1: *Axial drag measurements for the baseline scoop geometry against varying through-hub flow.*

through-hub flow, levelling off towards the low restriction cases. The overall reduction in drag between the two extreme cases is 2.9%, equating to 20 counts ($C_D = 0.020$), although the relationship is clearly not linear.

3.1.1.2 Flow-Field Observations

To determine the aerodynamic effects that were occurring at the scoop, and to test the conclusions of Williams [81] and Minto [73] with regard to inlet spillage separation to see if they could be applied to this trend, longitudinal PIV measurements were obtained on the centreline of the scoop inlet. That is, a vertical plane which intersects the y-coordinate location of the pitot-static probe in the duct. The velocity streamlines are presented and summarised in Figure 3.2 for two cases, fully open, and fully closed ducting.

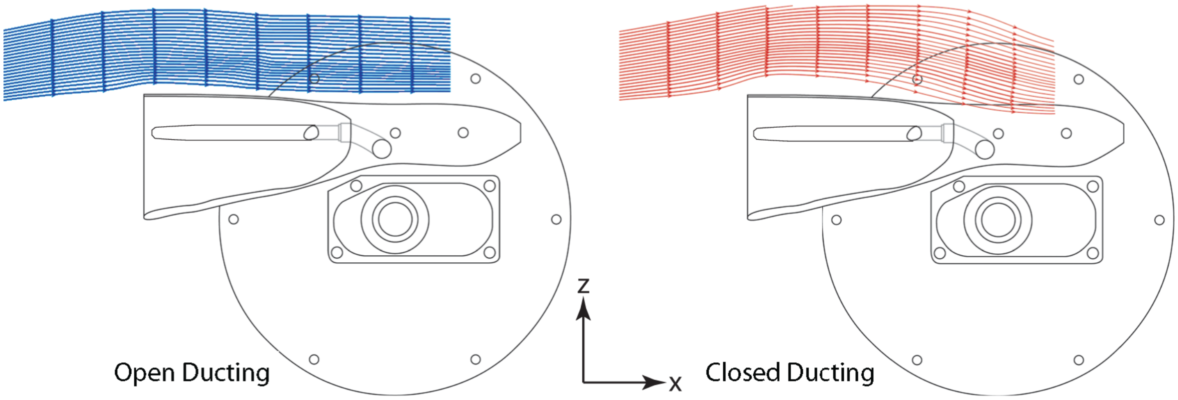

Figure 3.2: *PIV flow-field observation of the longitudinal centreline on the baseline scoop. Left: Open ducting; Right: Closed ducting.*

From this it is clear to see that there appears to be a spillage separation at the inlet of the brake scoop under both conditions but mainly under the closed condition. Specifically, this appears to be along the whole length of the open side of the duct, as opposed to simply the leading edge. It is assumed that the same is true for the lower side but due to laser shadowing from the sting, data were not obtainable from that region with PIV. Figure 3.3 shows surface flow visualisation oil on the scoop in plan-view.

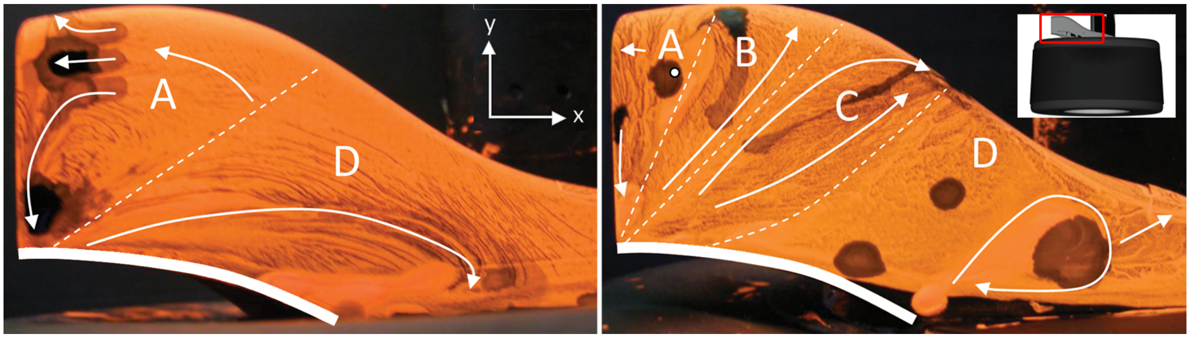

Figure 3.3: *Surface flow visualisation on the baseline scoop. Left: Open ducting; Right: Closed ducting.*

The regions highlighted on the photographs show the key features of the surface flow. The open ducting on the left (low restriction) results in a flow which, after an initial separation region (A), predominantly follows the freestream (x-axis). For the second case, with closed ducting (high-restriction), the surface flow appears to be predominantly transverse to the freestream (y-axis), introducing a crossflow across the duct (B and C). The thick white line denotes the upper open edge of the scoop and is the region which appears most affected by the spillage. The black ink dots used for visualising velocity contrast show the considerable differences between the flow features on this surface and allows inference of feature dominance. The recirculating regions (A and D) undertake only around 10% or less of the displacement in the same given test period as the dominant crossflow regions (B and C). Given such a radical change in local flow characteristics, these results prompted further investigation using CFD presented in Chapter 5.

From a more global perspective, PIV measurements as presented in figures 3.4 - 3.8, coloured by velocity magnitude, show the effect on the overall flow-field and hence the downstream wake. The thick black lines denote the author's interpretation of the important flow features and as such the lengths do not denote a magnitude. In addition, the smaller vectors denote velocity direction only.

Because of the higher blockage on the inboard side due to closed ducting, it is observed that the wake and recirculation zones are larger. In contrast, due to the reduction in the through-hub flow which usually exits the spokes in a highly turbulent nature, perpendicular to the freestream, the reverse is the case for the outboard side. The centreline is largely unaffected by any variation of through-hub flow rate. The effect of the varied through-hub flow has therefore had a significant impact on the global flow-field of this geometry.

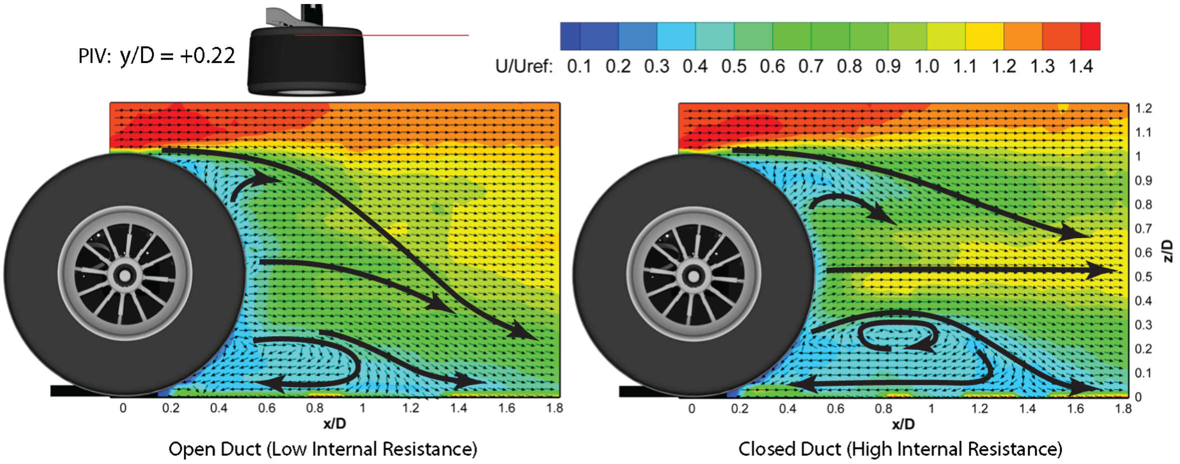

Figure 3.4: *Through-hub flow longitudinal PIV measurements: y/D=+0.22 plane (inboard sidewall).*

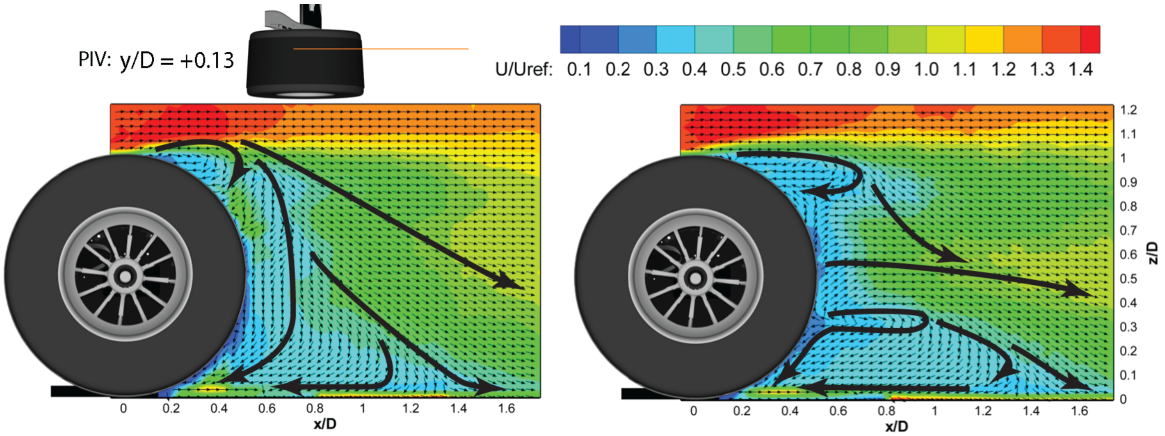

Open Duct (Low Internal Resistance)

Closed Duct (High Internal Resistance)

Figure 3.5: *Through-hub flow longitudinal PIV measurements: y/D=+0.13 plane (inboard tread).*

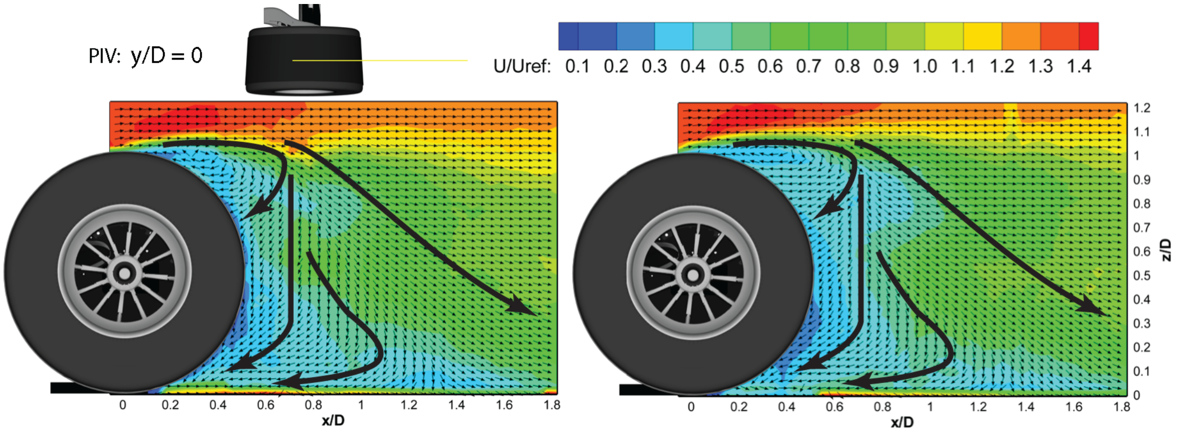

Open Duct (Low Internal Resistance)

Closed Duct (High Internal Resistance)

Figure 3.6: *Through-hub flow longitudinal PIV measurements: y/D=0.00 plane (centreline).*

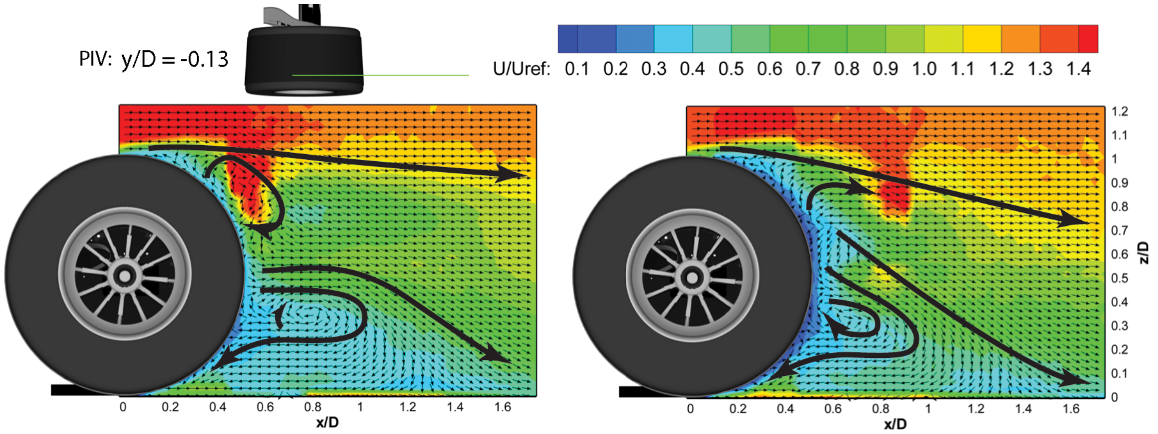

Open Duct (Low Internal Resistance)

Closed Duct (High Internal Resistance)

Figure 3.7: *Through-hub flow longitudinal PIV measurements: y/D=-0.13 plane (outboard tread).*

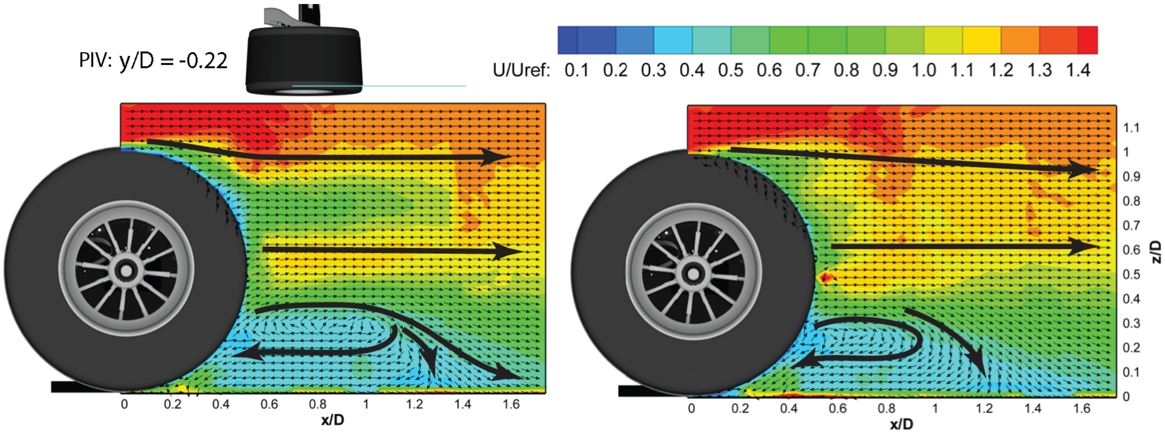

Open Duct (Low Internal Resistance)

Closed Duct (High Internal Resistance)

Figure 3.8: *Through-hub flow longitudinal PIV measurements: y/D=-0.22 plane (outboard sidewall).*

Starting from the inboard side, it is evident that not only is the wake of lower velocity in the low through-hub flow case, but the upper flow features observe a much more longitudinal nature than the unrestricted higher through-hub flow case. The downwash is less prominent, which does not necessarily suggest reduced trailing vortex strength, merely that the features may have moved and that the flow-field has greater asymmetry than for the high through-hub flow case. The lower wake recirculation lobes are far more complex in the case of the closed ducting and the wake from the scoop is clearly visible. This wake is investigated in more depth in Chapter 5 where it is postulated that the change in local flow vectors around the scoop in fact change the effective attack angle of the otherwise neutral sting. This causes a much larger separation visible in the wake structure of Figure 3.4.

It is worth noting at this point that the flow-field maps on the outboard side have in places been affected by vertical artefacts of the image-field processing stage, due to insufficient overlap of the interrogation planes closer to the lens. These, although not ideal, are obvious and therefore do not have an impact on any of the conclusions drawn.

The aerodynamic changes are progressive leading towards the opposite trend on the outboard side. From Figure 3.8, the horizontal exit flow from the spokes is clearly visible for the open duct case and less identifiable for the closed duct case. The general flow-field of the wake is of much higher velocity and due to the reduced outflow rate, downstream mixing has a larger effect. The visible jet at the same height and location as the scoop suggests there is also very little effect from the spokes and that the flow without any detailed internal geometries ejects directly in-line with the z-coordinate of the scoop, in the vertical direction. This distribution is a concern, as real internal flow geometries with a vented brake rotor have the entirety of the through-hub flow redistributed according to the design of the brake components used such as those in Figure 1.27. This inspired the internal geometry CFD investigation in Chapter 5.

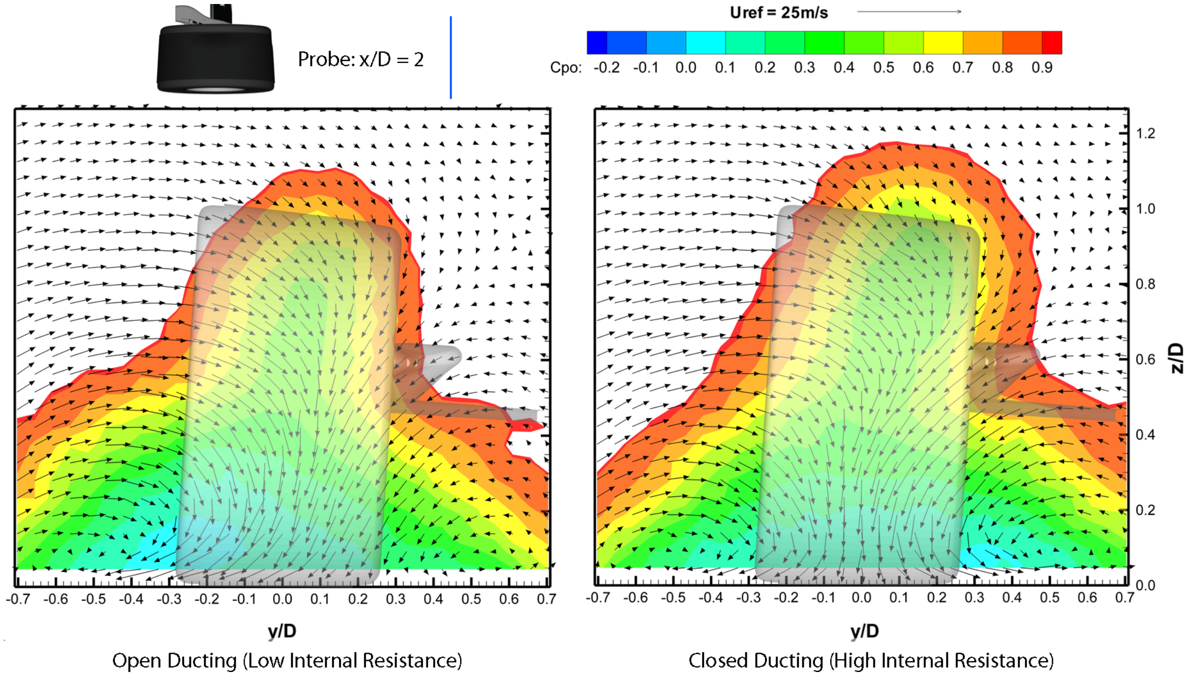

Figure 3.9: *Pneumatic pressure probe (5-Hole) crossplanes (y-z) at x/D = 2.0. Maximum against minimum through-hub flow condition.*

The five-hole pressure probe data for two wheel diameters downstream of the axle (2D) can be seen in Figure 3.9. The size of the wake (colour contours turn white above $Cp_0 = 0.9$) and the trend of the base-pressure magnitude is consistent to explain the drag force measurements in that for the closed ducting case, the low-velocity wake appears much larger and as suggested by the former PIV flow-fields, the inboard vortex structure is largely affected. The in-plane velocity vectors showing reduced downwash, are in fact deceptive, as confirmed by the out-of-plane velocities (aligned with y-axis) captured in the pneumatic probe data. The wake behind the scoop is also consistent with the increased blockage. Looking toward the outboard side, the open ducted case has a much larger wake outline although this far downstream there is no evidence of any transverse jetting deflecting the freestream which was suggested by the PIV.

3.1.2 Modified Scoop Geometries

In order to further understand the flow phenomena taking place at the inlet, several adaptations to the scoop geometry were made. It is necessary to emphasise that these were primarily not intended as an iteration to design for higher performance, but instead to emphasise or soften the flow features implied by the above results in order to confirm or deny inlet spillage hypotheses. Figure 3.10 shows the four scoop designs tested, including the original unmodified baseline scoop.

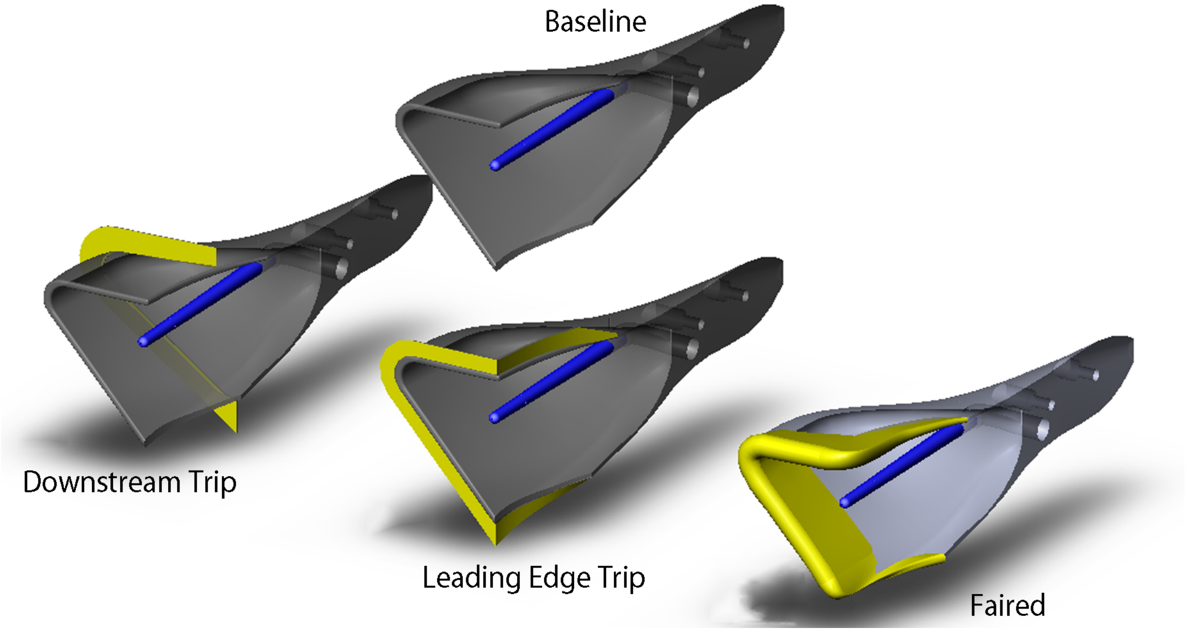

Figure 3.10: *Modified scoop geometries designed for further understanding by emphasis or curtailing of inferred flow features from initial results. 1) Baseline unmodified scoop; 2) Downstream trip (streamwise); 3) Leading edge trip; 4) Leading edge fairing.*

The concept of inlet spillage drag is emerging as being responsible for the negative cooling drag trend, due to the varying dominance of the inboard wake. As such, if a spillage separation could be induced along the whole through-hub flow range, not just for the highly restricted cases, then the drag trend should level out if not resume the positive (increasing with HFN_c) trend altogether. Therefore, the first two modifications were designed to deliberately induce a large separation (not to simply cause a boundary layer transition as 'trip strips' are conventionally used for). The third modification, with a faired leading edge, was also designed to level off the drag trend but instead by reducing the magnitude of the spillage separation at the higher blockages.

3.1.2.1 Drag Force Measurements

Aside from the fully logical drag offsets due to the increased projected frontal area of the additions in Figure 3.10, the above alterations have each led to a movement on the right hand side of the graph (Figure 3.11). This restores the expected increasing drag with hub flow rate trend. At the higher restrictions, or lower hub-flow numbers, the negative cooling drag trend is still present, although not as severe. This suggests that the strength of the spillage-induced drag is dominating at low hub-flow numbers. By this, the absolute value of the aerodynamic drag induced by the spillage effect is greater than the ram-drag delta as a result of changes in the inlet capture streamtube momentum. Isolating the overall trends by observing the two extremes, it is possible to confirm that the scoop modifications behaved as expected. The drag deltas between the maximum and minimum through-hub flow rates are shown in Figure 3.12.

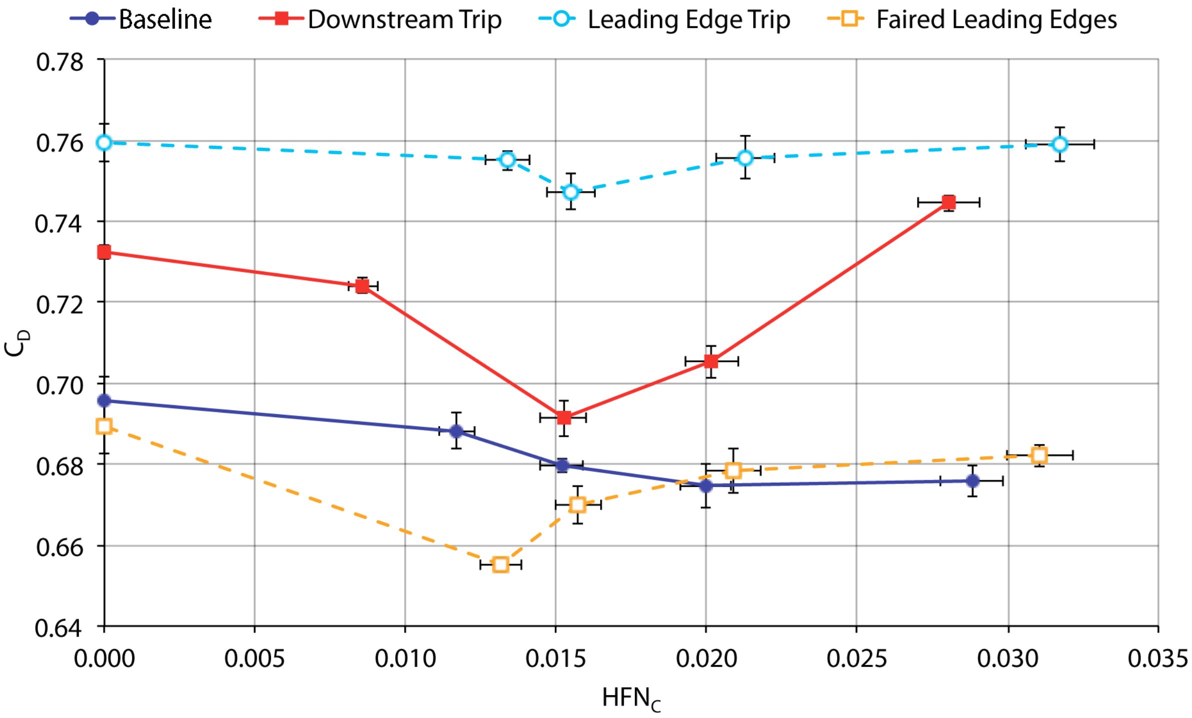

Figure 3.11: *Axial drag force measurements for the modified scoop geometries against* HFN_c.

The predicted spillage drag contribution across the range based on the predicted ram-drag,

$$D_{ram} = (1/2)\,\rho A_{ref} u^2 \tag{3.1}$$

and hence the thrust-recovery coefficients from Williams' equation (Equation 1.7) [81] are displayed in Table 3.1 and represented in Figure 3.13.

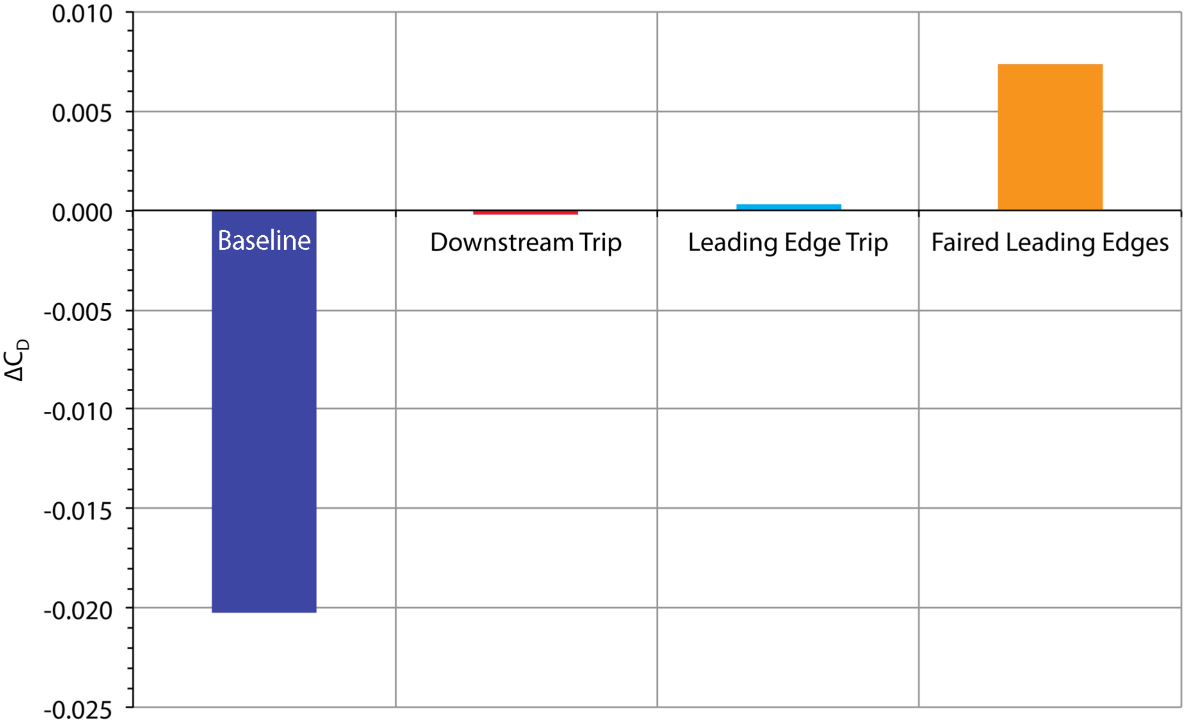

Figure 3.12: *Axial drag force deltas (maximum vs. minimum HFN_c) against associated scoop geometry.*

Table 3.1: *Inlet thrust-recovery coefficients and associated spillage drag (c.f. Williams [81]).*

Scoop Modification	Initial C_D	Ram Predicted Δ C_D	Actual Δ C_D	$c_{t,inlet}$	$C_{D,spill}$
Baseline	0.676	+0.0088	-0.0202	-0.186	0.047
Downstream Trip	0.745	+0.0079	-0.0002	0.340	0.029
Leading Edge Trips	0.759	+0.0066	+0.0003	-0.219	0.059
Smoothed Edges	0.682	+0.0079	+0.0073	0.104	0.039

From these thrust-recovery coefficients, the data presented in Figure 3.13 were produced. This is an application of Williams' model to predict the behaviour of the spillage drag over the whole range of hub-flow numbers. Due to a non 100% U_{ref} through-hub flow under any case, it is suggested that the spillage-induced drag does not completely disappear at the highest tested hub-flow numbers.

The leading edge trip scoop comprised a deep trip around the open inboard edge of the scoop, denoted by the thick white line in Figure 3.3 and was therefore expected to produce the largest spillage effect. This is the case, with the next most significant spillage case being the baseline scoop, with its sharp edges. The faired case has a smaller contribution although perhaps not as small as would be expected.

Although the downstream trip case would be expected to have higher absolute drag than the faired case, which is confirmed by Figure 3.11, the extracted spillage contribution has been much smaller. This can be explained by the location of the trip and its orientation to the scoop. Considering again the features observed in the surface flow visualisation investigation, the trip is likely to emphasise the crossflow over the whole range of conditions, not just for the highly restricted cases. As a result, the contribution responsible for producing a negative drag trend is minimal.

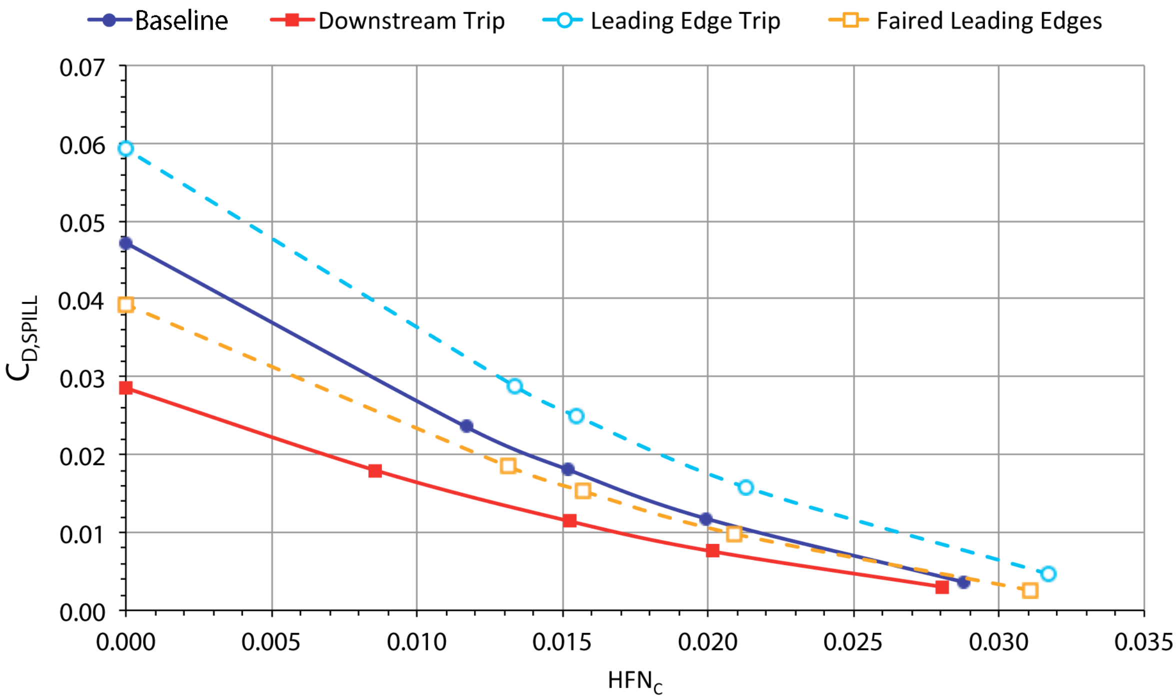

Figure 3.13: *Spillage drag strengths and contribution distribution across HFN_c range.*

The result of applying the basic ram-drag velocity-squared relationship model to the spillage prediction brought about by Williams' equation can be seen in Figure 3.14. This shows a conclusive model of the flow phenomena taking place across the hub flow range. There are several features which have varying local dominance depending upon the condition of the internal flow. These local effects are also evident in the global flow-field and have been presented already. In combining the above results and correcting for spillage drag, the drag trend has been completely reversed to the positive cooling drag trend expected by the increasing through-hub flow. These results can be seen in Figure 3.15. Overall the drag trend is positive although not with the velocity-squared relationship which would be expected by the ram-drag concept.

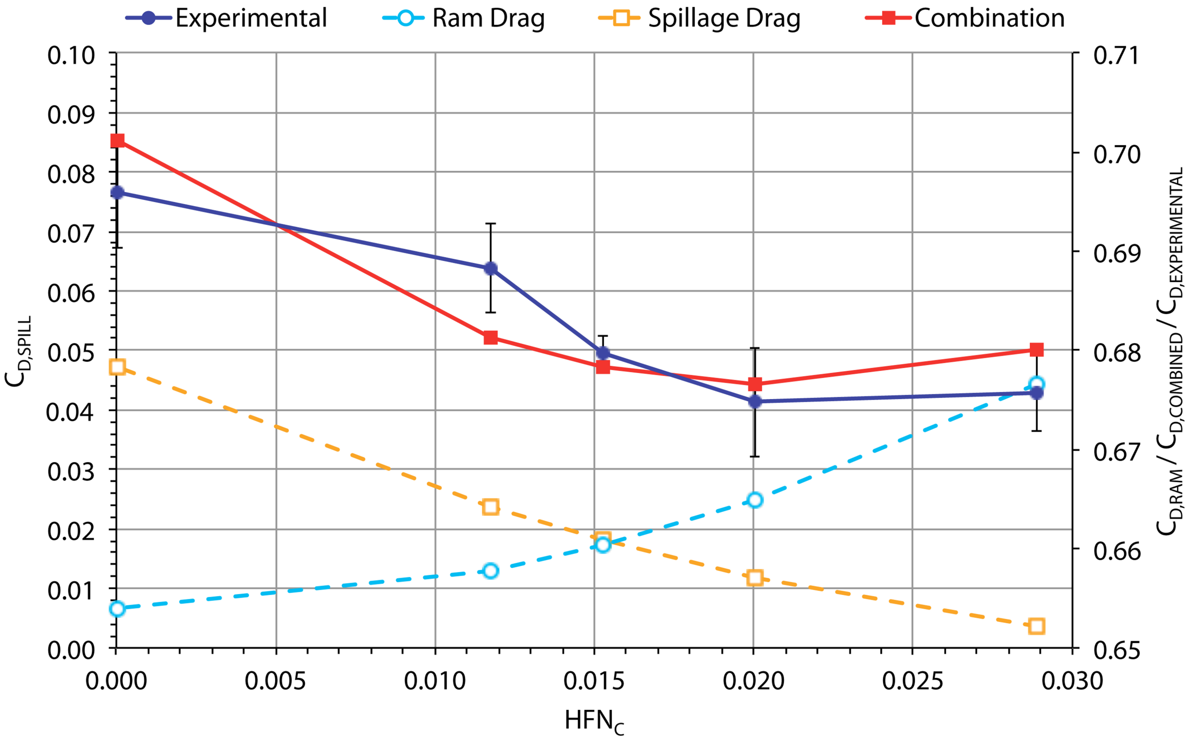

Figure 3.14: *Quantified and combined theoretical flow concepts compared to measured results.*

In addition to the subtleties of the drag force trends, it is also apparent from Figure 3.15 that the overall performance of the duct is extremely sensitive to the modifications applied, despite there being no change to the internal ducting shape or cross-sectional area. The cases which provided the highest hub-flow numbers, and indeed far superior to the baseline case, were those which induced leading edge acceleration either through a smoothed fairing or by a separation trip, providing increased frontal blockage encouraging accelerated flow within the scoop.

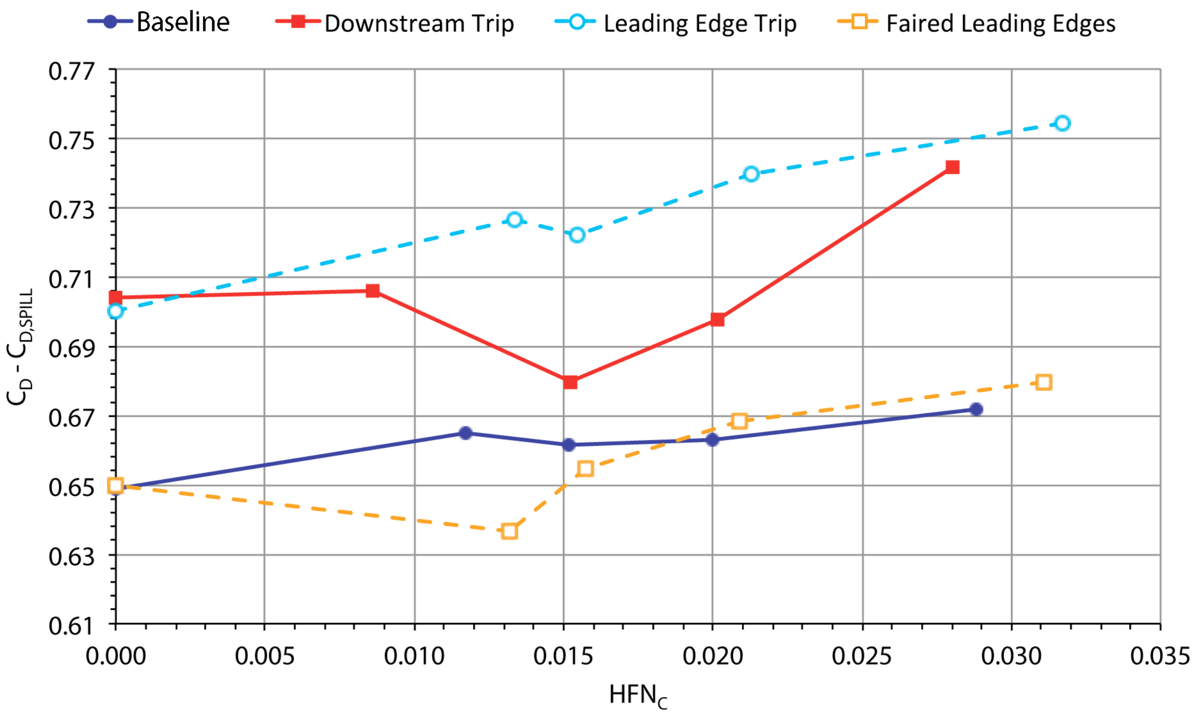

Figure 3.15: *Axial drag force measurements (spillage drag corrected) for the modified scoop geometries against* HFN_c.

3.2 Deformable Tyre - Geometrical Measurements

The following experiments were conducted using the deformable wind tunnel tyre to characterise its performance both geometrically and aerodynamically.

3.2.1 Contact Patch Measurements

Table 3.2 contains the measurements for the near elliptical contact patch and Figure 3.16 presents the calculated area based upon these data. Although the area trend is linear, the changes in length and width are not. Indeed the ‘major’ and ‘minor’ axis labels are seen to be deformation level dependent. The rate of change of area with axle height is also different depending upon the inflation pressure.

The contact patch area increases with vertical load, which is inversely proportional to the axle height. This is not a surprising result although the behaviour of the shape of the contact patch is perhaps less predictable. Initially, at a high axle height, the width of the contact patch is far greater than the length. Upon the decrease of axle height, the length is initially more responsive with the width eventually increasing. This measurement obviously has a physical limitation. However, the representative axle heights used here with a cambered wheel and tyre show that this limit is not reached under normal operating circumstances.

Table 3.2: *Measured length and width of the elliptical contact patches under varying loads (axle heights).*

Inflation Pressure (kPa, psi)	Axle Height (mm)	Length (mm)	Width (mm)
3.4, 0.5	150	121	111
	154	106	107
	156	98	104
	159	78	105
20.7, 3.0	150	103	100
	152	100	91
	155	94	88
	158	84	88

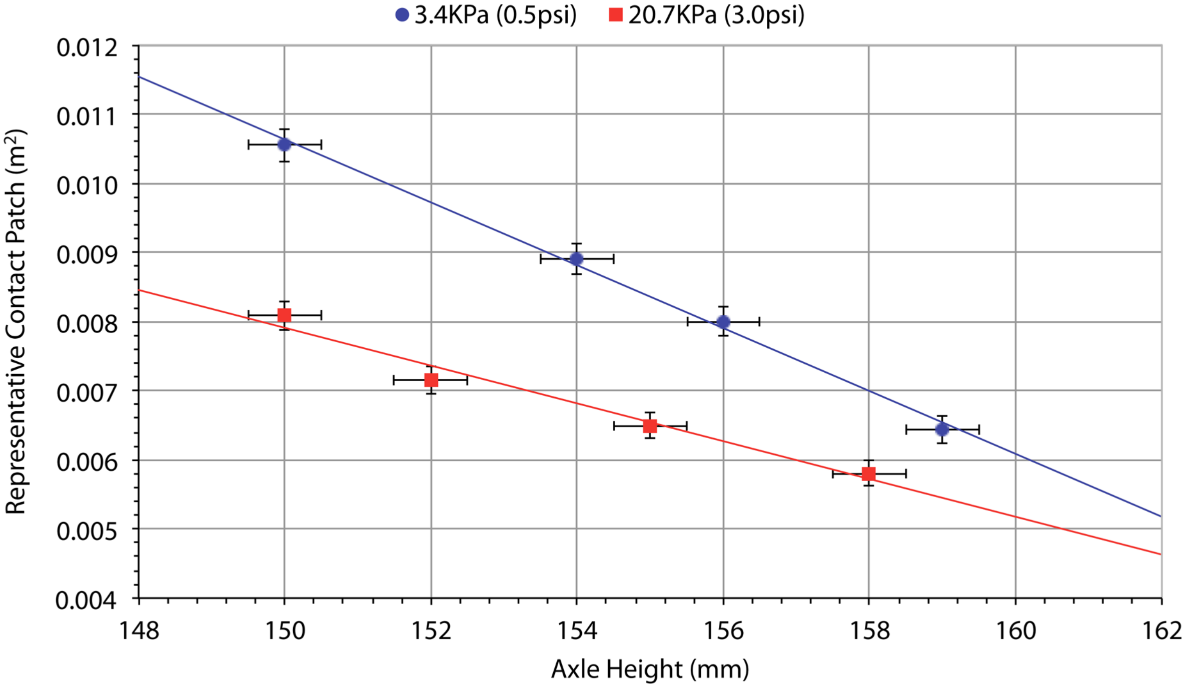

Figure 3.16: *Representative contact patch size (elliptical area from major and minor axis measurements in Table 3.2) against axle height for the extreme inflation pressures.*

At low axle heights the opposite is true, once a threshold vertical load has been applied, the contact patch width begins to change rapidly and the length becomes less sensitive. It is important to note that there was a camber angle range of around -(3.2 - 3.4)° which dictates the behaviour of the contact patch shape. Without camber, it may be assumed that the above length and width trends may not be visible with less interaction from the stiffer sidewalls on the contact patch's formation. Despite this, the contact patch area is a function of inflation pressure and vertical loading and will therefore be expected to change linearly in the same manner.

Quantifying the contact patch size change, the 20.7kPa case (3.0psi inflation pressure) comprises a reduction of the contact patch by 30% over the range, moving from low to high axle height. For the 3.4kPa case (0.5psi), this change is exactly double at 60%. This is of course only linear in the observed region. It would be unrealistic to expect the area to continue linearly at abnormally high or low loadings. Due to the complex nature of the sidewall structure, the increasing dependence for support with the higher loadings will yield non-linear results and also a non-elliptical contact patch shape. It is, however, reassuring that the two lines converge towards a constant value (around 165mm or 0.51D) which is the maximum feasible axle height of the tyre, complete with ballooning effects due to inflation.

Although this highly realistic deformable tyre is a valuable tool for industrial use, it is not a simple task to isolate the deformable variables such as contact patch size and sidewall deformation for study in order to identify the aerodynamic consequences of the geometrical changes. The discussion in Chapter 6, however, brings together all of the observations in this section (achievable by using the two degrees of freedom provided by establishing the two control variables 'axle height' and 'inflation pressure') with the aerodynamic conclusions from both results chapters in order to produce a conceptual description of the relationship.

3.2.2 Scanned Tyre Profiles

3.2.2.1 Effects of Rotation (Geometrical)

Figure 3.17 shows that there is an apparent 2-3 mm axle rise across the whole width due to the ground reaction to centrifugal rotational forces compared to a stationary wheel. The upper tread and lower outboard sidewall are the most significantly changed areas. The rotating case also exhibits slightly higher curvature to the upper tread which is flatter for the stationary case. This is consistent with the rotational forces argument. The contact patch is approximately 10mm wider (3% of the tyre diameter) for the static case than the rotating case which is far in excess of the axle height change due to rotation, leading to emphasise the importance of ensuring correct runtime axle height.

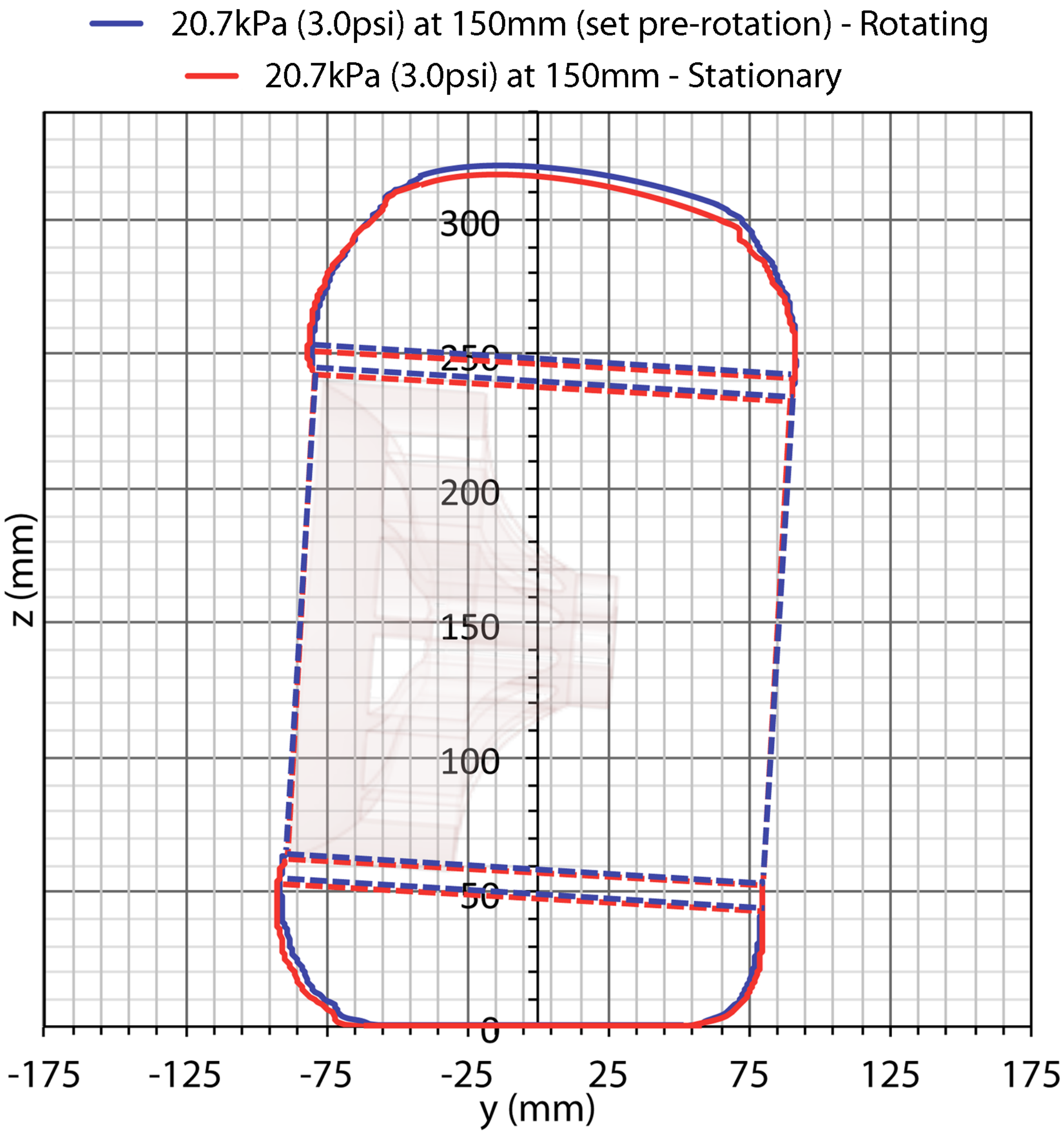

Figure 3.17: *Stationary vs. rotating tyre profile comparison at 20.7kPa (3.0psi).*

3.2.2.2 Effects of Deformation (Geometrical)

The geometrical variation between axle height extremes for a rotating tyre is presented in Figure 3.18. The difference in axle height is 9mm (0.03D) which is apparent as an offset across the majority of the profile. It is noticeable that for the higher axle height case the sidewalls are much straighter even on the upper shoulders. This implies that the structure of the tyre does not completely recover its non-deformed state at the top of its rotation.

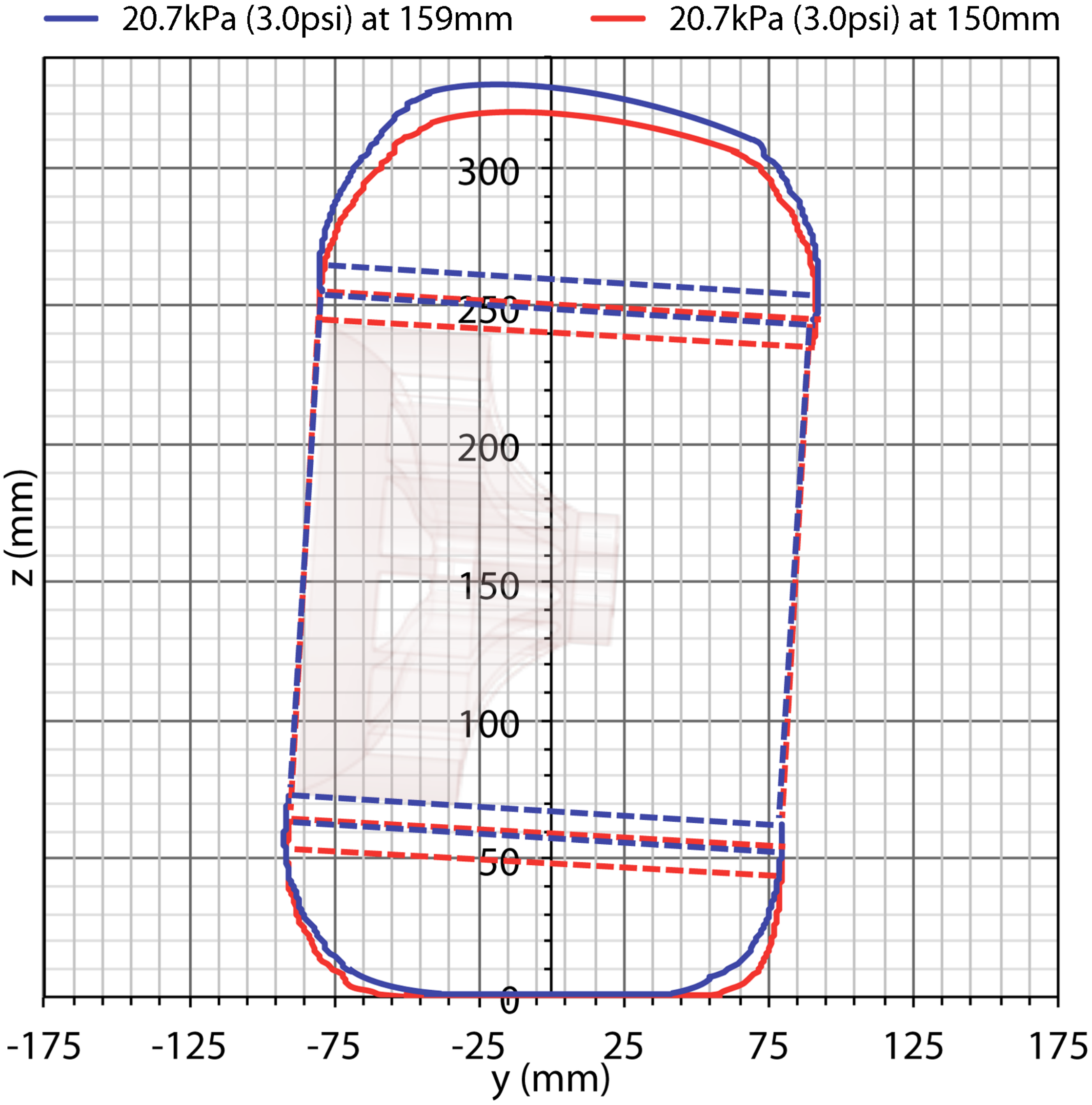

Figure 3.18: *Rotating tyre profiles comparing high and low axle heights at 20.7kPa (3.0psi).*

The upper tread observes a less continuous profile than would have been imagined. This results in a softened peak (as opposed to continuous tread curvature) which may look aggressive in some profiles. This is not necessarily the highest location on the figure, but instead the location where the gradual curvature of the upper tread suddenly tightens. For the low axle height case, this is not as visible as the conical nature (upper inboard shoulder smaller than the outboard) occurs over most of the tread reaching a soft peak around the y = -25mm line. For the high axle height, and much more evident, this occurs around the y = -15mm line. Drawing an intersecting line parallel to the camber, and indeed to the true centreline of the wheel, this projects onto the location of the outboard extreme of the contact patch. This confirms that the slightly conical shape of the upper tread is in fact due to the camber and confirms that the tyre does not recover its non-deformed state at the top of rotation.

The outboard lower sidewall is largely unchanged in character, however, the width of the contact patch has increased as a consequence of the camber. The width of the contact patch, measured using this laser scanning technique, has agreed well with the ink transfer method used to produce Table 3.2. There is a large area of reduced blockage in this lower outboard region which allows air to flow underneath. It is proposed that this accelerated air is responsible for the stronger outboard vortices observed in the flow-field investigations and therefore a larger wake and larger drag forces.

In addition to a much more severe step between the sidewall and tread (-50mm, 310mm) there is a maximum displacement of around 12mm at model-scale (nearly 4% of the wheel diameter) in the y-direction, whilst other profiles show a predictable change solely in the z-direction. This is due to the extreme ‘ballooning’ that occurs on this section of the tread when experiencing high load.

3.2.2.3 Surface Temperatures and Tyre Longevity

Due to such significant deformations and a high rotation speed the tyre surface was observed to heat up quickly. At low axle heights and high inflation pressures, the peak on the inboard tread was around 80°C compared to around 60°C on the outboard. For this test, increased roughness to the inboard tread surface began to be evident suggesting the longevity of the tyre was being affected. At the higher axle height the temperature was much more consistent and closer to the 60°C across the tread width.

This was observed for lower inflation pressures at both axle heights with temperatures not exceeding 60°C. It is therefore clear why compromises in inflation pressure and deformation level would be made in order to improve the longevity of the equipment.

3.2.2.4 Inboard Sidewall Profiles

Due to the camber of the deformable tyre, the inboard lower sidewall is arguably the most loaded section of the profile and therefore most susceptible to change. Figure 3.19 shows this under varying conditions. It is evident that the 20.7kPa (3.0psi) case is always more progressive (in terms of curvature continuity) and in general higher than the 3.4kPa (0.5psi) inflation pressure. However, the step from the sidewall to the tread is more pronounced on the higher axle heights and this could be conducive to more powerful vortices. Convincingly, the high drag cases that will be discussed in the following sections match the profiles with sharp edged geometry very close to the ground. This suggests an interaction between the shear-layers of inward flow with the ground. A sharper turn results in larger pressure gradients whereas a more progressive profile suggests the opposite. The narrower contact patch also allows for more local acceleration emphasising this.

3.2.2.5 Effect of Yaw (Geometrical)

Figure 3.20 shows photographic representation of a yawed profile which is quantified in Figure 3.21. When steering to negative yaw, neither the sidewall profile nor the size of the contact patch are largely affected. The opposite is true for the positive yaw. This is again a consequence of the camber of the tyre. The effect on the contact patch size depending on whether the tyre is yawed with or against the camber has already been covered in Chapter 1. The extent of this change, however, is extremely significant when at positive yaw (outside loaded wheel when cornering), with a contact patch width of 16mm (model-scale) wider than when the tyre is steering the opposite way (unloaded inside wheel). This results in an increase in contact patch width from the straight-ahead case of 31.6% in the positive yaw instance and 16.6% in the negative yaw instance.

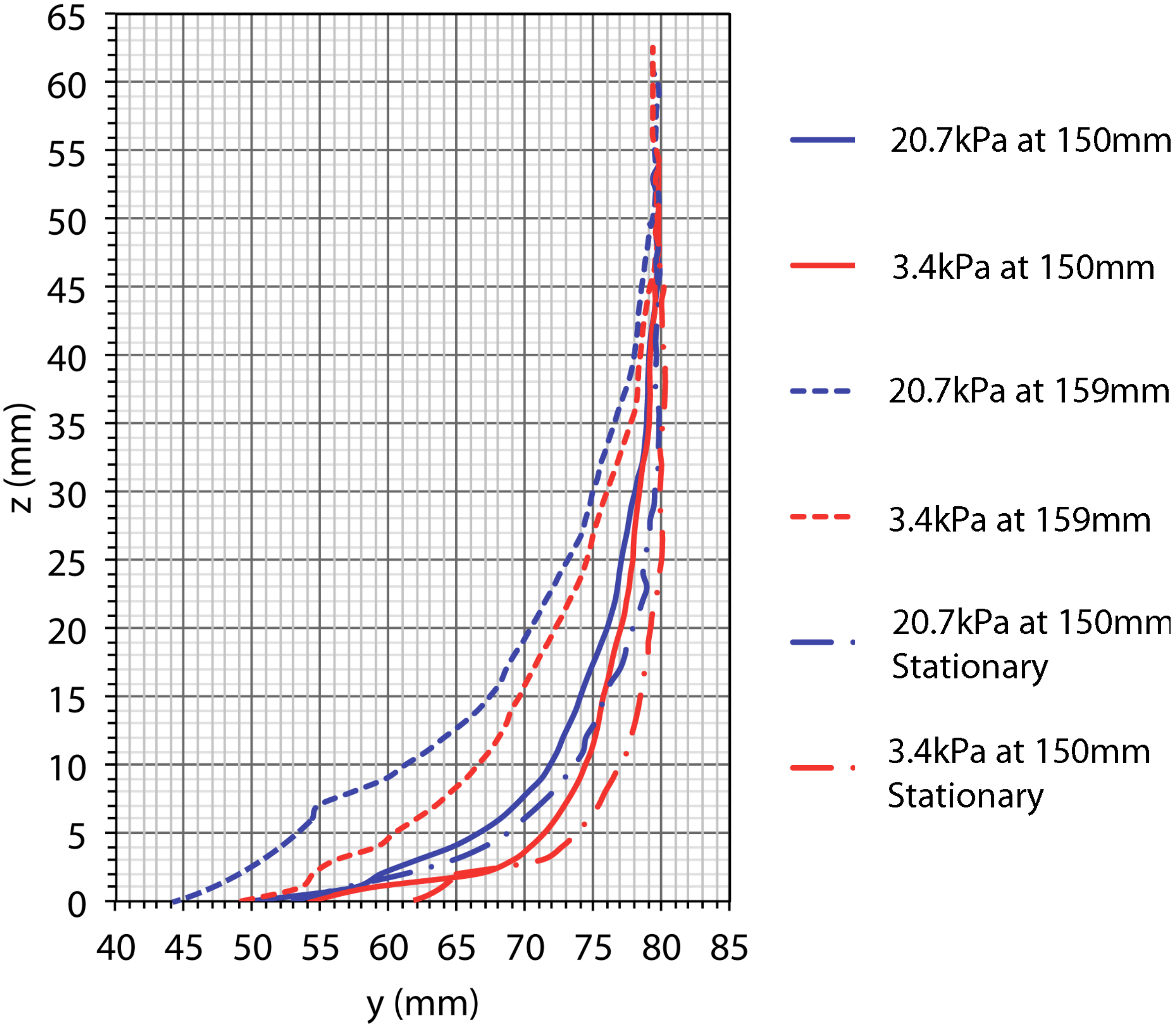

Figure 3.19: *Inboard lower profile measurements for high and low axle heights (under rotation), and low axle height (stationary) at two inflation pressures, 20.7kPa (3.0psi) and 3.4kPa (0.5psi).*

The same observations have been observed with the higher axle height in Figure 3.22 with the only differences being those already noted at 0° yaw. Figure 3.23 shows the direct comparison between the yawed profiles at the two axle heights. It is apparent again that the outboard sidewall does not differ significantly in character, only in terms of where it originates and terminates with the rim and ground respectively. For the inboard profiles there is a much larger difference. For example, the tyre at negative yaw with minimal loading is displaced laterally at the extreme by 28mm (model-scale) when compared to the positive yaw, high loading case. This is obviously one specific example, but the difference between the sharp edged profile of the high loading case to the progressive and smooth

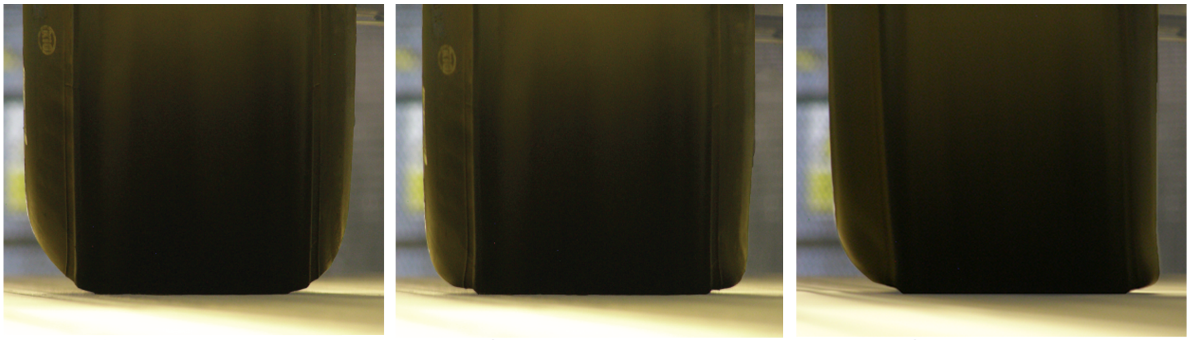

0° Yaw at 159mm

0° Yaw at 150mm

+5° Yaw at 150mm

Figure 3.20: *Photographic record of the deformable tyre at 0° yaw for the two extreme axle heights and +5° yaw for the lower axle height showing inboard sidewall dragging (as quantified by the orange curve in Figure 3.21).*

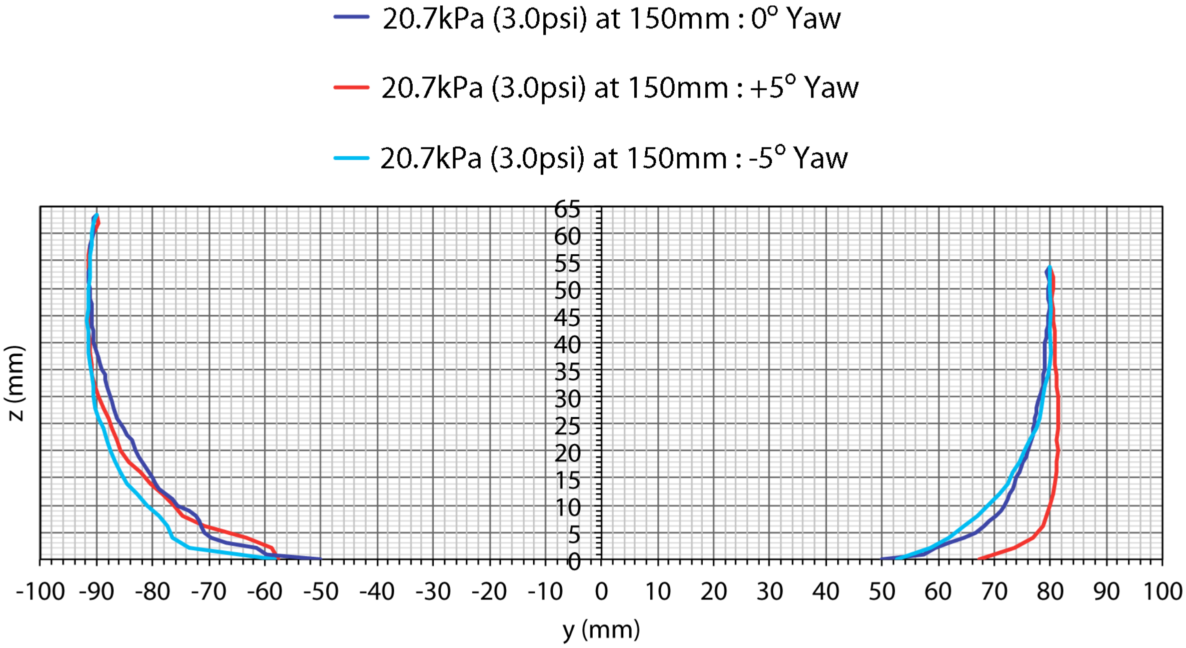

Figure 3.21: *Comparison of the lower sidewalls at 0°, ±5° yaw (150mm at 20.7kPa / 3.0psi).*

inboard profile of the slow-speed corner-exit case will lead to an upset in the delicate steady-state designed aerodynamic system of an F1 car.

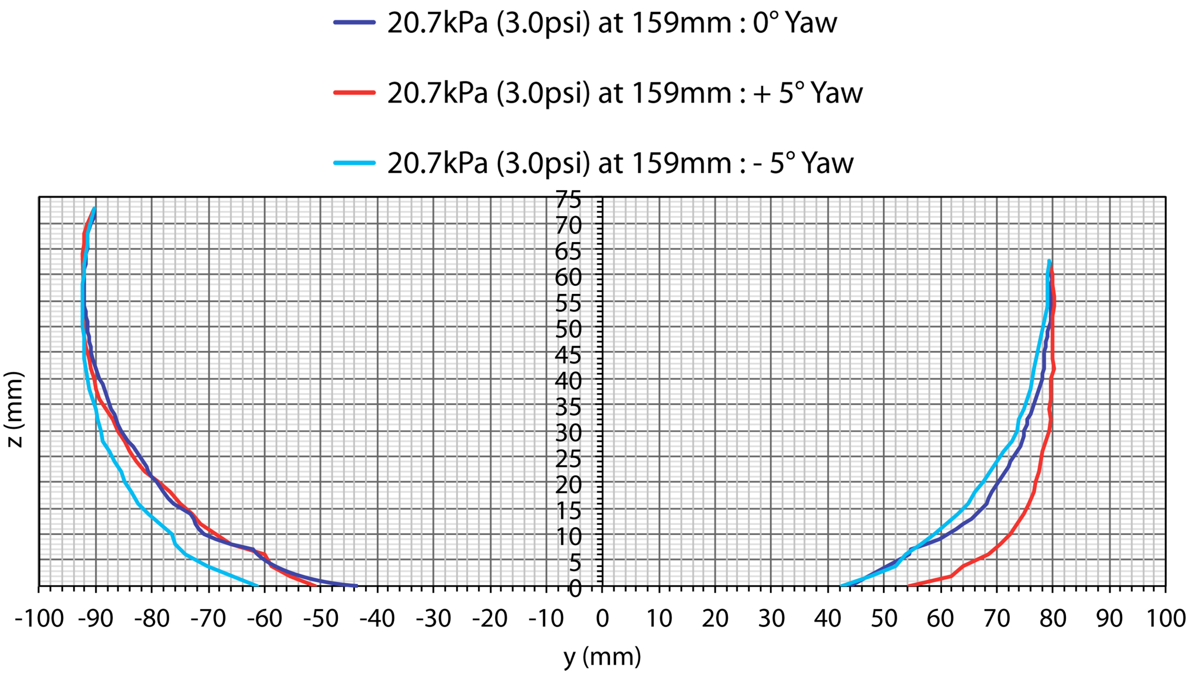

Figure 3.22: *Comparison of the lower sidewalls at 0°, ±5° yaw (159mm at 20.7kPa / 3.0psi).*

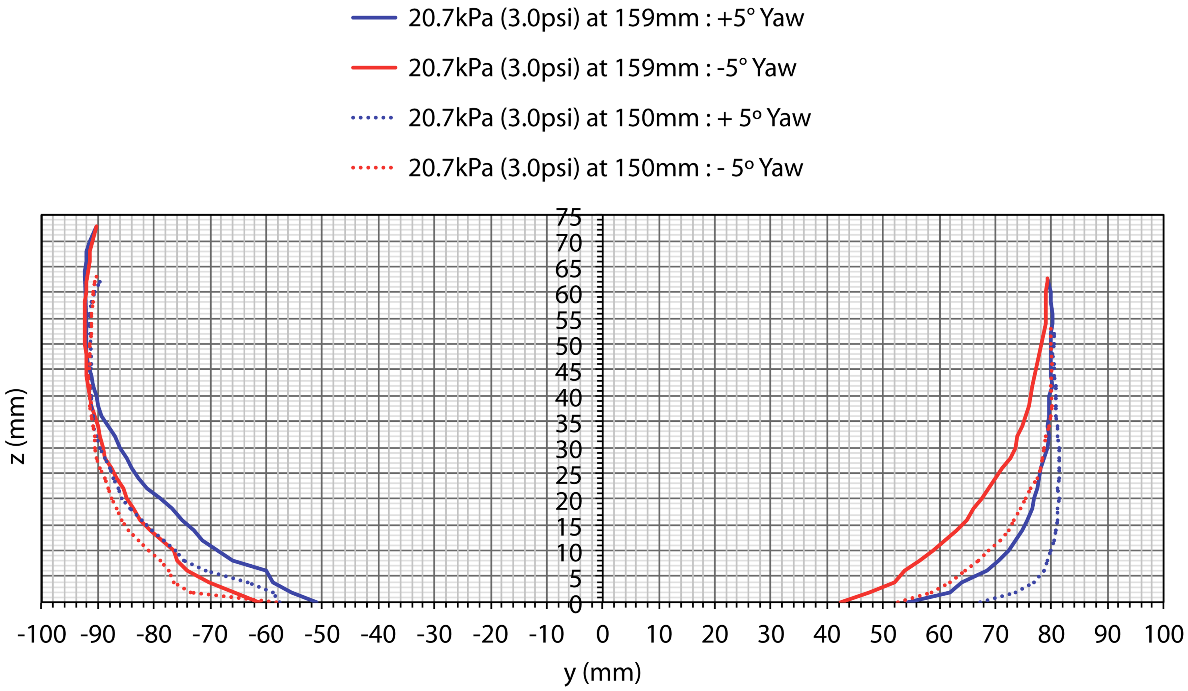

Figure 3.23: *Comparison of the lower sidewalls at ±5° yaw (150mm vs. 159mm at 20.7kPa / 3.0psi).*

3.2.2.6 Effect of Glycerol Use (Geometrical)

The use of glycerol on the rolling roads of F1 wind tunnels is employed in order to reduce required loading and friction under yawed (slip) conditions, and as a result to increase the longevity of equipment being used. As a one-off case, glycerol was applied to the rolling road as described in Chapter 2. Figures 3.24 and 3.25 suggest the profile does not adopt the correct characteristic of a yawed wheel, although more realistic than a rigid wheel with a fixed sidewall profile, the profile is clearly compromised.

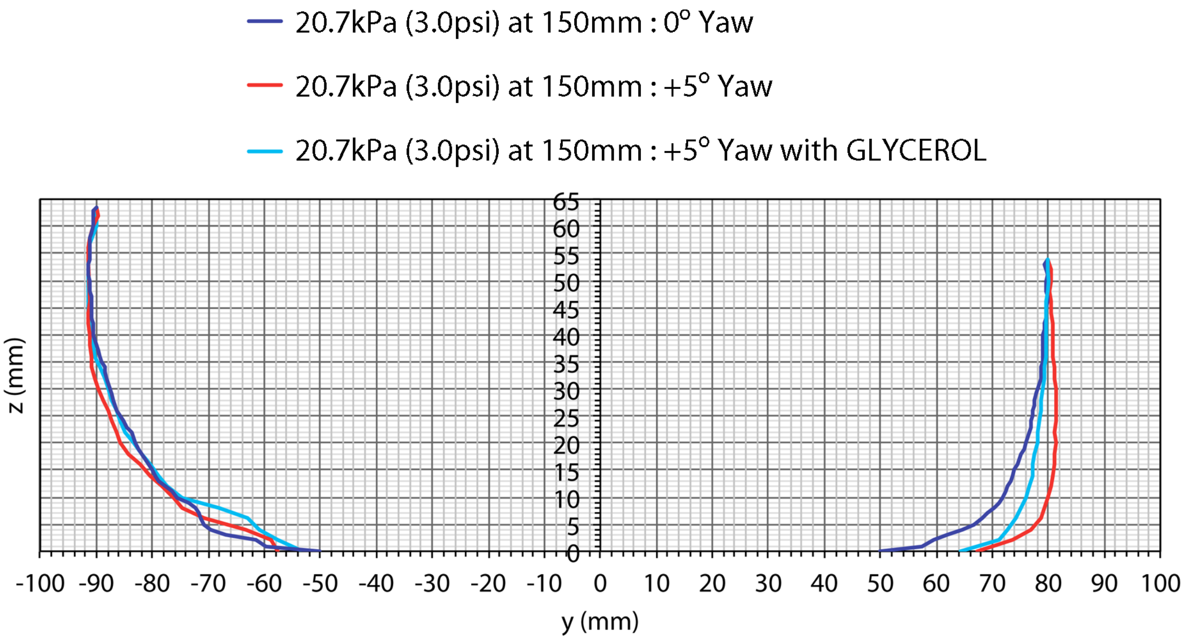

Figure 3.24: *Comparison of the 0° and +5° yaw case against the +5° case with glycerol (150mm at 20.7kPa / 3.0psi).*

There is evidence to suggest that the step from the sidewall to the tread, previously argued to be a potentially significant feature for wake development, has been smoothed out by perhaps being partially filled with excess glycerol build-up. This could result in much weaker features than either the straight-ahead case or the yawed case and may in fact produce unusual force measurements. It would also present a situation whereby test runs are more difficult to repeat, as evidence from the figures suggests the profile will wander between the straight-ahead non yaw-affected profile and the true +5° profile depending on the amount of glycerol on the belt. In the cases where the coating has been reapplied, any excess may change flow features which emanate from the front wheels and as a consequence affect the performance of the downstream components of the car. These profiles will be

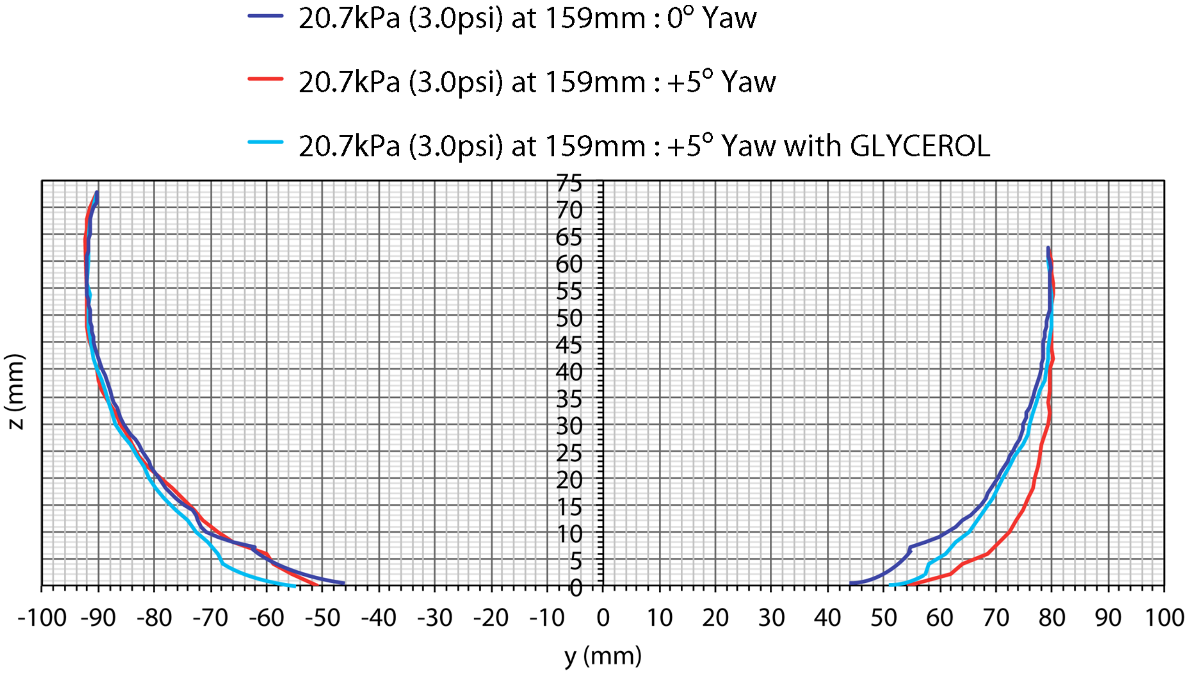

Figure 3.25: *As Figure 3.24 at the higher 159mm axle height.*

tested in CFD and presented in Chapter 5 for a more detailed breakdown and quantification of the aerodynamic consequences of the use of glycerol in a wind tunnel testing environment.

3.3 Deformable Tyre - Aerodynamic Effects of Tyre Deformation

3.3.1 Drag Force Measurements

As the tyre inflation pressure and axle height parameters were determined as being the dominating variables for size and form of both the sidewalls and contact patch, a number of experiments were performed in order to quantify the differences and to qualitatively describe the flow-field response. The aerodynamic drag force variations with axle height can be found in Figure 3.26.

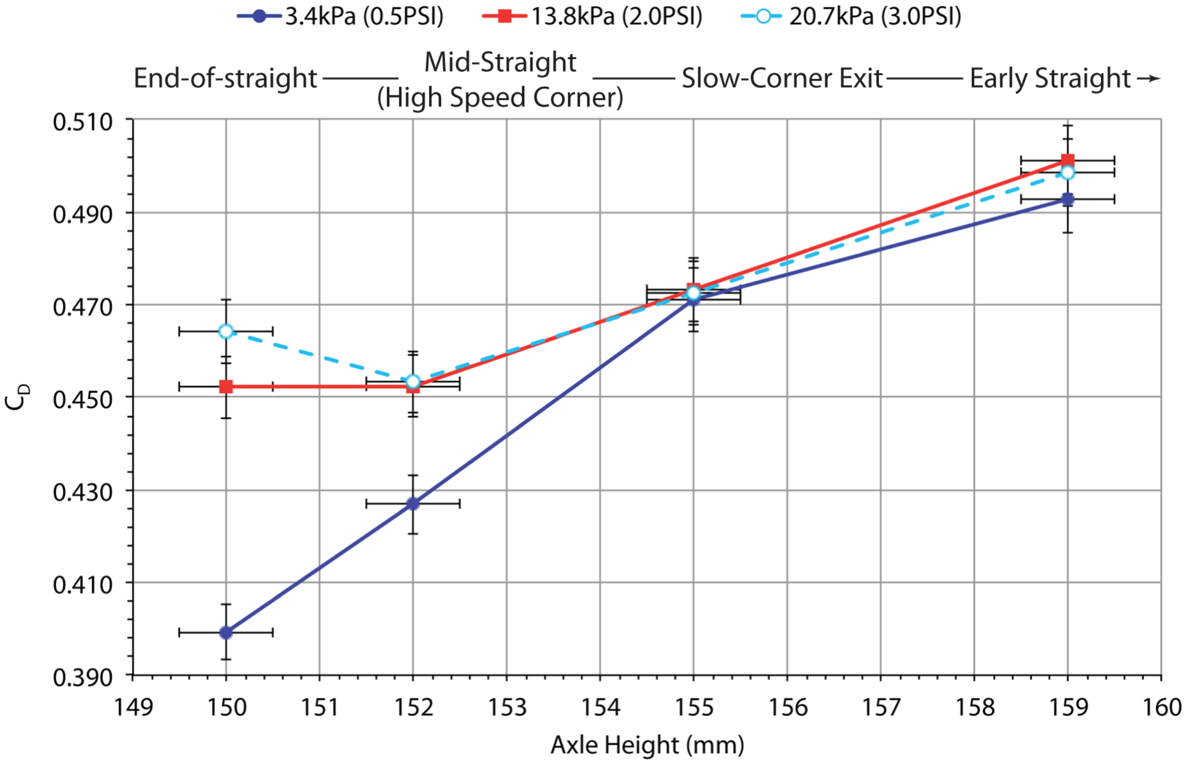

Figure 3.26: *Axial drag forces for the three tyre pressures over a range of axle heights (associated with slow-corner to end-of-straight downforce levels).*

There is a significant decrease in the aerodynamic drag of the wheel assembly upon going from the high to low axle heights (slow-corner exit to end-of-straight condition respectively). This amounts to 19% in the most extreme case (low inflation pressure). Comparing the effect of inflation pressures, the data exhibit a convergence (all cases within uncertainty) at higher axle heights. As larger loads are applied (150mm axle height), differences appear as large as 16%.

It is proposed that this high-load divergence takes place at the point where the inboard sidewall of the tyre no longer supports the load linearly and folds to a sharper profile as observed in the previous section. After this point the geometrical profile and indeed aerodynamic relationship changes significantly.

A possible explanation for part of the drag reduction with lower axle heights is the reduced frontal area of the whole assembly (although C_D was calculated with a nominal reference area throughout). Although there is some bulging of the sidewalls, there is also a radial deformation which does not change the frontal area. The projected frontal area of the 20.7kPa (3.0psi) inflation pressure changes from 0.0554m^2 to 0.0544m^2, a reduction of only 2%. Since drag is proportional to the reference area, this area change can only account for a around a fifth of the observed drag reduction. The rest of the change is therefore attributed to changes in the local flow-field and downstream wake. Further analysis of the forces and flow-field wake maps follow in order to assist the further understanding of the aerodynamic effect of the change in geometrical profiles.

3.3.2 Drag Force Frequency Spectra

The drag force measurements for the deformable tyre were taken at a frequency of 1KHz for 4 seconds. As a consequence, deeper analysis could be performed than simply presenting the final averaged load values. By performing Fourier spectrum analysis on four individual load-cell voltage measurements, a representation of the dominant frequencies apparent in the aerodynamic behaviour of the wheel assembly could be produced. The averaged spectra are shown in Figure 3.27.

Two traces have been plotted, the first is the usual test condition with moving ground plane and wind synchronised at the full test speed. The second case is the wind-off condition with the road and tyre rotation still active. It is therefore possible to determine which of the peaks are caused by mechanical or aerodynamic means. A horizontal line showing what is deemed to be statistically significant (average amplitude spectral density plus five standard deviations) has been plotted, from the wind-on case, to identify which of the peaks are worthy of observation.

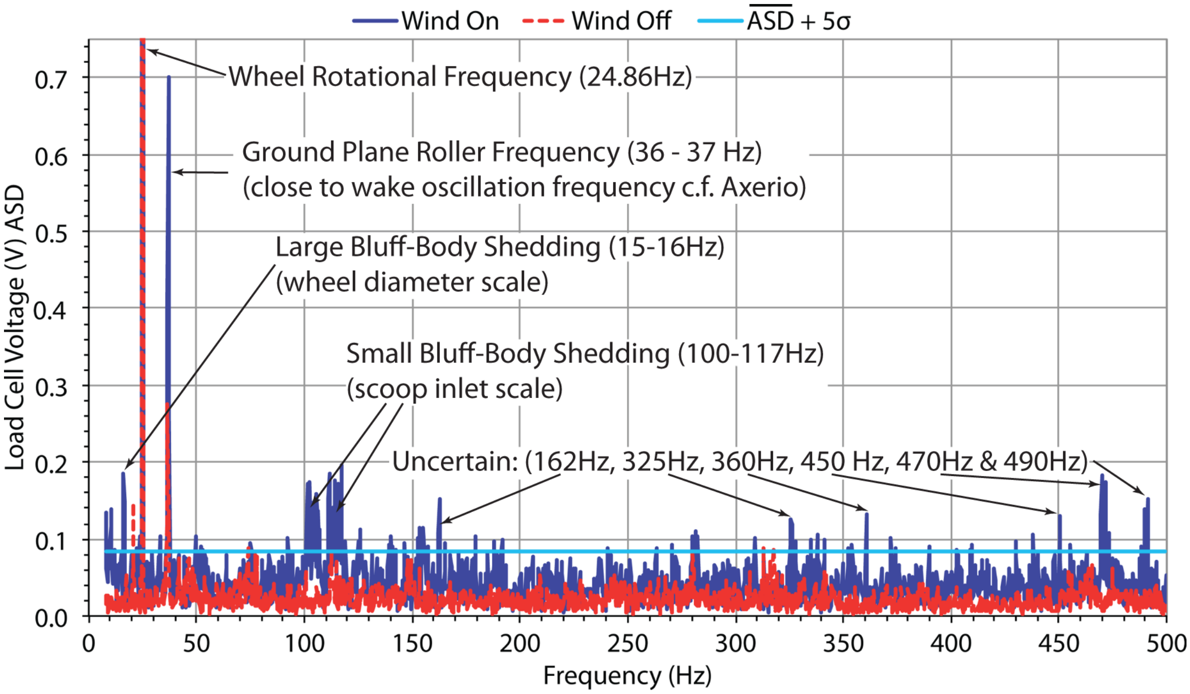

Figure 3.27: *Frequency spectra of the 20.7kPa (3.0psi) 150mm axle height deformable tyre baseline case for wind-on and wind-off.*

There are a few discrete peaks around 10Hz, 15Hz and 16Hz which are not present mechanically. The theoretical shedding frequency (determined by Equation 3.2) of a bluff cylinder of diameter 0.32m is 15.5Hz. For this calculation U_{ref} was taken to be 25ms^{-1}. The resulting frequency is consistent with all of the frequencies observed in this region and it would be expected that the shedding would be suppressed for a wheel as discussed in Chapter 1. This suppression is due to the fact that the wheel is in contact with the ground. For the cambered deformable tyre with its curved sidewalls, however, air is still capable of passing over and under the cylindrical section for the outer quarter of the wheel width. This may explain the presence of these peaks albeit at their relatively low amplitude.

$$f = \frac{U_{ref}}{l} 0.198 \left(1 - \frac{19.7}{Re}\right) \tag{3.2}$$

At 24.9Hz there is a very large and dominant spike. The average peak of this spike with the wind-off is 89.9% of the wind-on case. It can be argued that the spike is caused entirely because of the mechanical effect of a slight imbalance of the wheel as this is the same as the rotational frequency. There may be a slight wind-on amplification, as with the whole spectrum although the full-scale inflation valve on the model-scale tyre may have a small aerodynamic effect at this frequency.

The next peak is at 36-37Hz. This is the most interesting peak on the spectra as the amplitude and width of the peak is significantly different for the mechanical and aerodynamic traces. With the wind-on, the peak is 4.1 times the size of the wind-off case.

The mechanical explanation for the 36Hz frequency is known to be due to the rolling road roller frequency which is exactly 36Hz for the 25ms^{-1} peripheral speed. However, there is also a possible aerodynamic reason for a spike at this location. Axerio et al. [57] observed a wake oscillation for a deformable tyre whereby the vortex core location moved with a set frequency and was defined as having a period of twice the wheel flow-through time. Based upon the tunnel speed and diameter of the wheel used in this investigation, this equates to 39Hz. A different aspect ratio tyre was used, consistent with the tyres used in F1 of that year, which suggests that a small uncertainty as to the exact location of this peak could be expected. Indeed, their definition of the time period was also non-exact and could lead to a discrepancy by a few Hertz.

It is therefore possible that the load-cell measurements have recorded this wake oscillation, thus explaining the aerodynamic dominance for the peak around 36-37Hz. In addition to this, the peak for the wind-on case was 36.9Hz, closer to 37Hz than 36Hz. The mechanical frequency of the rollers should not have an error as great as this, further justifying the possibility of a measured aerodynamic effect. Given no unsteady flow-field observations were conducted, it is, however, impossible to confirm this within the scope of this investigation.

A broad range of peaks between 100Hz and 117Hz have been observed, which would be consistent with shedding frequencies of the order of the effective diameter of the inlet scoop. Given the highly complex nature of the scoop's profile, a range of frequencies could be expected from this bluff body.

Higher frequencies towards the high 400Hz region could be consistent with blade passing frequencies of the two fans in the wind tunnel, although the likelihood of their influence on a load-cell placed almost 10m upstream of these is not expected to be detectable. The spoke passing frequency for this experimental setup is known to be 298Hz, and there is no significant peak observed at this location, which further disproves the chance of fan blade passing frequencies being evident in the load-cell data. There are many systems, support struts and potential causes of higher frequencies, and harmonics of the lower ones which can be made responsible for the minor peaks.

3.3.3 Flow-Field Observations

For the deformable tyre, the flow features most likely to change are those from the lower sidewalls and contact patch. Specifically, this refers to the lower lobes of the wake as outlined in Figure 1.24. Therefore, crossplanes are perfectly suited to visualise this. Figure 3.28 shows the development of the wake from x/D = 0.5 to 2.0 in terms of stagnation pressure coefficient recorded with the pressure probe and compares the two extreme axle heights. Figure 3.29 shows the same range of data coloured by vorticity with added velocity vectors. The difference in the development of the wake between the two axle heights, only previously surmised by the tyre profiles, becomes apparent when observing these figures. The higher axle heights, corresponding to smaller vertical load-induced deflections, appear to have significantly larger primary vortex structures (lower lobes) which become more pronounced with increased downstream distance. This is exemplified in Figure 3.30 which shows the outline of the wake for an example crossplane extracted from the above figures. The outline is defined by $Cp_0 = 0.9$. The most significant change in the flow-field appears to occur on the outboard side as opposed to the inboard side. Air is allowed to pass underneath the outboard side of the tyre as a result of the change in height giving rise to a significantly altered wake structure. The higher axle height also exposes the ridge from the sidewall to the tread, inferring stronger vortices from the more aggressive profile. The wake size in general between the two axle heights also corresponds to the drag data presented.

The wake appears to be biased towards the inboard side, with the wake outline on the outboard side following closely the outboard edges of the rim. There is a small bulge in the wake at the scoop height on the outboard side. This is particularly visible on the top row of the figures. This suggests that the through-hub flow is exiting in a tightly concentrated stream, as shown by the PIV in the through-hub flow experiments. It would be expected that with more complicated internal geometry, this mass-flow would be ejected in a more distributed manner covering the whole spoke diameter.

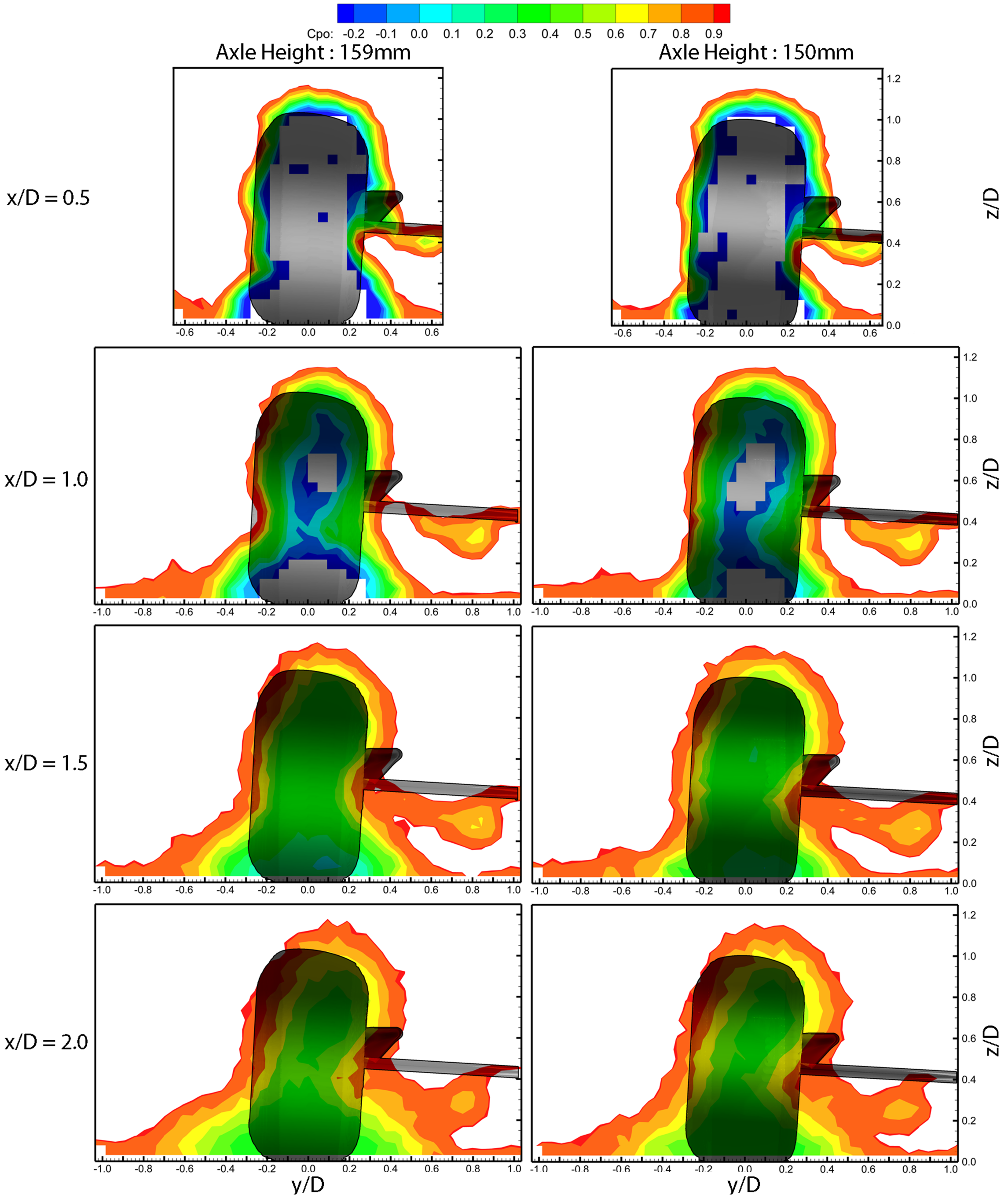

Figure 3.28: *Crossplanes (y-z), coloured by Cp_0 presenting axle height comparison of wake development.*

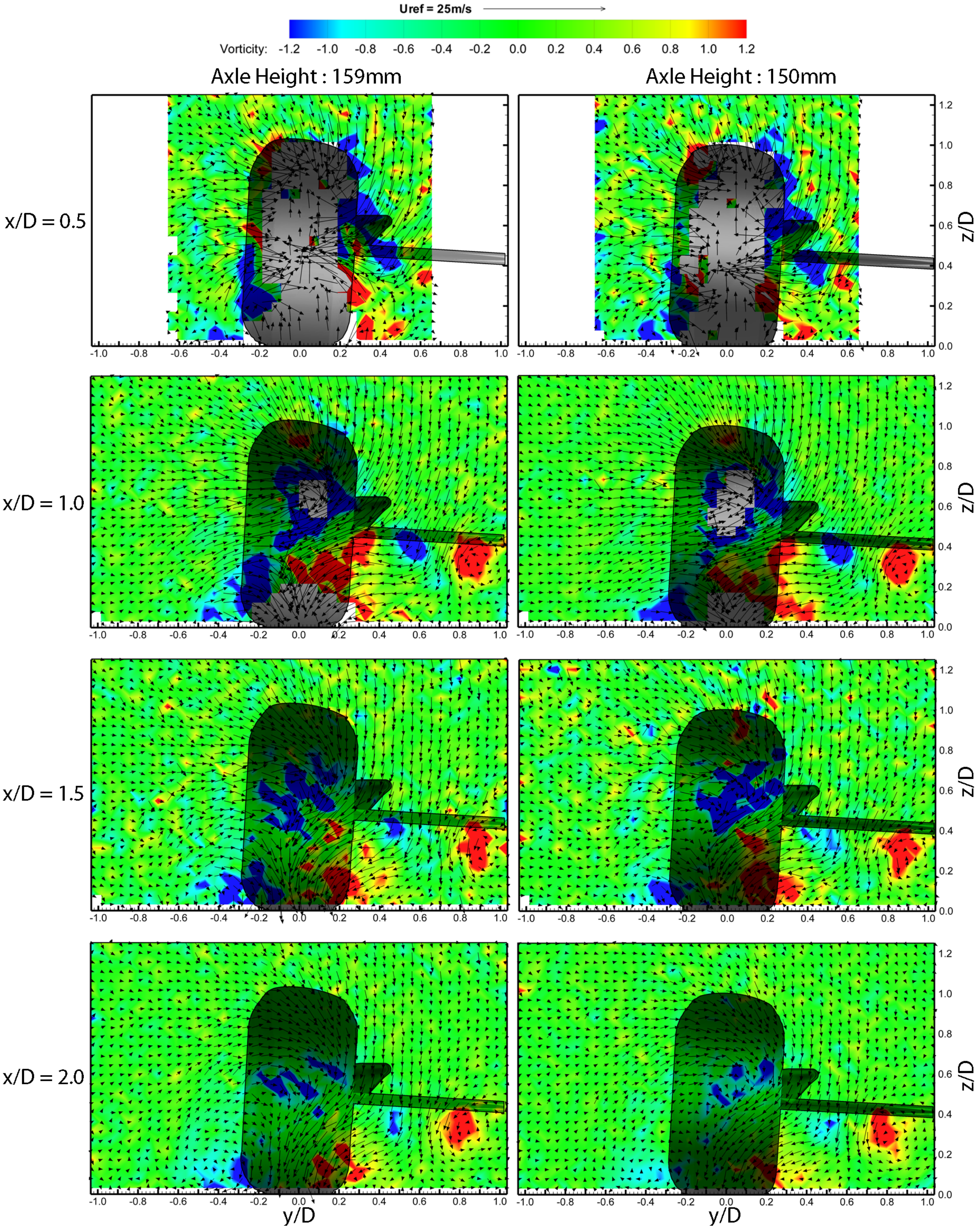

Figure 3.29: *Pressure probe crossplanes (as Figure 3.28) with velocity vectors and coloured by vorticity.*

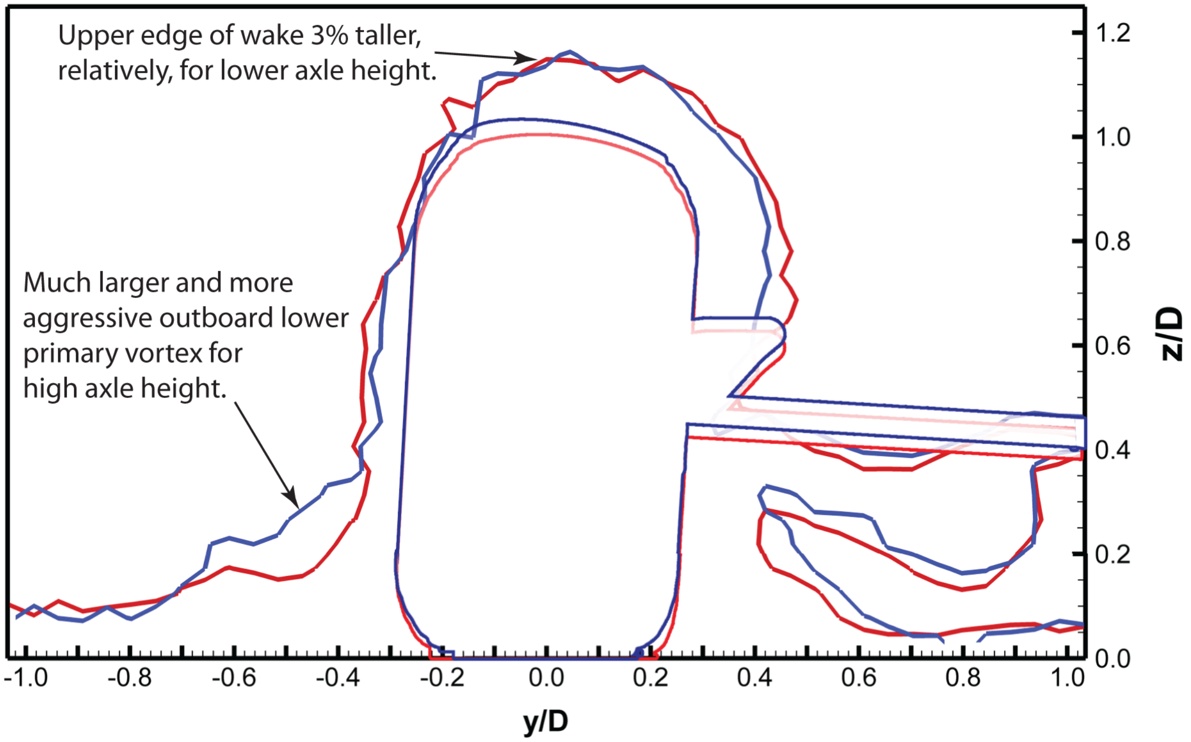

Figure 3.30: *Wake outlines (Cp_0 = 0.9) from Figure 3.28 x/D = 1.5: High (blue) against low (red) axle height comparison.*

The outboard side of the wake also spreads out further from the wheel than the inboard side. This leads to a much more oval shaped vortex rather than the tightly packed and aggressive circular vortex on the inboard. The wake does not appear to fully recover on the outboard side within the scope of the probe measurements. By this, the wake outline does not disappear down to the boundary layer height as shown on the inboard side.

The inboard wake shows much more evidence of upstream disturbance, almost definitely brought about by the components mounted to the inboard of the wheel. There is an interfering vortex feature formed from the support bar on the sting which propagates all the way downstream and is still visible in the x/D = 2.0 plane. This feature has formed because of the ground proximity of what has effectively become a vortex generator due to the bracing strut. Perhaps as expected, for the lower axle heights where the strut is closer to the ground, the vortex appears to be larger and more intense. This feature has not interfered significantly with the vectors in the immediate downstream of the tyre, and has therefore not affected the conclusions made.

Figures 3.31, 3.32 and 3.33 show the longitudinal centreline PIV and 0.16D either side of the centreline, on the edge of the tread-to-sidewall transition. Again, the thick black lines denote the author's representation of the salient flow features with no magnitude. The velocity vectors represent direction only. The transition between the tread and the sidewall is an area of interest as it forms a discontinuity in the geometry, likely responsible for the intensity of the formation of the isolated wheel flow-field features. A direct comparison of both axle height and inflation pressure has been presented for each plane in order to determine which of the two variables the flow-field was most sensitive to.

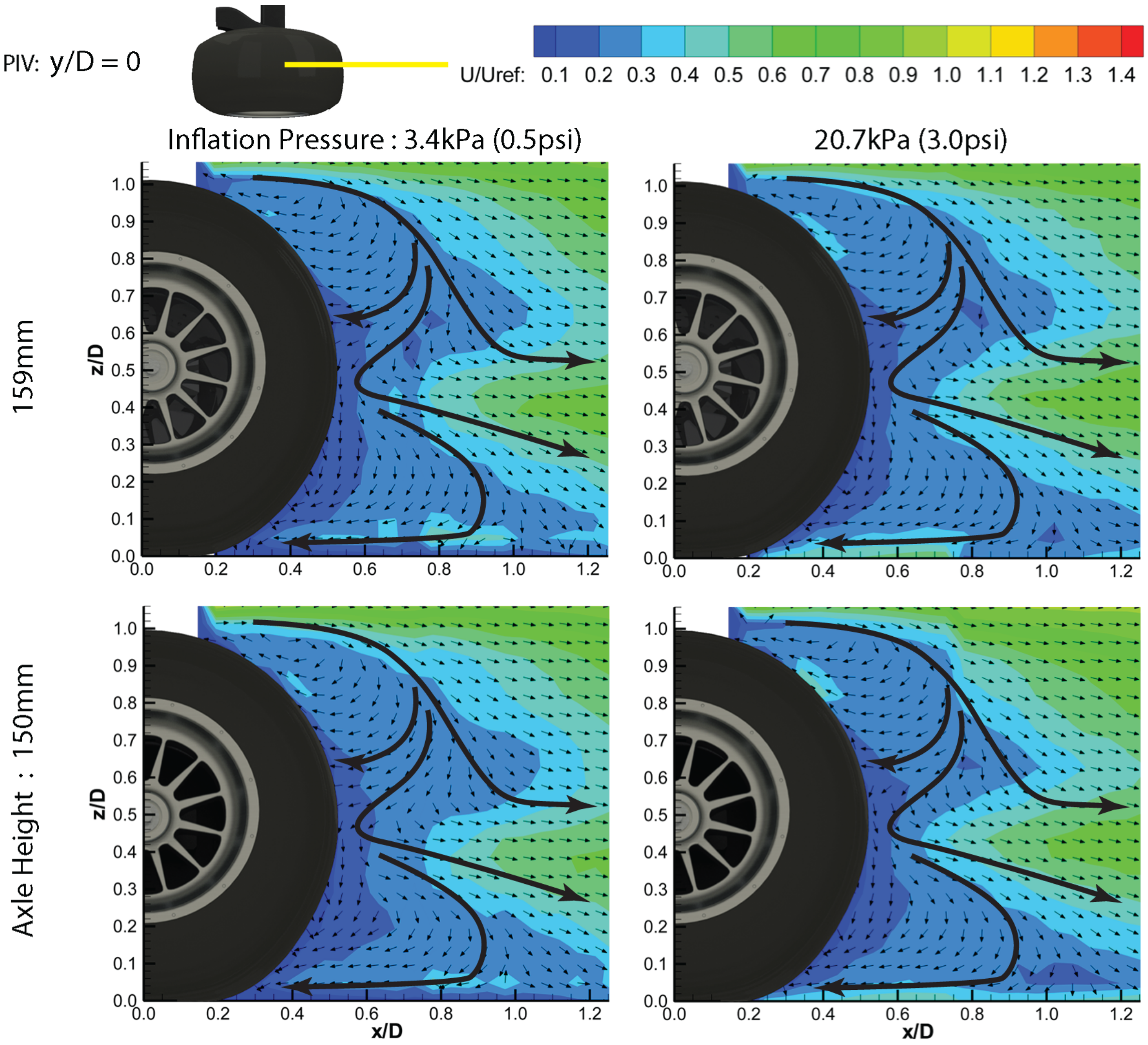

Figure 3.31: *Longitudinal PIV (y/D = 0) of two extreme axle heights and two extreme tyre pressures.*

As Figure 3.31 shows, there is no visible difference in the centreline velocities or absolute size of the wake for the change in axle height or inflation pressure. Because this is the case, there is evidence to suggest that the wake of the deformed case (lower axle height) is of greater proportion to the geometry than the higher axle height case. In fact, Figure 3.30 also showed using a different technique that the overall height of the wake stays the same despite the upper tread changing by as much as 9mm (0.03D). The PIV figures all suggest little change in flow structure between inflation pressures and indeed where there has been a change to the flow-field due to the axle height change, as illustrated in figures 3.32 and 3.33, the same change has been reflected by the tyre with the different inflation pressures.

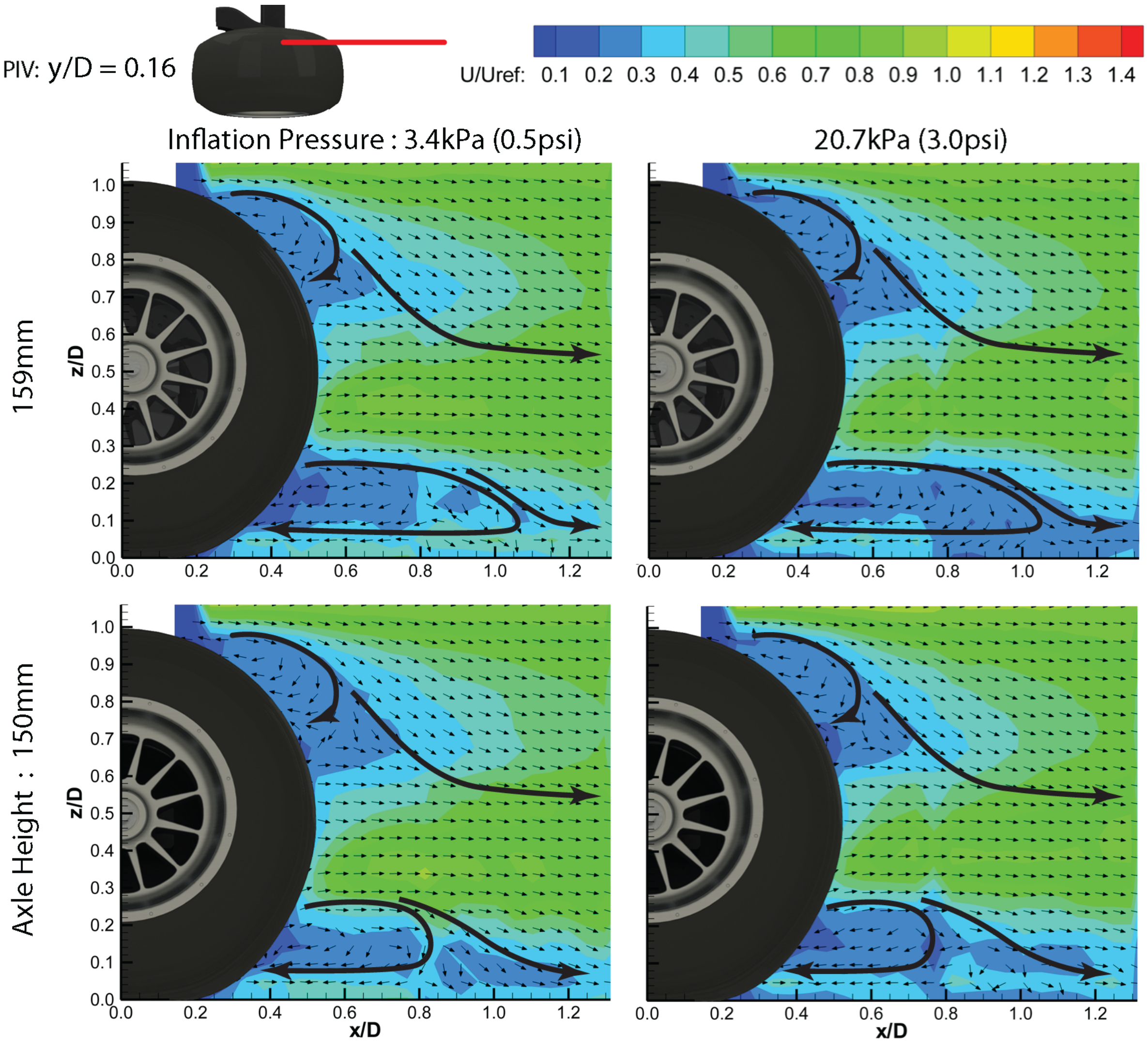

Figure 3.32: *Longitudinal PIV (y/D = 0.16) of two extreme axle heights and two extreme tyre pressures.*

This suggests that although the geometry may be appreciably different, the changes responsible for the aerodynamic force trends are very subtle local effects changing static pressure and not significant to the global stagnation pressure or the flow-field. PIV has shown that the recirculation lobe on the inboard sidewall is longer and less aggressive than the lower axle height. The outboard flow-fields are only subtly different in this orientation. In general the flow directionality is unchanged but there is a slightly larger area of lower velocity in the lower wake for the higher axle heights. This is consistent with what has been observed in the probe data, whereby larger wakes are usually accountable in their entirety for higher drag forces.

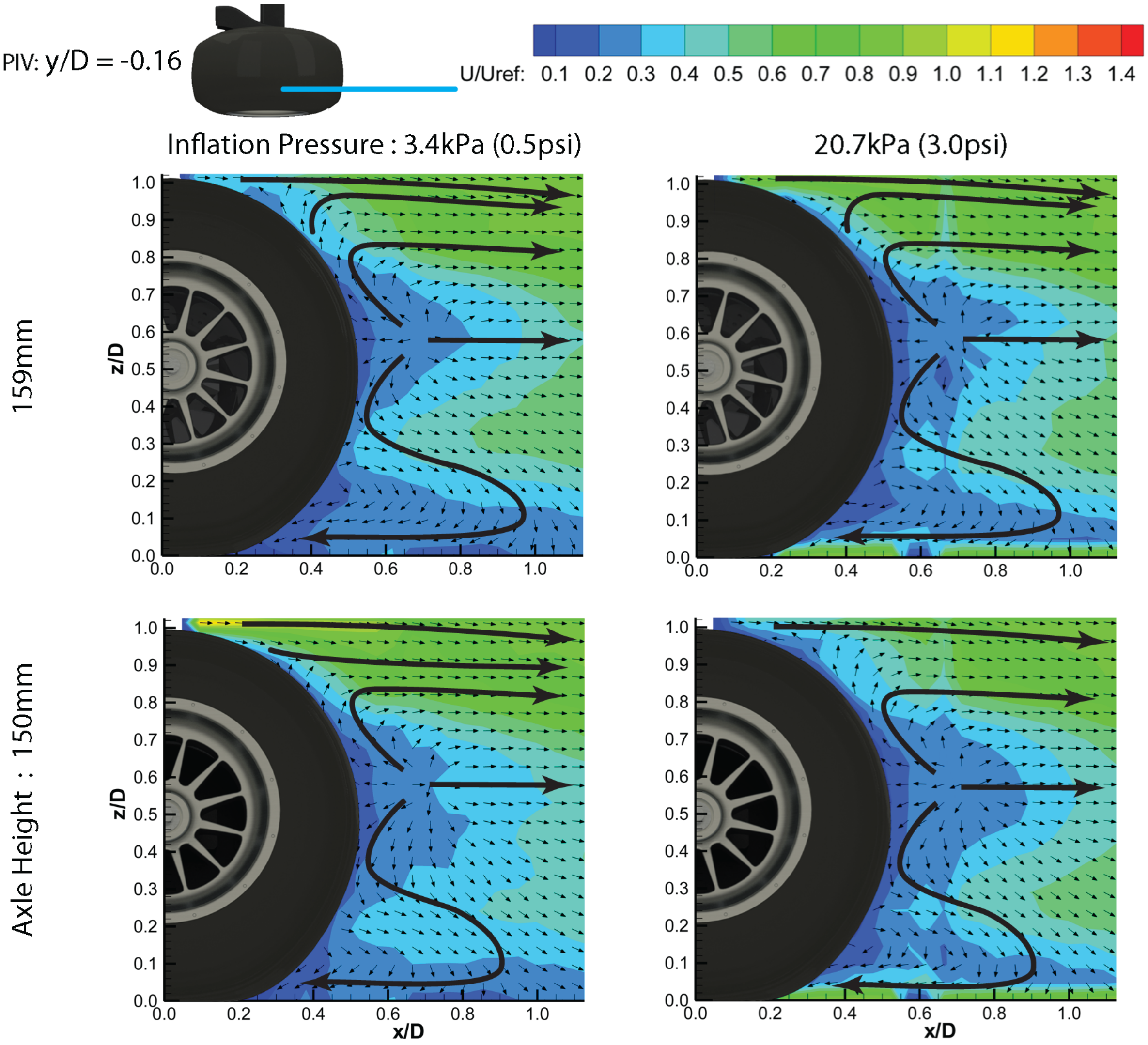

Figure 3.33: *Longitudinal PIV (y/D=-0.16) of two extreme axle heights and two extreme tyre pressures.*

3.4 Deformable Tyre - Aerodynamic Effect of Yaw

The effect of yaw is covered in more depth in the CFD chapter, with regard to fewer limitations due to equipment longevity. The experimental flow-field study presented here, however, provides useful quantitative data which are used in conjunction with the CFD to form the conclusions in Chapter 6.

3.4.1 Flow-Field Observations

A PIV flow-field study was conducted with the cameras situated above the test section in order to obtain horizontal x-y plane wake data. This method was chosen as being the most likely to detect the sensitive changes brought about by the yawing of the wheel in order to capture local separations at the leading edge, if present. Figures 3.34 - 3.36 show horizontal PIV planes taken at axle height for 0°, +5° and -5° yaw respectively. The vectors denote flow direction only as with previous convention.

Mears [3] detected little deflection of the flow around a wheel when observed in this orientation, with the majority of the flow always exhibiting freestream-like behaviour. The examples here show a different trend although this is likely to be skewed by the camber. This is even true of the non-yawed case. There appears to be an outwash towards the negative y-direction for positive and zero yaw but in the negative yaw case the flow has straightened up due to the flow following the outline of the wheel.

In addition to the local separations that were observed at the leading edge, there is evidence to suggest that the global flow direction changes significantly as a result of yaw. As covered in Chapter 1, the most excessive yaw angle likely to be observed by a front wheel is of similar magnitude to the ones tested here and it suggests that the details of the wake are changed with respect to the location of vortex core centres and magnitudes of vorticity. Whilst this is a general observation based upon one plane orientation, it is vital to quantify the exact relationship between these vortex movements and yaw as the sensitive vortex chain of an F1 car could be undone by an excessive movement.

From Figure 3.34 the flow-field of the tyre under straight line conditions can be observed. There is minimal disruption around the leading edge of the scoop although observing the slight flow angularity

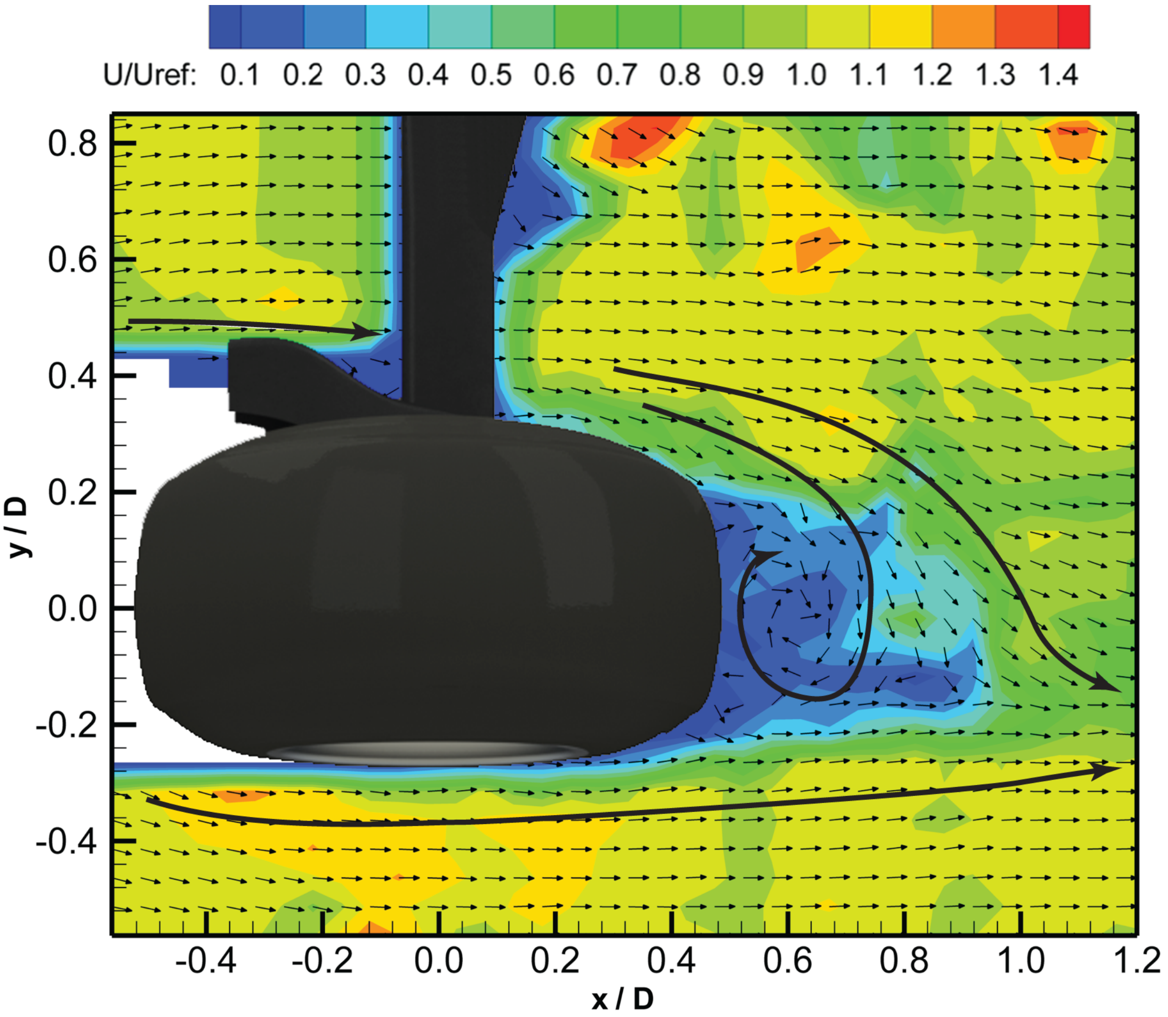

Figure 3.34: *Horizontal plane (x-y) of PIV measurements for z=150mm (axle height) for 0° yaw case.*

on the outboard front of the tyre, it would be expected that there would be a higher degree of angularity in order to deflect around the scoop. There is also evidence of locally accelerated flow towards the tyre from the reinforcement of the sting. This is the same section responsible for a dominant flow feature in the crossplanes presented earlier. In addition to the camber of the wheel there is an asymmetry to the flow-field due to the inboard components such as the sting and brake scoop. This results in a more angular outwash behind the tyre and therefore a tight clockwise (with respect to the figure) recirculation zone. The extent of the recirculation is around 0.3D in the x-direction.

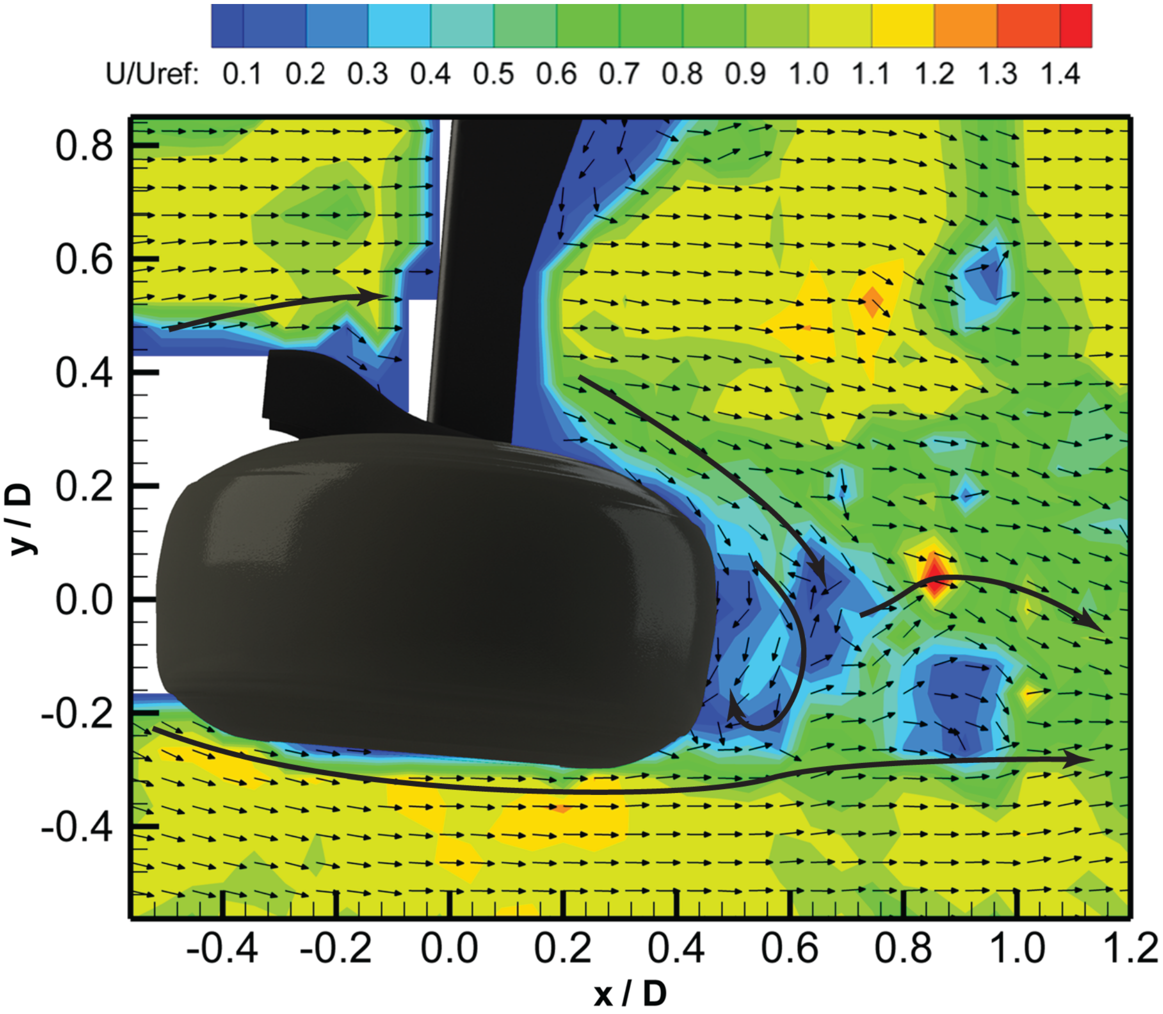

Figure 3.35: *Horizontal plane (x-y) of PIV measurements for z=150mm (axle height) for +5° yaw case.*

Unlike the previous figure, Figure 3.35 exhibits extreme global flow deflection in the wake with respect to the freestream. There is also an area of excessive flow angularity and indeed a local separation around the scoop. This separation was not present for the zero yaw case and therefore not simply evidence of inlet spillage. Due to the higher rate of change for the inboard flow-field when compared to the outboard, it is evident that the steep outwash (global flow from inboard to outboard) results in a smaller recirculation region followed by a heavily unsteady region. The depth of the recirculation region in this instance is around 0.15D, half that of the straight-ahead case. The case presented here, combined with the camber, would be considered the outside wheel (therefore load bearing, with the highest demand for grip) on a right hand turn.

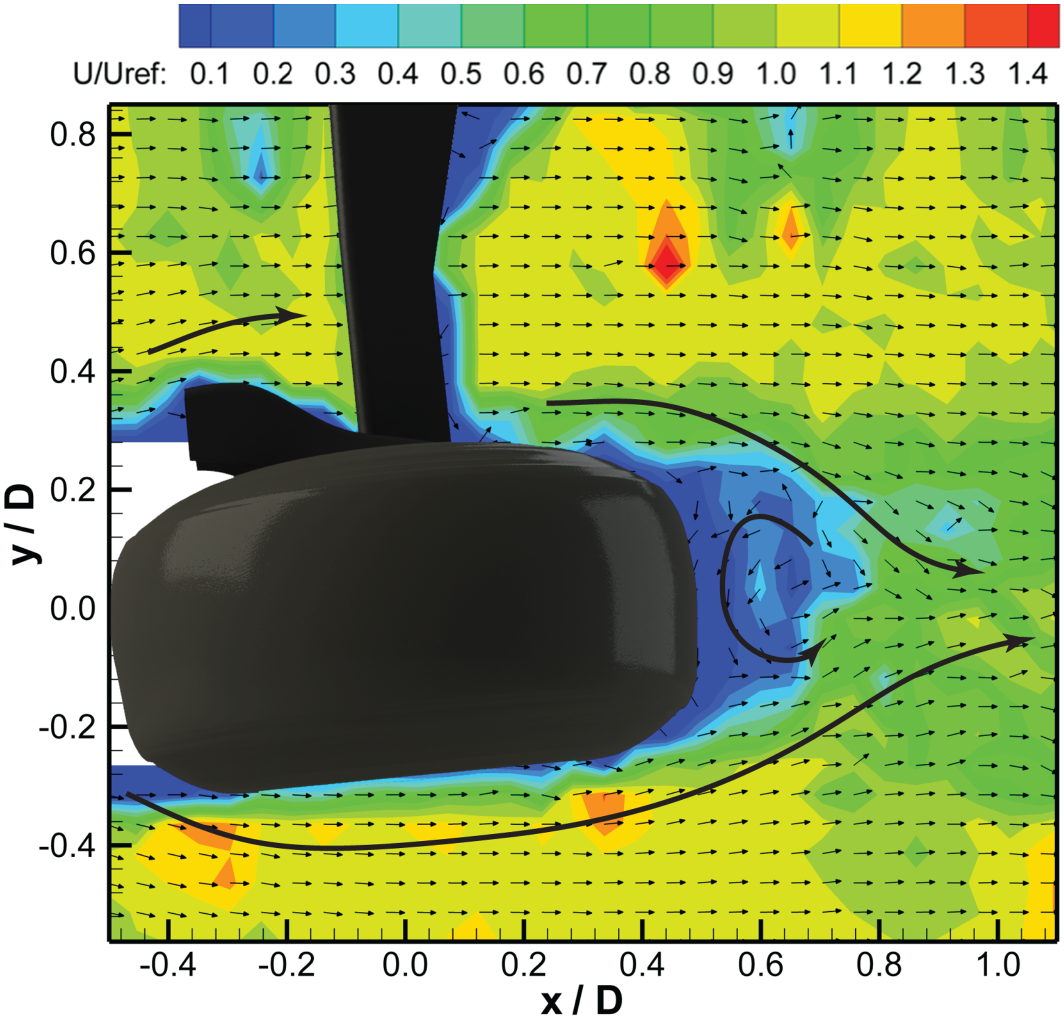

Figure 3.36: *Horizontal plane (x-y) of PIV measurements for z=150mm (axle height) for -5° yaw case.*

Negative yaw, as shown in Figure 3.36, exhibits evidence of frontal tyre separation in this plane. The result of the accelerated outboard flow leads to a much more symmetrical wake distribution balancing the effects of the inboard components as previously presented. Due to this, the recirculating region has in fact reversed to an anticlockwise (with respect to the figure) motion. The depth of this region is similar in magnitude to the positive yaw case. It must be noted, however, that the magnitude of the velocity in this region is so small in this case that the local vectors are quite noisy.

From these conclusions it is evident that there are some major local and global wake changes. CFD has been used to capture more depth in this investigation. These results are presented in Chapter 5.

3.5 Deformable Tyre - Aerodynamic Effect of Camber

This section is presented in order to determine the sensitivity of the camber parameter in order to establish its importance when performing experimental studies and simulations. The camber angle was altered as described in the preceding methodology chapter (Chapter 2).

3.5.1 Drag Force Measurements

The drag forces associated with varying camber were measured and a trend was discovered whereby there was a reduction in drag with increasing negative camber. This reached a minimum before increasing again. In order to be thorough, a lower resolution sweep of camber angles was conducted without the scoop inlet to investigate if the same trend was present. By this, the duct on the assembly would likely have been designed at a fixed camber angle in CFD and a wind tunnel and could therefore have been optimised for the -3.2° camber angle. Delta forces to the non-cambered case have been presented in Figure 3.37 to eliminate the drag offset brought on by removing the duct. The results show that the trend is comparable in both character and magnitude regardless of whether or not the brake duct is present. This shows that, for camber, it is the tyre geometry and not the ancillary components which are responsible for the aerodynamic changes presented here.

3.5.2 Flow-Field Observations

Figure 3.38 shows pneumatic probe data for the wheel's longitudinal centreline (x-z plane) between the two extreme camber parameters. By observing the size of the out-of-range data, here highlighted by the white region, the size of the recirculating wake can be visualised. The grey line labelled 'A' marks the extent of the upper lobe for the zero camber case whereas 'B' shows the extreme of the lower recirculation lobe. Line 'C' shows a point in the far-field downstream wake. All three of which are consistent with the drag force trends above.

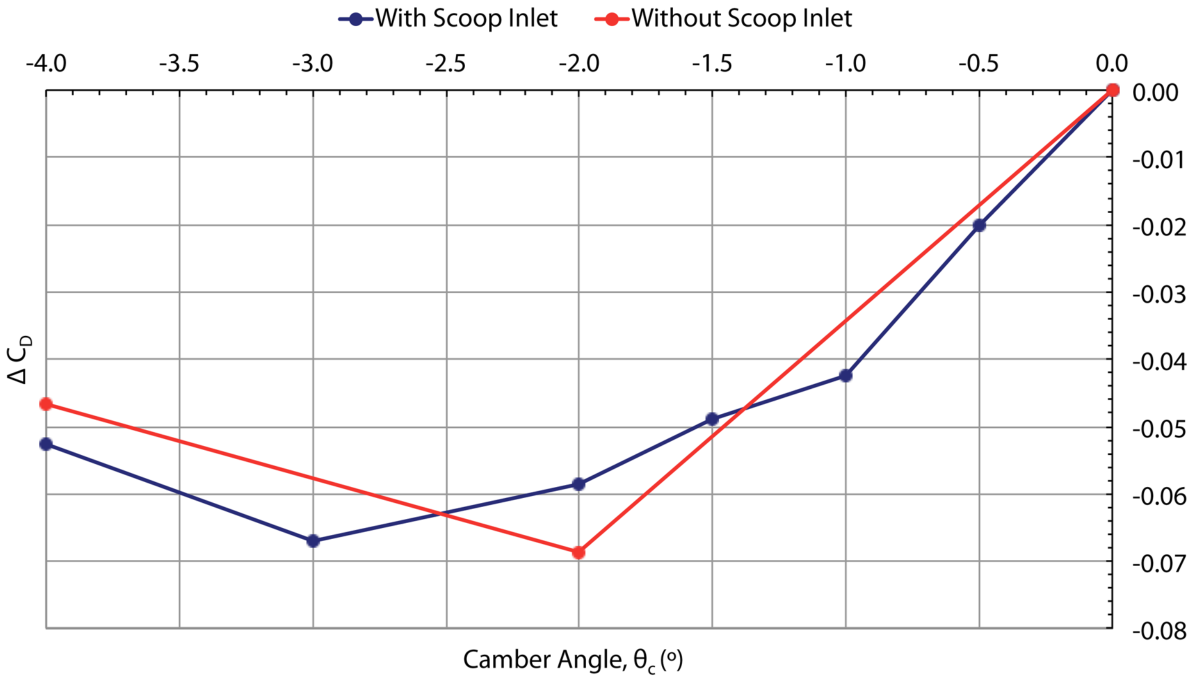

Figure 3.37: *Axial drag force deltas for the camber sweep with and without brake duct.*

The detailed probe flow-field measurements present in Figure 3.39 show the comparison of the overall structure of the wake. The shape of the global flow structure appears to be generally consistent between the two cases with the exception of a rotation in the lean of the wake profile in the same direction as the camber. By this, the lower features are translated towards the outboard side of the wake and the upper features are translated to the inboard side. The overall size of the wake, using the $Cp_0 = 0.9$ cut off, seems unaffected despite the redistribution of the primary features.

Figure 3.40 presents the vorticity and vector distribution for the planes presented in Figure 3.39. Although it has been concluded that the overall size of the wake has been unaffected albeit redistributed, the vorticity map suggests that the case with no camber has stronger features on the outboard side. The inboard side remains similar between the two cases.

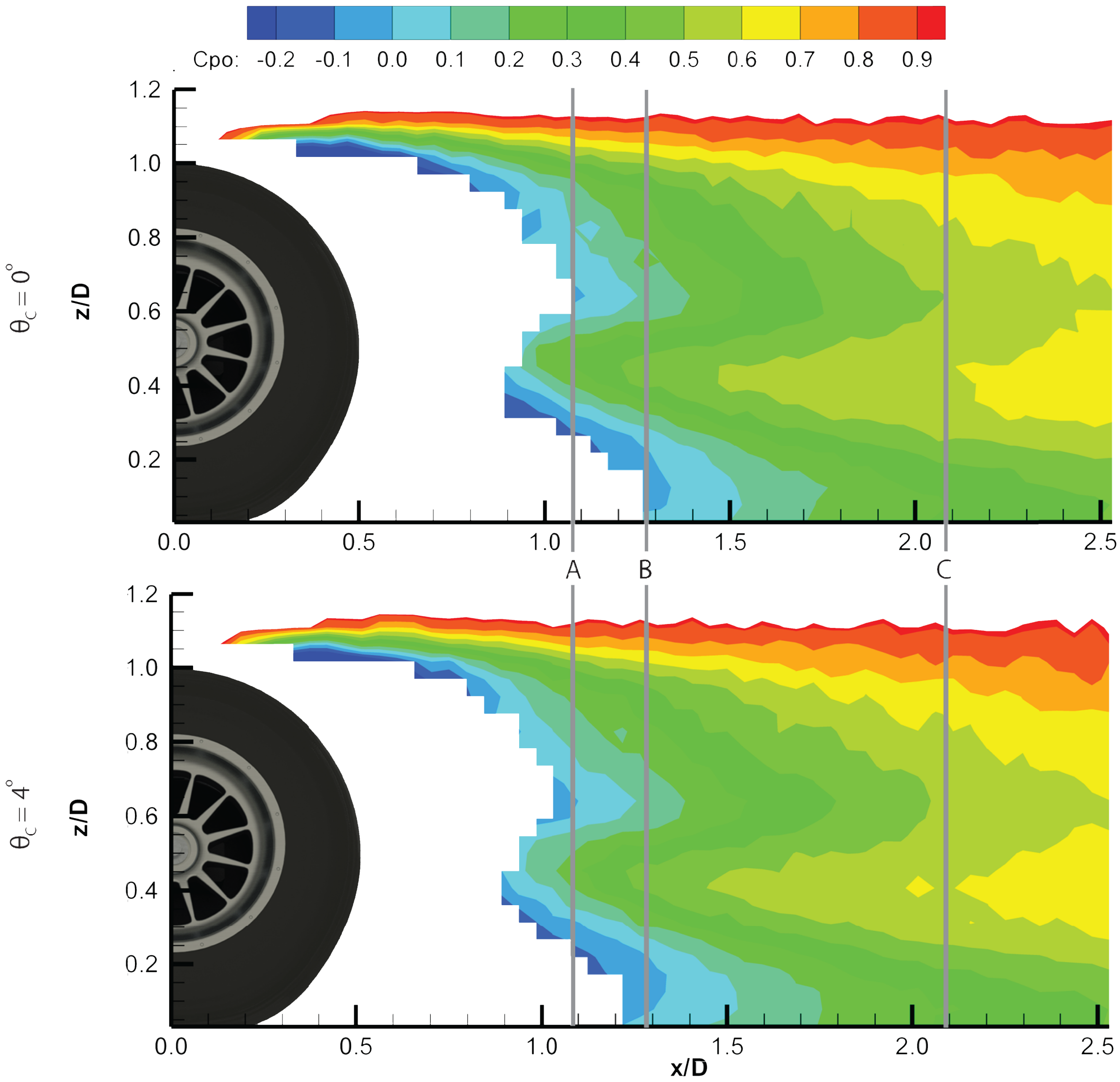

Figure 3.38: *Camber flow-field comparison (longitudinal probe at y = 0) between* $\theta_c = 0°$ *and* $4°$.

For both cases under high load the inboard side of the tyre forms a sharp edged profile, arguably a strong candidate for a large and strong vortex feature. The case of the outboard, however, illustrates a smooth progressive curvature for high camber and tends towards the sharper profile at zero camber (in fact, symmetrical to the inboard at $\theta_c = 0°$). This is consistent with the flow-field observed here. More discussion regarding the form of sidewall profiles and their effect on the flow-field can be found in Chapter 6.

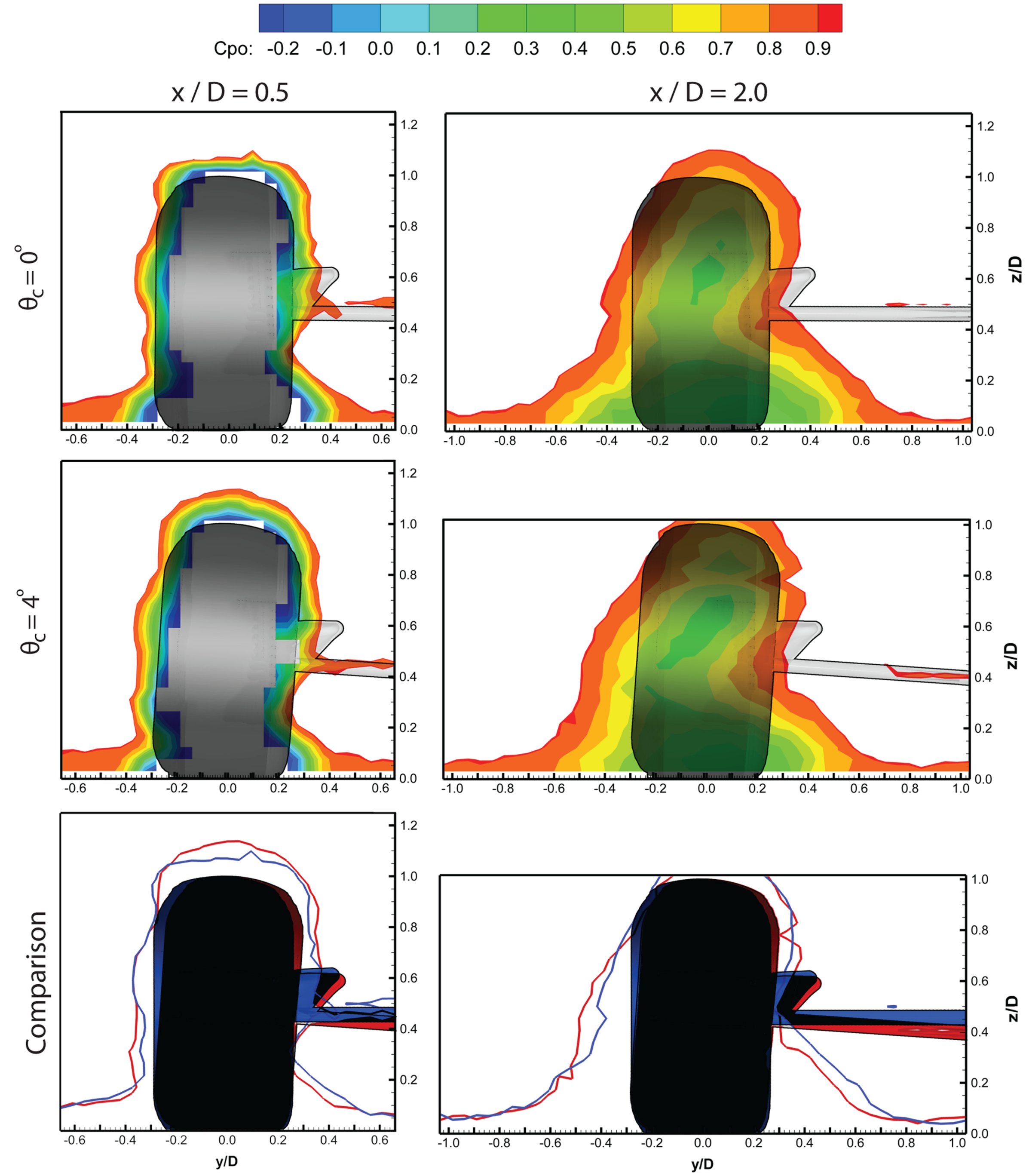

Figure 3.39: *Camber flow-field comparison - Crossplane (y - z plane) at x / D = 0.5 and 2.0 for* $\theta_c =$ 0° *and* 4°. *Upper and Middle: Coloured by* Cp_0 *with cutoff at* $Cp_0 > 0.9$. *Lower: Direct wake outline comparison at* Cp_0*=0.9.*

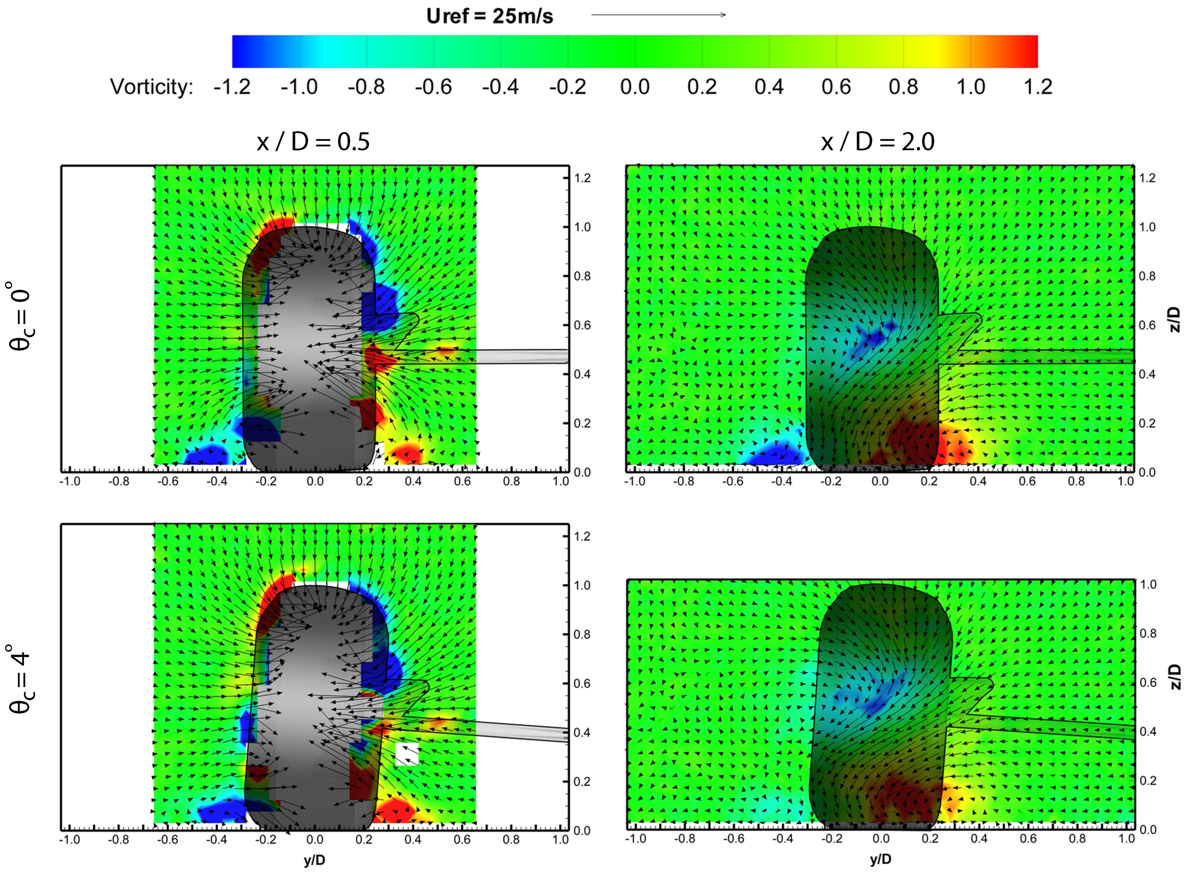

Figure 3.40: *Camber flow-field comparison, as Figure 3.39 with velocity vectors and coloured by vorticity.*

Whilst it is apparent that there are subtle redistributions in the flow-field from the crossplanes and, from longitudinal probe data, the size of the recirculating wake differs by an absolute distance in the x-direction, there is an argument to suggest that the greatest change will be observed in horizontal planes (x-y). Because of this, PIV measurements were taken for this orientation. These are presented in Figure 3.41. Three values of camber were interrogated in order to try to capture a progressive change.

Starting at zero camber (top of figure), the wake behind the sting appears to be straight and with the freestream at both ground level and mid-diameter (axle height). The wake from the sting is evident in the latter case although not as large as may have been expected. Although the wheel in this case is vertical and therefore has as close to a symmetrical geometrical profile as possible (other than the inboard face furniture), the wake is far from having the same properties. In all cases the wake washes out towards the outboard with a recirculation region directly behind the tyre. At zero camber this recirculation bubble appears to be predominantly clockwise as shown in the figure, gradually becoming more neutral then anti-clockwise as extreme camber is introduced. Along with this anti-clockwise local flow-field trend, the downstream wake stars to wash further and further inboard for the lower height. This is due to the stronger vortex feature from the inboard sidewall which has a low-pressure core. Interestingly, although the vortex core centres have moved outboard as shown by the probe data, the velocity vectors show the opposite trend with stronger inwash. This is a consequence of only observing a single plane which happens to coincide with one part of the previously mentioned vortex structure and not evidence for a contradictory inward moving global feature.

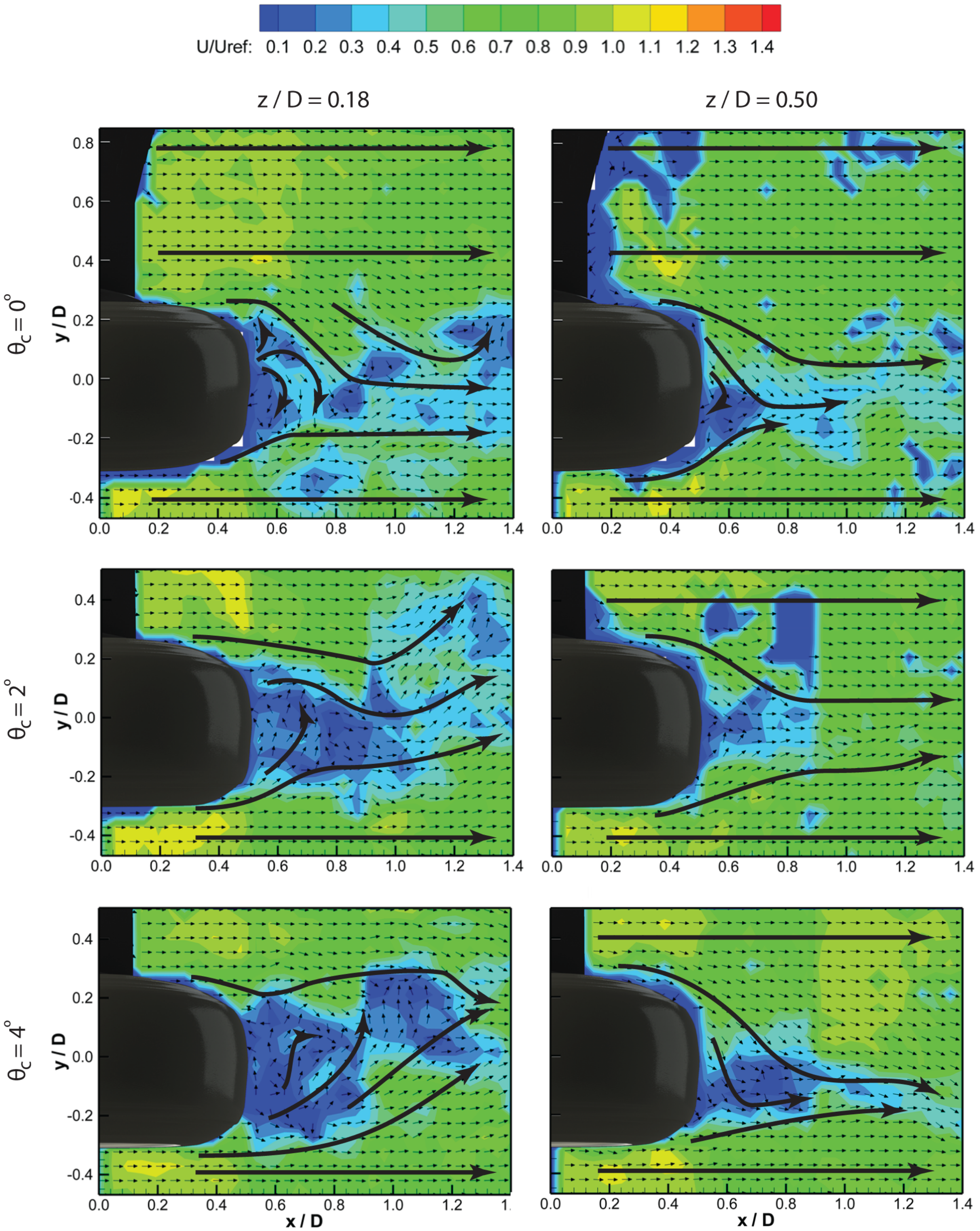

Figure 3.41: *Horizontal planes of PIV (z = 150mm (axle height)) for varying camber. Top:* θ_c = *0°; Middle:* θ_c = *2°; Bottom:* θ_c = *4°. The bold lines denote important features (not representing magnitude) and the small vectors represent flow direction only.*

Chapter 4

Methodology - CFD

4.1 Software Packages

Two software packages were implemented in the investigations undertaken within this research. Each package is described in this section in terms of their functionality and hence their specific application. This is supported with details of the mesh generation and the simulation parameters for each test performed. Ansys Fluent was used for studies based upon the rigid tyre experimental work and Exa PowerFLOW was used for those in relation to the deformable tyre.

4.1.1 Ansys Gambit and Fluent

4.1.1.1 Background

Ansys Fluent is well regarded as the industry standard for computational fluid dynamics (CFD). It is fundamentally based upon the Reynolds-Averaged Navier-Stokes method (hence often labelled as a 'RANS' solver) and is fully versatile in its application. This type of solver typically determines the flow-field of a given geometry based upon cell discretisation, driven by the input mesh, and by maintaining adjacent cell flux-quantities such as velocity for a complete overall solution. The input mesh, which is fed into the software, is generated outside of the solver package. The accuracy of such a solution therefore relies largely upon two main parameters, the mesh quality (cell shape, distribution and density), and the selection of an appropriate turbulence model.

The Navier-Stokes equations govern fluid flow and are momentum based time-dependent partial differential equations which have no analytical solution. By separating the quantities such as velocity into both mean and variable components via decomposition and Reynolds averaging [103], a solution can be achieved using assumptions and mathematical models for the non-linear component. The result can either be time-averaged for a steady state problem, or for a highly unsteady case, a spatial or ensemble average. Fluent has the ability to represent turbulence using one of many built-in turbulence models, each of varying complexity. The simplifications that the RANS method brings allows for generic hardware to be implemented for realistic solutions in terms of turnaround and accuracy.

Fluent has wall treatment features which benefit the determination of the laminar-turbulent transition point and these therefore assist boundary layer modelling. This, in turn, benefits the determination of separation points, surface pressure modelling and hence, since forces are determined by integration of the skin friction and surface static pressures, improved force measurements.

Almost all of the CFD investigations relating to wheel aerodynamics in the literature rely upon the use of Fluent [33] [35] [42] [61] [104] [105] [106]. The only exceptions that could be found were those by Kellar et al. [4] and Skea et al. [107] [108] who used an in-house RANS CFD code and a much earlier industry standard, Star-CD (RANS), respectively. Fluent boasts excellent linearity in simulation time when utilising multiple cores, processors or nodes of a cluster. As such, for large automotive, aerospace and F1 manufacturers, it is the standard choice.

For most cases there will be a strong unsteadiness or transience in the flow. This leads to an impossible steady-state RANS solution and the simulation's residuals (the difference between iteration-by-iteration imbalances of pressure and momentum conservation) will simply increase (divergence). For cases where there is a low level of unsteadiness the iterative RANS solver can find a solution and this will produce the equivalent of a time-averaged solution. For cases where there exists a heavy unsteadiness or periodic shedding, the time-resolved Unsteady RANS (URANS) solver must be used. This works by determining a time-step and iterating the cell values in the domain over a set length of time. This brings a further element, the time increment, into the determination of the accuracy of the solution. For a case where there is moving geometry (non axially symmetric), the common choice is the time-dependent solution.

From a wheel aerodynamics perspective, the majority of previous studies have been performed with a wheel housing. The only isolated wheel investigations of the above examples were by Knowles et al. [61], Mears & Dominy [104] and McManus & Zhang [33]. Most examples of CFD studies result in an underestimation of forces, particularly in the rare case where an experimental lift is available for comparison (experimental wheel lift measured by McManus & Zhang [33], Mears [3] and shroud lift measured by Axon et al. [105] [106]). Discrepancies for lift forces can be as much as 46% as shown in McManus and Zhang's work. The source of the empirical wheel lift force was, however, not necessarily trustworthy (under belt load-cell), as discussed in Chapter 1. The values in the work by Axon et al. [105] [106] are also seen as being in good agreement for drag but around 40% in error for the shroud lift. However, the drag force was broken down into components and although the total force was around 8% different from the experimentally measured value, the components were much further from this and the errors cancelled each other out.

An essential part of the simulation setup is in assigning boundary conditions to the geometry such as (but not limited to) moving walls, which affect the treatment of the boundary layer and therefore the shear layers and developing flow-physics. Most of the examples from the literature in the preceding paragraph made many compromises, particularly involving the blocking of through-hub flow, the lack of a rotating mesh (for non axially symmetric geometry rotations such as spokes) or even a lack of rotating wall treatment (such as the tread) and in most instances incorporated a 'sunken wheel', into the floor. The latter was done to improve local cell skewness as in the case of Mears & Dominy [104], Axon et al. [105] [106], McManus & Zhang [33] and Minto [73]. Most of these are a consequence of resource restrictions as opposed to preferable test parameters. A useful result shown by Bienz et al. [110], however, shows that Fluent's MRF feature (multiple reference frame) allows a very similar result to a sliding mesh to be obtained with far less computational requirement and without the need for a time-dependent solution.

4.1.1.2 Mesh Production

For the preliminary investigations ‘Fluent 6’ was utilised whilst ‘Gambit’ was used for mesh generation. Gambit’s simplicity allows the user to produce very clean mesh files which rarely fail once the end-user appreciates the intricacies and idiosyncrasies of CFD mesh generation.

Mesh sizes vary largely depending upon available hardware resources. The general trend shows mesh sizes increase from around 340,000 to 1.5M cells at the turn of the millenium [4] [105] [106]to around 3M cells in the mid 2000’s [33] [104]. However, the capability was clearly available even in 2003 for CFD facilities to have meshes in the region of 100M cells, as in the case of the Sauber Petronas F1 team [110].

The domain for the mesh used in this study spanned 7 wheel diameters (7D) upstream of the axle, 10D downstream and had an area blockage of less than 4%, similar to that of the wind tunnel experimentation. No attempt was made to match the exact geometry of the wind tunnel. The mesh made use of unstructured tetrahedral cells with higher density in areas of small corner radii and sensitive flow regions such as the contact patch and inside the hub. The resulting total mesh size was 4.4 million cells. An axle-line cross-section of the mesh can be seen in Figure 4.1.

Areas inside the hub and close to the tread walls comprised cells of node-spacing size equal to 1mm. Zones were defined in the hub, around the wheel, around the whole wheel and sting geometry and in the wake. These were all defined with reducing resolution further away from the solid geometry. As discussed above, an issue whereby high cell-skewness created an unusable mesh for the contact patch region of the wheel had to be resolved in the same way as in the literature, by sinking the wheel into the ground by a small amount (around 0.6% of the wheel diameter). This in many ways created a more realistic geometry with a contact patch as opposed to a line but this is not true to the wind tunnel environment. By increasing the angle between the tread’s lowest point and the floor, better quality cells could be grown and therefore allow for a solution to converge.

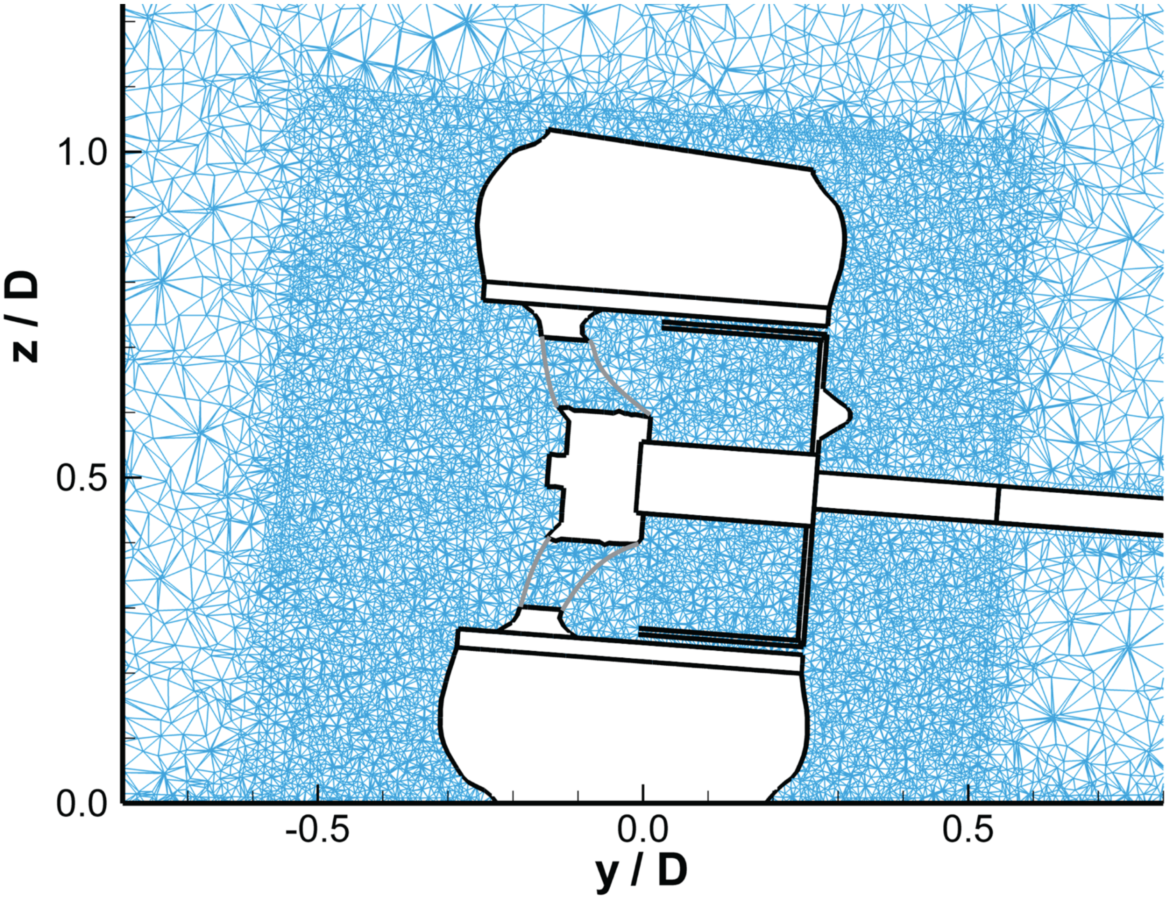

Figure 4.1: *Cross-sectional representation of the geometry, mesh density and mesh quality for the Ansys Fluent calculations.*

4.1.1.3 Simulation Parameters

Fluent offers several turbulence models, the most commonly used are k-ϵ, k-ω and LES (Large Eddy Simulation - time-dependent only). Several examples in literature make use of the k-ϵ or k-ω models, such as Kellar et al. [4], Regert & Lajos [35] [42], Axon et al. [105] [106], Skea et al. [107] [108], McManus & Zhang [33], Knowles [61] and Mears & Dominy [104]. McManus & Zhang [33] also investigated the use of the Spalart Allmaras turbulence model with closer results to the wind tunnel tests. The resulting total drag was differed from the tunnel measured value by 7% in the case of Spalart whereas for RKE (realizable k-ϵ) this was of similar magnitude at 9%.

Preliminary studies with various turbulence models using a variety of parameters and options all predicted extremely late separation. In fact, an artificially exaggerated downwash was present for both k-ϵ and k-ω which led to vastly strengthened trailing vortices and a very different flow-field from that observed in the wind tunnel. This was also commented on by Mears & Dominy [104], who noted that the early boundary layer separation (i.e. before the top of the wheel), which is characteristic of the flow about a rotating wheel, had been generally poorly predicted by CFD.

It was decided that the Spalart Allmaras (single equation) turbulence model most accurately predicted the separation point of the wheel referring to both wind tunnel studies and expected separation points from work such as Mears [3], Fackrell [23] and Hinson [32]. This was with default wall treatment settings.

For comparison with wind tunnel acquired flow-field measurements, a steady-state (equivalent to time-averaged) solution was desirable. Due to the unsteadiness in the wake, fine tuning of the pressure, momentum and turbulent viscosity discretisation solver options, set to ‘second order’, ‘QUICK’ and ‘QUICK’ respectively allowed the solution to solve under standard RANS calculations. This would only work if a short preliminary simulation was run with default values.

4.1.1.4 Computational Hardware and Resource Requirements

For the Fluent simulations, the Durham University High Performance Computing Network cluster, named ‘Hamilton’ was used. This, at the time, comprised 264 compute nodes (786 cores) each comprising 8GB RAM. For mesh production, only 4GB of RAM was available which severely limited the generation. As a general rule, it appeared that one million unstructured cells equated to a requirement of around 1GB of RAM.

Each simulation was placed on one node of the cluster and took a total of 20 CPU hours to complete. This is a typical turnaround time when comparing with the literature. Convergence was deemed to have been achieved when the drag force of the wheel assembly reached a steady value as well as the residuals meeting their default 1×10^{-3} condition. This was around 10,000 iterations and as such, each test case of 20 CPU hours equates to 10,000 iterations of a steady-state solution following the preliminary runs to establish the domain.

4.1.2 Exa PowerFLOW

4.1.2.1 Background

Exa PowerFLOW is a more targeted solver than Fluent with several features tailored specifically towards the automotive industry. Instead of establishing a traditional RANS solver, the software package is built upon a solver engine called 'Digital Physics' which utilises the Lattice-Boltzmann method [109]. The concept of this solver is to track the motion of macromolecules which is applicable to the movement of gases and liquids. Essentially the same parameters are conserved as with RANS but the calculation involves exact solutions of discrete particles observing Newtonian physics as opposed to relying upon statistical boundary modelling and iterating partial differential equations. By modelling the densities of particles as a fluid, reliable and accurate flow-fields can be captured. Computing resources are also much less demanding comparing like-for-like mesh sizes with RANS and therefore the scale of the simulation can be considerably larger.

PowerFLOW does, however, currently only have one built-in turbulence model called VLES (Very Large Eddy Simulation). This code is based upon a time-dependent version of the k-ϵ turbulence model and is used in conjunction with the "law of the wall" boundary treatment, allowing a more accurate solution for lower surfel resolution (a surfel being the PowerFLOW term for a two-dimensional surface mesh cell) than would otherwise be required. The latter applies an automated y^+ dependent function to the surface flow and thus allows accurate prediction of separation from large bluff bodies such as those dominant in automotive applications.

PowerFLOW has one major advantage over any other solver in that it boasts ease of use and adaptability for case-by-case changes. With Fluent, for example, a geometry change results in going through the meshing process again, either fully or partially, which utilises user hours as well as computing resources. PowerFLOW uses an automated Cartesian meshing algorithm (essentially cube shaped cells of varying size, ‘stacked up’ to represent the volume mesh) which takes care of this discretisation automatically. The user simply defines regions of interest, known as variable resolution zones (VR regions) which progressively half in resolution for each interest level. The automated discretisation then takes this parameter set by the user to fill the volume with voxels (PowerFLOW equivalent of a cell) and surfels, which are the surface projection of the intersecting voxel at the fluid-solid boundaries.

The solver then resolves three different flow defining scenarios. Those are particle-to-particle interactions, particle-to-surface interactions and general particle movement known as advection. The latter is dealt with as a statistical density distribution as opposed to individual particle tracking, much the same as in the way that PIV does not track particles in cross-correlation, but instead uses a window of multiple particles to determine the most probable direction of travel.

For particle-to-surface interaction it follows a four-step process. Particles are initially noted in their ungathered state away from the surface. Upon interaction with a surface after their usual discrete voxel-to-voxel displacement there is a voxel-surface advection which applies boundary conditions based on conservation of mass, transferring momentum based on pressure and friction, and then applies surfel-to-voxel advection with their new trajectory.

4.1.2.2 Simulation Parameters

The simulation options within PowerFLOW were largely based upon a parametrised calculation system whereby parameters such as wheel yaw and camber could be altered in order to match the specific tyre profile loaded in. The preparation of the output file for solving then performed these calculations which realigned the geometry as necessary. This saved a lot of time in set up but also ensured consistency between the constant components such as the sting, hub and scoop. There were eight variable resolution zones (VR regions) starting at a resolution of 1mm in the boundary layers (enlargements or offsets from the imported model-scale CAD geometry). The final simulation resulted in a cell count of 26.6M voxels, which is almost an order of magnitude higher than that of the Fluent simulations. The domain size comprised a region 10 diameters (10D) downstream, 10D upstream, 5D wide and 6D high. A summary of the global parameters set in the simulation environment were as shown in Table 4.1. Figure 4.2 shows how the VR regions were distributed.

Table 4.1: *Simulation parameters for the Exa PowerFLOW simulations.*

Parameter	Value
Reference Velocity	$25ms^{-1}$
Characteristic Pressure	100877Pa
Characteristic Temperature	293.15°C
Floor / Road Velocity	$25ms^{-1}$
Wheel Rotational velocity	156.25 rad/sec
Turbulence Length Scale	0.02m
Turbulence Intensity	1.5%
Finest Resolution	1mm
Simulation Time (after priming with 200,000 iteration seeding file)	0.512sec (80,803 timesteps)

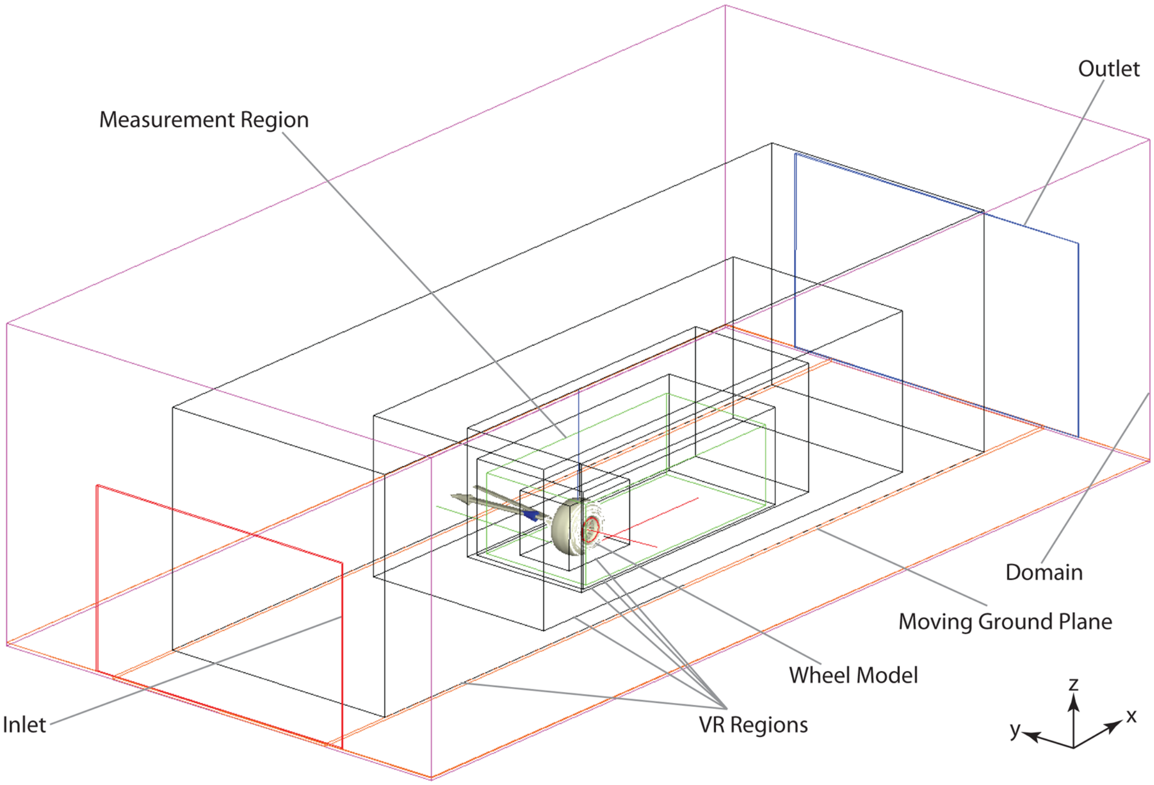

Figure 4.2: *Domain geometry (representing a simplified version of the wind tunnel used for experimental measurements) and overall view defining the VR regions for the Exa PowerFLOW CFD simulations.*

With PowerFLOW's links to the automotive industry, the rotating geometry model has been developed and refined. The rotating wheels of the geometries tested were therefore applied to the PowerFLOW simulations by setting a cylindrical volume around the spoke region of the rim. By setting a rotational reference frame for this cylinder, any solid parts within that region were given a rotational frequency. Because all meshing was done automatically, it again offered vastly more complicated simulation parameters in a given job turnaround time than alternative software packages.

4.1.2.3 Computational Hardware and Resource Requirements

The Exa PowerFLOW simulations used much higher specification hardware than Ansys Fluent investigations. The Cartesian mesh methodology requires a much higher mesh density than a traditional unstructured tetrahedral mesh, which in turn requires higher density than a structured hexahedral mesh. This is due in-part to the relatively disorganised (relative to geometry) structure of the mesh, which does not follow the velocity contours and gradients near walls and solid-to-fluid boundaries. For a Cartesian mesh, the issue lies in badly resolved surfaces in the case of a low-resolution mesh. An advantage to the Cartesian mesh system, however, is that the storage of the mesh requires less run-time memory, hence the higher cell count is not as computationally expensive as it might suggest.

The hardware used for this set of simulations was a purpose bought twin-node server system dedicated to running PowerFLOW simulations. Each node comprised two quad-core processors and 32GB of RAM. The mini-cluster therefore comprised 16 cores and 64GB of RAM which were each used concurrently for the duration of the experimentation undertaken within this thesis.

Simulations were primed with a two-week long run of 200,000 time-steps of the validation geometry (see Section 4.3.2). This was the point at which the solution was deemed to have converged, based upon total force measurements. This equates to 100 hub flush-throughs based upon the wheel diameter. The drag appeared to converge faster than the lift which is discussed in the validation section. Each individual simulation was seeded with the results of the initial priming solution as the geometry was largely similar in every case. Even the cases with the largest discrepancies, with the wheel at yaw, only had 3-5% of voxels which required resolving from scratch. This saved both simulation time and increased the accuracy of such a large sweep of geometries. The main simulation for each geometry comprised exactly 40 flush-throughs based on wheel diameter, the final 12 of those were used for data-averaging. Specifically this was equivalent to 4 full wheel revolutions to minimise any pulsing.

A convergence plot can be found in Figure 4.3 which illustrates the drag force throughout this initial seeding run (blue) and the additional processing for the case specific run (red).

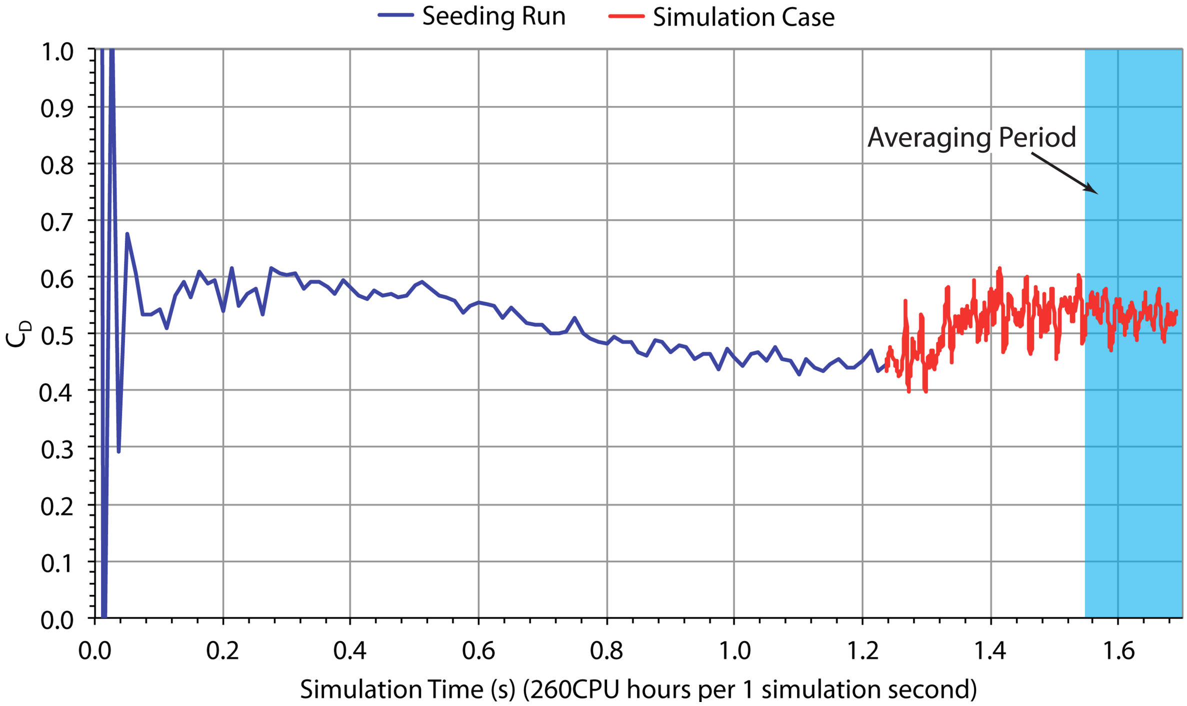

Figure 4.3: *Drag force convergence plot for the initial 200,000 time-step seeding run and the subsequent case-specific 80,803 time-step run. The area highlighted in light blue illustrates the averaging period.*

The blue trace approaches the converging drag force and allows all of the major flow regimes to be set up including the downwash, correct separation region and wake structures. The red zone then shows the settling of the new test case and finally its convergent behaviour. Whilst the initial jump appears initially to be an artefact of seeding a simulation, it is in fact the true force development for a test equivalent to the overall length. This is known because the red trace is comprised of eleven separate runs which were each seeded from each other (this was a requirement given the high measurement frequency and resource limitations). The averaging period is highlighted at the end. The frequency of measurement for the convergence trace in this instance was higher than the seeding run and this is why the data appear more noisy.

The error based upon standard deviation over the root of samples (as outlined in Hase et al. [87]) equates to an uncertainty in the drag force measurements of $C_D = 0.001$ (equivalent of one count of drag). This should be considered when observing all force measurements in Chapter 5.

4.2 Geometry

4.2.1 Rigid Tyre and Through-Hub Flow (Fluent)

The porting of the rigid tyre geometry into CFD was a relatively straightforward technique as the conical wheel had a constant profile around its circumference. By measuring with a set of digital calipers, accurate to one hundredth of a millimetre, using a flat steel plate as a reference, the profile of the tyre was carefully reproduced using points and splines using Ansys Gambit. These profiles were connected to produce a cross section of the tyre and then revolved around a central axis in order to produce the wheel. The wind tunnel parts for the hub and scoop inlet were originally produced (via rapid prototyping) from CAD drawings and therefore the exact coordinates of these could be transferred into Gambit to reproduce the geometry precisely. The interface between the scoop and the hub was filled with a plane matching the shape exactly and the plane was assigned properties of a porous medium. All other surfaces were defined as walls, as outlined in more detail in the Ansys Fluent simulation parameters section above. Figure 4.4 shows the geometry in Gambit post-meshing, showing the different resolution regions applied.

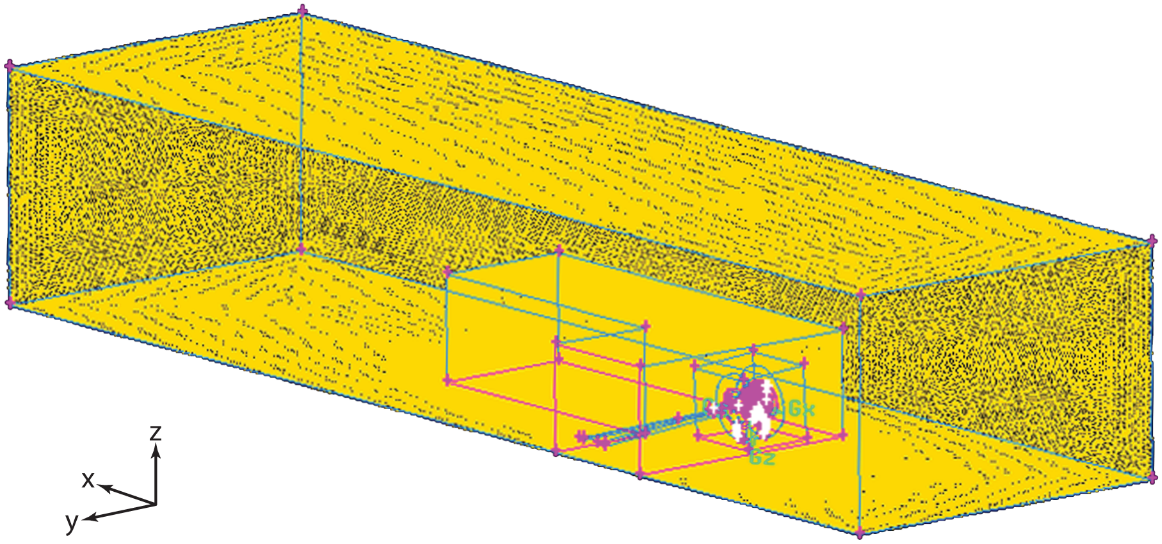

Figure 4.4: *Post-meshed view of the geometry and mesh density of the rigid wheel Ansys Fluent CFD experiments.*

4.2.2 Deformable Tyre : Deformation and Yaw Studies (PowerFLOW)

Modelling the deformable tyre geometry in CAD and then CFD was a much more complicated task than for the consistent rigid geometry. The profile scans from Chapter 3 were applied in point-by-point form using Dassault's Solidworks and the profiles as shown in Figure 4.5 were the result.

These cross sections were then lofted together using a perfect cylinder in the centre as a guide, where later the exact spoked geometry was inserted. The contact patch was defined by the length and width measurements also taken from the wind tunnel. The result was as shown in Figure 4.5.

The CAD geometries could then be exported individually to be loaded by PowerCASE (the setup application for PowerFLOW). As most of the geometry was consistent between runs, only the tyre profile was changed in the majority of cases, with the remainder of the geometry being altered according to the new axle height, yaw and camber angles. This was done using the calculations feature of PowerFLOW and all axes of rotation were as defined in the CAD package so as to ensure no gaps or leaks would appear between the components of differing case geometry.

4.2.3 Detailed Internal Geometry (PowerFLOW)

For the internal geometry tests an internal flow system was based on the design from the full-car 50% scale model as used throughout this work. The brake rotor (or disc), carrier and caliper were modelled in CAD using measurements to the nearest tenth of a millimetre. The exact geometry can be seen in exploded form in Figure 4.6.

The brake scoop inlet led to a single internal duct which entered an annulus. This forms part of the suspension upright on the real vehicle. It then fed the centre of the brake rotor, allowing air to pass through the channels, encouraged by a centrifugal pumping action, in order to cool the rotor. A small quantity of air was allowed to pass over the surface but essentially all of the exit flow passed to the spoked area via the outer diameter. The brake rotor was allowed to rotate when desired by means of a moving mesh just as for the rim spokes.

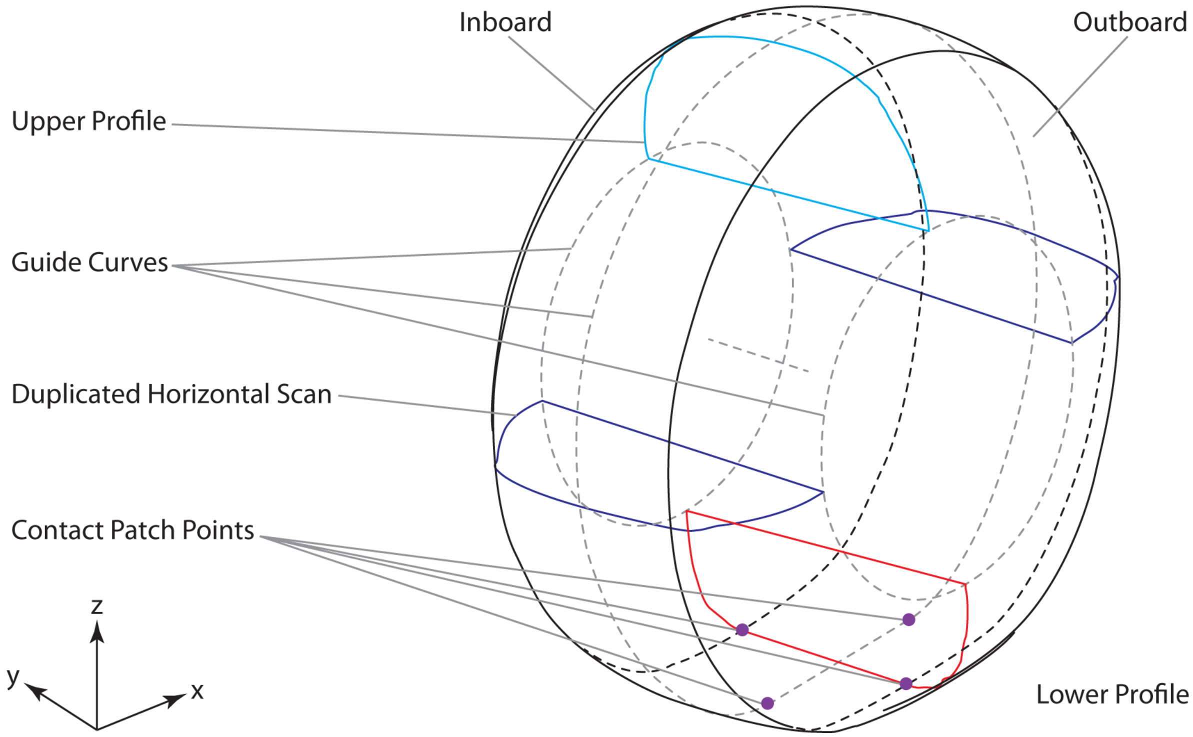

Figure 4.5: *Assembly of scanned tyre sidewall profiles from wind tunnel experiments used to create the CAD model for PowerFLOW simulations.*

Figure 4.6: *Exploded diagram of the internal hub geometry structure used for CFD simulation.*

Several variations exist on this geometry, particularly in the current era of F1. However, this geometry was chosen due to it being a highly generic concept which lies at the centre of all brake cooling flows. Additional brake cooling passages such as those from dividers within the scoop, additional mini-scoops and inlets between the tyre and the barrel face are specific to individual teams and therefore not applicable to a generic study. Most of these are utilised for caliper cooling and that again requires specific knowledge of an individual make and model of caliper. Furthermore, this is the exact geometry taken from the full-car model from which the scoop design and wheel originated. This ensures consistency and validity in the dimensions and aerodynamic synergy between components.

The key questions which were intended to be addressed were: How does the presence of internal geometry differ from a simple restriction at the scoop inlet and is the centrifugal pumping action of the brake rotor superior or inferior to the high loss trajectory of the through-hub flow?

The brake rotor was measured using the standard validation case (Section 4.3) and was tested under stationary and rotating conditions (wheel always rotating). This was to examine the effect of the subtleties of the internal geometry on the global flow-field. The rotation of the disc rotor was applied in the same way as for the wheel spokes. Despite the close proximity of other components and the number of surrounding components, this was achievable without rotating the calliper or brake pads at the same time.

4.3 Validation

As with any computational simulation, there must be some form of validation with known real-world results, ideally with on-track data or at least from a wind tunnel, a tried and trusted methodology. In the absence of this, the plausibility and integrity of the results obtained cannot be quantified. This section outlines the results taken from direct replications of wind tunnel tests in a computational environment. Test cases were selectively chosen for validation so as to sufficiently measure both quantitatively and qualitatively the discrepancies (if any), to trust that the salient flow physics were being captured, and yet small enough to avoid the common route of excessive validation followed by a limited scope of experimentation.

4.3.1 Ansys Fluent

The drag force was used as an initial guide to compare trends with the wind tunnel and to ensure that the correct flow features were being captured. In addition, comparisons of the downstream crossplane (y-z plane) flow-fields with the five-hole probe data were conducted.

The forces show the same decreasing drag trend with increasing through-hub flow as observed in the wind tunnel and previously by Minto [73]. However, the magnitude of the drag coefficient was a consistent 8% to 10% lower than the wind tunnel results. The separation point as denoted by the flow-field results shows a late separation similar to that observed by Mears & Dominy [104]. Given all other turbulence models resulted in later or no appreciable separation, this was deemed suitable enough for the small sweep of through-hub flow experiments.

4.3.2 Exa PowerFLOW

The PowerFLOW experiments utilised the benefits of CFD more so than the Fluent experiments. Where the Fluent experiments were used as a tool for understanding the flow physics around the brake duct conditions applied in the wind tunnel, the PowerFLOW simulations were intended to test a variety of conditions that were not practical in the wind tunnel, due to longevity of equipment, and therefore it was essential that the setup could be trusted before venturing into unknown cases.

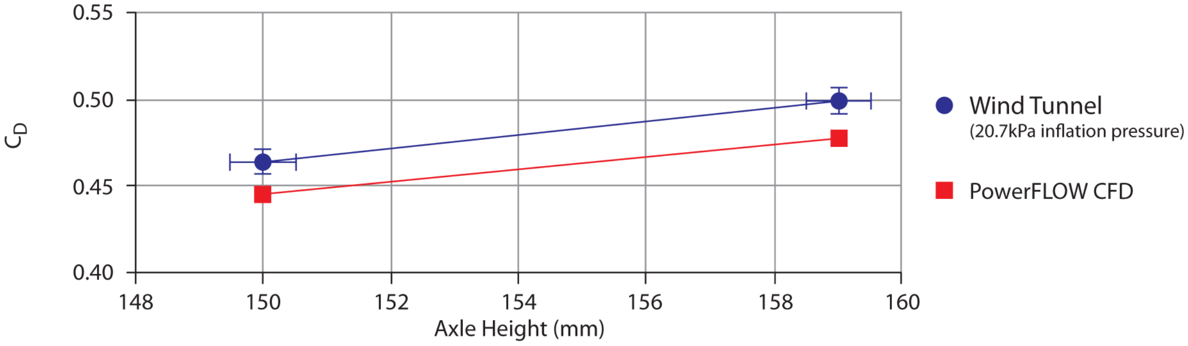

Figure 4.7: *Drag coefficient against axle height for the PowerFLOW validation cases, presented with corresponding wind tunnel tests.*

One case was set as the baseline case for all comparisons, this was the 20.7kPa inflation pressure high deformation (low axle height at 150mm) zero yaw case. The high and low axle height conditions were tested for this inflation pressure at zero yaw, both of which were tested in the wind tunnel and as such the forces and flow-field from these two cases were used to validate the CFD. A summary graph of the drag forces can be seen in Figure 4.7. This shows how the trend of the two cases is matched exactly and the absolute values are between 3% and 4% away from the wind tunnel data.

In comparison to the Fluent simulations, the separation point is much closer to (in fact, exactly) the experimentally measured values by other authors (279° as shown by Figure 4.8). This reduces the artificial strong downwash behind the wheel, from Fluent's separation point nearer 300°, and yields more realistic flow features. The separation agrees with those measured by Fackrell [23] and Mears [3] who measured separation points at 279° as shown by Figure 1.16. In addition to this, the surface static pressure distribution of the baseline case has been presented with that of Mears. The agreement is impressive, especially considering the difference in aspect ratio and measurement techniques. The area in the blue shaded region corresponds to the contact patch region and is therefore not as reliable as the areas outside of this region. Despite this, the high spike and low trough have both been observed. These are much larger than those seen by Mears in the wind tunnel and this is discussed in more depth at the end of Chapter 5.

The flow-field shows the same asymmetrical vortex structure with the inverse 'S' shaped downwash as picked up by the five-hole probe. Figure 4.9 shows the difference between the x/D = 2.0 crossplane (y-z orientation) for the baseline case at 150mm axle height with a 20.7kPa (3.0psi) inflation pressure. The plots show that the CFD has accurately predicted the same features although the pressures of the primary vortex cores are lower than measured experimentally. There is a region of higher pressure around the upper inboard shoulder of the tyre too. The velocity vectors illustrating the difference in velocity show a higher turnover rate for the vortices, implying strengthened features from both the vectors and the lower pressure cores. This is likely to make the features more persistent in the wake. Despite this emphasis of already known features, the primary characteristics have been captured without extra flow-structures developing. The features are also of similar size and form.

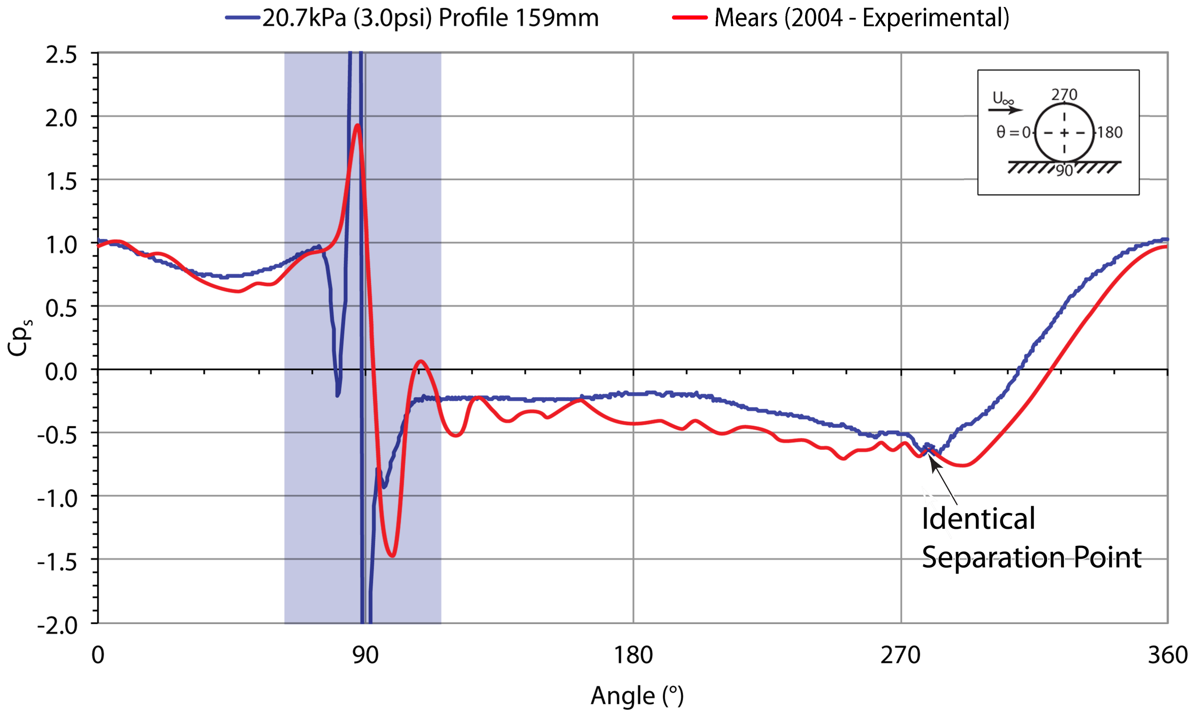

Figure 4.8: *Surface static pressure distributions around the centreline of the baseline case. Overlaid graph of Mears [3].*

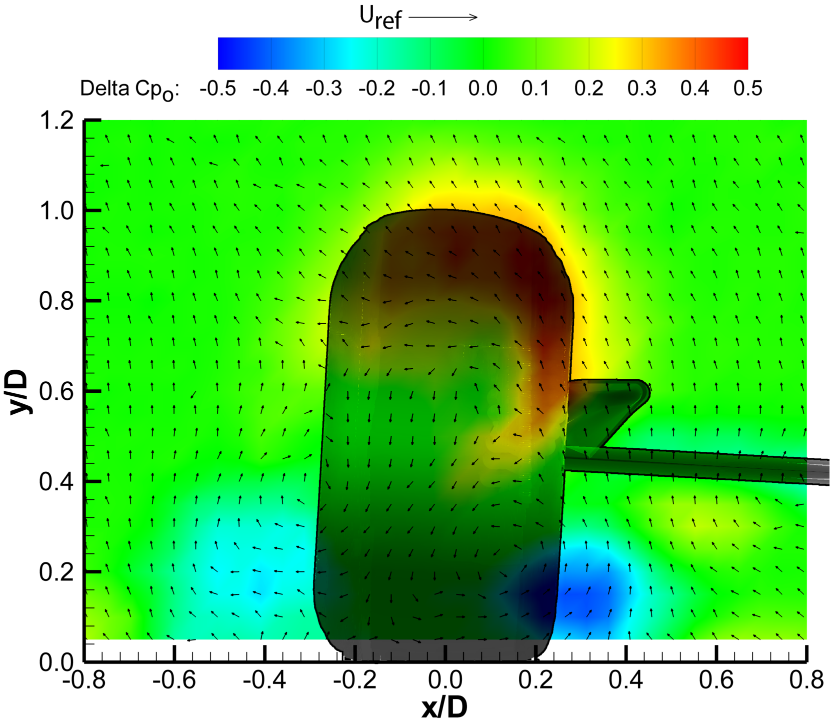

Figure 4.9: *Delta plot of the y-z crossplane at x/D = 2.0: CFD - Wind Tunnel Probe Data.*

Figure 4.10 shows the surface streamlines of the scoop coloured by velocity. The figure also displays the two wind tunnel flow visualisation results from Chapter 3. The flow-field is very similar in both cases but can be described as being a half-way compromise of both hub-flow conditions. The HFN_c value measured for a fully open duct in CFD was 0.0156 (compared to $HFN_c = 0.0288$ in the wind tunnel case, a discrepancy of around 45%) which shows there is a lot more restriction to internal flows in the PowerFLOW simulations leading to an exaggerated spillage effect and therefore more cross-scoop vectors than would be expected for a fully open case. Reassuringly, this hub-flow number is almost exactly that of the middle case tested in the wind tunnel (Section 5.1) and therefore a half way flow-field is to be expected. Despite the discrepancy, the hub-flow number is well within the expected region of through-hub flow rates for a realistic car.

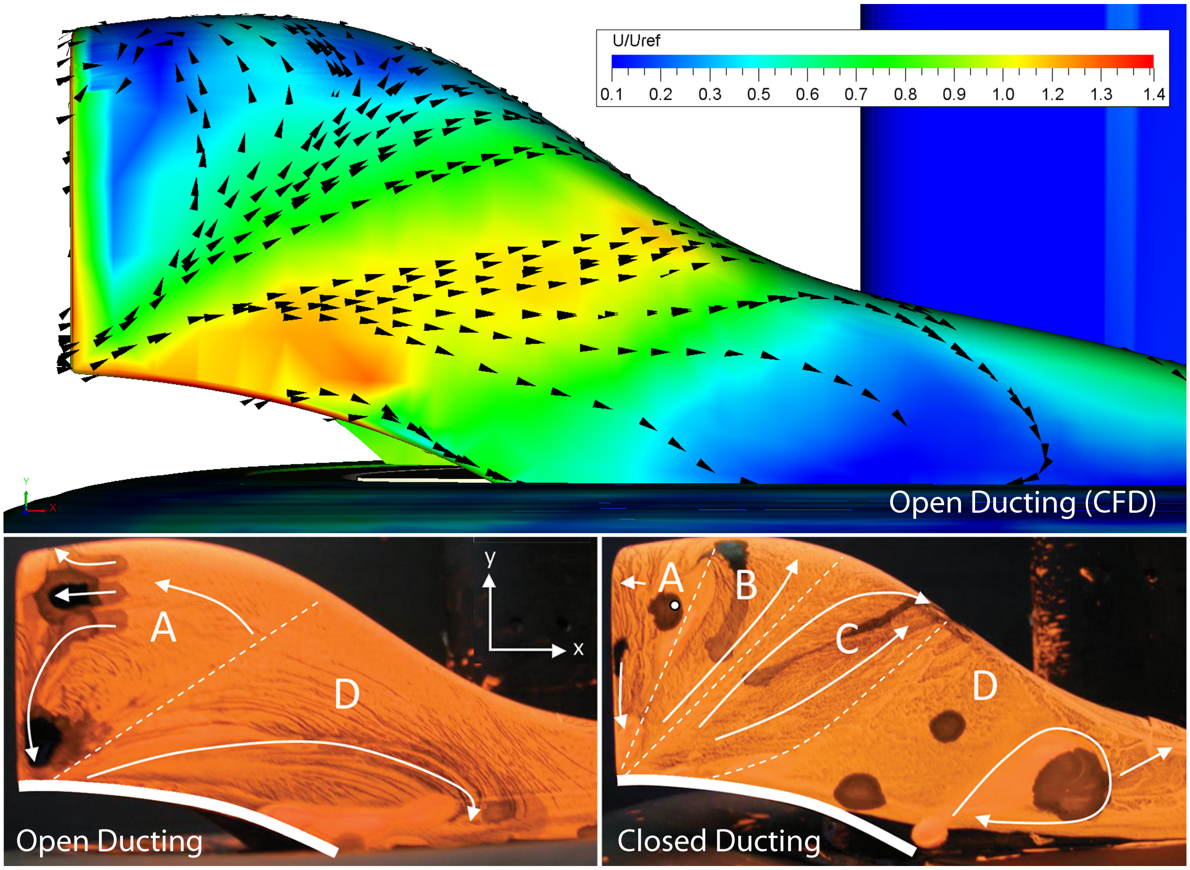

Figure 4.10: *CFD Validation of scoop flow characteristics. PowerFLOW baseline test compared with wind tunnel surface flow visualisation experiment.*

This gives confidence that the simulation did accurately detect the key flow features, both globally and locally. As a result, full yaw sweep and internal geometry studies could be performed and trusted.

Chapter 5

Results and Discussion - CFD

Whilst CFD methodologies are not often considered as credible as traditional wind tunnel techniques for producing absolute figures, their improved accuracy over time has led to tools which allow details of the flow-field to be extracted and for trends to be accurately predicted. There is also the undeniable benefit in the use of these techniques in being able to interrogate the entire flow-field, including inaccessible regions such as inside a wheel, without significant probe interference.

As Bienz et al. [110] stated almost a decade ago, “It is not likely that these advanced CFD simulations will, in the near future, reduce the amount of hours spent in the wind tunnel. But indisputably, CFD helps to improve wind tunnel testing productivity”. This is indeed a good philosophy.

It is the purpose of this chapter to present the results obtained using the CFD methodologies outlined in Chapter 4. The individual details, motivation for the experiments and detailed breakdown of the figures are all presented here. The simulations carried out have all been inspired by the results presented in Chapter 3 and are intended to both further the knowledge of aerodynamic sensitivities as well as the understanding of the source of previously discovered trends. For a more global discussion of the results the reader is directed to Chapter 6 which draws together the findings from both of the results chapters in order to extract the finer details and conclusions from the data.

5.1 Rigid Tyre - Through-Hub Flow (Ansys Fluent)

The simulations for the rigid tyre with standard brake scoop and simplified internal geometry are presented here. The simple CAD geometry, such as the hub, inboard disc (suspension upright - not to be confused with an internal brake rotor) and even the rim and the tyre itself were produced using measurements taken directly from the wind tunnel models. The more complex geometry of the brake scoop was taken directly from the source file used to produce the printed 3D part for the experimental work. Finally, the full sting was also included in this geometry.

For a detailed breakdown of the domain size, simulation setup parameters and mesh generation, the reader is referred to Chapter 4.

5.1.1 Hub-Flow Number (HFN) Correction

A virtual probe was situated in the same location as in the experimental work and measured x-velocity in order to be used as a calibration for the wind tunnel data (Section 3.1.1). A plane was then created inside the rim to measure the mass-flow and calculate the average through-hub velocity. The ratio between these two values was then calculated and the resulting value used in the hub-flow number correction as seen in Figure 3.1 onwards (Chapter 3). The nature of the open sided duct allows a higher velocity to be present in the scoop compared to the internal hub. This is due to the effect of spillage allowing part of the mass-flow that has entered the scoop, and registered as a high velocity on the probe, to then proceed without traversing the complex internal path. In order for the true through-hub value to be observed, the ratio between the through-hub velocity (constrained to zero in CFD) and the scoop intake velocity was applied to the measurements in the wind tunnel data thus creating a true zero hub-flow number for the fully blocked case and a more accurate overall range.

The through-hub flow rates from the experimental data were then reproduced by means of a porous medium at the interface between the disc upright and the scoop. This allowed the matching of the scoop velocity as observed in the wind tunnel and the total reproduction of the experimental setup in the simulation domain. The parameters set for the porous media are available in Table 5.1.

Table 5.1: *Fluent CFD simulation scoop to hub interface parameters to match experimental hub-flow numbers.*

Condition	Scoop-Hub Boundary	Permeability ($\times 10^2$ m^{-1})	Pressure Jump ($\times 10^{-4}$ m^2)	HFN_c
Fully Closed	Wall	N/A	N/A	0.000
3 Meshes	Porous Medium	9.5	-5.0	0.010
2 Meshes	Porous Medium	9.5	-3.0	0.012
1 Mesh	Porous Medium	9.5	-1.5	0.018
Fully Open	Internal Wall	N/A	N/A	0.024

5.1.2 Aerodynamic Drag Measurements

The equivalent drag force measurements as shown experimentally in Figure 3.1 were extracted from the simulations and are presented here in Figure 5.1. Due to the offset in drag produced by the simulation technique, an under-prediction of approximately 11% when compared to the experimental wind tunnel data, a delta plot (constraining the lowest HFN_c value, and its corresponding drag measurement, to zero) has been produced (Figure 5.2) to show the accuracy of the trend. This is confirmation that the correct flow features were being captured if not the absolute values.

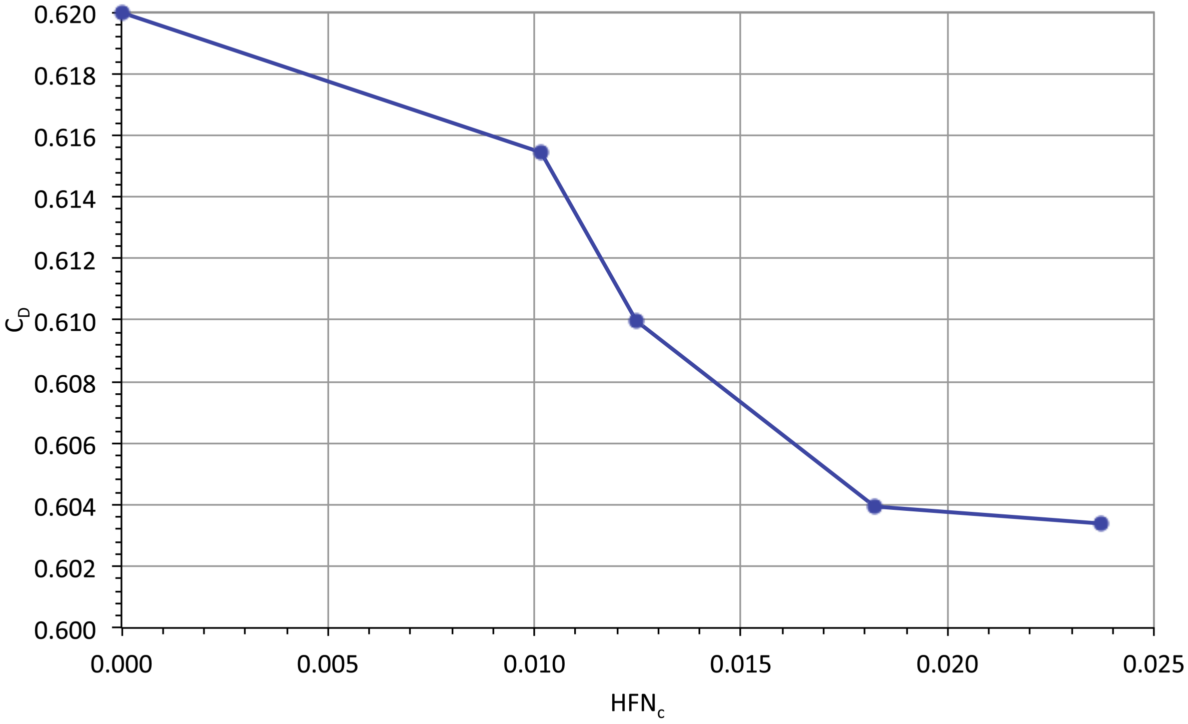

Figure 5.1: *CFD simulation aerodynamic axial drag measurements for the baseline scoop geometry against varying through-hub flow.*

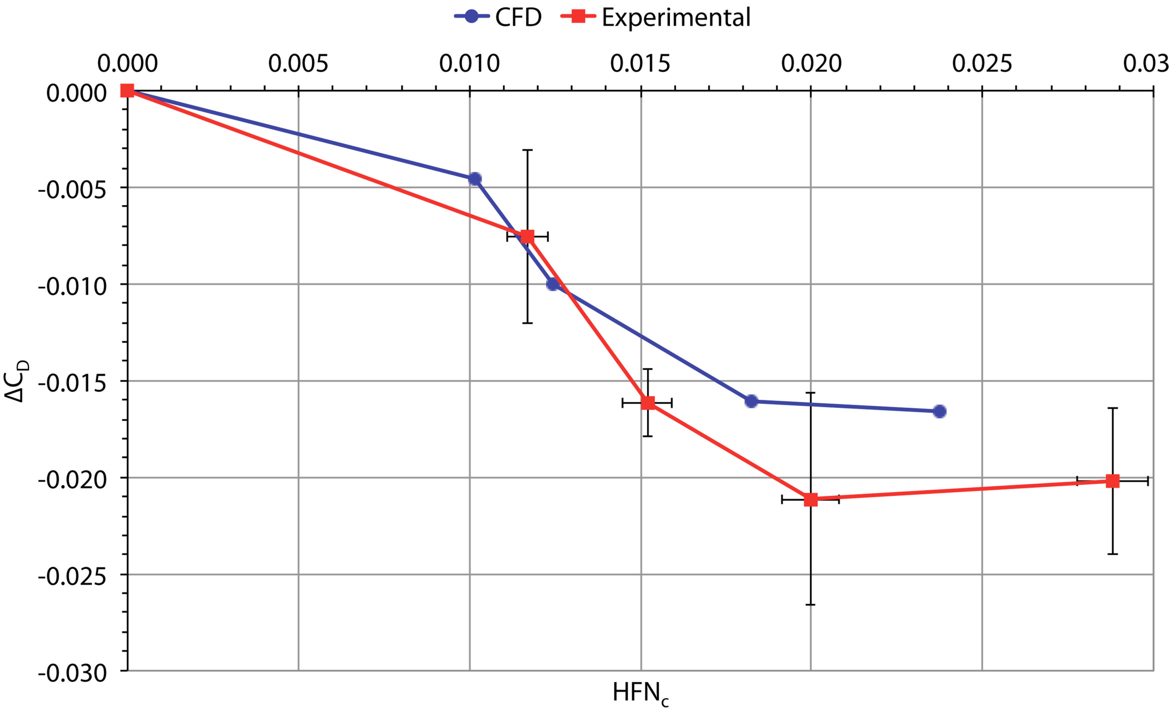

Figure 5.2: *Axial drag measurement comparison for the baseline scoop geometry against varying through-hub flow. Experimental data against CFD simulation.*

The range tested, as outlined by the porous media parameters in Table 5.1, shows a good spread of HFN_c values similar to those observed experimentally. However, the biggest discrepancy arises from the case with a fully open duct ('internal' wall condition). This has produced a through-hub flow rate of 83% of the largest value observed in the wind tunnel which was already noted to be around 75% of the total freestream velocity at the empirical probe location. What this suggests is that the CFD simulations are much less inclined to allow through-hub flow than the physical model. This apparent phenomenon in the Fluent simulation is consistent with the observation already made in the PowerFLOW validation at the end of the previous chapter.

Observing the relative values in Figure 5.2, the drag trend is very similar to the wind tunnel. The overall reduction in drag with increased hub-flow number has been observed with the most rapid change between the three intermediate data points. Mostly, the simulation data lie within the uncertainty of the experimental data. This agreement gives credence to a study into aerodynamic lift and local flow-features around the scoop.

5.1.3 Aerodynamic Lift Measurements

Unlike the experimental measurements, the CFD technique does not require a mechanical tare and in fact all mechanical characteristics are eliminated. This enables the lift force to be extracted for the equivalent experimental setup. These lift values are plotted in Figure 5.3.

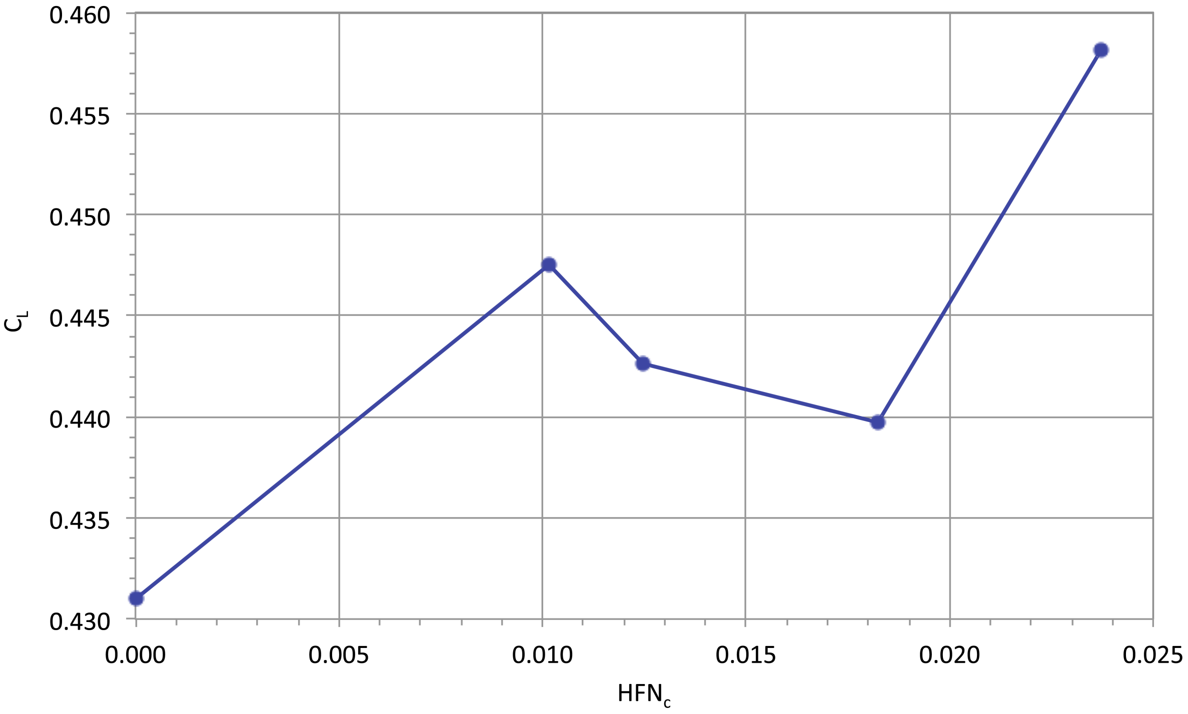

Figure 5.3: *CFD simulation aerodynamic lift measurements for the baseline scoop geometry against varying through-hub flow.*

It can be seen at first that the approximate magnitude of the lift force is similar to the drag force, being around 75% in terms of C_L. Whilst this seems significant in the context of an F1 car, the proportion of the overall vehicle force is much smaller than for the drag.

The overall change between closed and open cases results in an increase in positive lift by 6.3%. This is more significant than the change in aerodynamic drag over the same range which was recorded experimentally to be a reduction of 2.9%, and 2.7% in these CFD simulations. At intermediate hub-flow numbers there is a drop in the lift force which suggests either that the flow physics undergo a transition throughout the range or the lift force is less reliable than the drag force in CFD.

Using the description of the flow physics determined by the experimental drag investigations, and the observations on the local flow through and around the scoop, it is not a surprise that the lift of the wheel has increased at extremes of HFN_c. Whilst the aerodynamic drag is affected by the global wake as well as the local effects, lift is less sensitive to the former (such as downstream wake). Therefore, given the relatively large plan-view area of the scoop compared to the whole model, any attached and accelerated flow on the upper surface will lead to an increased lift force. In the case where the duct is fully closed and therefore allows a large spillage separation, the static pressure on the upper surface of the scoop will be increased.

It is not unknown for separation zones and recirculation bubbles to reattach, and given the unsteady nature of the wake, it is not unreasonable to assume that the already proven sensitive nature of the scoop design will lead to unpredictable behaviour in the intermediate hub-flow region.

5.1.4 Local Flow-Field Observations

These results demonstrate evidence of the accurate capture of the local flow-physics around the scoop and through the hub of the simplified internal geometry as used in the wind tunnel. Figure 5.4 shows the equivalent of the PIV measurements in Figure 3.2 but without the loss of data from laser shadowing.

For the fully open ducting (Figure 5.4a), the dashed line represents the flow which enters the scoop and flows through the hub, exiting slightly higher on the outboard side. This is consistent with the probe crossplanes from Chapter 3 (Figure 3.2). The lower solid black line shows evidence of spillage on the lower edge of the scoop. This was assumed but not conclusively observed experimentally due to laser shadowing from the sting. The combination of aerodynamic models to explain the form of the negative drag trend (Figure 3.14) did indeed suggest that spillage drag still had a significant contribution even for a fully open duct. The streamlines to the right of Figure 5.4 are visible proof of that fact.

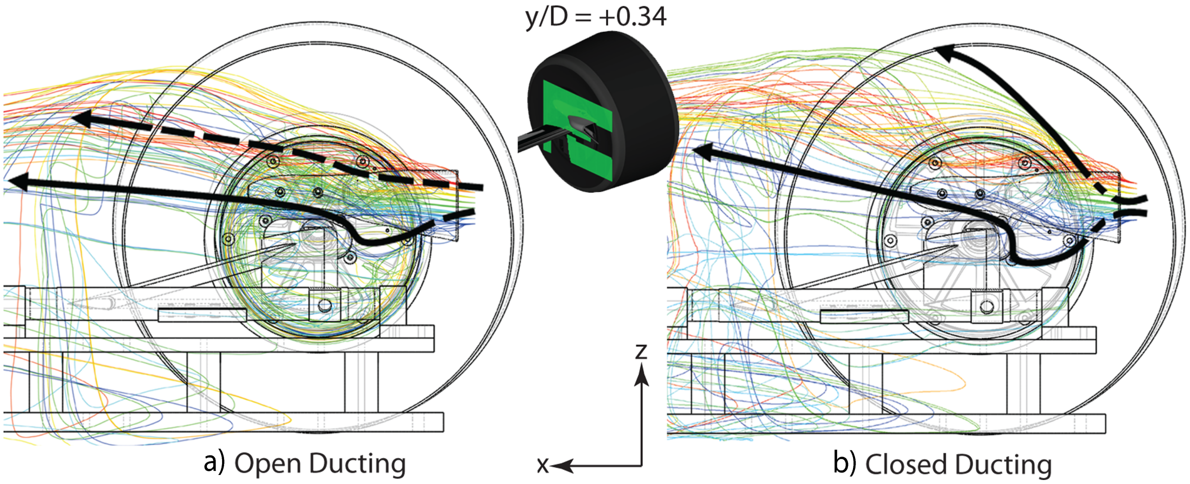

Figure 5.4: *CFD simulation flow-field showing streamlines of the $y/D = +0.34$ plane scoop behaviour for fully open to fully closed ducting (c.f. PIV measurements in Figure 3.2).*

For the closed case the separation shows further proof of the spillage on the upper lip. The most extreme streamline has been highlighted in Figure 5.4 to emphasise the extent of the separation, although the experimental surface flow has suggested reattachment at some point downstream of the scoop and this is shown by the red streamlines on the right-hand side of the figure.

An additional observation from this flow-field investigation is that the lower separation has a significant effect on the relative attack angle of the otherwise neutral sting. The fully open ducting shows a relatively small deviation although not perfect attachment over the sting. The closed ducting shows a much more extreme attack angle which results in a large wake behind the sting.

5.2 Deformable Tyre Profiles - Yaw Study (Exa PowerFLOW)

In order to expand upon the experimental yaw study presented in Chapter 3, CFD simulations were carried out to investigate any significant flow features and trends which could not be observed in the wind tunnel and also to help to understand those already presented. A range of techniques have been used to quantify the force changes and to visualise the changes in the flow-field. Tables of forces are accompanied by comparative line drawings of the geometry, with iso-surface plots of $Cp_o < 0.3$ to visualise the shape and form of the wake. Horizontal and crossplane orientation flow-fields have been presented in order to coincide with the same measurement areas the empirical data in Chapter 3.

In order to get the most out of the CFD simulation data, of which there are many, each case has been assigned a reference case known as a ‘baseline’. By doing this, the most logical comparison has been plotted alongside most of the flow-field figures and forces. Although in some cases there are multiple cases to compare to, this assists the ‘at a glance’ appreciation of the results and allows better visualisation of the conclusions made.

The tyre profiles used in this study were measured from the geometrical scans presented in Chapter 3 and the methodology of the translation into 3D CAD has been covered in Chapter 4. All profiles used here belonged to the higher inflation pressure (20.7kPa, 3.0psi), as it has been concluded that although the changes are effectively limited to local effects, in relation to the change in inflation pressure, the higher pressures are more realistic to the geometry found on-track. CFD was used for this investigation due to the advantage of having no limitations in terms of the longevity of the equipment in CFD based upon testing parameters.

5.2.1 Overview of Simulations

A summary of the simulations carried out can be found in Table 5.2. A brief description of each case has been given and a reference to the page to the simulation's first appearance has been given. In many cases, it will be necessary to look back at other figures in order to see differences in the flow-field. This table should therefore be used as a reference throughout this section.

Table 5.2: *List of CFD simulations for PowerFLOW yaw sweeps. Summary of profile used and which case is used as its baseline for flow-field and aerodynamic force comparison.*

Case	Page	Axle Height (mm)	Yaw (°)	Baseline	Description
1	170	150	0	N/A	Geometry as in Wind Tunnel Case
2	174	159	0	1	Geometry as in Wind Tunnel Case
3	178	150	0	1	No Sting
4	182	150	+5	1	Experimentally Measured +5° Profile
5	186	150	+5	4	Non-Yawed Profile at +5° Yaw
6	190	150	+5	4	Glycerol Profile
7	194	159	+5	2	Experimentally Measured +5° Profile
8	198	159	+5	7	Non-Yawed Profile at +5° Yaw
9	201	150	-5	1	Experimentally Measured -5° Profile
10	205	150	-5	9	Non-Yawed Profile at -5° Yaw
11	209	159	-5	2	Experimentally Measured -5° Profile
12	213	159	-5	11	Non-Yawed Profile at -5° Yaw

5.2.2 Case 1 - 150mm Axle, 0° Yaw

Case 1 makes use of one of the most commonly used experimental configurations. The PowerFLOW simulation performed here was used as a validation experiment as well as to be used as a baseline for further investigations in order to quantitatively explore the differences in flow-fields and forces.

Table 5.3: *Yaw simulation detail: Case 1 geometry schematic and forces (absolute & baseline deltas).*

<table>
<tr><td colspan="2">Case: 1</td><td>Axle Height: 150mm</td><td>Yaw (β): 0°</td><td rowspan="4">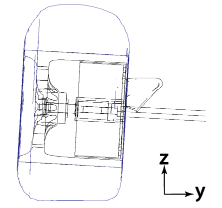 </td></tr>
<tr><td colspan="2">Description:
Geometry as in Wind Tunnel Case</td><td colspan="2">Baseline Case: N/A</td></tr>
<tr><td colspan="2">Aerodynamic Forces:</td><td colspan="2">(Case - Baseline) Force Deltas:</td></tr>
<tr><td>$C_{D,axial} = 0.450$</td><td>$C_L = 0.466$</td><td>$\Delta C_{D,axial} = 0.000$</td><td>$\Delta C_L = 0.000$</td></tr>
</table>

Table 5.4: *Aerodynamic force breakdown (absolute and baseline deltas) of yaw simulation Case 1.*

Component	**Absolute Forces**			**(Case - Baseline) Force Deltas**		
	$C_{D,axial}$	C_{side}	C_L	$\Delta C_{D,axial}$	ΔC_{side}	ΔC_L
Wheel (Rim and Tyre)	0.422	0.041	0.459	0.000	0.000	0.000
Brake Scoop	0.034	0.095	0.002	0.000	0.000	0.000
Barrel / Shroud	-0.011	-0.100	0.010	0.000	0.000	0.000
Hub	0.004	-0.028	0.000	0.000	0.000	0.000
Inboard Disc (Upright)	0.002	0.087	-0.005	0.000	0.000	0.000
Wheel Nut	0.000	-0.006	0.000	0.000	0.000	0.000

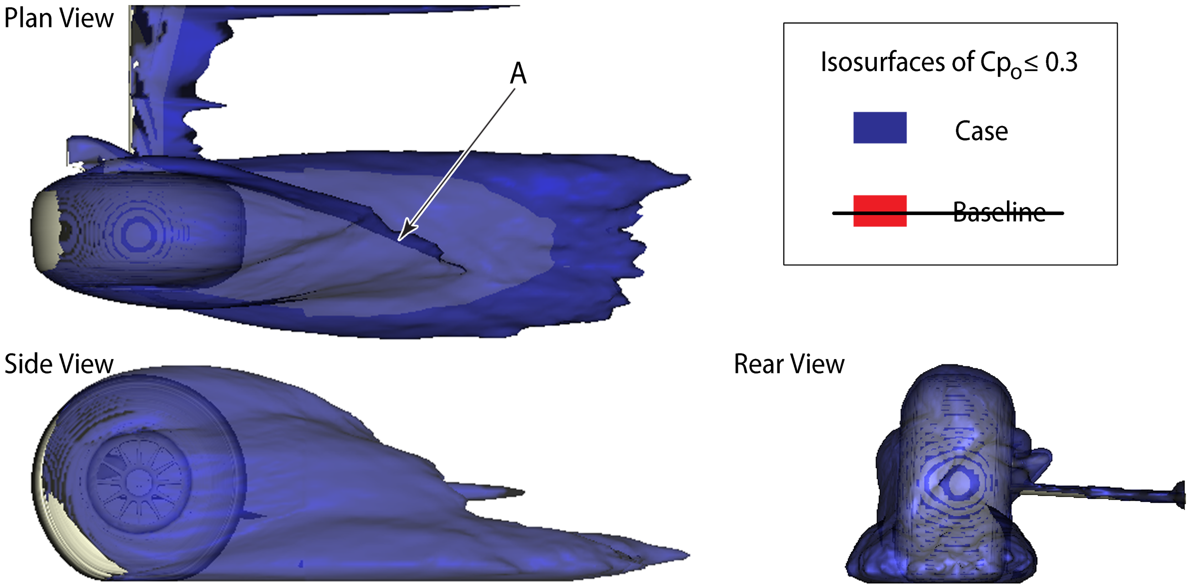

Figure 5.5: *Isosurface plots of $Cp_o \leq 0.3$, comparing Case 1 (blue) with its associated baseline (red).*

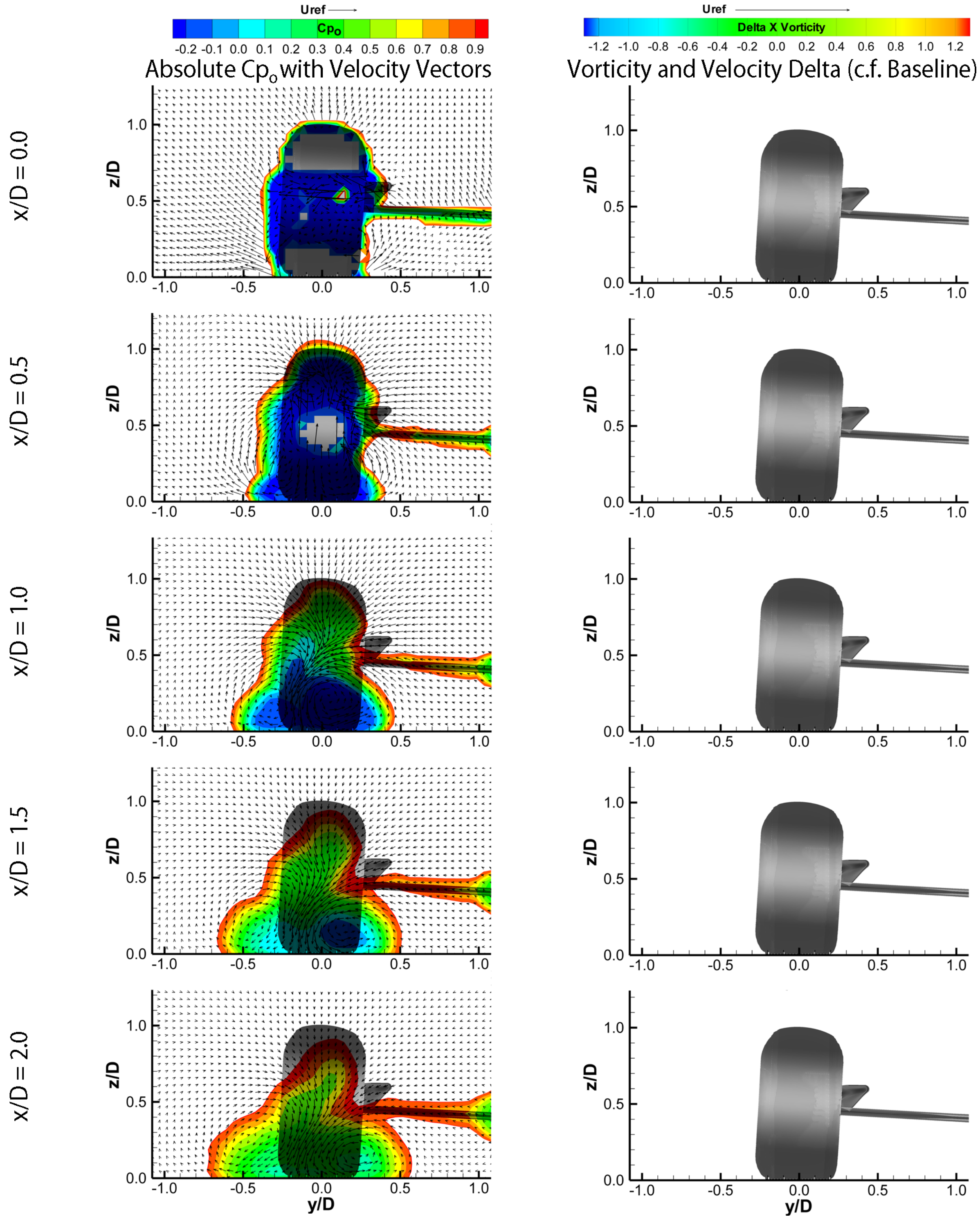

Figure 5.6: *Case 1: Y-Z crossplanes of: Absolute stagnation pressure and velocity vectors (left); Vorticity and velocity vector baseline deltas (right).*

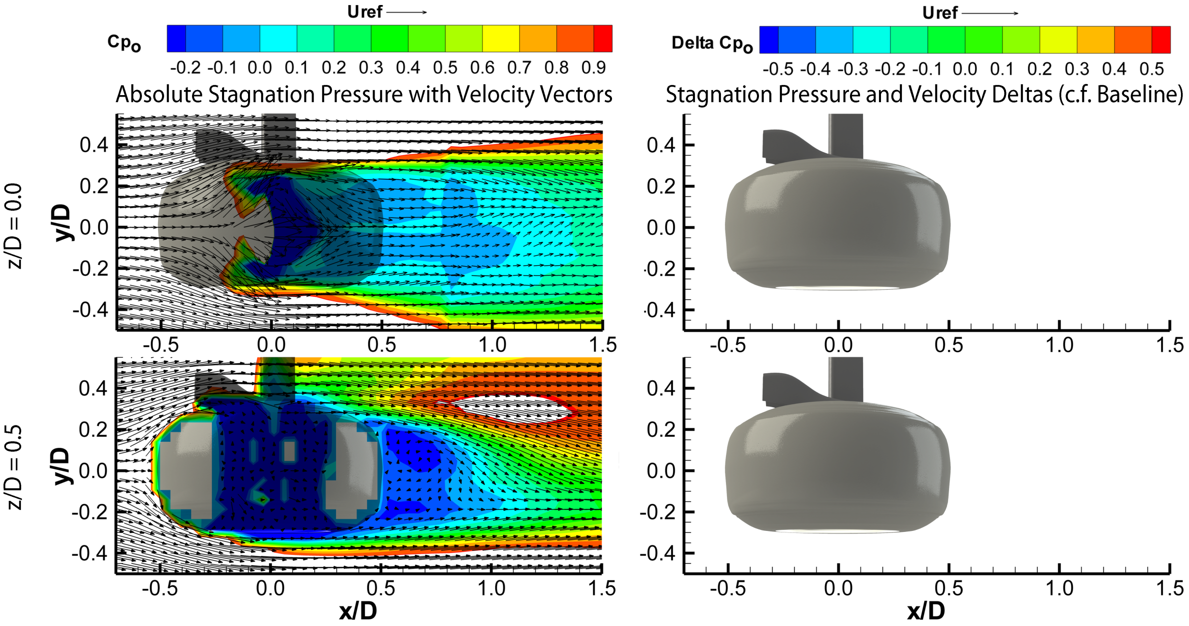

Figure 5.7: *Case 1: X-Y horizontal planes of stagnation pressure with velocity vectors. Absolute values (left) and baseline deltas (right).*

As the global baseline case there are no comparisons to be made. Instead, a detailed description of the forces and flow features will be discussed here.

Table 5.3 summarises the salient details of the simulation along with a y-z cut through of the geometry tested (right-hand side of table). Here this is simply a single case, whereas the future cases show (in red) the baseline geometry to which the simulation was compared to.

Table 5.4 shows a detailed breakdown of the component forces. For consistency with later tables comparing various test cases with this datum, the differences are also shown to indicate which of the components are more sensitive to the change observed in each case. For this baseline case, these differences are all zero. The scoop drag is around 8% of the total drag of the assembly and indeed internal components have a small contribution too, due in-part to the through-hub flow not being evenly distributed with simplified internals. In terms of lift, almost 100% of the total is due to the external components of the rim and tyre, with a negligible amount on the scoop.

The iso-surface plots (Figure 5.5) show an encapsulated wake with a threshold of $Cp_o < 0.3$. This number was chosen in order to capture the general structure of the wake, showing areas of low pressure and ultimately infers flow features such as vortices which are contained within this surface. The flow vectors presented in Figure 5.6 reveal quantitatively the vorticity aspect of the flow-field.

The iso-surfaces in Figure 5.5 show a wake which is fairly symmetrical, on the lower sections at least. Towards the upper wake, the features from the upper shoulders are washed outboard (highlighted by the letter ‘A’) and this is confirmed by the clockwise (relative to the figure) feature shown by the bottom left of Figure 5.7 (horizontal x-y plane at axle height). This feature is in agreement with the observations in the PIV in Chapter 3 (Figure 3.34).

The horizontal planes in Figure 5.7 show the near-ground level flow-field (at 2mm off the surface, labelled as z/D = 0.0) on the top row and the axle height flow-field on the bottom. The through-hub flow evident from the axle-height figure shows an area of extremely low velocity which is rather unsteady in nature and there is not much evidence of external influence upon its exit. The ground level shows some interesting features whereby the shape of the wake is biased towards the outboard side of the wheel. There is an area of extremely low pressure behind the contact patch and high pressure directly in front. This is expected given the surface static pressure distributions of Fackrell [23], Mears [3] and Hinson [32] among others. The delta plot on future cases (case-specific values from the baseline equivalents), at the top right of the figure, is a valuable figure to assess the relative sizes of the contact patch pressures and therefore give an insight as to the behaviour of the flow around the contact patch, ultimately affecting the lift directly and the wake development indirectly.

The wake development, as evident in Figure 5.6 agrees very well with the probe and PIV work of Chapter 3 for this geometry. The reverse ‘S’ shaped downwash with an oversized inboard vortex feature, which dominates the flow-field is exactly as observed by the aforementioned methods. The strength of the feature is evident in the fact that it does not appear to decay even by two diameters downstream. The outboard vortex, although small, is strong in nature and as it decays downstream it becomes larger and less aggressive, matching the size of the inboard feature. These two vortices are the dominant features of the wheel wake and the location and behaviour of these two features is used to qualitatively describe changes to the flow-field throughout this section.

5.2.3 Case 2 - 159mm Axle, 0° Yaw

Case 2 makes use of the second of the most commonly used experimental configurations (higher axle height signifying lower levels of deformation). The PowerFLOW simulation performed here was used as a validation experiment as well as to quantitatively explore the differences in flow-fields and forces.

Table 5.5: *Yaw simulation detail: Case 2 geometry schematic and forces (absolute & baseline deltas).*

<table>
<tr><td colspan="2">Case: 2</td><td colspan="2">Axle Height: 159mm</td><td>Yaw (β): 0°</td><td rowspan="4">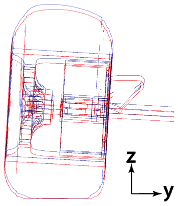 </td></tr>
<tr><td colspan="2">Description:
Geometry as in Wind Tunnel Case</td><td colspan="3">Baseline Case: 1</td></tr>
<tr><td colspan="2">Aerodynamic Forces:</td><td colspan="3">(Case - Baseline) Force Deltas:</td></tr>
<tr><td>$C_{D,axial}$ = 0.482</td><td>C_L = 0.390</td><td colspan="2">$\Delta C_{D,axial}$ = +0.032</td><td>ΔC_L = -0.076</td></tr>
</table>

Table 5.6: *Aerodynamic force breakdown (absolute and baseline deltas) of yaw simulation Case 2.*

Component	Absolute Forces			(Case - Baseline) Force Deltas		
	$C_{D,axial}$	C_{side}	C_L	$\Delta C_{D,axial}$	ΔC_{side}	ΔC_L
Wheel (Rim and Tyre)	0.446	-0.014	0.383	+0.023	-0.056	-0.076
Brake Scoop	0.037	0.101	0.008	+0.004	+0.006	+0.006
Barrel / Shroud	-0.010	-0.069	0.010	+0.001	+0.030	-0.001
Hub	0.009	-0.089	-0.003	+0.005	-0.061	-0.003
Inboard Disc (Upright)	0.001	0.114	-0.007	-0.001	+0.027	-0.002
Wheel Nut	0.000	-0.003	0.000	0.000	+0.003	0.000

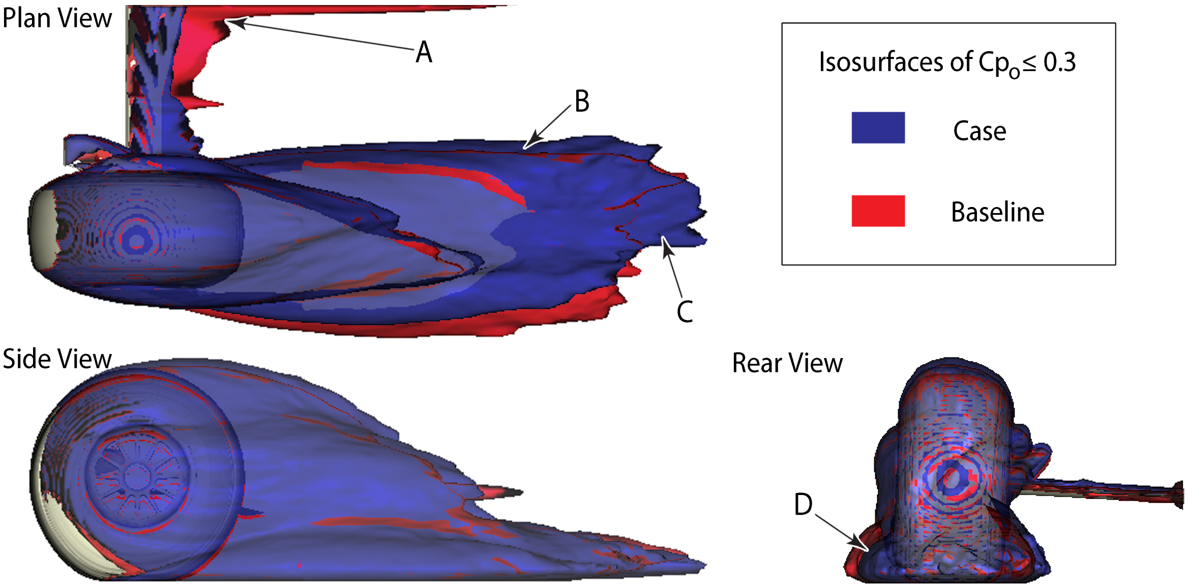

Figure 5.8: *Isosurface plots of* $Cp_o \leq 0.3$*, comparing Case 2 (blue) with its associated baseline (red).*

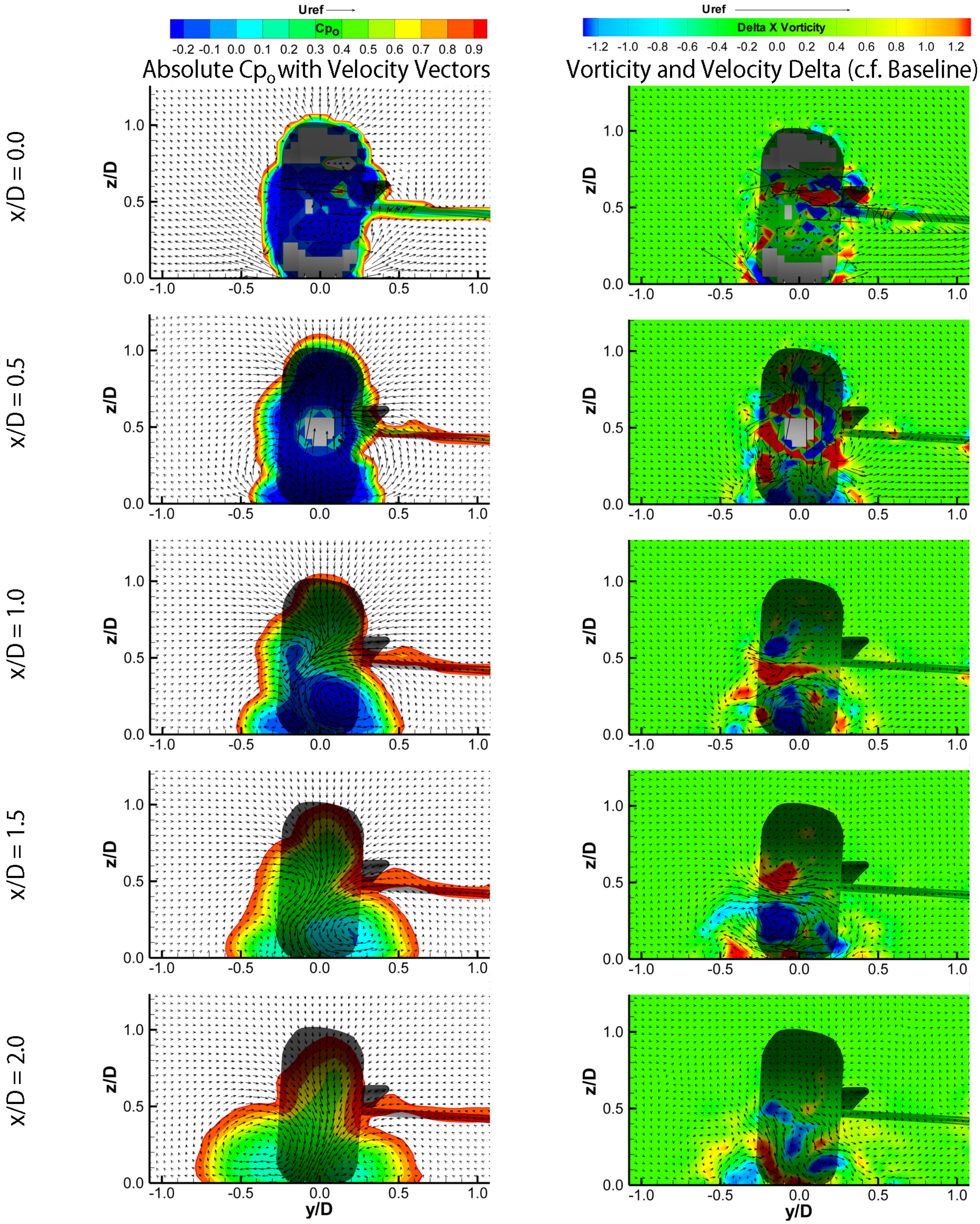

Figure 5.9: *Case 2: Y-Z crossplanes of: Absolute stagnation pressure and velocity vectors (left); Vorticity and velocity vector baseline deltas (right).*

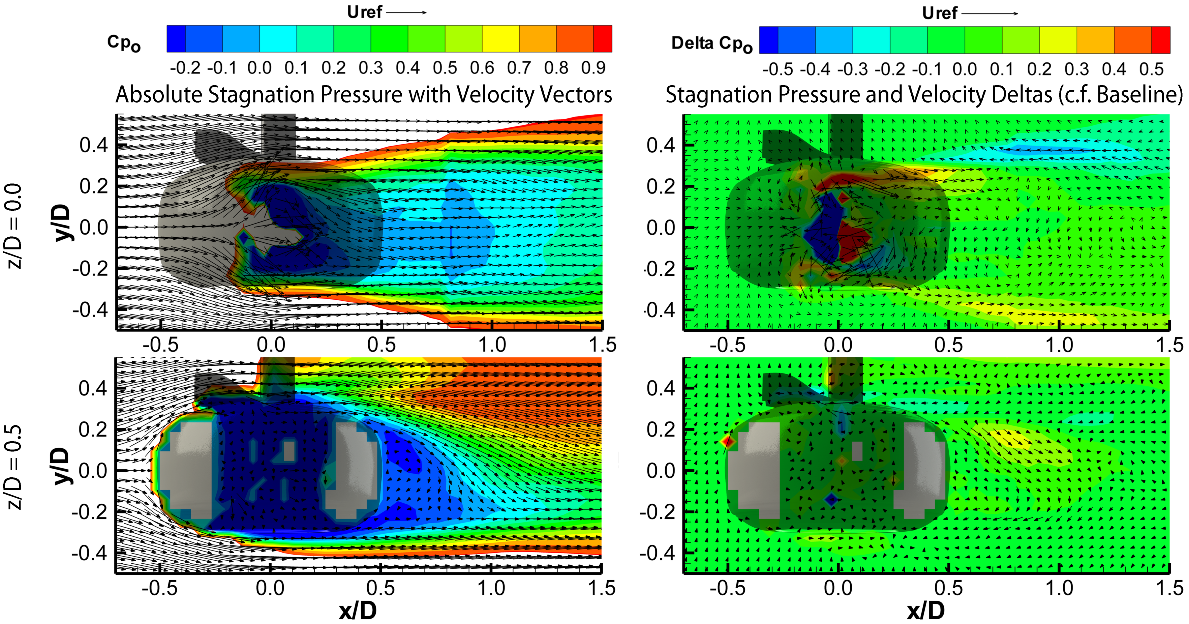

Figure 5.10: *Case 2: X-Y horizontal planes of stagnation pressure with velocity vectors. Absolute values (left) and baseline deltas (right).*

The forces as summarised in Table 5.5 show the increase in drag and decrease of lift by 32 and 76 counts respectively. Observing the breakdown of the force deltas to the baseline that are presented in Table 5.6, it is apparent that over two thirds of the drag change is due to the external flow features of the tyre and rim. The remainder is split evenly between the brake scoop and the internal hub features. The lift change of the rim and tyre is entirely responsible for the overall force trend. The scoop has also shown an increase in lift of 6 counts but reductions caused by the internal components cancel this out. It is assumed that the higher axle height has led to a smaller ground effect from the sting which has reduced the suction underneath the scoop, which is thought to be present due to the negligible absolute value of the scoop lift. By this, the scoop is a bluff body and would be generally expected to develop positive lift given the onset flow conditions. In the event that the lift contribution was small overall, which is the case, there is clearly another effect taking place which neutralises this. Indeed, the considerably smaller wake of the sting has been observed in the iso-surface plots in Figure 5.8 (A). Care must be taken when observing this figure as although the wake is smaller, it appears to not be present at all for case 2 (blue). The red case, representing Case 1 (the baseline) is dominant and has entirely enclosed this iso-surface.

The iso-surface plots show a wake which is biased towards the inboard side of the geometry (B), although similar in size and nature (C). The outboard feature is shown to have reduced in size (D) as well as being moved inboard with the rest of the wake. Flow feature changes such as these can have a dramatic impact upon the aerodynamic performance of downstream surfaces. These changes represent the wake changes likely to be seen when accelerating from a corner exit up to a braking zone and display a gradual inboard movement. Given the design of the car requires aerodynamic features such as those in the front wheel wake to steer clear of the downstream components, testing wheels at one axle height could be costly in terms of high-speed performance.

Unlike the wake captured by the probe in the experimental measurements, the overall wake height appears to follow the height of the tyre and does not suggest earlier separation for the lower axle height. This is visualised in both the iso-surface plots and the crossplanes in Figure 5.9.

Although the axle height change in itself is a relatively small one there is a disproportionate change in the wake. The outboard feature of the wake is far more intense to begin with and develops to be larger than the inboard feature, which was dominant for the baseline case. The inboard feature has become more elliptical in nature and indeed the vorticity delta plots show patches of blue on both the inboard and outboard features. These patches suggest the strengthening of the outboard feature, which appears to develop very late, and the retardation or weakening of the inboard feature.

The geometrical change that was observed by raising the axle height suggested the exposure of the sidewall to tread step on the outboard and the wind tunnel flow-field data show this strengthened outboard feature as well.

In studying the horizontal planes in Figure 5.10, the initial appearance shows that this case is very similar to its baseline. The top right image, representing the difference between the stagnation pressure and velocity vectors with the baseline show what appear to be two linear jets emanating from the inboard and outboard contact patch. These are in fact areas of higher and lower pressure as a result of the entire wake moving inboard and due to their equal size, it suggests that the width of the wake has not been affected. At the axle height plane there is little difference between the stagnation pressure fields. However, the vectors show evidence of a stronger recirculation.

5.2.4 Case 3 - 150mm Axle, 0° Yaw (No Sting)

Case 3 is built from Case 1, the baseline case, by removing the support sting. Although this configuration could never exist in reality, the flow-field changes are significant to understanding the sensitivity to inboard components for improved vehicle design.

Table 5.7: *Yaw simulation detail: Case 3 geometry schematic and forces (absolute & baseline deltas).*

<table>
<tr><td colspan="2">Case: 3</td><td>Axle Height: 150mm</td><td>Yaw (β): 0°</td><td rowspan="4">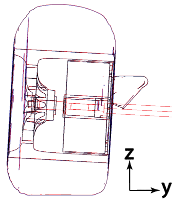 </td></tr>
<tr><td colspan="2">Description:
No Support Sting</td><td colspan="2">Baseline Case: 1</td></tr>
<tr><td colspan="2">Aerodynamic Forces:</td><td colspan="2">(Case - Baseline) Force Deltas:</td></tr>
<tr><td>$C_{D,axial} = 0.489$</td><td>$C_L = 0.468$</td><td>$\Delta C_{D,axial} = +0.039$</td><td>$\Delta C_L = +0.002$</td></tr>
</table>

Table 5.8: *Aerodynamic force breakdown (absolute and baseline deltas) of yaw simulation Case 3.*

Component	Absolute Forces			(Case - Baseline) Force Deltas		
	$C_{D,axial}$	C_{side}	C_L	$\Delta C_{D,axial}$	ΔC_{side}	ΔC_L
Wheel (Rim and Tyre)	0.456	0.054	0.458	+0.034	+0.013	0.000
Brake Scoop	0.038	0.104	0.005	+0.005	+0.009	+0.003
Barrel / Shroud	-0.011	-0.107	0.011	0.000	-0.008	+0.001
Hub	0.004	-0.020	-0.001	+0.001	+0.008	-0.001
Inboard Disc (Upright)	0.002	0.091	-0.006	0.000	+0.004	0.000
Wheel Nut	0.000	-0.005	0.000	0.000	+0.001	0.000

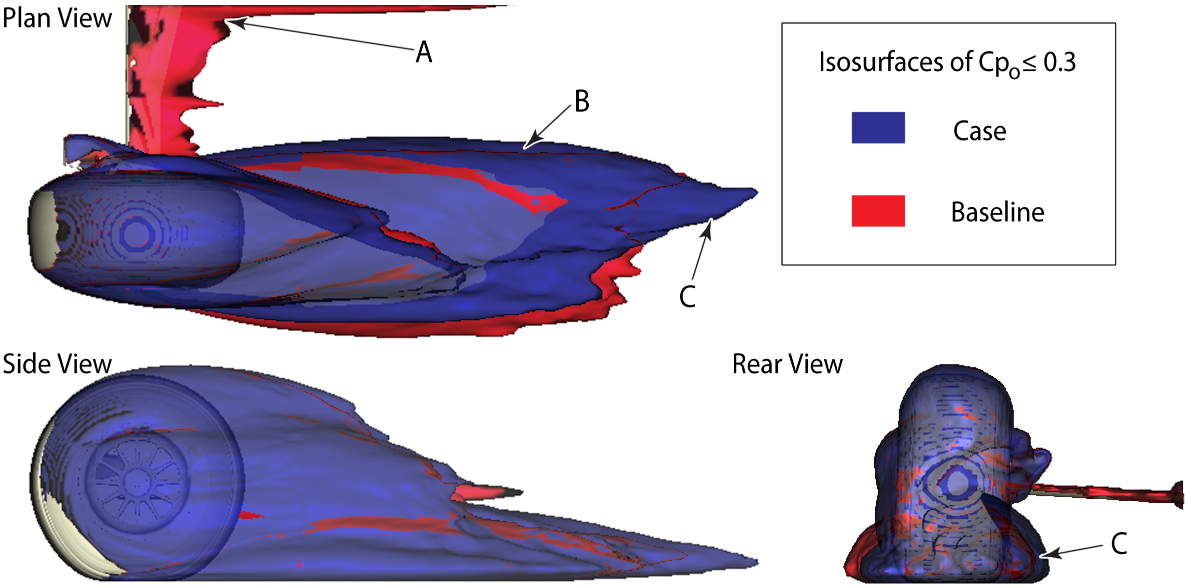

Figure 5.11: *Isosurface plots of $Cp_o \leq 0.3$, comparing Case 3 (blue) with its associated baseline (red).*

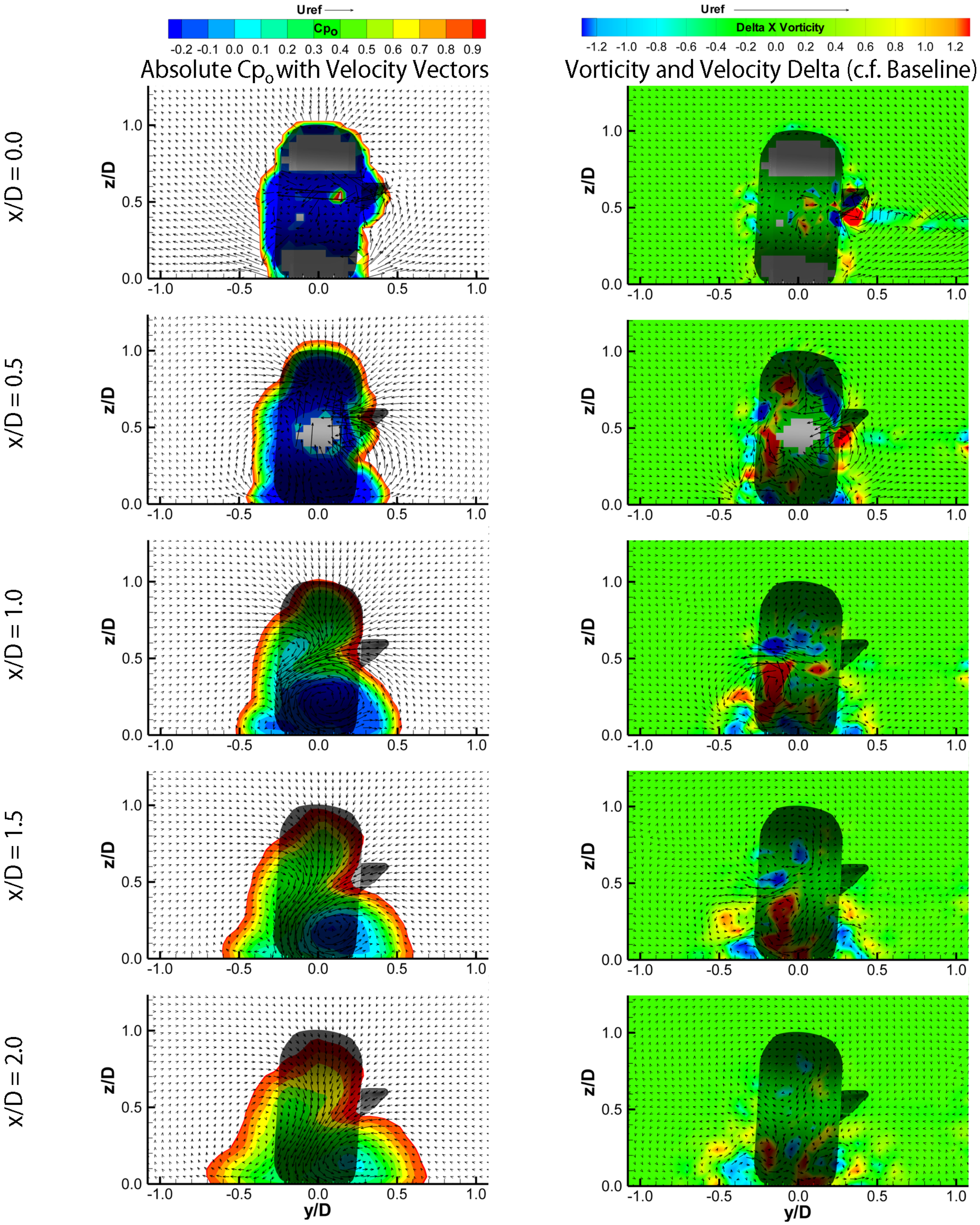

Figure 5.12: *Case 3: Y-Z crossplanes of: Absolute stagnation pressure and velocity vectors (left); Vorticity and velocity vector baseline deltas (right).*

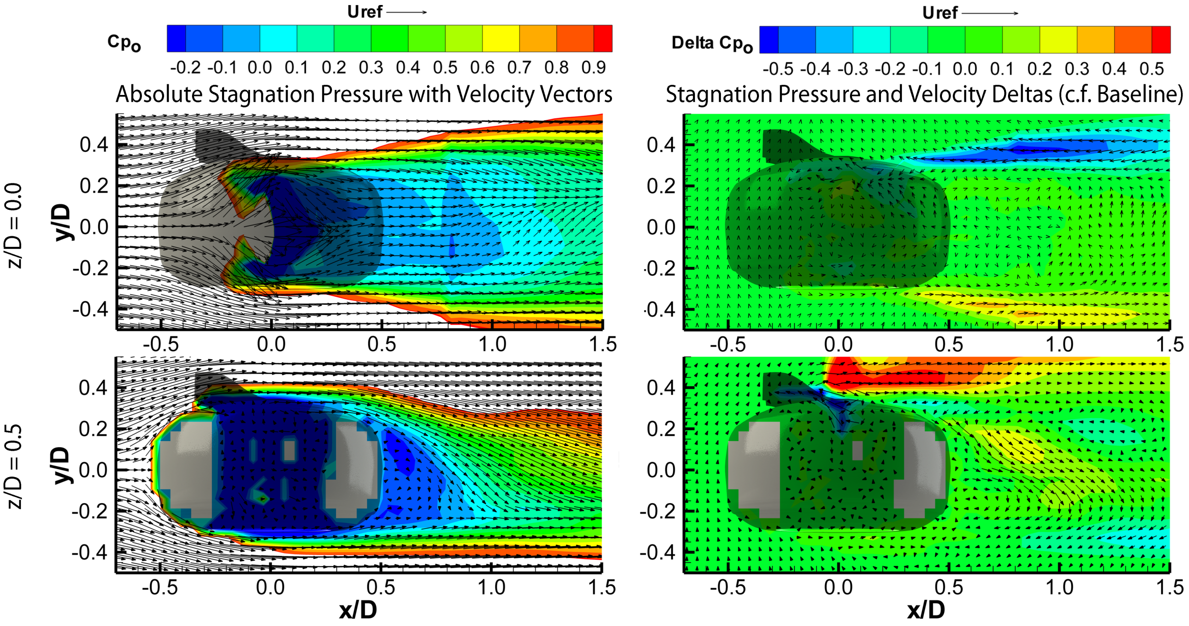

Figure 5.13: *Case 3: X-Y horizontal planes of stagnation pressure with velocity vectors. Absolute values (left) and baseline deltas (right).*

The case without the support sting is intended to quantify the effect of the support sting on the model for the wind tunnel, but also to give an idea as to the importance of the suspension arms of an F1 car on the wheel wake. By removing the sting it is quite apparent that there are both quantifiable force changes as well as visible alterations to the flow-field and wake development.

The aerodynamic force summaries, as presented in Table 5.7 show that the lift is not affected by the removal of the sting. Table 5.8 shows that there is a local increase in lift around the scoop as a result of the removal of the suction from the ground effect of the neutral aerofoil section, as in Case 2, but this is counteracted by internal geometry changes and the overall difference is small. However, the axial drag increase is significant at 39 counts. This is made up of an 87% contribution from the rim and tyre and the rest from the scoop.

In observing the iso-surface plots, the obvious change is the lack of wake due to the sting (A). This has led to an inboard movement of the whole wake (B), similar to the effect of raising the axle height. The most interesting development however is the more prominent and longer lived inboard feature (likely a vortex) which extends well beyond that of the baseline (C). The inboard feature is therefore assumed to be suppressed under normal operation with the sting in place, and by removing it, the low pressure core has been allowed to become stronger as shown as far down as x/D = 2.0 in Figure 5.12. The core of the inboard feature is still strongly blue ($-0.1 < Cp_o < 0.1$), as opposed to the green core ($0.2 < Cp_o < 0.4$) from Case 1.

Further to this, the wake has a higher general Cp_o value than the baseline, as would be expected, but this does not describe an increased drag conclusion as observed. The only evidence to suggest increased drag is from the larger and lower pressure core for the inboard vortex feature, which for this low axle height is behind a large blockage from the inboard sidewall bulge. The width of the wake at the x/D = 2.0 point spans from $-0.7 < x/D < 0.7$ whereas for the baseline it covers $-0.7 < x/D < 0.5$. This wider wake, although not as high on the outboard side, suggests a much more persistent wake. The height of the wake decays at much the same rate as in the baseline case, down to around z/D = 0.9 by the most downstream observation point.

A similar observation to that of Case 2 has been presented in Figure 5.13 whereby the apparent 'jets' behind the contact patch lead to conclusions of the wake moving towards the inboard side. There is no evidence to suggest that there are any changes in pressure around the contact patch and this is reflected in the overall lift measurement. This further suggests that the shape and size of the contact patch is responsible for the lift force more so than the sidewall profile details which are more conducive to drag force and wake development changes. At the axle height plane, this is less obvious, in fact there is evidence to suggest that the effect is slightly reversed. There is also higher vorticity present, shown by the delta vectors emphasising the clockwise recirculation region behind the wheel. This recirculation region has also been extended to x/D = 0.9 downstream of axle as opposed to only around x/D = 0.8.

The consequences of the findings here are not necessarily bad for the development of a race car. Given the inboard flow of a realistic wheel on a car is highly dominated by air disrupted by multiple faired suspension arms, this suggests that the wake is likely to tend towards the outboard side, away from critical downstream components. The lack of front wing and other components in this investigation is obviously another factor but the localised changes brought about by inboard faired arms has been quantified here.

5.2.5 Case 4 - 150mm Axle, +5° Yaw (Realistic Profile)

Case 4 is the first of the yaw studies. By rotating Case 1 through +5° yaw, after replacing the straight-ahead tyre model with the experimentally measured profile (Chapter 3), the aerodynamic characteristics of the realistic yawed wheel are presented. All image planes are coincident with Case 1.

Table 5.9: *Yaw simulation detail: Case 4 geometry schematic and forces (absolute & baseline deltas).*

<table>
<tr><td colspan="2">Case: 4</td><td>Axle Height: 150mm</td><td>Yaw (β): +5°</td><td rowspan="3">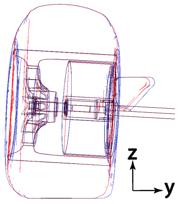 </td></tr>
<tr><td colspan="2">Description:
Experimentally Measured Profile</td><td colspan="2">Baseline Case: 1</td></tr>
<tr><td colspan="2">Aerodynamic Forces:</td><td colspan="2">(Case - Baseline) Force Deltas:</td></tr>
<tr><td>$C_{D,axial} = 0.499$</td><td>$C_L = 0.575$</td><td>$\Delta C_{D,axial} = +0.049$</td><td>$\Delta C_L = +0.109$</td><td></td></tr>
</table>

Table 5.10: *Aerodynamic force breakdown (absolute and baseline deltas) of yaw simulation Case 4.*

Component	**Absolute Forces**			**(Case - Baseline) Force Deltas**		
	$C_{D,axial}$	C_{side}	C_L	$\Delta C_{D,axial}$	ΔC_{side}	ΔC_L
Wheel (Rim and Tyre)	0.449	0.122	0.563	+0.027	+0.080	+0.104
Brake Scoop	0.052	0.107	0.008	+0.018	+0.012	+0.006
Barrel / Shroud	-0.018	-0.102	0.011	-0.007	-0.002	+0.001
Hub	0.004	0.002	0.000	0.000	+0.029	0.000
Inboard Disc (Upright)	0.012	0.115	-0.007	+0.010	+0.027	-0.002
Wheel Nut	0.000	-0.004	0.000	0.000	+0.002	0.000

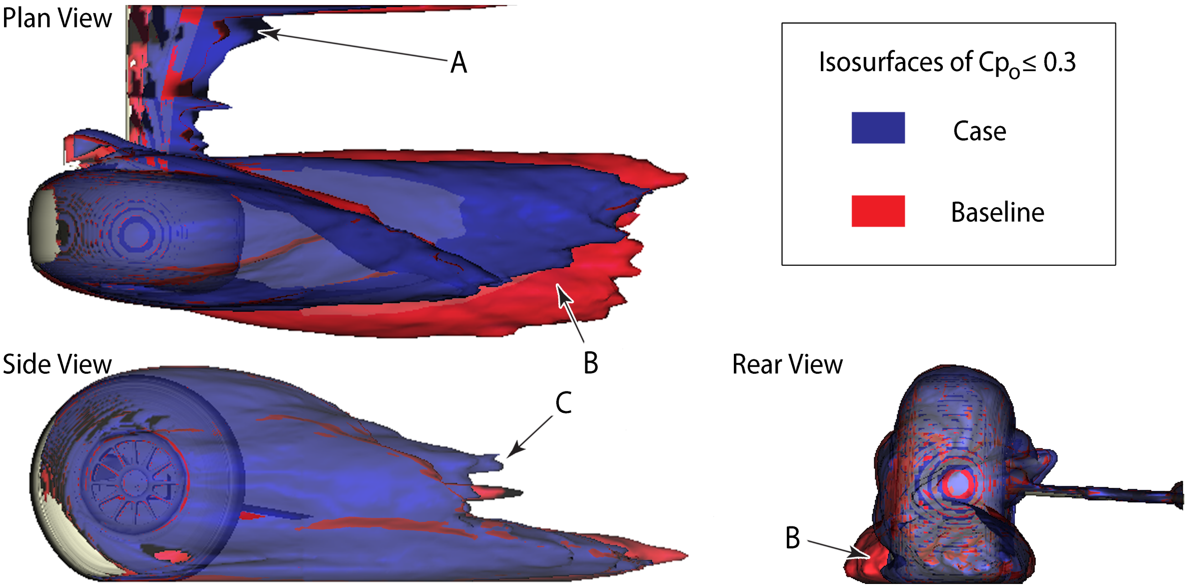

Figure 5.14: *Isosurface plots of $Cp_o \leq 0.3$, comparing Case 4 (blue) with its associated baseline (red).*

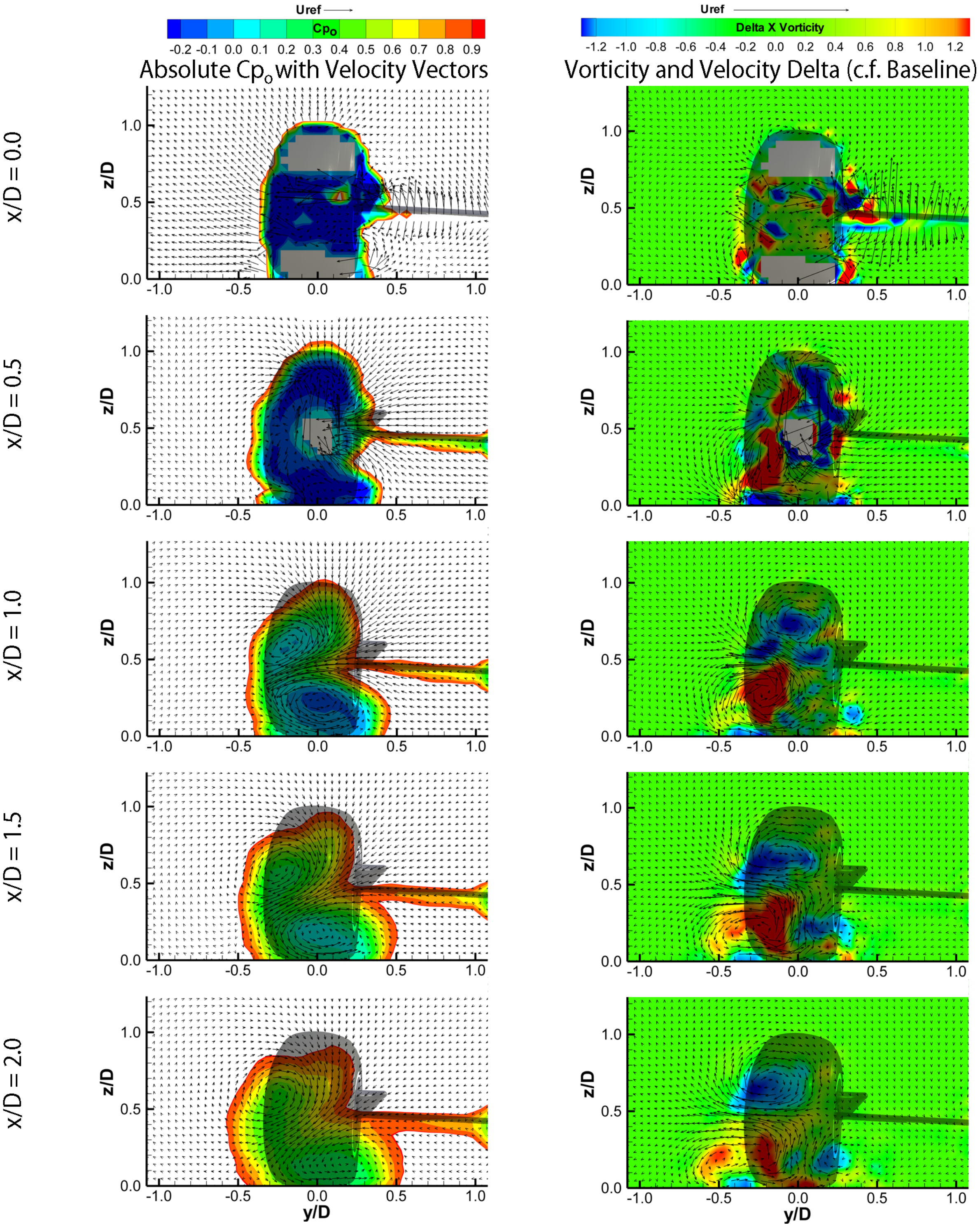

Figure 5.15: *Case 4: Y-Z crossplanes of: Absolute stagnation pressure and velocity vectors (left); Vorticity and velocity vector baseline deltas (right).*

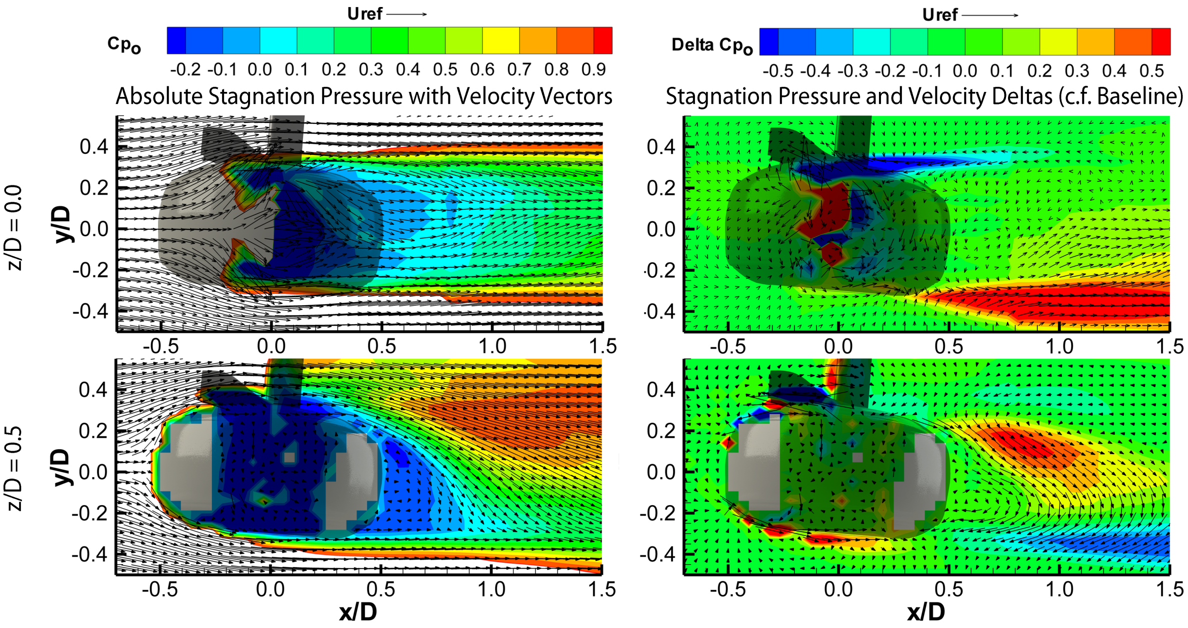

Figure 5.16: *Case 4: X-Y horizontal planes of stagnation pressure with velocity vectors. Absolute values (left) and baseline deltas (right).*

The force summary in Table 5.9 shows a significant increase in both lift and axial drag relative to the baseline. These values correspond to 109 and 49 counts respectively. Interestingly, a significant proportion of the drag and a larger proportion of the lift increase (than for the baseline) is due to the scoop. For drag this corresponds to 37% and for lift this is 6%. By turning the wheel to positive yaw the scoop is within the wake of the wheel. Any slight separation that may be caused by the tyre itself at yaw is emphasised by the extra blockage from the scoop. Some of the internal components have also started to contribute towards drag. The inboard disc, to which the brake scoop and hub internals are mounted (equivalent of the suspension upright), has contributed 10 counts of drag towards the total, as a result putting only a little over half of the overall change down to the rim and tyre alone. The cause of this drag from the inboard disc is obvious, given it is of around 150mm in diameter and only around 2mm thick. The disc was previously aligned with the freestream with no wake directly behind.

The increased blockage from the dragged sidewall, due to the increased contact patch width in conjunction with the camber of the wheel, is arguably responsible for the reduced suction underneath the sidewalls and therefore a net gain in positive lift. This geometrical change can be seen in the overlaid profiles to the right-hand side of the summary table and aerodynamically in Figure 5.16.

The iso-surface plots in Figure 5.14 show a completely different structure to that of the non-yawed wheel. An increased contribution of sting wake (A), this time much closer to the wake of the wheel has been observed. The consequences of this are not obvious at this stage but more will become apparent from the crossplane plots. The wake in general appears much narrower and the presence of the outboard feature has almost disappeared (B). There appears to be a much greater emphasis on the upper wake with a significant outwash of the global features compared to that of the non-yawed case (C).

Figure 5.15 confirms the fact that the wake structure is almost unrecognisable from the non-yawed case. Instead of a predominant downwash with an inverse 'S' wake shape, the local-wake exhibits almost 100% outwash at axle height with no vertical downwash component. The inboard feature which was so dominant in the non-yawed cases has elongated and covered the entire underside of the wake whereas the outboard feature which was minimised (B) has in fact rotated to be positioned directly above the inboard feature. This was also noted in the iso-surface plots (C).

As the wake develops, the upper feature begins to travel downwards when the strength of the lower vortex reduces. This forms a diagonal downwash but still does not resemble the wake of the non-yawed wheel. Whilst it could be argued that this plane of observation is at an angle to the wheel plane, this is the wake that downstream components would observe. It is therefore significant to observe these different behaviour patterns as the wheel is constantly moving, and indeed with minor setup parameters such as toe (covered in Chapter 1) effectively inducing a small permanent yaw of the wheel, the flow-field could be biased towards one of these yawed wakes as opposed to the well behaved steady-state two lower features with central downwash structure. For this geometry, positive yaw would be an exaggerated example of the flow-field for a car with 'toe-in' setup.

The vorticity deltas show in the large red patches the suppressed outboard vortex and the blue area shows the development of the new feature much higher up. The wake remains very compact and tightly formed, which is surprising given the relatively large increase in projected frontal area of around 6.5%. The narrowing of the wake and movement of the upper features are much clearer from the stagnation pressure delta plots in Figure 5.16. There is also evidence of increased horizontal recirculation, which remains in the same orientation.

5.2.6 Case 5 - 150mm Axle, +5° Yaw (Straight-Ahead Profile)

Case 5 is a study into the aerodynamic sensitivity to lower profile dragging at yaw. CFD studies usually take a non-yawed profile which is simply rotated for yaw tests. The findings are compared to Case 4, which had a scanned tyre geometry, thus quantifying the error in making such a simplification.

Table 5.11: *Yaw simulation detail: Case 5 geometry schematic and forces (absolute & baseline deltas).*

<table>
<tr><td colspan="2">Case: 5</td><td>Axle Height: 150mm</td><td>Yaw (β): +5°</td><td rowspan="3">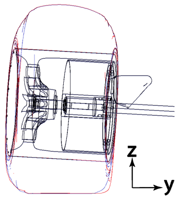 </td></tr>
<tr><td colspan="2">Description:
Straight-Ahead Profile at 5° Yaw</td><td colspan="2">Baseline Case: 4</td></tr>
<tr><td colspan="2">Aerodynamic Forces:</td><td colspan="2">(Case - Baseline) Force Deltas:</td></tr>
<tr><td>$C_{D,axial}$ = 0.484</td><td>C_L = 0.425</td><td>$\Delta C_{D,axial}$ = -0.014</td><td>ΔC_L = -0.151</td><td></td></tr>
</table>

Table 5.12: *Aerodynamic force breakdown (absolute and baseline deltas) of yaw simulation Case 5.*

Component	Absolute Forces			(Case - Baseline) Force Deltas		
	$C_{D,axial}$	C_{side}	C_L	$\Delta C_{D,axial}$	ΔC_{side}	ΔC_L
Wheel (Rim and Tyre)	0.440	0.119	0.413	-0.010	-0.002	-0.150
Brake Scoop	0.051	0.105	0.007	-0.001	-0.002	-0.001
Barrel / Shroud	-0.020	-0.101	0.011	-0.002	+0.001	0.000
Hub	0.003	-0.008	0.000	-0.001	-0.010	0.000
Inboard Disc (Upright)	0.011	0.109	-0.007	-0.001	-0.006	0.000
Wheel Nut	0.000	-0.004	0.000	0.000	0.000	0.000

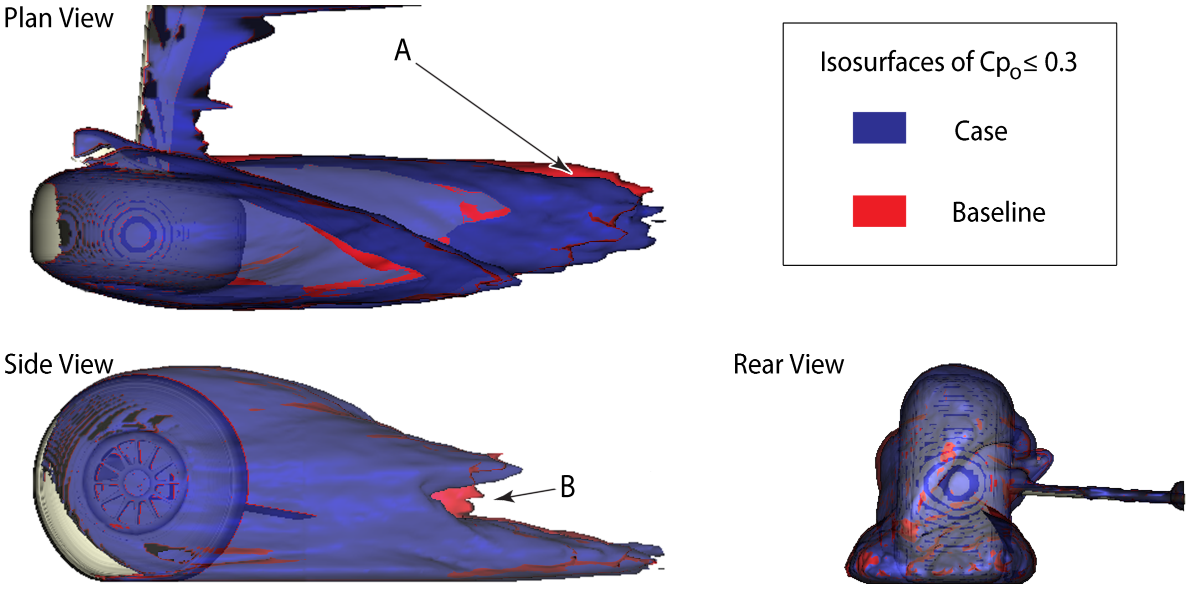

Figure 5.17: *Isosurface plots of* $Cp_o \leq 0.3$*, comparing Case 5 (blue) with its associated baseline (red).*

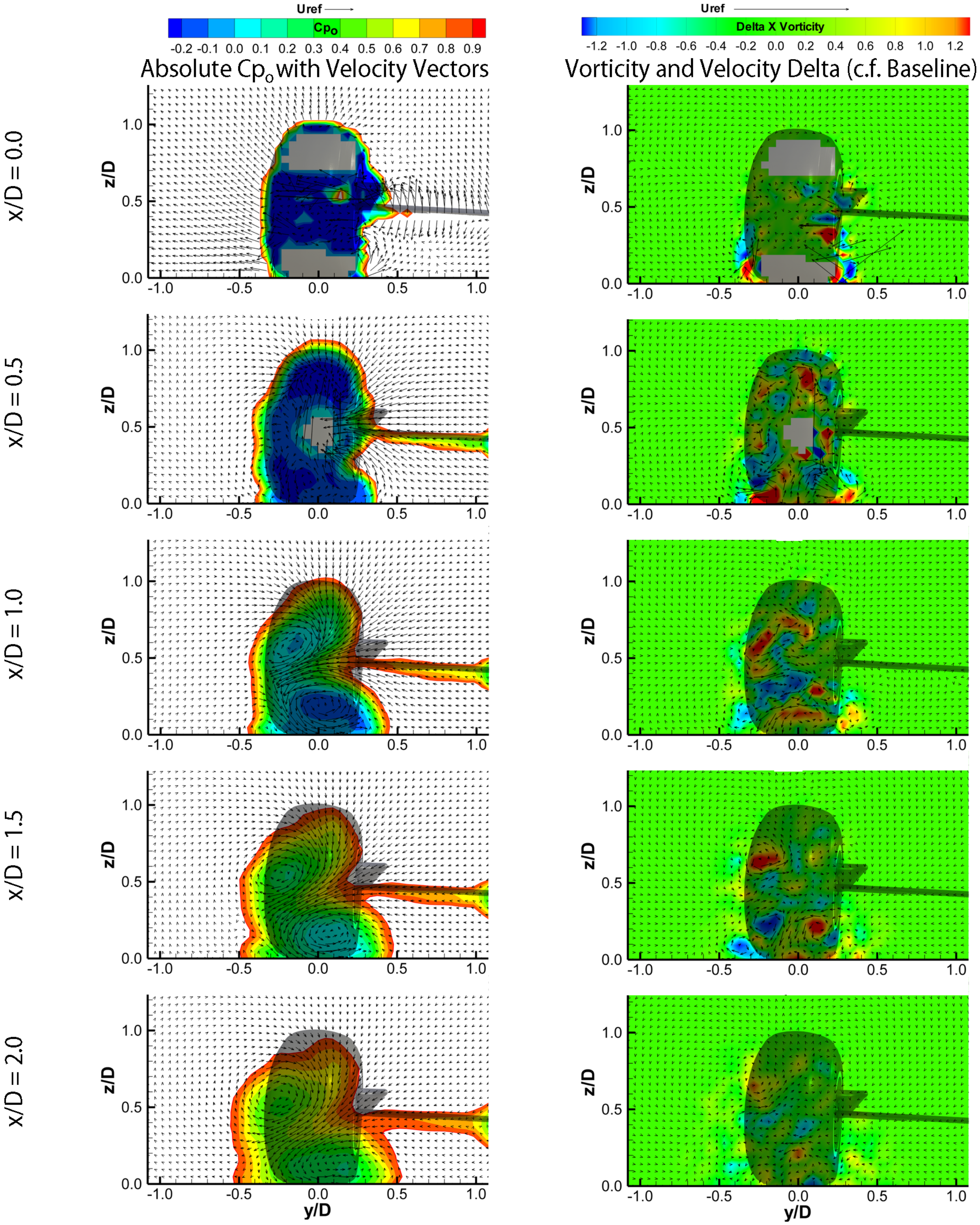

Figure 5.18: *Case 5: Y-Z crossplanes of: Absolute stagnation pressure and velocity vectors (left); Vorticity and velocity vector baseline deltas (right).*

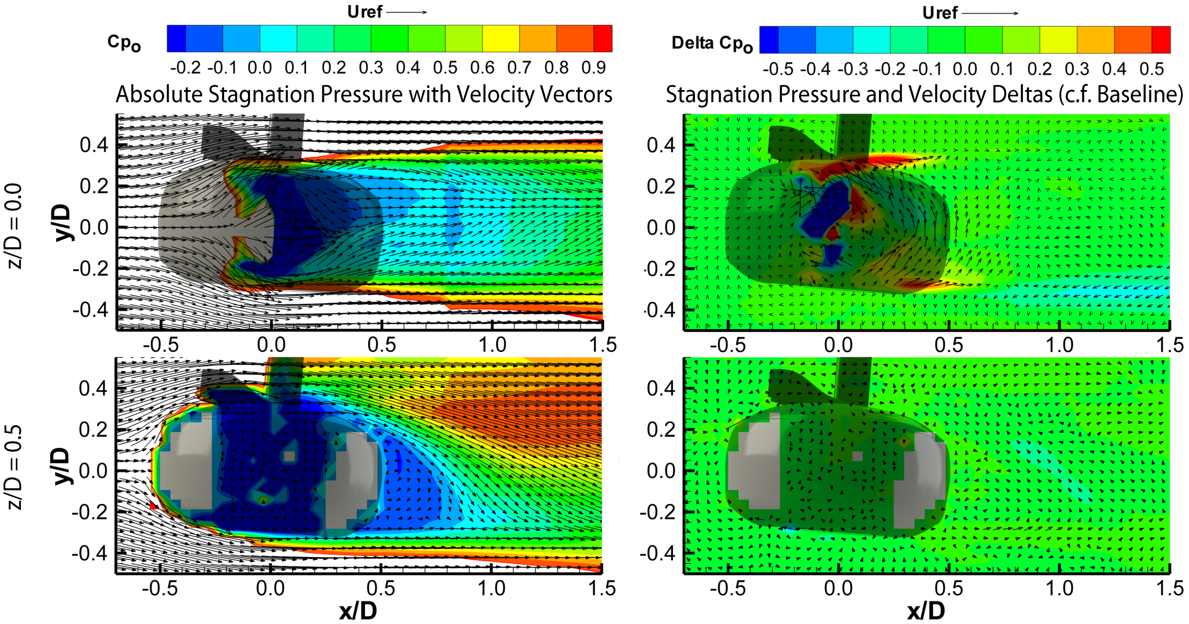

Figure 5.19: *Case 5: X-Y horizontal planes of stagnation pressure with velocity vectors. Absolute values (left) and baseline deltas (right).*

For the purpose of this analysis it is important to remember that the only difference between the case tested here and the baseline to which it is compared is the lower profile (as seen at the far right of Table 5.11). The upper and mid-profiles are the same and the wheels are both angled to +5° yaw.

Both the lift and drag forces show a reduction compared to the baseline. The lift reduction is as would be expected from the emerging trend based on contact patch width, although the size of this reduction is extreme at 151 counts (around 20%). The shape and size of the contact patch appear to be extremely sensitive to the lift force and although the geometrical changes are small relative to the overall test subject, they are significant relative to the contact patch.

It appears from Table 5.12 that the changes in forces are almost entirely due to the rim and tyre and very little from internal components. This is expected as only the tyre profile was changed. There is a small sideforce difference developed by the internal hub. This is in the outboard direction and implies lower pressures on the outboard side of the wheel. Indeed, this would be the case due to higher blockage from the more outboard biased lower profile. This would also infer a potentially favourable environment for higher through-hub flow rates.

The iso-surface plots show two cases which essentially coincide. From the rear-view, there is very little between them and the only evidence of any difference is a slight outboard bias towards the far-field of the wake (A) and a less persistent mid-height wake (B).

The crossplane development in Figure 5.18 shows essentially the same behaviour as for Case 4 (Figure 5.15). There is slight evidence of a third vortex feature developing where the outboard vortex would normally be found straight-ahead, although this is small and is only present around x/D = 1.5. Again comparing to the baseline, the wake is slightly narrower by almost 0.1D in the y-direction at the furthest downstream point. The vorticity deltas show two regions of intense vortex strengthening at the contact patch edges, this is particularly visible at x/D = 1.0. By x/D = 2.0, the vorticity changes are negligible, despite slight discrepancies in the wake width at this point.

The horizontal planes show some critical flow structure differences. Firstly, there is indeed a much lower pressure on the forward inboard contact patch. This results in much higher pressure in the immediate vicinity of the sidewall jet although this is not below a surface, and so does not have an effect on the force measurement. There is also evidence of strong inwash from the outboard contact patch behind the tyre. This infill is also visible at the axle height, leading to a retardation of the vorticity of the recirculation region. This information suggests that the local changes are significant and their impact on the global flow-field is a lot greater than would be expected from a movement of around 10mm (0.03D) laterally on the sidewall.

The consequences of these findings show that there is an appreciable difference between the wake and forces for a yawed tyre with and without the correct profile. These changes are significantly larger than the characteristic lengths of most of the downstream car components. With that in mind, a wider lower-wake by 0.1D, which equates to 32mm, is something that should be of concern when developing concepts in CFD. If time is invested performing yawed CFD runs for car development, it is important to therefore match the tyre profile as well as the global geometry angle.

5.2.7 Case 6 - 150mm Axle, +5° Yaw (Glycerol Profile)

Case 6 is an extension to the principal of Case 5. By observing simplifications made in experimental environments, such as the use of glycerol to improve the longevity of equipment, the resulting tyre profile is compromised (see Chapter 3). The aerodynamic consequences are presented.

Table 5.13: *Yaw simulation detail: Case 6 geometry schematic and forces (absolute & baseline deltas).*

Case: 6		**Axle Height:** 150mm	**Yaw (β):** +5°	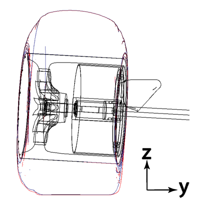
Description: Glycerol Profile		**Baseline Case:** 4		
Aerodynamic Forces: $C_{D,axial} = 0.516$	$C_L = 0.525$	**(Case - Baseline) Force Deltas:** $\Delta C_{D,axial} =$ +0.017	$\Delta C_L =$ -0.050	

Table 5.14: *Aerodynamic force breakdown (absolute and baseline deltas) of yaw simulation Case 6.*

Component	Absolute Forces			(Case - Baseline) Force Deltas		
	$C_{D,axial}$	C_{side}	C_L	$\Delta C_{D,axial}$	ΔC_{side}	ΔC_L
Wheel (Rim and Tyre)	0.490	0.053	0.516	+0.040	-0.069	-0.047
Brake Scoop	0.049	0.102	0.007	-0.003	-0.005	-0.001
Barrel / Shroud	-0.032	-0.105	0.006	-0.014	-0.003	-0.004
Hub	-0.001	-0.008	0.002	-0.005	-0.010	+0.002
Inboard Disc (Upright)	0.011	0.106	-0.006	-0.001	-0.008	+0.001
Wheel Nut	0.000	-0.004	0.000	0.000	0.000	0.000

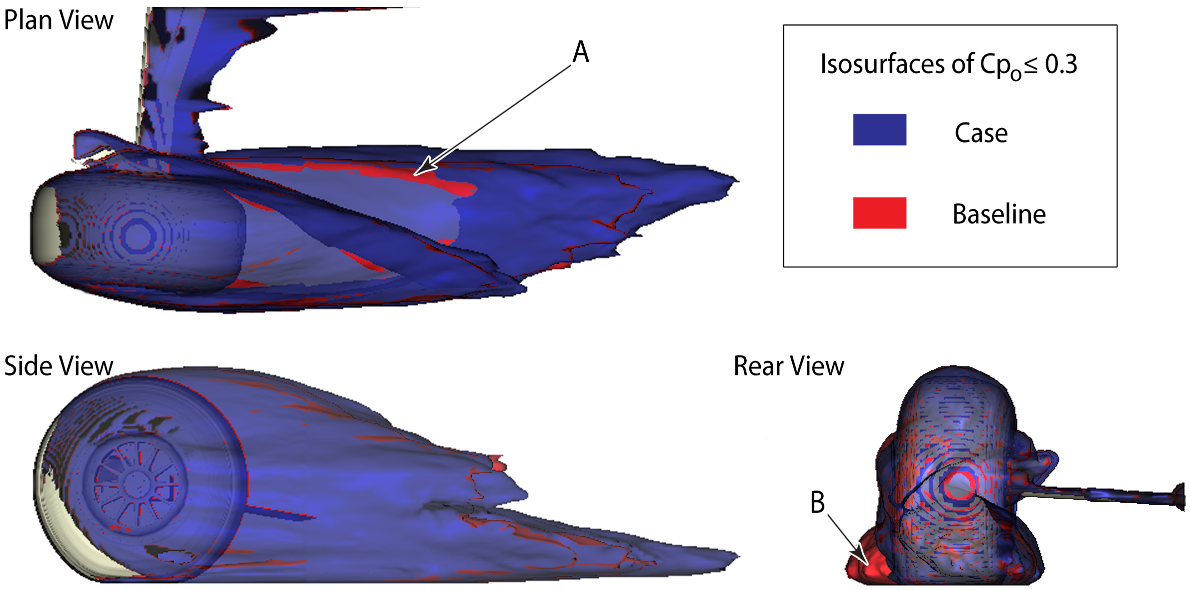

Figure 5.20: *Isosurface plots of $Cp_o \leq 0.3$, comparing Case 6 (blue) with its associated baseline (red).*

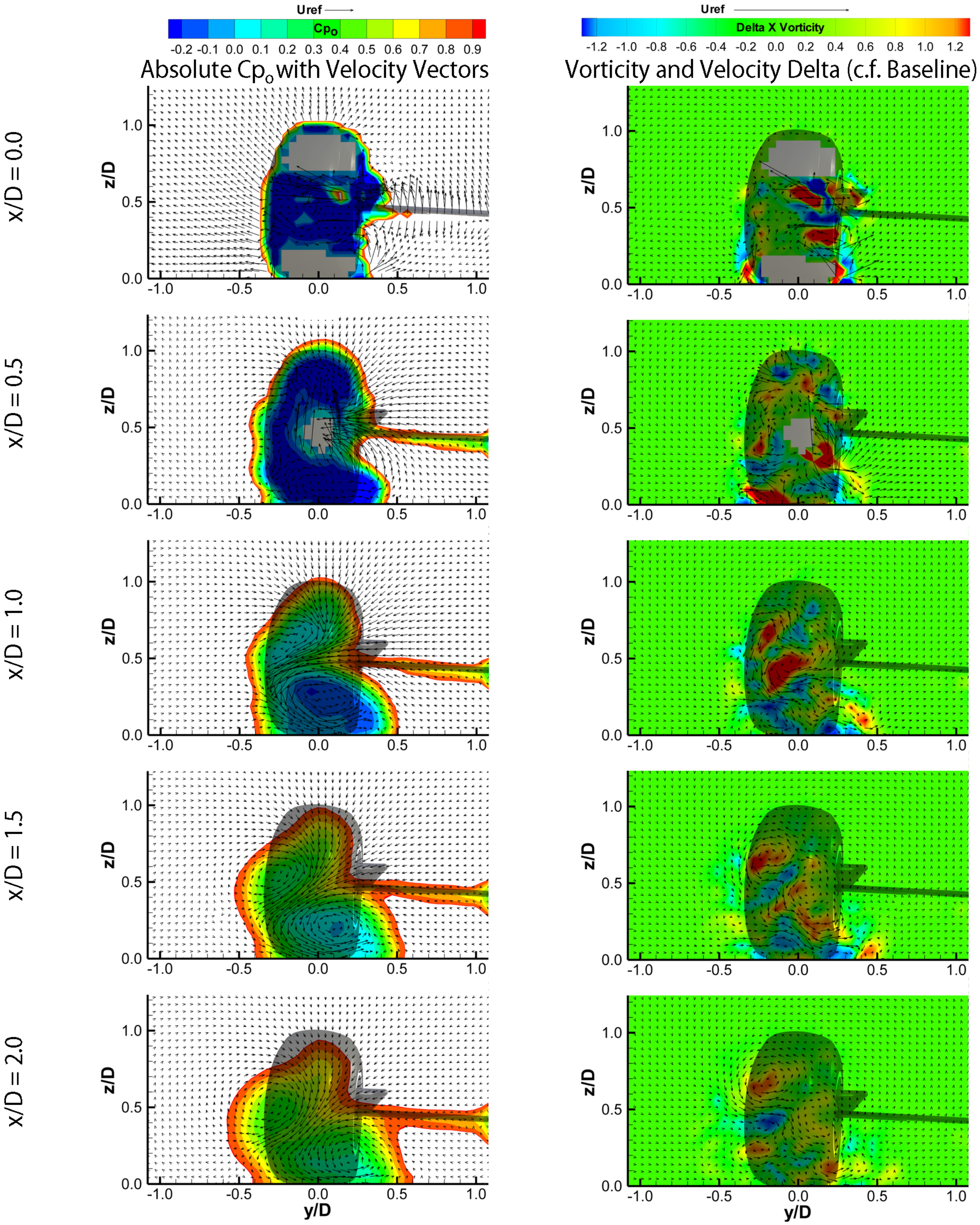
Absolute Cp_o with Velocity Vectors

Vorticity and Velocity Delta (c.f. Baseline)

Figure 5.21: *Case 6: Y-Z crossplanes of: Absolute stagnation pressure and velocity vectors (left); Vorticity and velocity vector baseline deltas (right).*

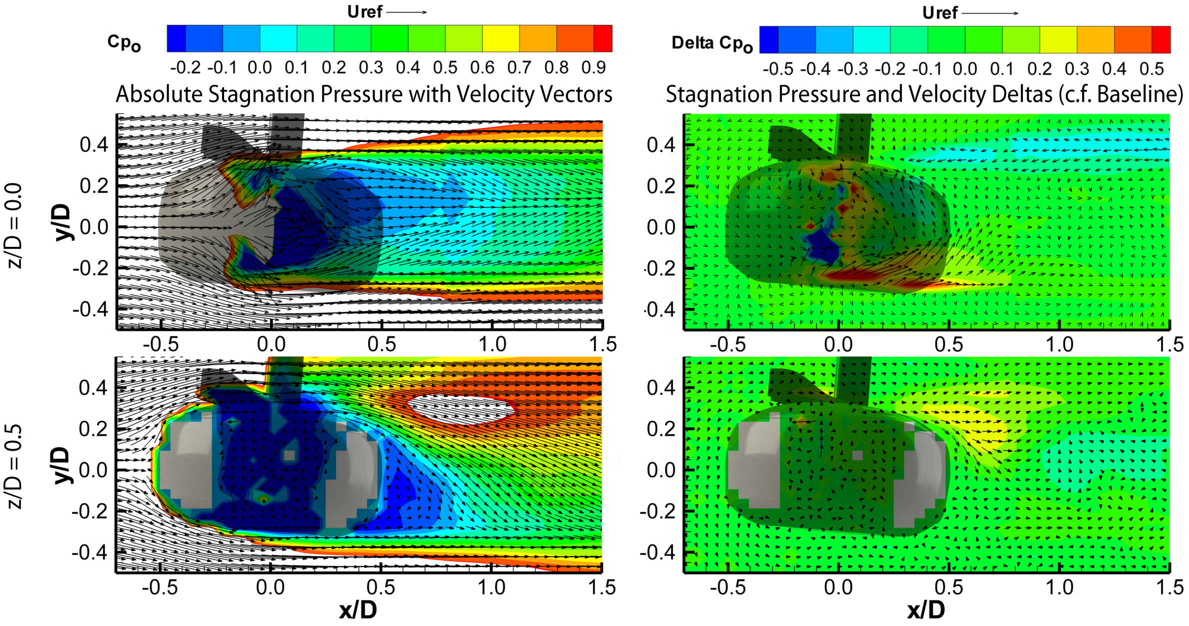

Figure 5.22: *Case 6: X-Y horizontal planes of stagnation pressure with velocity vectors. Absolute values (left) and baseline deltas (right).*

The summary found in Table 5.13 shows forces that lie in-between the geometry changes that were applied to cases 4 and 5. The profile measured in the wind tunnel showed evidence of reduced sharpness of the transition between the sidewall and the tread. This was suggested in Chapter 3 as being a potential cause for reduced vorticity and a more spread out wake.

The opposite but similar in magnitude drag trend to Case 5 (to respective baselines) has been measured. Unlike Case 5, the drag change is not purely down to the external components shown by Table 5.14. There is a significant 14 count reduction from the shrouding barrel, of similar magnitude to the overall increase. This means that the effect on the drag of the external components is in fact much larger. It is not clear why there has been such a big change on an internal component. A likely reason might be a smaller wake from the scoop, compared to the realistic profile in Case 4, which has then been responsible for less of an effect on the component (which is otherwise neutral at zero yaw). Indeed a small reduction in drag for the scoop has been observed which strengthens this argument.

The lift force has again reduced, but this time by only a third as much as between cases 4 and 5 (exactly 33%). This is perfectly consistent with the change in contact patch width which was measured to be narrower than the yawed profile by 28% of the difference between the realistic and non-yawed profile. This change is again almost entirely visible in the external rim and tyre contribution.

In observing the iso-surface plots in Figure 5.20 there is evidence to suggest a smaller inboard wake than the baseline (A). In addition, the persistence of the outboard feature is much reduced (B). This follows the expectation from the wind tunnel results Chapter 3.

The crossplanes in Figure 5.21 show the development in more detail. The vorticity deltas show around x/D = 0.5 and 1.0 that there is a blue area on the inboard contact patch and a red area on the ouboard contact patch. This shows that locally, the vorticity has been reduced (as the absolute values are usually the opposite colours). There is also a significant and consistent reduction in the upper feature which has resulted in a much more outboard biased core and more vertical downwash towards the furthest downstream observation point. There is still evidence of a blue core for the stagnation pressure on the inboard feature at this point, which was not present for the baseline case. Therefore, although the vorticity has reduced, it seems the low-pressure core is lower and more persistent on the inboard side. The slightly wider wake combined with this lower pressure is likely to be responsible for the small drag increase compared to the realistic profile (Case 4).

The horizontal planes in Figure 5.22 show a lower pressure on the frontal outboard contact patch but the inboard exhibits an increase compared to the realistic profile. The flow-field has not changed significantly despite the smaller blockage on the inboard side. The outboard ‘jet’ is of very high pressure relative to the realistic profile and unlike the last case, this is directly underneath the sidewall of the tyre and likely to be responsible for a suction effect. There is also evidence at near-ground level of a slightly more dispersed wake on the inboard, as predicted.

At axle height there is little difference between the vectors and there is a higher pressure region around the inboard trailing edge of the tyre. This shows there is evidence of a significant change to the wake from a relatively small global geometry change. The consequences of using a glycerol coated tyre in the wind tunnel are discussed more in Chapter 6, due to the importance and relevance of this technique in an industrial setting.

5.2.8 Case 7 - 159mm Axle, +5° Yaw (Realistic Profile)

Case 7 is a low deformation (high axle height) equivalent of Case 4. Whilst this comprises the same parameter change to the low deformation baseline (Case 2) as Case 4 did to Case 1, this is intended to test if the same sensitivities are present for slow corner-exit (high axle height) conditions.

Table 5.15: *Yaw simulation detail: Case 7 geometry schematic and forces (absolute & baseline deltas).*

<table>
<tr><td>Case: 7</td><td>Axle Height: 159mm</td><td>Yaw (<i>β</i>): +5°</td><td rowspan="3">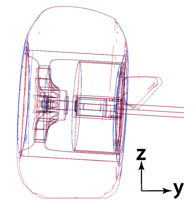
</td></tr>
<tr><td>Description:
Experimentally Measured Profile</td><td colspan="2">Baseline Case: 2</td></tr>
<tr><td>Aerodynamic Forces:
$C_{D,axial} = 0.486$ | $C_L = 0.577$</td><td colspan="2">(Case - Baseline) Force Deltas:
$\Delta C_{D,axial} = +0.003$ | $\Delta C_L = +0.187$</td></tr>
</table>

Table 5.16: *Aerodynamic force breakdown (absolute and baseline deltas) of yaw simulation Case 7.*

Component	**Absolute Forces**			**(Case - Baseline) Force Deltas**		
	$C_{D,axial}$	C_{side}	C_L	$\Delta C_{D,axial}$	ΔC_{side}	ΔC_L
Wheel (Rim and Tyre)	0.437	0.143	0.561	-0.009	+0.158	+0.178
Brake Scoop	0.049	0.101	0.013	+0.012	-0.001	+0.005
Barrel / Shroud	-0.016	-0.090	0.010	-0.006	-0.020	+0.001
Hub	0.004	-0.010	0.000	-0.005	+0.078	+0.003
Inboard Disc (Upright)	0.011	0.105	-0.007	+0.010	-0.009	0.000
Wheel Nut	0.000	-0.003	0.000	0.000	0.000	0.000

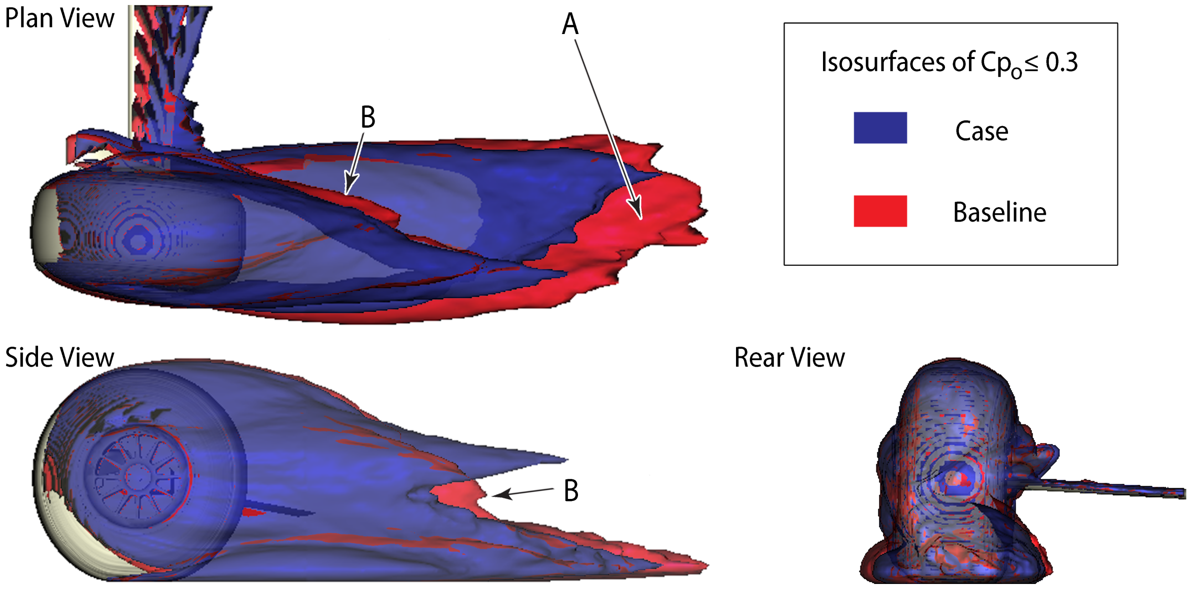

Figure 5.23: *Isosurface plots of* $Cp_o \leq 0.3$*, comparing Case 7 (blue) with its associated baseline (red).*

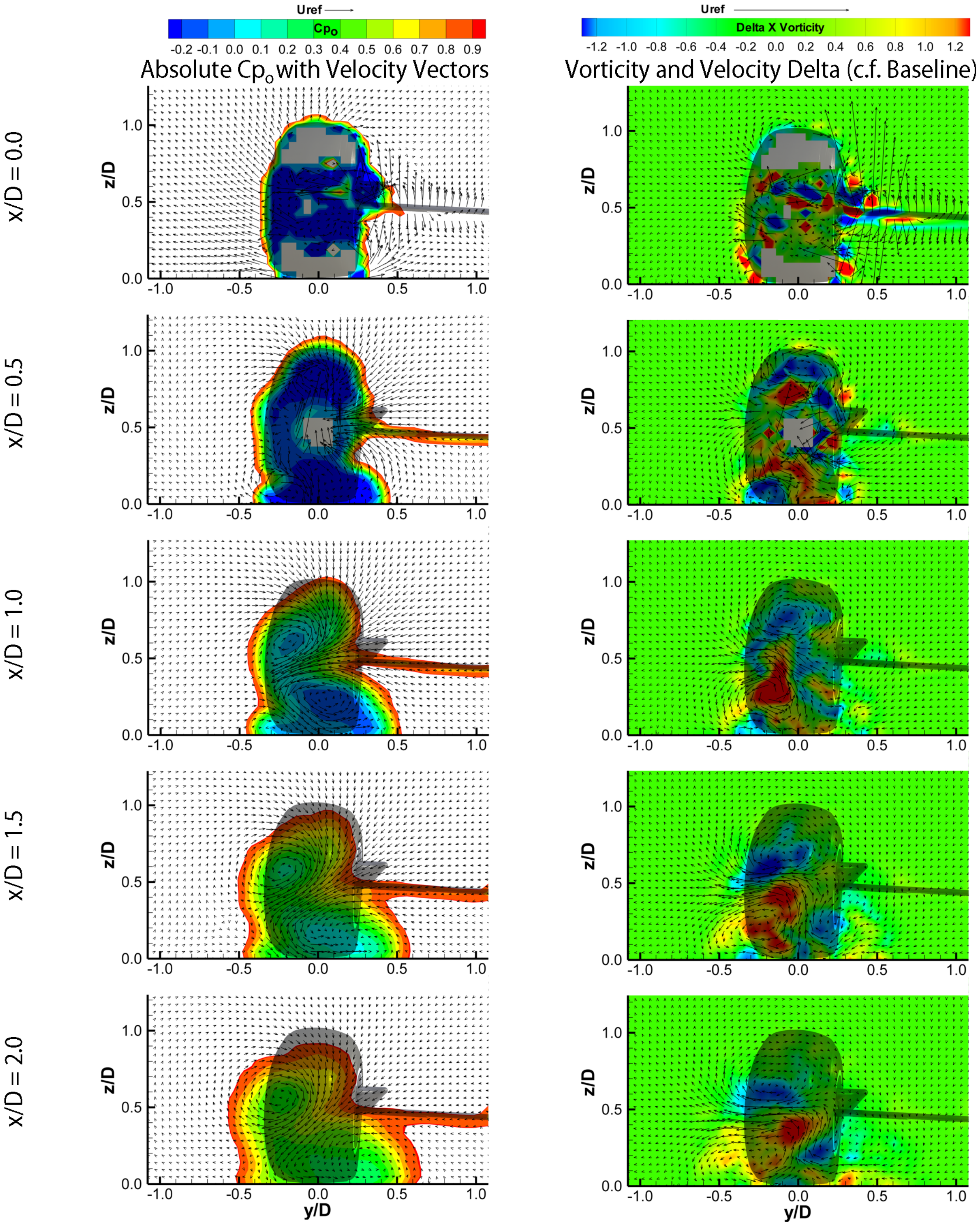

Figure 5.24: *Case 7: Y-Z crossplanes of: Absolute stagnation pressure and velocity vectors (left); Vorticity and velocity vector baseline deltas (right).*

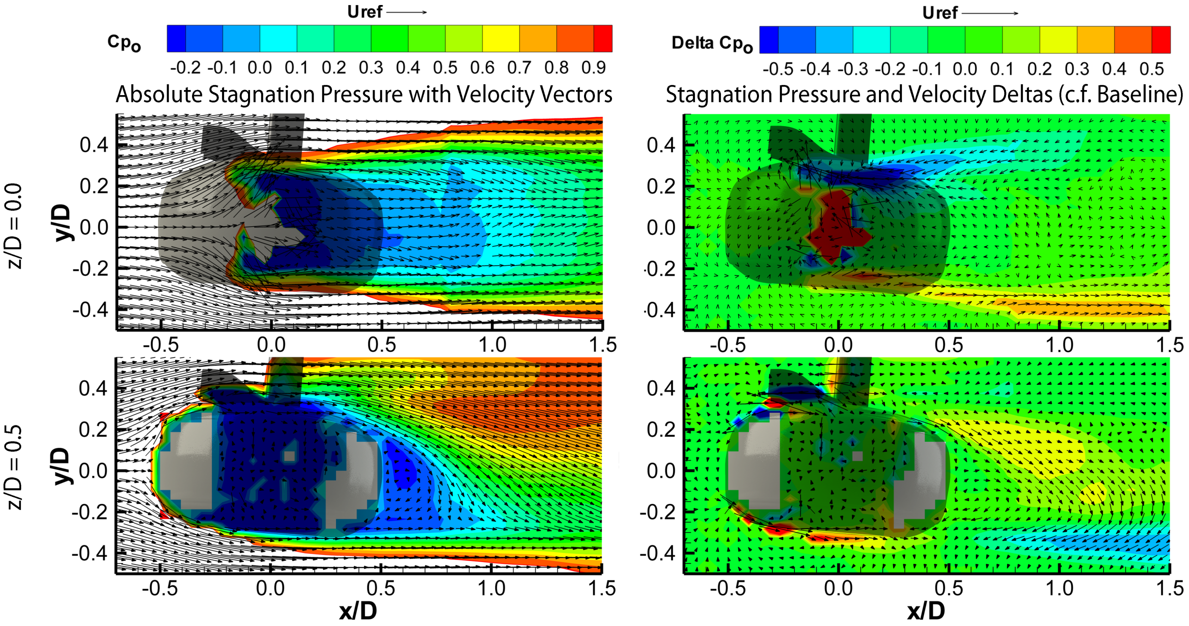

Figure 5.25: *Case 7: X-Y horizontal planes of stagnation pressure with velocity vectors. Absolute values (left) and baseline deltas (right).*

This case has been compared to the non-yawed high axle case (Case 2) in order to make the differences comparable to those of Case 4 (with Case 1). This is to test if the same changes occur in the flow-field when a higher axle height wheel is yawed. However, it is also interesting to observe the direct differences between this case and Case 4 to see the effect of axle height when at yaw. Perhaps the most significant result, when compared to the non-yawed case, is that there is a negligible change in drag, whereas the lower axle height case had an increase by 48 counts. That drag change was around 10% of the absolute value with an increase in frontal area, as discussed, of 6.5%. The increase in frontal area for the higher axle height is smaller, at 6.0%, but this has not been reflected at all in the drag force.

The force breakdown in Table 5.16 shows that the external features are actually responsible for a reduction in drag, and the increase of the drag of the inboard disc (suspension upright) and brake scoop has counteracted this. The change in lift is as expected but this time by only by 58% of the change observed by the lower axle height at yaw. This is explained by the fact that there is a smaller relative change in the contact patch size for a higher axle height tyre at yaw than a lower one. Clearly there are some profile-related changes taking place in the downstream flow-field which affect the drag.

Figure 5.23 shows the iso-surface plots of the higher axle height at yaw. It is again clearly visible that the yawed wake is much narrower than the non-yawed case (A), despite the larger frontal area. The outboard feature has not been suppressed as much as it had been in Case 4 and is visible in the crossplane wake development in Figure 5.24.

The axle height wake from the iso-surfaces shows a much slower decay in height (B) than the non-yawed case. This was not the case for the lower axle height which appeared to behave similarly to its baseline. There is a slightly wider wake than for Case 4, which does not explain the drag observation. What is apparent is that the vortex core locations are much closer to the outboard side than for Case 4 (around $y/D = +0.2$). This is seen by comparing the left-hand side of the figure with Figure 5.15 and by observing the more inboard biased red and blue regions of the vorticity plot for this case. This has led to the two main features being more vertically aligned which results in a more diagonal downwash (still predominantly outwash as opposed to vertical downwash) than in Case 4. There is also evidence of a small vortex feature at near-ground level on the outboard contact patch, not present in Case 4. This has also suppressed the decay of the overall height of the wake.

The contact patch pressure in Figure 5.25 shows a significant difference relative to Case 4. The contact patch is much smaller which has reduced the localised blockage and reduced the loss of stagnation pressure. This may be responsible for the suppressed drag increase which would have been expected from the size of the wake being similar to Case 4.

It would appear that the higher axle height is less sensitive to yaw than the lower axle height in terms of aerodynamic drag and flow-field. Because of this, the two cases are very different. This again brings about a discussion of the application of these two scenarios. Whilst up to now the performance in a straight line for low speed (high axle) and high speed (low axle) have been compared and found to be different, there appears to be an even greater difference for the wheel at yaw. In competition, the wheel is at yaw far more often than it is pointing directly ahead parallel to the axis of the car, therefore this is a significant discovery. Whilst a straight-ahead test will over-predict drag forces and change the flow-field (see Chapter 3), a yawed case will under-predict the drag and change the formation of the downstream wake even more than just reducing the outboard vortex feature size.

5.2.9 Case 8 - 159mm Axle, +5° Yaw (Straight-Ahead Profile)

Case 8 is an extension of the study in Case 5, investigating the differences brought about by using a straight-ahead profile instead of a correctly deformed tyre. Less deformation (higher axle height) has already shown less significant geometrical changes at yaw than the more deformed case.

Table 5.17: *Yaw simulation detail: Case 8 geometry schematic and forces (absolute & baseline deltas).*

Case: 8		**Axle Height:** 159mm	**Yaw (β):** +5°	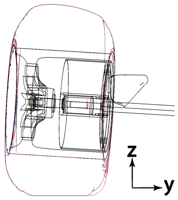
Description: Straight-Ahead Profile at 5° Yaw		**Baseline Case:** 7		
Aerodynamic Forces:		**(Case - Baseline) Force Deltas:**		
$C_{D,axial} = 0.497$	$C_L = 0.391$	$\Delta C_{D,axial} = +0.011$	$\Delta C_L = -0.185$	

Table 5.18: *Aerodynamic force breakdown (absolute and baseline deltas) of yaw simulation Case 8.*

Component	Absolute Forces			(Case - Baseline) Force Deltas		
	$C_{D,axial}$	C_{side}	C_L	$\Delta C_{D,axial}$	ΔC_{side}	ΔC_L
Wheel (Rim and Tyre)	0.446	0.095	0.379	+0.010	-0.048	-0.182
Brake Scoop	0.052	0.106	0.011	+0.002	+0.006	-0.001
Barrel / Shroud	-0.016	-0.088	0.008	0.000	+0.001	-0.003
Hub	0.003	-0.008	0.001	-0.001	+0.002	+0.001
Inboard Disc (Upright)	0.011	0.107	-0.007	0.000	+0.002	0.000
Wheel Nut	0.000	-0.003	0.000	0.000	0.000	0.000

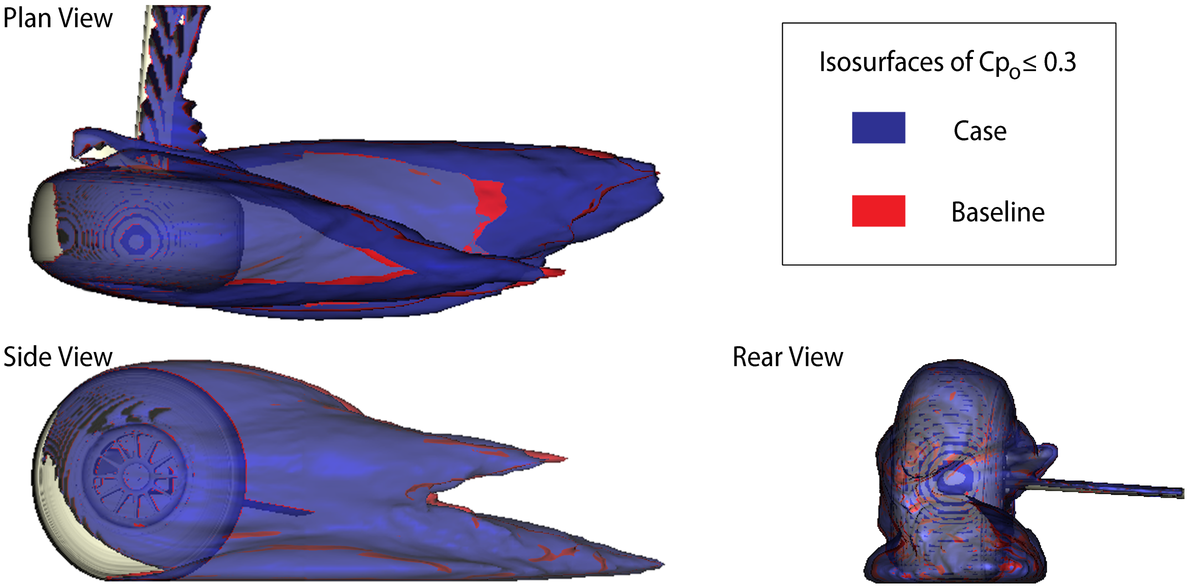

Figure 5.26: *Isosurface plots of $Cp_o \leq 0.3$, comparing Case 8 (blue) with its associated baseline (red).*

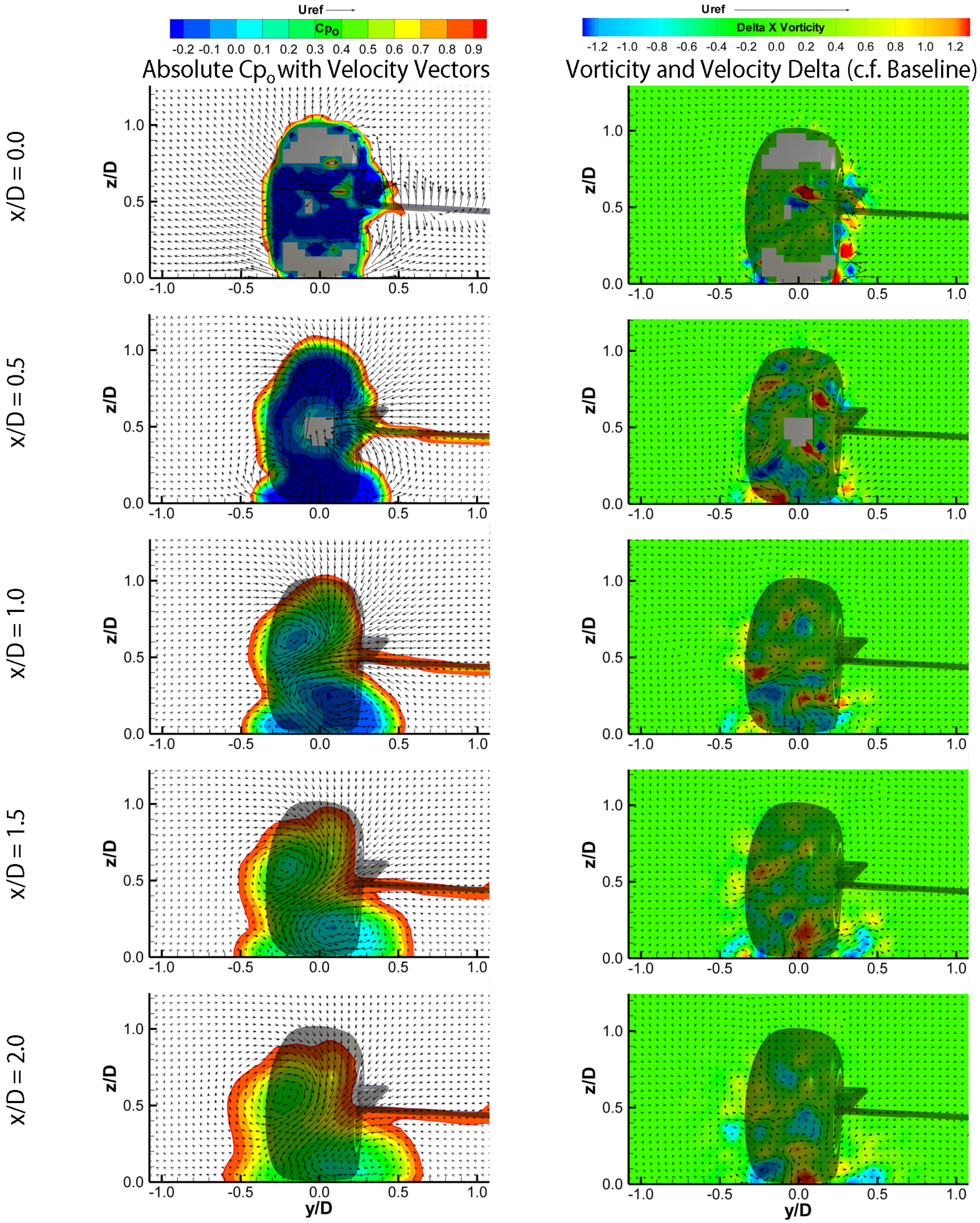

Figure 5.27: *Case 8: Y-Z crossplanes of: Absolute stagnation pressure and velocity vectors (left); Vorticity and velocity vector baseline deltas (right).*

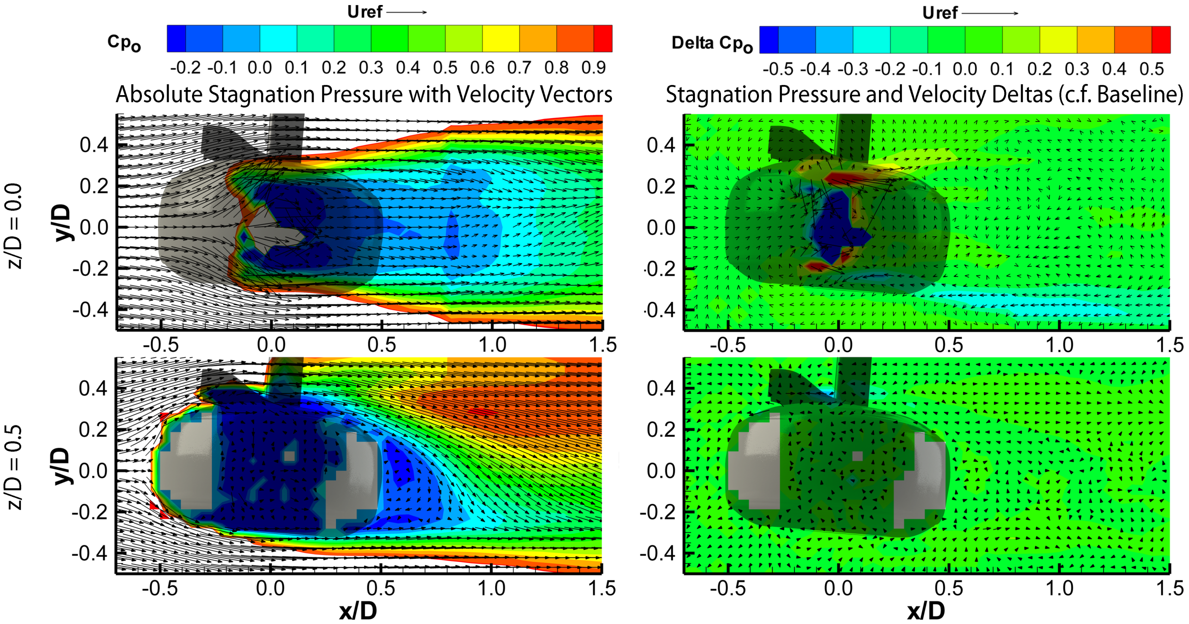

Figure 5.28: *Case 8: X-Y horizontal planes of stagnation pressure with velocity vectors. Absolute values (left) and baseline deltas (right).*

From Tables 5.17 and 5.18, the second of the investigations into the effect of using a non-yawed profile, at yaw, has yielded similar results in terms of lift and a similar size drag force albeit opposite in polarity to Case 5. There is no appreciable difference from the iso-surface plots in Figure 5.26, which was not the true of Case 5. In fact, despite much smaller blockage on the inboard sidewall, the resulting wake could be argued to be effectively negligible in difference.

Subtle changes can be observed in the crossplanes, but when comparing the left side of Figure 5.27 with Figure 5.18 there is very little difference. The delta plot for vorticity on the right-hand side shows a stronger ground level outboard contact patch vorticity (c.f. baseline) throughout. This was true of Case 5 although this had decayed by x/D = 1.5.

The horizontal wakes show little evidence of change other than a slight lowering of the pressure for the outboard wake and of course, a significant reduction in contact patch stagnation pressure. This suggests that, at a high axle height, the effect of yawing the tyre has a much less global effect than at low axle heights. In addition to absolute forces and local pressures, the changes to a full-car development with this compromise would be minor.

5.2.10 Case 9 - 150mm Axle, -5° Yaw (Realistic Profile)

Case 9 represents a wheel at negative yaw with low axle height. For a front-left wheel, negative yaw represents the inside wheel on a left-hand turn which would usually become unloaded. It is therefore intended as a direct comparison of flow-field sensitivities to yaw, given real-world likelihood is low.

Table 5.19: *Yaw simulation detail: Case 9 geometry schematic and forces (absolute & baseline deltas).*

Case: 9		**Axle Height:** 150mm	**Yaw (β):** -5°	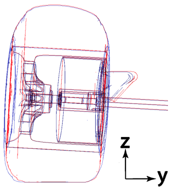
Description: Experimentally Measured Profile		**Baseline Case:** 1		
Aerodynamic Forces: $C_{D,axial} = 0.517$	$C_L = 0.510$	**(Case - Baseline) Force Deltas:** $\Delta C_{D,axial} = +0.067$	$\Delta C_L = +0.045$	

Table 5.20: *Aerodynamic force breakdown (absolute and baseline deltas) of yaw simulation Case 9.*

Component	Absolute Forces			(Case - Baseline) Force Deltas		
	$C_{D,axial}$	C_{side}	C_L	$\Delta C_{D,axial}$	ΔC_{side}	ΔC_L
Wheel (Rim and Tyre)	0.491	0.004	0.500	+0.069	-0.038	+0.041
Brake Scoop	0.024	0.090	0.004	-0.010	-0.004	+0.002
Barrel / Shroud	-0.005	-0.054	0.010	+0.007	+0.046	0.000
Hub	0.007	-0.028	0.000	+0.003	0.000	0.000
Inboard Disc (Upright)	-0.001	0.032	-0.003	-0.003	-0.055	+0.003
Wheel Nut	0.000	-0.005	0.000	0.000	+0.001	0.000

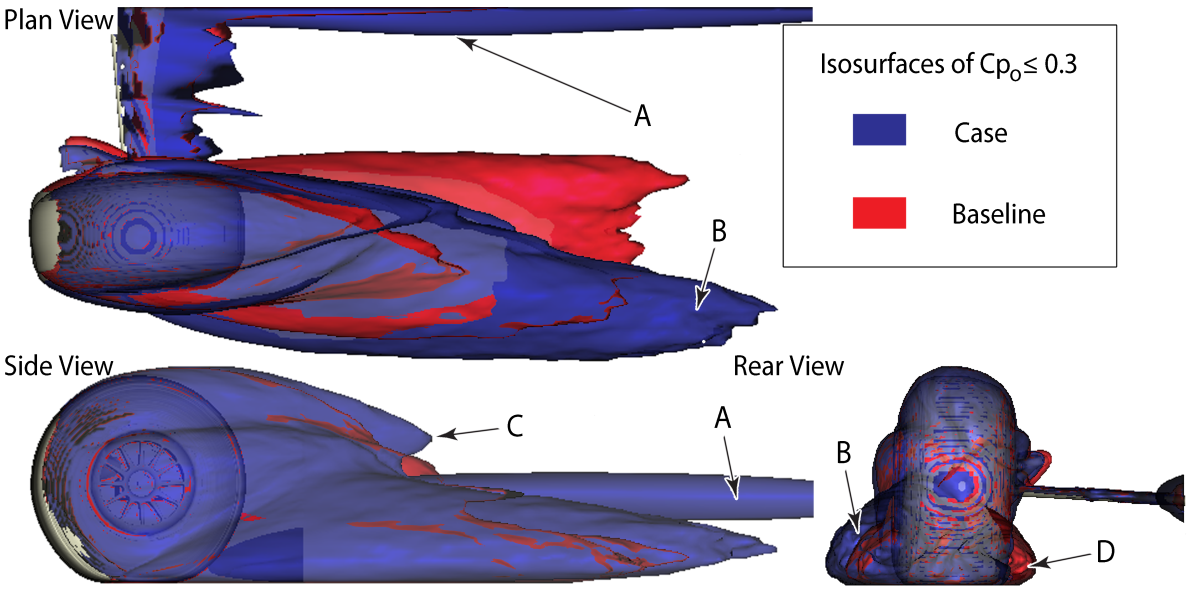

Figure 5.29: *Isosurface plots of $Cp_o \leq 0.3$, comparing Case 9 (blue) with its associated baseline (red).*

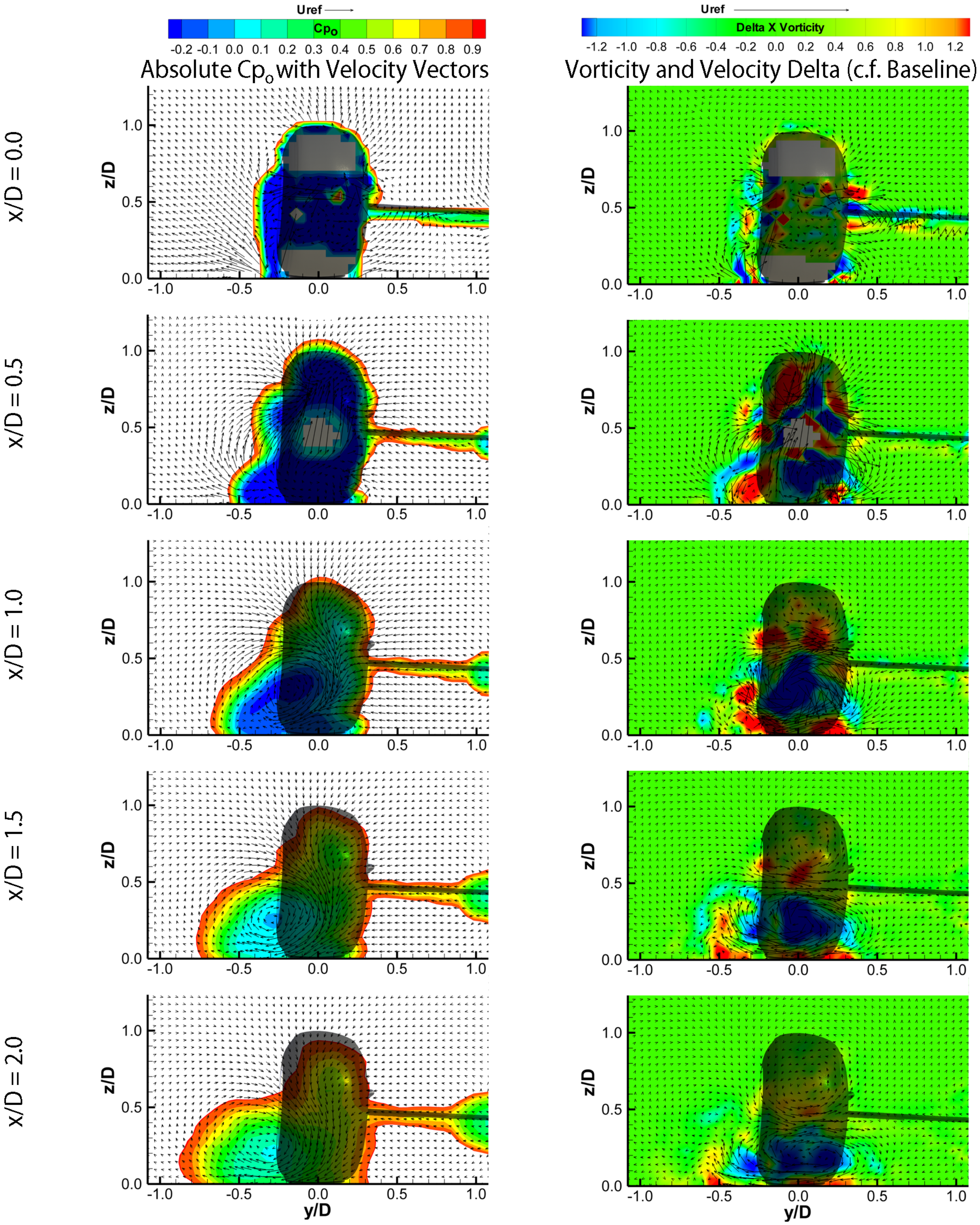

Figure 5.30: *Case 9: Y-Z crossplanes of: Absolute stagnation pressure and velocity vectors (left); Vorticity and velocity vector baseline deltas (right).*

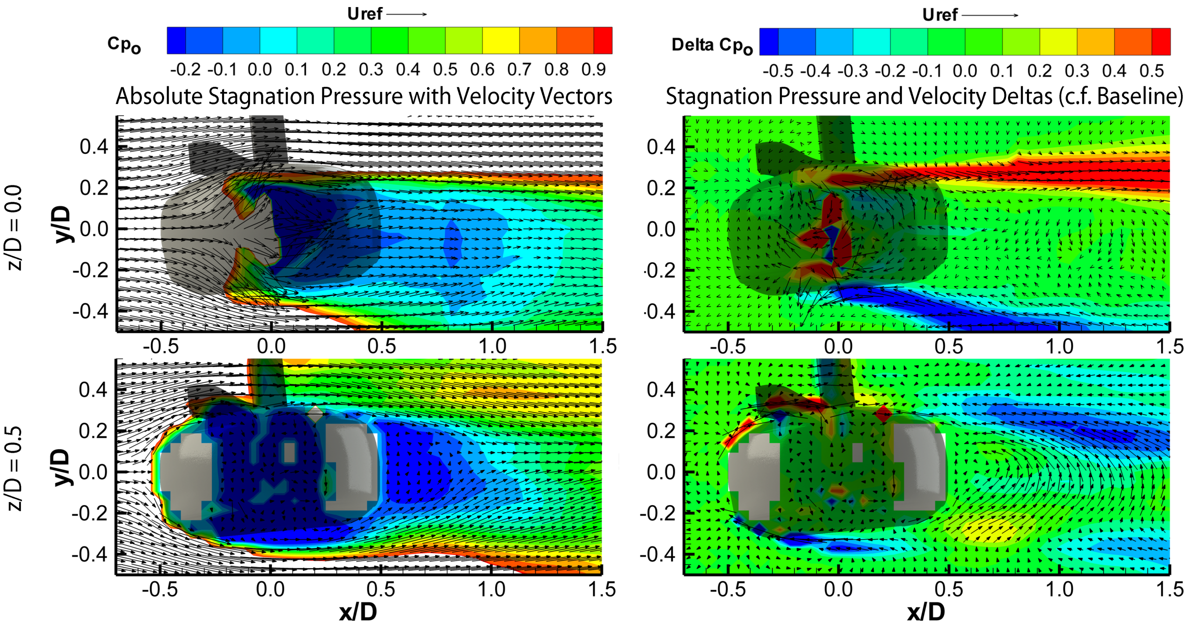

Figure 5.31: *Case 9: X-Y horizontal planes of stagnation pressure with velocity vectors. Absolute values (left) and baseline deltas (right).*

At negative yaw the tyre is not maximising its full potential with this camber set up. The sensitivity to the contact patch geometry is less than at positive yaw and therefore, as seen in Chapter 3, the changes to the lower sidewalls are much less dramatic. Similar trends would therefore be expected to those of the positive yaw cases, but instead with reduced magnitude.

From Table 5.19 the inboard sidewall is almost identical to the non-yawed case and as such the biggest change due to geometry detail would be expected on the outboard of the tyre and wake. Whilst the magnitude of the drag increase from the tyre and rim is similar to the overall change, it is important to note that the drag of the scoop has been significantly reduced by around 10 counts and this has been balanced out by changes to the drag of the internal geometry, as was the case with positive yaw. Again, when determining the change to the lift, this has been solely due to the rim and tyre.

Comparing with Case 4's deltas-to-baseline (the equivalent axle height but at positive yaw), the drag increase was slightly smaller at 10% as opposed to 15% in this case, and the lift increase slightly bigger at 23% as opposed to 9%. The lift is understandable through less blockage and a smaller change in contact patch width. The larger change in drag becomes clear when observing the flow-field.

The iso-surfaces presented in Figure 5.29 show a further structural change to the flow-field. The sting has produced a dominant structure at the join between the main section and the reinforcement (A). This is at least one diameter away from the wake so is not a major concern. More significantly, the wake appears to be narrowed, again, and almost entirely biased towards the outboard side (B). In fact, when observing from the rear, the wake is not visible any further inboard than the tyre's inboard sidewall (D). There is also a section of the upper wake which is more persistent and does not decay away as quickly as in the baseline case (C).

Figure 5.30 shows the crossplane development of the wake. This exhibits yet another vastly different flow system to either the straight-ahead or positive yaw cases. The vertical downwash usually observed on the straight-ahead cases has resumed and the flow is now dominated by an outboard vortex feature and a near enough non-existant inboard feature. This is consistent with the data from the iso-surface plots. The significant patches of blue in the vorticity delta plot (clockwise with figure) shows the outboard feature is strong. Where the extent of the wake used to range from around x/D = ±0.5 the wake now, at the furthest dowstream and most dispersed point, ranges from $-0.9 < x/D < 0.3$. The persistent low pressure core and increase in total width is reflected in the drag.

Looking toward the horizontal planes in Figure 5.31 the pressures at the contact patch are much higher than the baseline case, even though there is higher blockage. This is clearly responsible for the increase in lift. The downstream section of the wake at ground height emphasises the outboard shift of the propagating features. Perhaps the most significant observation from this figure is that the axle height vectors have reversed in recirculation direction. This was also observed in the PIV measurements in Figure 3.33 in Chapter 3.

Summarising the observations here, it would appear that negative yaw is as inclined to change the flow-field as positive yaw. The major changes appear to be the effect of the global change as opposed to the subtleties of the lower tyre profile. This will be investigated in the coming case studies.

When considering a car with a 'toe-out' setup, which is known to be mechanically favourable for a modern F1 car (Chapter 1), the wake is washed away from the downstream components of the car with minimal vorticity on the inboard side.

5.2.11 Case 10 - 150mm Axle, -5° Yaw (Straight-Ahead Profile)

Case 10 is an extension of the principal used for Case 5, using a straight-ahead profile instead of a correctly yawed tyre. It has been shown experimentally that the geometry of the tyre profile changes much less at negative yaw than for positive yaw, due to the camber of the wheel (Figure 3.21).

Table 5.21: *Yaw simulation detail: Case 10 geometry schematic and forces (absolute & baseline deltas).*

<table>
<tr><td>Case: 10</td><td>Axle Height: 150mm</td><td>Yaw (β): -5°</td><td rowspan="3">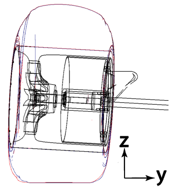
</td></tr>
<tr><td>Description:
Straight-Ahead Profile at -5° Yaw</td><td colspan="2">Baseline Case: 9</td></tr>
<tr><td>Aerodynamic Forces:
$C_{D,axial} = 0.519$ | $C_L = 0.531$</td><td colspan="2">(Case - Baseline) Force Deltas:
$\Delta C_{D,axial} = +0.002$ | $\Delta C_L = +0.021$</td></tr>
</table>

Table 5.22: *Aerodynamic force breakdown (absolute & baseline deltas) of yaw simulation Case 10.*

Component	**Absolute Forces**			**(Case - Baseline) Force Deltas**		
	$C_{D,axial}$	C_{side}	C_L	$\Delta C_{D,axial}$	ΔC_{side}	ΔC_L
Wheel (Rim and Tyre)	0.492	0.003	0.522	+0.001	0.000	+0.023
Brake Scoop	0.024	0.091	0.005	0.000	0.000	+0.001
Barrel / Shroud	-0.005	-0.053	0.007	0.000	0.000	-0.003
Hub	0.008	-0.028	0.000	+0.001	0.000	0.000
Inboard Disc (Upright)	-0.001	0.031	-0.003	0.000	-0.001	0.000
Wheel Nut	0.000	-0.006	0.000	0.000	0.000	0.000

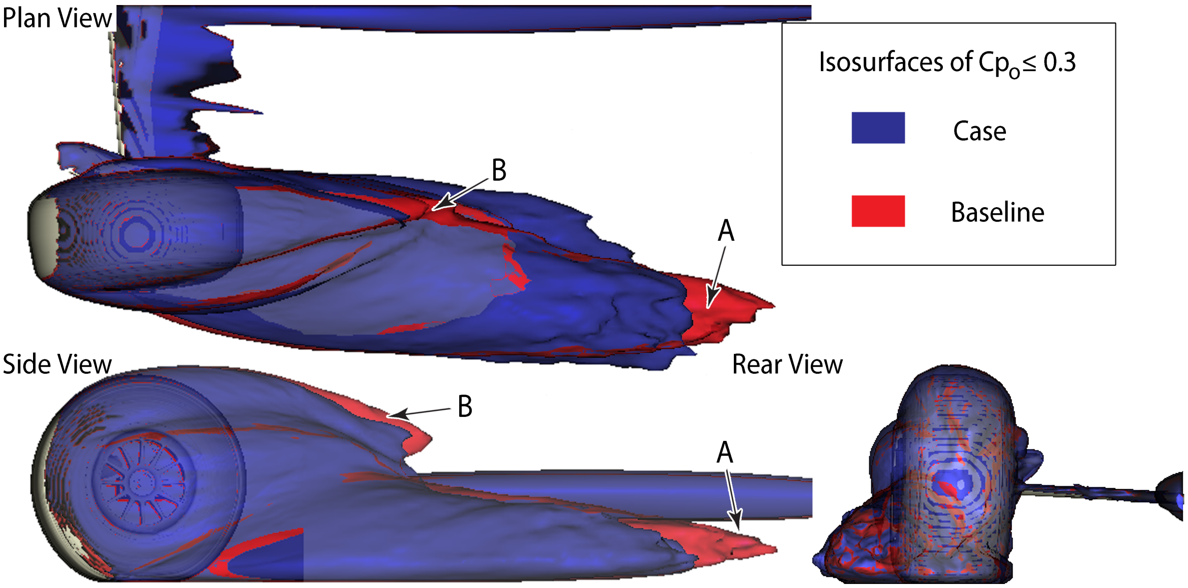

Figure 5.32: *Isosurface plots of $Cp_o \leq 0.3$, comparing Case 10 (blue) with its associated baseline (red).*

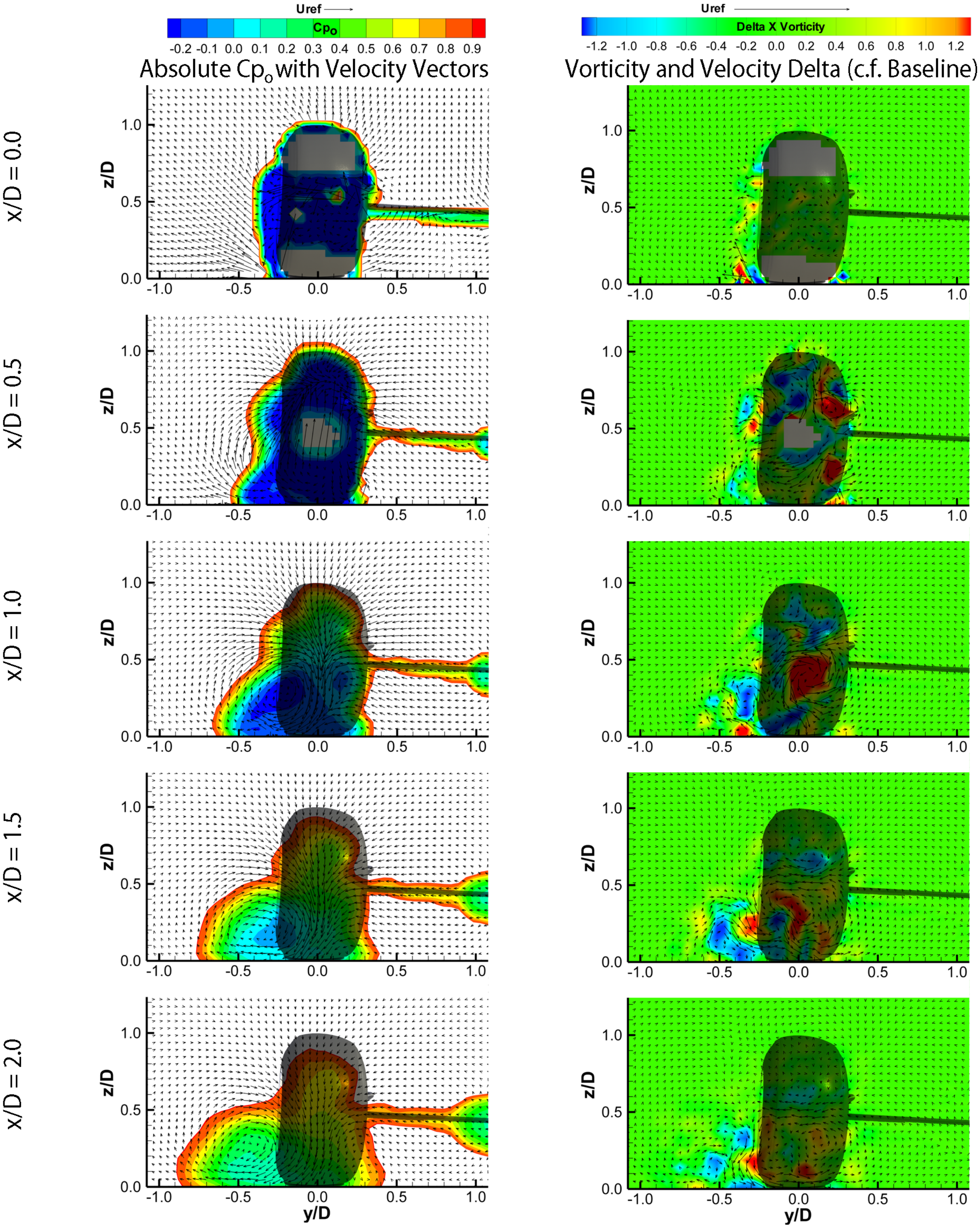

Figure 5.33: *Case 10: Y-Z crossplanes of: Absolute stagnation pressure and velocity vectors (left); Vorticity and velocity vector baseline deltas (right).*

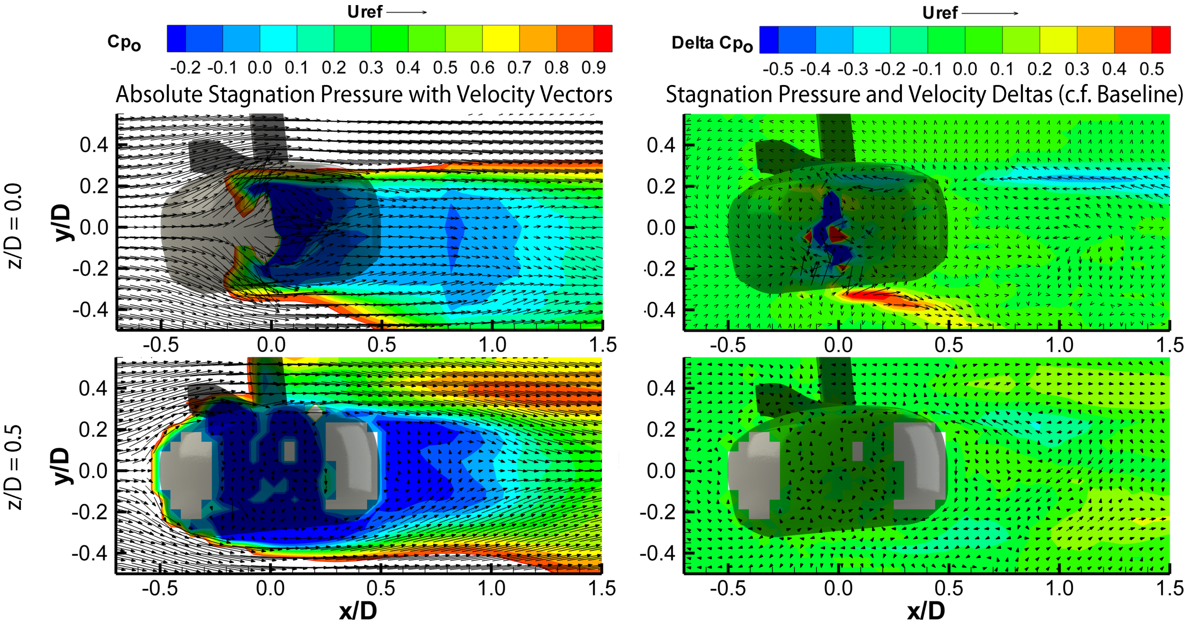

Figure 5.34: *Case 10: X-Y horizontal planes of stagnation pressure with velocity vectors. Absolute values (left) and baseline deltas (right).*

The previous simulations of a non-yawed tyre profile, at yaw, yielded mixed results. The low axle height cases showed differences to both the local and far-field wake whereas the higher axle height showed very little difference other than local forces.

The drag result from Table 5.21 shows negligible difference to the baseline. Unlike other cases where there was actually a significant change which was cancelled out by another area, this is a true insensitivity. The lift, however, shows an increase by 23 counts. This is opposite to the trend expected by using a non-yawed profile, which by the very nature has less low-down blockage. The two profiles are geometrically similar as can be seen in the summary table and in more detail in Chapter 3.

Aerodynamic drag is determined not only by local effects but also by the global flow-field. The iso-surfaces in Figure 5.32 do not tell the same story of insensitivity to lower profile dragging at yaw. The wake is much shorter (A) than the baseline case with a realistic profile and the upper wake also decays much faster (B). The general form from a rearward view confirms that there is nothing substantially different in the structure but more that these features have been weakened in the presence of a non-yawed profile.

Taking this argument further and looking at the detail in the crossplane figure (Figure 5.33), the shape of the wake is quite different from the case with the realistic profile. The now perfectly vertical downwash is centred much more outboard than previously, thus opening up a small inboard vortex feature bulging out beyond the tyre. This was the region mentioned in the previous case as being completely free of any wake structure. The outboard feature is similar in size and shape although higher in average stagnation pressure. The height of the wake is also lower from x/D = 1.0 and downstream of that. This suggests faster decay of the wake which would be logical given the higher core pressure.

The vorticity plots show the retardation of the core centre for the outboard feature (red region surrounded by yellow). The core is surrounded by a blue region suggesting the vortex has increased in size and consistency despite the core not being as tightly formed.

Further significant differences are observed at the ground for the horizontal planes. There is a large region of higher pressure on the outboard contact patch wake which is as a result of the reduced blockage from a non-yawed profile. This propagates downstream at a rather severe angle, similar to that of the wake direction for a negatively yawed wheel. The frontal contact patch shows a pressure reduction suggesting energy has been taken out of the flow at this point, despite the relatively easier path to be taken. Chapter 6 discusses the effect of contact patch shape and the favourable conditions for local flow to accelerate which appears to be responsible for lift sensitivity in this section. The axle height plane shows practically no change to the wake.

This is perhaps the most severe example of the effect that a compromise in experimental or simulation technique can make on the aerodynamics of the system. It is becoming more and more obvious that the changes even locally at such low heights have dramatic effects on the overall wake and the forces. This case is not achievable in a wind tunnel (except perhaps for the use of a rigid tyre at yaw) but is almost certainly a common technique, in the literature at least, of simulating a wheel at yaw in CFD.

5.2.12 Case 11 - 159mm Axle, -5° Yaw (Realistic Profile)

Case 11 is as Case 9 but at a higher axle height. However, Case 11 is a much more realistic combination of parameters due to the fact that the wheel in question turned to negative yaw describes the unloaded inside wheel of a corner. This is simulated more accurately with a higher axle height.

Table 5.23: *Yaw simulation detail: Case 11 geometry schematic and forces (absolute & baseline deltas).*

Case: 11		**Axle Height:** 159mm	**Yaw (β):** -5°	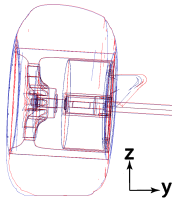
Description: Experimentally Measured Profile		**Baseline Case:** 2		
Aerodynamic Forces: $C_{D,axial} = 0.494$	$C_L = 0.598$	**(Case - Baseline) Force Deltas:** $\Delta C_{D,axial} = +0.012$	$\Delta C_L = +0.209$	

Table 5.24: *Aerodynamic force breakdown (absolute & baseline deltas) of yaw simulation Case 11.*

Component	**Absolute Forces**			**(Case - Baseline) Force Deltas**		
	$C_{D,axial}$	C_{side}	C_L	$\Delta C_{D,axial}$	ΔC_{side}	ΔC_L
Wheel (Rim and Tyre)	0.466	-0.021	0.588	+0.020	-0.006	+0.206
Brake Scoop	0.025	0.094	0.003	-0.012	-0.007	-0.005
Barrel / Shroud	0.000	-0.072	0.011	+0.010	-0.002	+0.002
Hub	0.006	-0.018	0.000	-0.003	+0.071	+0.003
Inboard Disc (Upright)	-0.003	0.056	-0.004	-0.004	-0.059	+0.003
Wheel Nut	0.000	-0.003	0.000	0.000	0.000	0.000

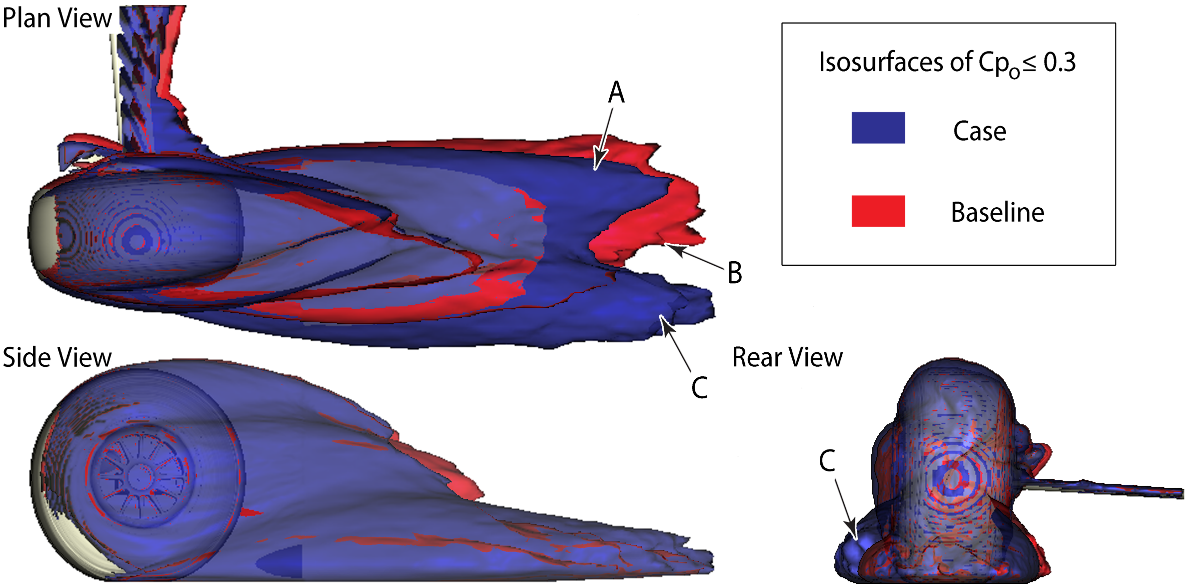

Figure 5.35: *Isosurface plots of $Cp_o \leq 0.3$, comparing Case 11 (blue) with its associated baseline (red).*

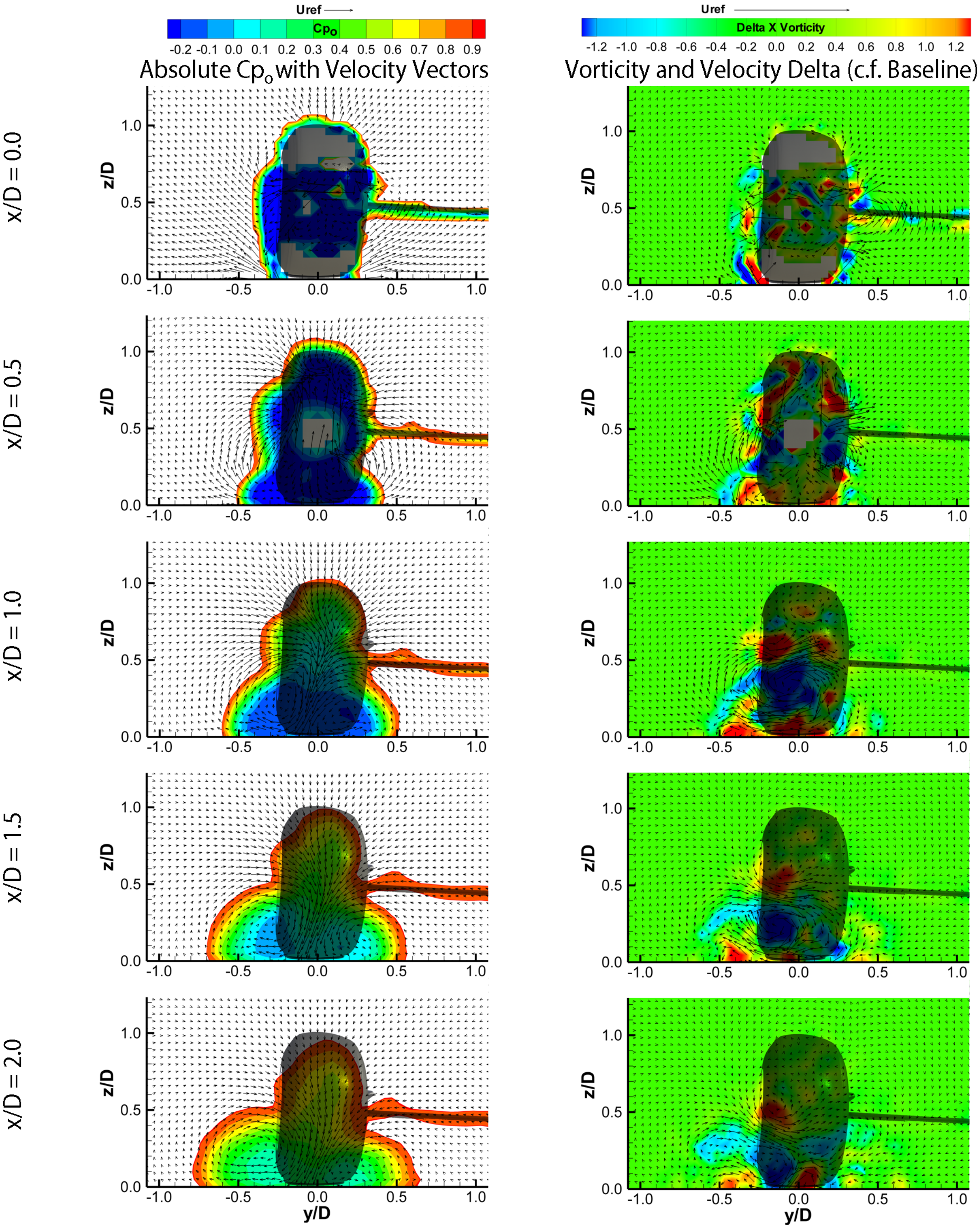

Figure 5.36: *Case 11: Y-Z crossplanes of: Absolute stagnation pressure and velocity vectors (left); Vorticity and velocity vector baseline deltas (right).*

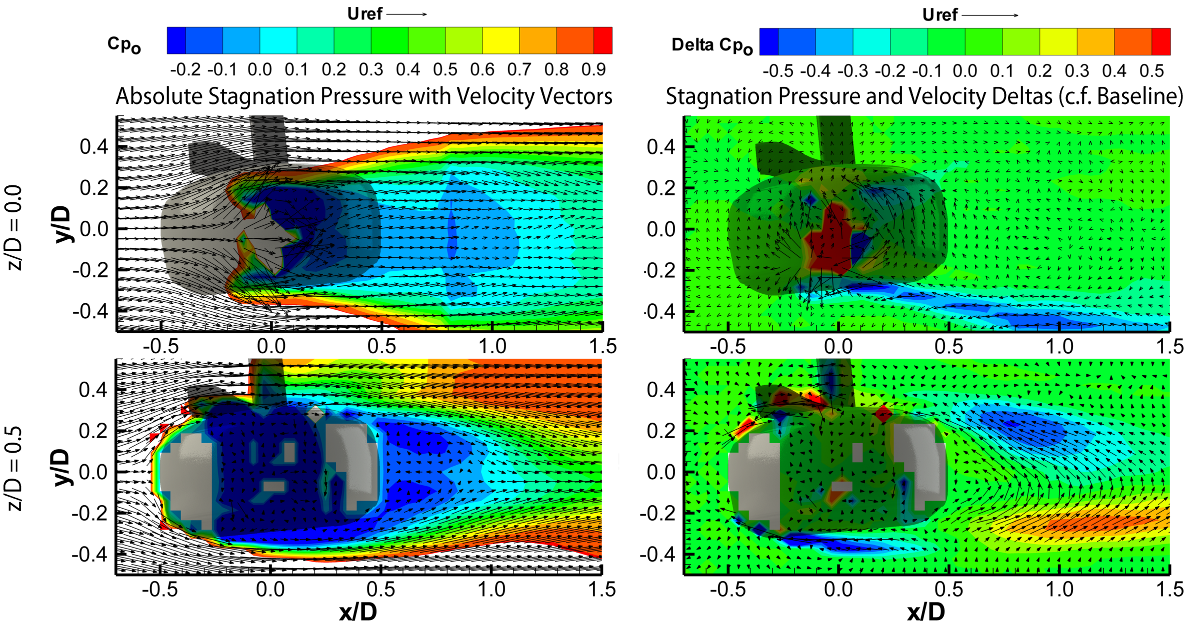

Figure 5.37: *Case 11: X-Y horizontal planes of stagnation pressure with velocity vectors. Absolute values (left) and baseline deltas (right).*

This case is similar to Case 7 in that it effectively has two baselines. Case 2 has again been chosen to observe the effect of yawing the wheel with a higher axle height but constant references will be made to Case 9 (with its baseline, Case 1) which is the same as this case but at a lower axle height.

The force measurements in Table 5.23 show an increase in both lift and drag relative to the lower axle height case (Case 9). The drag increase is only 12 counts as opposed to 67 and the lift increase is a considerable 209 counts instead of 45. Table 5.24 shows that there is in fact a large increase in drag for both the rim and tyre combination as well as the barrel. The brake scoop reduces the drag increase by 12 counts compared to the straight-ahead case. This is similar to the change in the low axle height case (Case 9). The difference between the high and low axle case is therefore solely to do with the external flow effect due to the rim and tyre and this is also true of the lift force.

The lack of similarities to either baseline are a continued theme for the iso-surface plots in Figure 5.35. In Case 9 the wake was drastically narrowed compared to Case 2 and washed outboard by nearly a wheel diameter in the negative y-direction, the structure of the wake here is very similar to that found in Case 2 (at zero yaw).

There is still evidence of an outboard feature movement although the inboard feature has now reappeared. The missing inboard feature in Case 9 was not purely a case of the blue iso-surface engulfing it. The crossplane wake development also showed no evidence of its presence.

The crossplane wake development in Figure 5.36 reveals the implied features from the iso-surfaces. The inboard feature is indeed recovered and has a width of around y/D = 0.5 and a height of z/D = 0.3 by the furthest downstream point. Given this feature was non-existent for the lower axle height, this is significant. The vertical downwash is present as was the case for the lower axle height. When comparing to the baseline, the non-yawed case, the flow-field is similar with the exception that the outboard vortex is the dominant feature. There is also evidence of separation at the leading edge of the tyre which is never fully recovered in the wake. This is most visible at the x/D = 0.5 position. The height of the wake is does not decay very quickly either. The outboard feature, although still dominant, is smaller and of higher average pressure than the lower axle case. Again, taking the furthest downstream observation point, the outboard feature is around 0.5D in height and width, as opposed to having the same height but with a width of 0.8D. Overall, however, this is the widest wake of all the test cases.

The vorticity delta plot again shows fairly noisy patches of changed vorticity. The mid-to-outboard is dominated by a large blue patch showing emphasis of a clockwise vortex structure (outboard feature's direction). The ground plane does, however, feature a few red patches which represent the retardation of the vorticity in that region and therefore the smaller feature as explained.

The horizontal planes also show differences to the lower axle case. The reversal of recirculation zone vorticity is present again, although the sizes of the red and blue streaks are different or in one case (inboard ground level) not present. This shows a change to the width as well as location of the wake.

It is clear that there is an entirely different flow-field for high and low axle heights at the same yaw angle. Throughout it has been observed that applying the incorrect, or not being able to apply sufficient deformation leads to a change in the wake structures that would interfere with downstream components and therefore affect the performance of any car developed with those methodologies.

5.2.13 Case 12 - 159mm Axle, -5° Yaw (Straight-Ahead Profile)

Case 12 is a further investigation into the differences between the non-yawed profile and the realistic geometry as tested in Case 11. At higher axle height, for negative yaw, this case was geometrically the most similar to a straight-ahead profile (as can be seen in the geometry schematic in the table below).

Table 5.25: *Yaw simulation detail: Case 12 geometry schematic and forces (absolute & baseline deltas).*

Case: 12	**Axle Height:** 159mm	**Yaw (β):** -5°	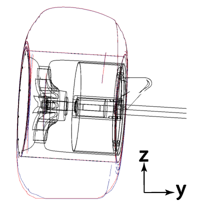
Description: Straight-Ahead Profile at -5° Yaw	**Baseline Case:** 11		
Aerodynamic Forces: $C_{D,axial} = 0.486$ $C_L = 0.409$	**(Case - Baseline) Force Deltas:** $\Delta C_{D,axial} =$ -0.009 $\Delta C_L =$ -0.189		

Table 5.26: *Aerodynamic force breakdown (absolute & baseline deltas) of yaw simulation Case 12.*

Component	**Absolute Forces**			**(Case - Baseline) Force Deltas**		
	$C_{D,axial}$	C_{side}	C_L	$\Delta C_{D,axial}$	ΔC_{side}	ΔC_L
Wheel (Rim and Tyre)	0.457	-0.074	0.397	-0.008	-0.053	-0.192
Brake Scoop	0.025	0.093	0.003	-0.001	-0.002	0.000
Barrel / Shroud	-0.001	-0.074	0.012	-0.001	-0.002	+0.001
Hub	0.007	-0.020	0.000	+0.001	-0.002	0.000
Inboard Disc (Upright)	-0.002	0.046	-0.003	+0.001	-0.009	+0.001
Wheel Nut	0.000	-0.003	0.000	0.000	0.000	0.000

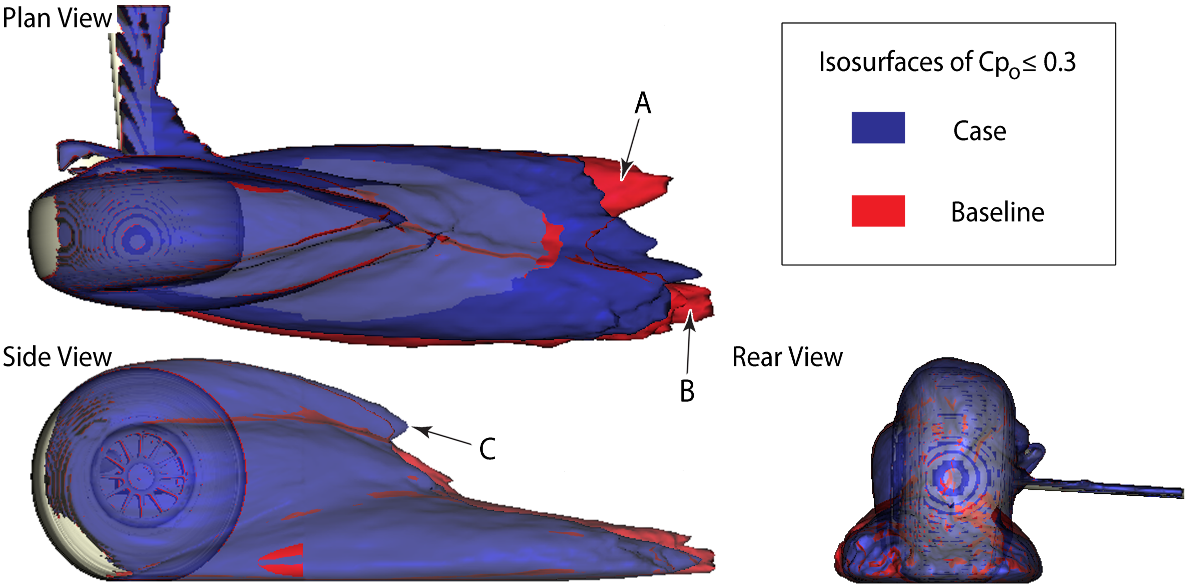

Figure 5.38: *Isosurface plots of $Cp_o \leq 0.3$, comparing Case 12 (blue) with its associated baseline (red).*

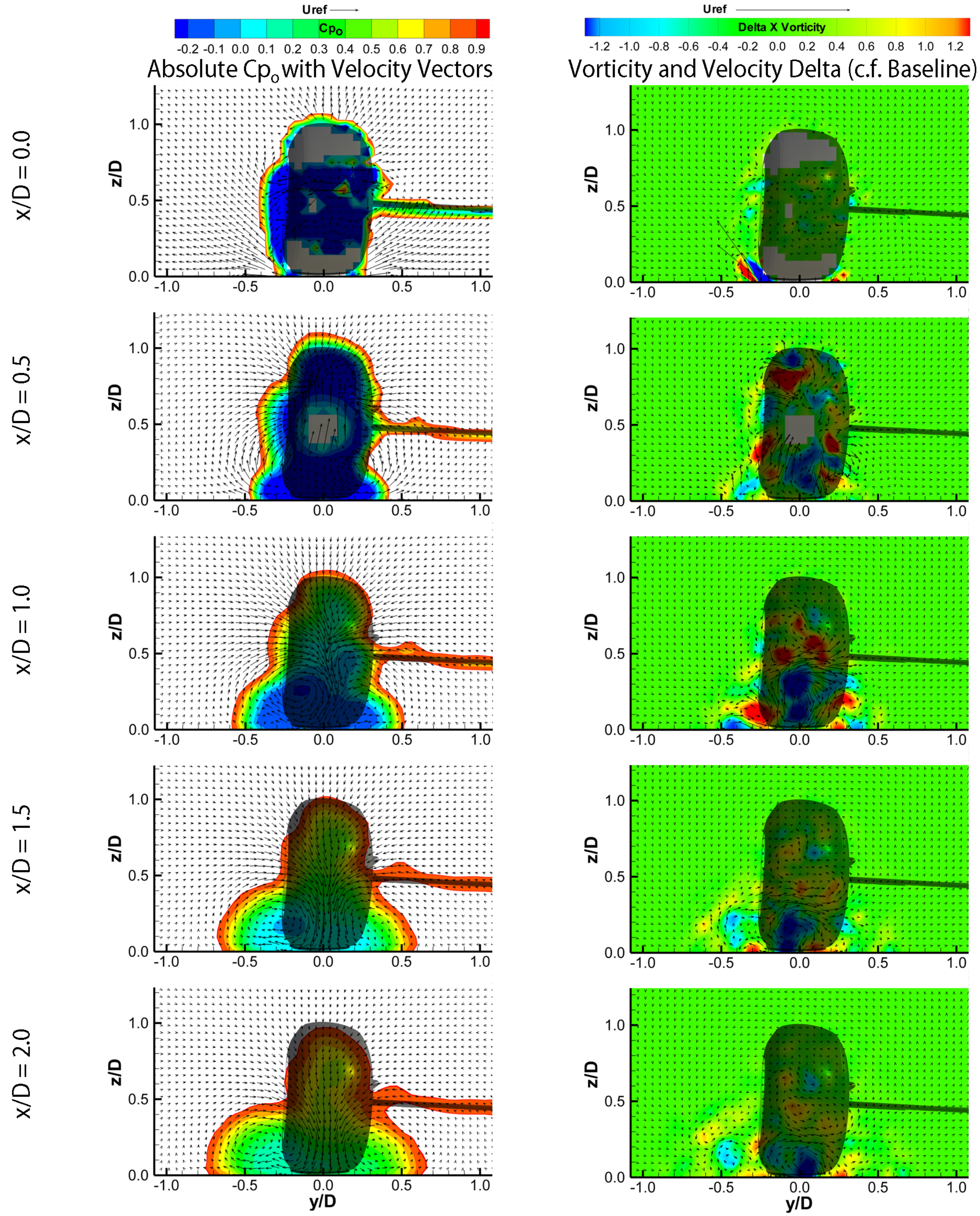

Figure 5.39: *Case 12: Y-Z crossplanes of: Absolute stagnation pressure and velocity vectors (left); Vorticity and velocity vector baseline deltas (right).*

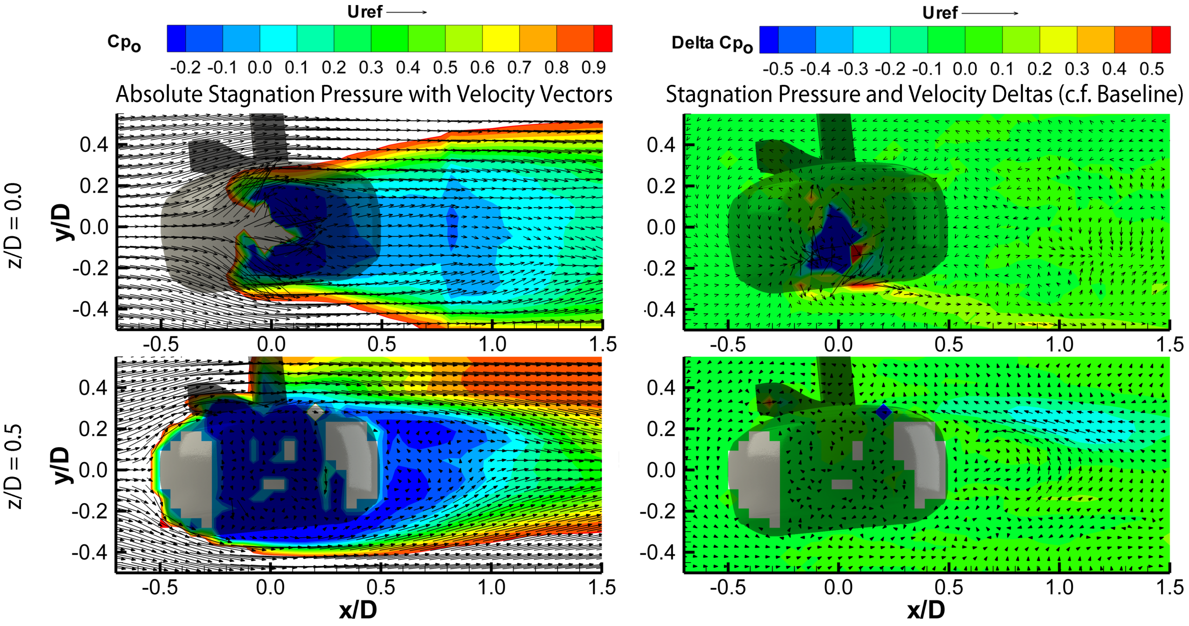

Figure 5.40: *Case 12: X-Y horizontal planes of stagnation pressure with velocity vectors. Absolute values (left) and baseline deltas (right).*

In this last of the sensitivity tests of CFD geometry simplification, not much has changed in the global flow-field relative to the baseline. The forces in tables 5.25 and 5.26 have both resulted in decreases of similar magnitude to the non-yawed profiles at positive yaw. This was not the case for the low axle height case for negative yaw, although it has already been shown that the higher axle height flow-field is significantly different.

Indeed the general flow-field of the iso-surface plots (Figure 5.38) and the crossplane development show minimal changes to Case 11 (baseline). The vorticity deltas show areas of red mainly on the outboard side of the tyre which suggests a retarding vortex core although the changes by x/D = 1.5 are minimal. The horizontal planes shown in Figure 5.40 show the smallest sensitivity yet, aside from the large blue patch below the contact patch which is consistent with the non-yawed cases at positive yaw.

From the evidence presented here it would appear that Case 12 is the least sensitive geometrical change, aerodynamically, and by examining the profiles tested in the summary table (Table 5.25) this is perhaps no surprise. All of the results within this section are discussed in detail in combination with the findings in the wind tunnel results in Chapter 6.

5.2.14 Force and Pressure Comparisons Across Simulations

The case-by-case analysis above has shown some key areas and comparisons between mostly similar geometries. This section is intended to extract extra information from those simulations before concluding with an investigation into detailed internal geometry.

5.2.14.1 Aerodynamic Drag

The aerodynamic drag forces for the non-yawed baseline cases (cases 1 and 2) have been presented as part of the CFD validation (end of Chapter 4). Building on this, the data presented in Figure 5.41 show the drag for the full sweep between negative yaw through to positive yaw. The two baseline sweeps each represent the two axle heights with realistic profiles inclusive of lower profile dragging as a result of yaw. These were cases 1, 2, 4, 7, 9 and 11.

Now that the case-by-case analysis has been established, Figure 5.41 shows the global trends. There is an increase in drag with yaw, which, although expected due to at least the increase in frontal area, is highly sensitive to the axle height. It is clear that at the higher axle height the drag undergoes a much smaller change throughout the range and is therefore considered less sensitive. In fact, the two axle heights cross over through the range. The zero yaw condition for the higher axle height is 7% higher in drag but for both yaw angles tested, it is at least 3% lower than the lower axle height cases. The trends are also not symmetrical showing a smaller increase and therefore lower absolute drag for the positive yaw case compared to the negative yaw case. The geometrical measurements in Chapter 3 suggested greater sensitivity to the width of the contact patch for positive yaw in conjunction with the camber angle being used. This suggests the drag changes are not dominated by changes at the contact patch but instead by to the details of the profile shape.

In addition to the realistic profile sweeps, non-yawed profiles were tested at yaw (cases 5, 8, 10 and 12) in order to observe the differences between the profiles on the aerodynamic system. It is important to note, for this and for the individual case studies, that the only difference in the profiles is due to the compression of the lower section due to axle height. As a simplification, the contact patch size and

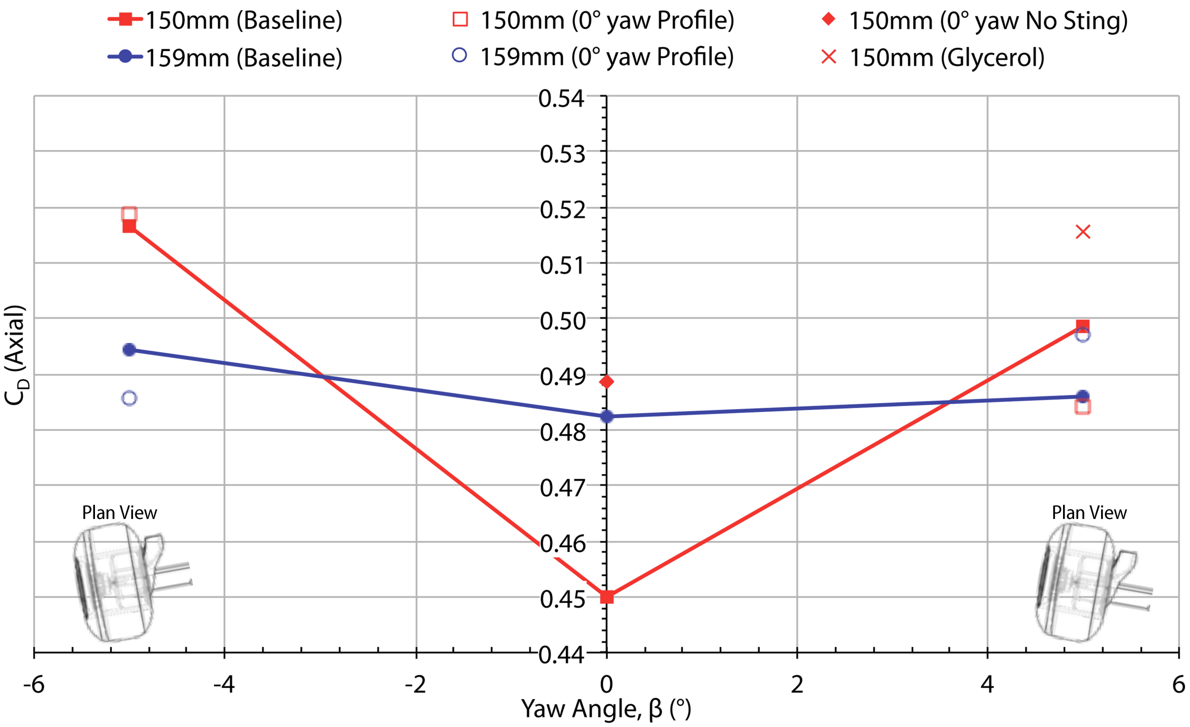

Figure 5.41: *Axial drag forces for 0, ±5° yaw at 150mm and 159mm. Realistic profiles, non-yawed profile, glycerol profile and case without a sting.*

shape, the horizontal mid-height profiles and the upper shoulders of the realistic profiles are exactly the same as the non-yawed tyre. Therefore any changes to the simulation geometry were solely as a result of the lower profile change going from straight-ahead to ±5° yaw.

Observing the drag force measurements, the largest difference is at positive yaw at 3% lower than its realistic profile. For the high axle height, the positive yaw case over-predicts with a simple straight-ahead profile whereas for negative yaw the drag under-predicts. However, the exact opposite is true for the low axle height.

Further discrepancies arise from the glycerol profile, which was expected to be a half-way case between the non-yawed profile and the realistic one. In this case, the glycerol drag measurement is 3.5% in excess of the realistic profile, and 6.5% higher than the non-yawed condition.

It is considered that the observation made in Chapter 3, whereby the transition between the sidewall and the tread was smoothed out because of glycerol build-up has led to an inconsistent drag reading. The relationship with this step and its effect on the aerodynamic features is discussed in Chapter 6.

Likewise, an observation has been made whereby the case without a sting has resulted in an increase in drag. The likely cause of this is due to a difference to the drag of the scoop, responsible for the increase by 8%. This is of the same magnitude as the scoop's contribution to the overall drag.

5.2.14.2 Aerodynamic Lift

In addition to the drag forces, a study into the behaviour of the aerodynamic lift has been summarised in Figure 5.42. The data were taken from the same set of simulations as the drag measurements for the same set of geometrical profiles.

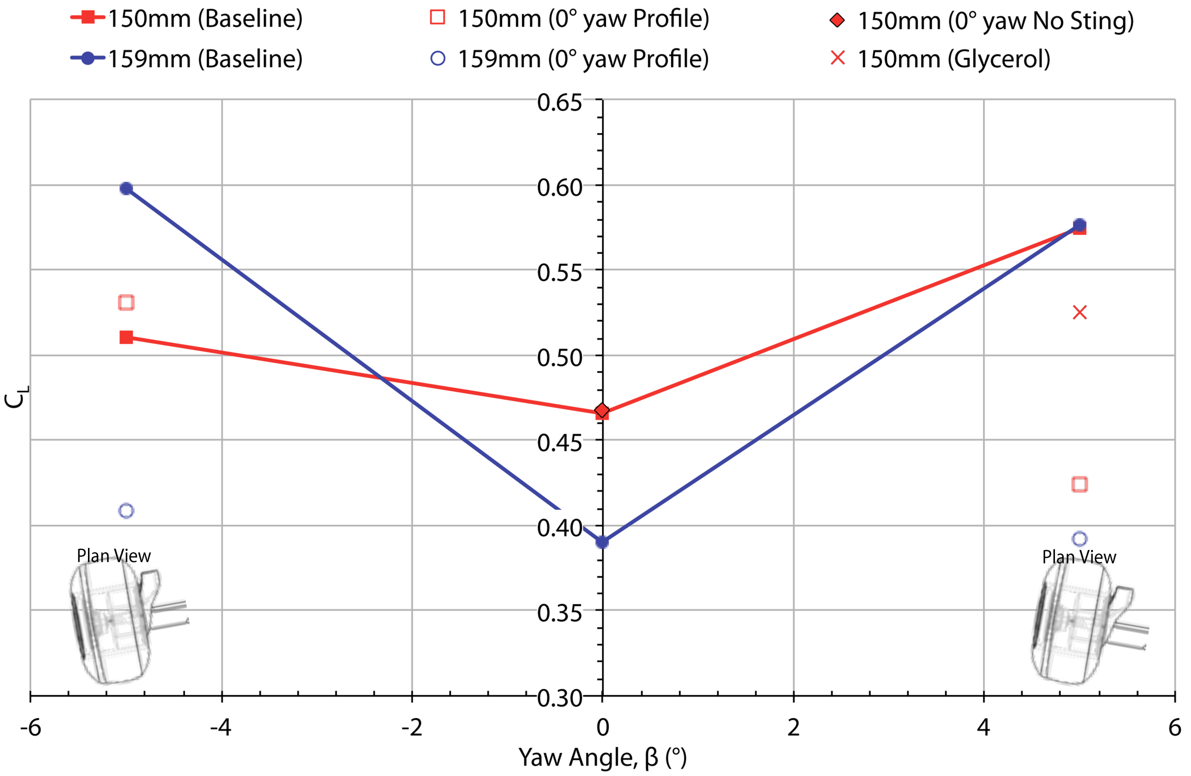

Figure 5.42: *Lift forces for 0,±5° yaw at 150mm and 159mm. Realistic profiles, non-yawed profile, glycerol profile and case without a sting.*

The magnitude of the lift at zero yaw is similar to that of the drag and when moving to yaw it becomes greater. The reason for this is perhaps less obvious than the drag increase. The most logical reasoning for the change in lift would be due to the reduction in relative blockage width underneath the tyre, now available to the fluid. Whilst this does not explain the opposite trend for the zero yaw cases, it is consistent with all of the trends observed by yawing the wheel. It is perceivable that the higher axle height has a more progressive and rounded contact patch shape and this encourages low-loss accelerated flow underneath the tyre. This too will be compared on a case-by-case basis in Chapter 6.

The higher axle height shows greater sensitivity to yaw than the lower one. This is the opposite trend to the drag forces. It is also evident that at higher axle heights the increase is more symmetrical whereas the low axle height is more sensitive to positive yaw. Geometrically, when considering the camber and positive yaw combination of the wheel, this leads to a more significant change and so this is expected to be reflected in the aerodynamics of the system. The glycerol case is in between the lift measurement for the realistic profile and the straight-ahead one. This is of the same proportion as the amount by which the contact patch has been reduced compared to the realistic shape. This is consistent with both the explanation for the lift force generation and the observations in the geometrical measurements.

The cases with non-yawed profiles are mostly below the realistic profiles. Again this would be explained by the reduced contact patch width and smaller low-down blockage than the highly deformed cases. This smaller blockage results in a much smaller area of high pressure stagnation which in turn causes high lift. This change is much more severe, being up to a 33% reduction compared to the realistic profile.

It was found that the removal of the sting had no appreciable effect on the lift of the wheel. In fact, the data points for cases 1 and 3 overlay almost perfectly. This suggests that the changes to the lift force are much more focused on local effects than global wake-development.

5.2.14.3 Surface Static Pressure Distribution

The static pressure distribution around the wheel centreline for Case 1 has been compared with the same parameter for the higher axle height in order to extract the separation points (the moment where the graph breaks free of the sinusoidal form consistent with a suspended cylinder in inviscid flow). These have been marked with an 'x' in Figure 5.43 and the value has been calculated based upon the measurement resolution of 0.4°.

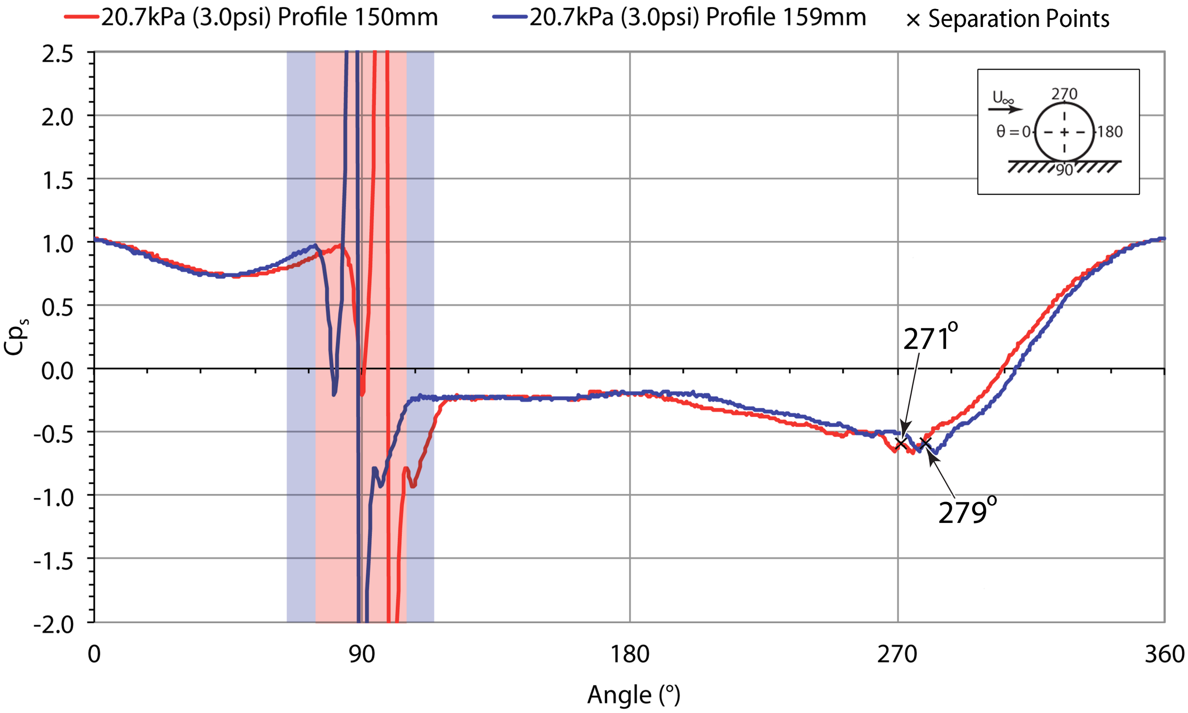

Figure 5.43: *Surface static pressure measurements of Case 1 (red) and Case 2 (blue) comparing low and high axle heights respectively at zero yaw. The shaded regions represents the contact patch regions for each respective coloured trace.*

As discussed in the validation section, the separation point of the low axle case was 271°. This is 8° earlier than the higher axle height which had a separation point of 279°, exactly that of Mears [3] and Fackrell [23]. Overlaying the higher axle height (blue) shows a similarity in the distrubution, albeit more stretched in the x-axis. The shaded regions represent the contact patches and although data are recorded within these regions they are not necessarily to be trusted. The region underneath the tyre was checked to ensure that there was no leaked airflow under the tyre, as confirmed by the vectors in the x-y horizontal planes in the previous section.

Due to the construction of the CAD geometry (Figure 4.5) it is possible that the perimeter of the ellipse shaped contact patch ‘curled up’ in the lofting process. The line constraints dictating the length and width of the contact patch will have prevented any leakage longitudinally or transversely but it is possible that very low down there is flow encroaching into, and therefore reducing the size of, the contact patch. This would be an explanation as to why the pressure distribution indicating jetting only spans a short range as opposed to the full length of the contact patch.

A later separation point usually corresponds to a higher drag and lift value when applying Fackrell’s postulated flow-physics [23]. Indeed the higher axle height did result in a higher drag although a lower lift force was recorded. This suggests that the pressures underneath the contact patch are not necessarily allowing the full picture to be observed, and therefore, unlike the drag measurements which are validated against experiment, they should be taken with caution. Further experimentation is recommended at the end of this work to develop the understanding of this region.

Both traces observe a spike consistent with Fackrell’s jetting phenomenon around the contact patch. The peak in both cases reach a maximum of Cp_s = 26.3 and a minimum of Cp_s = -3.03. These values are an order of magnitude higher than those observed by Mears [3] but similar to those observed by Hinson [32]. Although Hinson explained these by non-aerodynamic effects due to unwanted compression of the air in the static pressure tappings and tubes.

5.3 Effect of Internal Geometry (Spinning Rotor)

Case 13 is a new line of investigation to discover the effects, locally and globally, of including accurate internal geometry. The intention of this case is to discover if the rotation of the brake disc (rotor) assists the internal flow rate or if the blockage restriction reduces the maximum through-hub flow rate.

Table 5.27: *Yaw simulation detail: Case 13 geometry schematic and forces (absolute & baseline deltas).*

<table>
<tr><td colspan="2">Case: 13</td><td>Axle Height: 150mm</td><td>Yaw (β): 0°</td><td rowspan="3">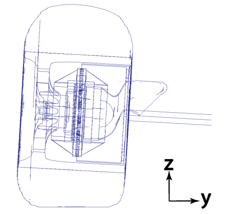 </td></tr>
<tr><td colspan="2">Description:
Case 1 with internal geometry</td><td colspan="2">Baseline Case: 1</td></tr>
<tr><td colspan="2">Aerodynamic Forces:</td><td colspan="2">(Case - Baseline) Force Deltas:</td></tr>
<tr><td>$C_{D,axial} = 0.552$</td><td>$C_L = 0.422$</td><td>$\Delta C_{D,axial} = +0.102$</td><td>$\Delta C_L = -0.043$</td><td></td></tr>
</table>

Table 5.28: *Aerodynamic force breakdown (absolute & baseline deltas) of yaw simulation Case 13.*

Component	**Absolute Forces**			**(Case - Baseline) Force Deltas**		
	$C_{D,axial}$	C_{side}	C_L	$\Delta C_{D,axial}$	ΔC_{side}	ΔC_L
Wheel (Rim and Tyre)	0.451	0.046	0.435	+0.029	+0.005	-0.024
Brake Scoop and Ducting	0.067	0.239	-0.003	N/A	N/A	N/A
Brake Disc	0.042	-0.052	-0.012	N/A	N/A	N/A
Barrel / Shroud	-0.008	-0.108	0.002	+0.003	-0.008	-0.008
Wheel Nut	0.000	-0.006	0.000	0.000	0.000	0.000

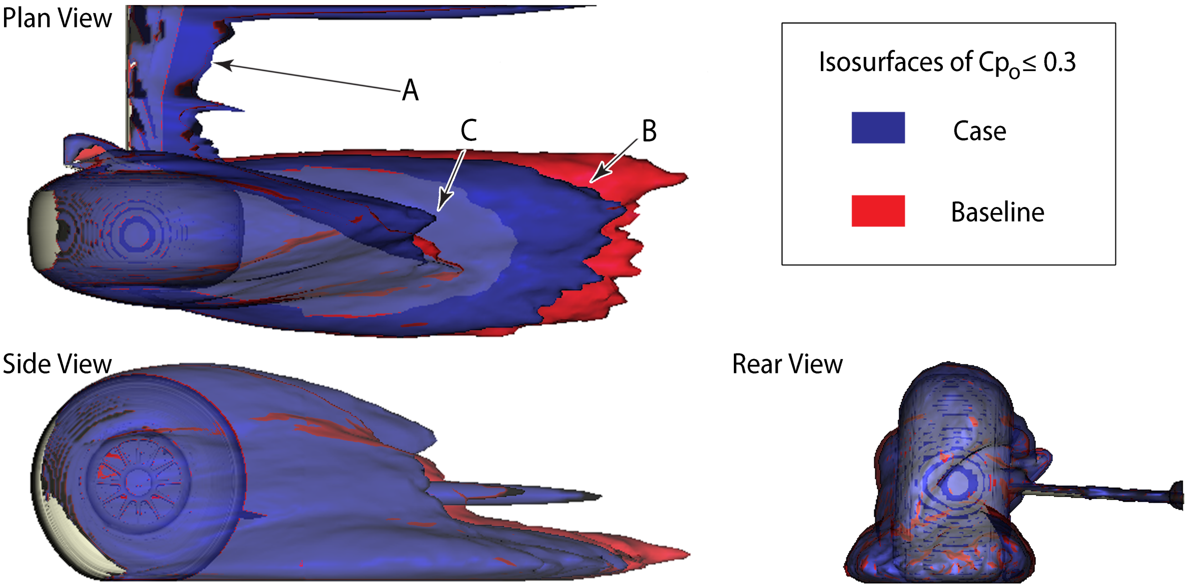

Figure 5.44: *Isosurface plots of $Cp_o \leq 0.3$, comparing Case 13 (blue) with its associated baseline (red).*

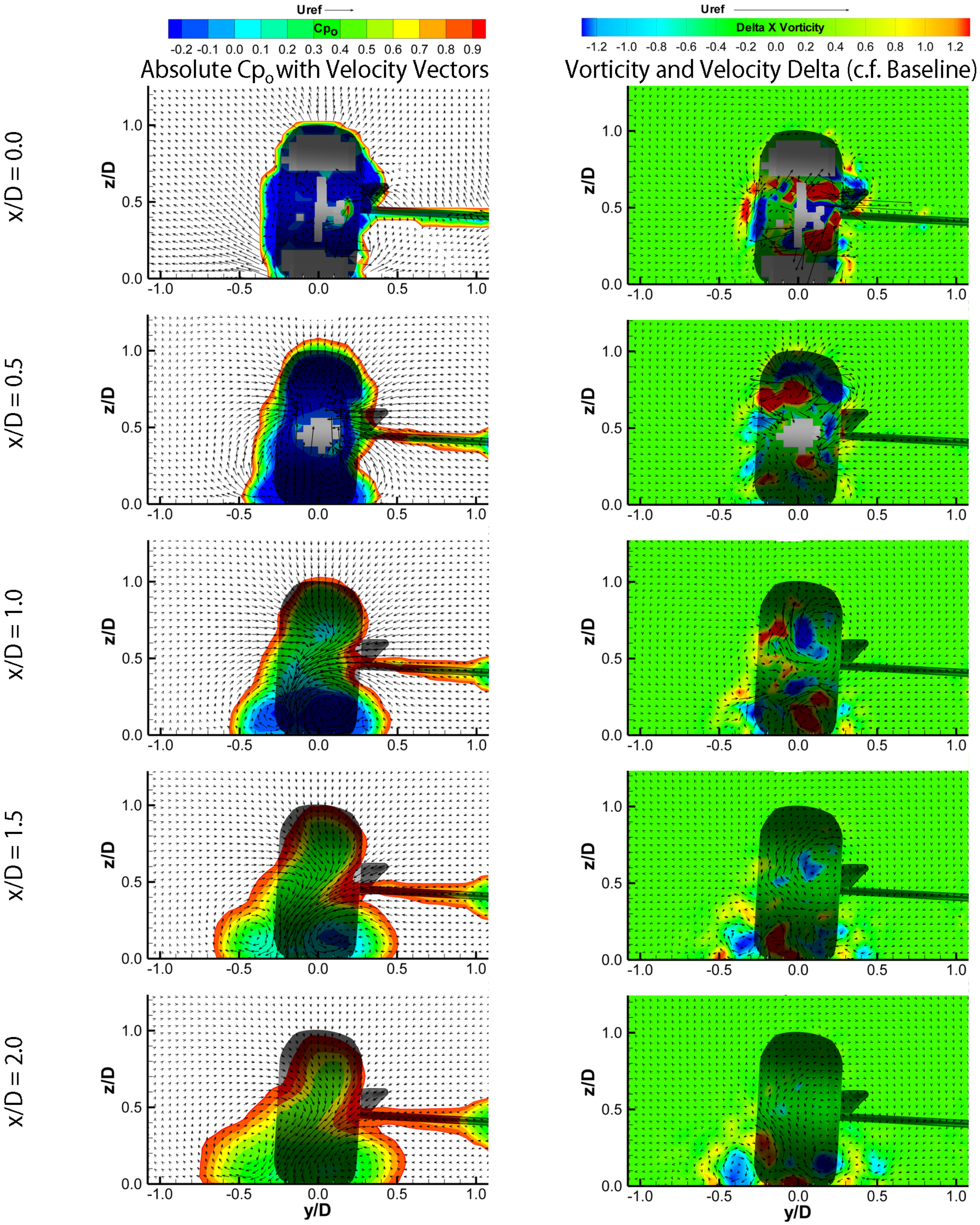

Figure 5.45: *Case 13: Y-Z crossplanes of: Absolute stagnation pressure and velocity vectors (left); Vorticity and velocity vector baseline deltas (right).*

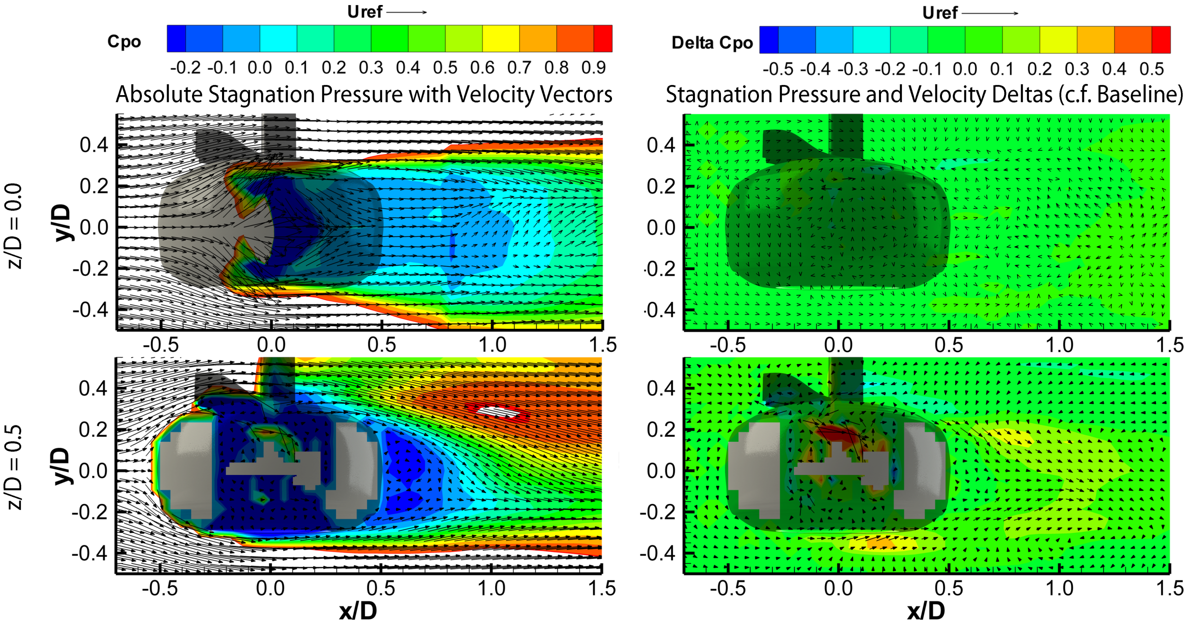

Figure 5.46: *Case 13: X-Y horizontal planes of stagnation pressure with velocity vectors. Absolute values (left) and baseline deltas (right).*

The force measurements for this case, as shown in Table 5.27, illustrate the significant drag increase brought about by the addition of the internal components. This is contrary to the trend expected from the previous work on the effect of through-hub flow rates and inlet spillage (Chapter 3).

The force breakdown in Table 5.28 shows a moderate increase in the drag of the wheel (tyre and rim), around 29% of the total increase. No other component that is available for direct comparison shows a significant drag force delta. Observing absolutes, the contribution from the scoop and ducting, compared to the scoop alone, in addition to the drag of the brake rotor would appear responsible for the remainder of the total increased drag. The lift is predominantly described by the directly comparable components, with up to 25% being unaccounted for in the internal geometry.

The iso-surface plots in Figure 5.44 show a similar local flow-field for the wheel and sting as for the simplified internal geometries (A) but further downstream show a shortening in the wake (B). The immediate suggestion from the plan-view plot is that the inboard vortex feature is smaller in size than for the baseline case. There is evidence to support this in Figure 5.45, the crossplane development figure through the slightly smaller dark blue zone at x/D $\geq$ 1.5 and changes in vorticity.

Observing the crossplane figure in more depth, the only major differences appear at x/D = 1.0, which shows a more outboard biased central downwash. It has previously been noted from the wake plots in the wind tunnel study on through-hub flow that a lower rate of through-hub flow results in a lower outboard pressure which would encourage a more outboard bias to the wake. Indeed, the vorticity deltas on the right-hand side of Figure 5.45 show a strengthened and tighter outboard vortex (central region more negative yet a more positive halo surrounding it).

The horizontal planes in Figure 5.46 show negligible difference in the wake at near-ground level. This means that the change in lift due to the wheel is an upper surface effect, and not due to the region around the contact patch. Geometrically and aerodynamically it is the same as in the baseline case in this region. At the axle height plane, there is a much more significant change. There is a high pressure region inside the wheel on the inlet for the brake disc (the output for these planes are far lower resolution (15x15mm) than the simulation voxels (2x2x2mm)). There is a much more general outwash oriented wake, as observed previously, and there is a higher pressure on the local exit region for the through-hub flow. This can be explained by the streamlines in Figure 5.47.

The streamlines were calculated by using the same rectangular region in both cases. The rectangular region intersected the brake disc and contained 500 streamline seeds which were extrapolated in both directions. The simplified geometry case is much more difficult to observe internally due to the freedom of the streamlines. They describe a swirl which is in the opposite direction to the wheel rotation. The flow primarily exits on the rearward surface and wraps around the tyre before making a contribution towards the wake on both the inboard and outboard sides. The case with internals is much more restrictive and the streamlines mostly remain contained within the rim geometry.

For the case with the rotating detailed internal geometry the swirl is reversed to be in the same direction as the wheel rotation. Unlike the previous case, this seems to tightly focus around the stub-axle of the wheel and as a result the majority of the exit flow is situated around the wheel nut. As the exit flow is situated further upstream and much more tightly distributed, the effect on the wake is very different.

The measured HFN was 0.0141 which is significantly lower (27.3%) than the 0.0193 in the simplified internals case. Although this is not apparent from figures 5.44 or 5.45, evidence to confirm a scoop velocity reduction has been suggested in Figure 5.46 and in the streamline traces in Figure 5.47. The increase in drag, despite reduced through-hub flow, is due to the physical drag of the brake disc being more significant than the spillage effect around the duct. This has been captured in Figure 4.10. Therefore, when comparing the drag between these two cases it is not a fair assessment of the negative cooling drag trend with increased through-hub flow due to the largely increased complexity of the physical components within the internal flow.

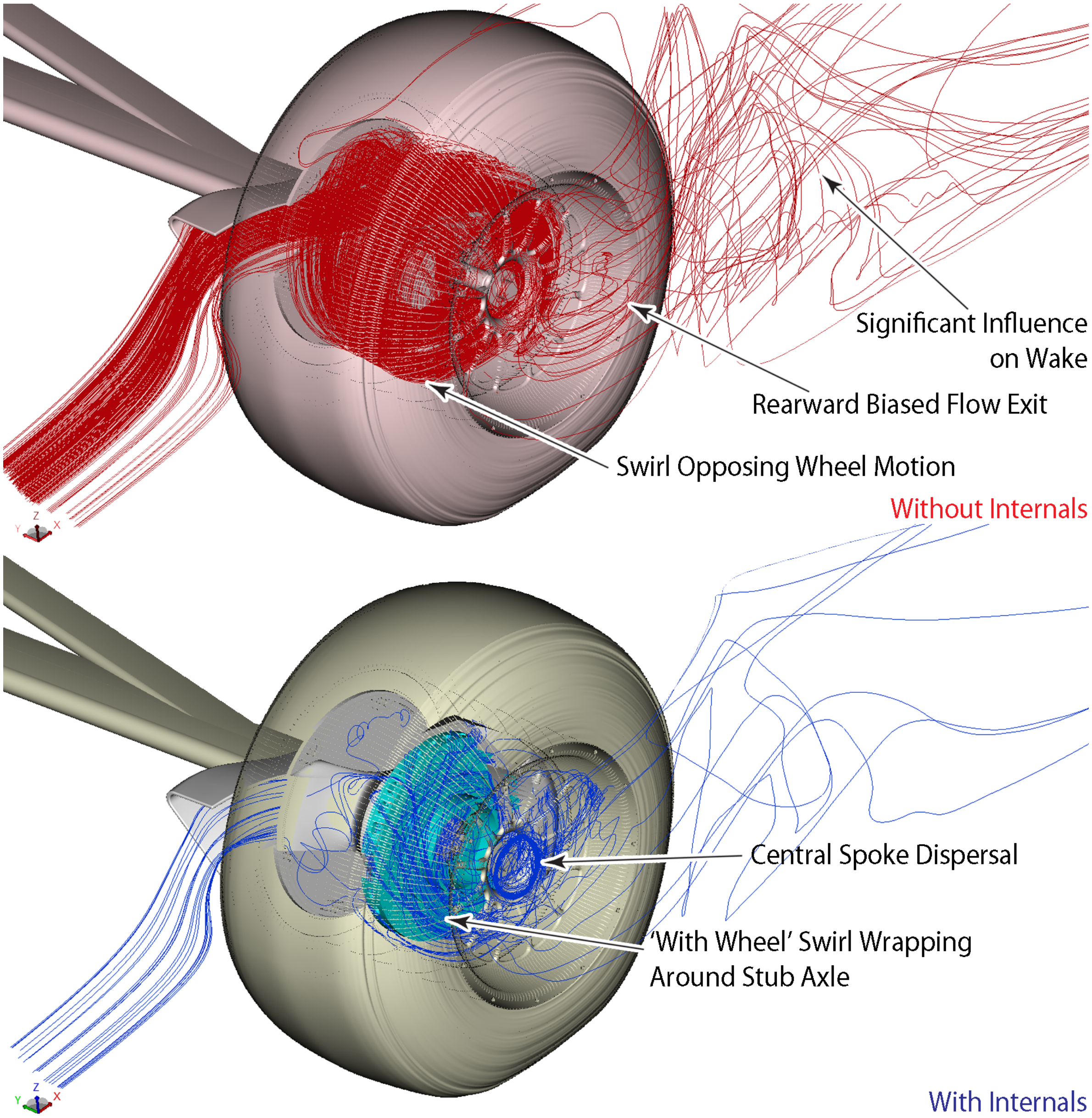

Figure 5.47: *Internal flow streamlines. Top: Simplified, Bottom: Realistic internal geometry.*

5.4 Effect of Internal Geometry (Stationary Rotor)

Case 14 is a comparison to the previous case but with a stationary brake rotor. This is to quantify the effect of the pumped through-hub flow as well as to investigate if there are any global flow-field consequences should this compromise be made in a wind tunnel or other CFD simulations.

Table 5.29: *Yaw simulation detail: Case 14 geometry schematic and forces (absolute & baseline deltas).*

<table>
<tr><td colspan="2">Case: 14</td><td>Axle Height: 150mm</td><td>Yaw (β): 0°</td><td rowspan="3">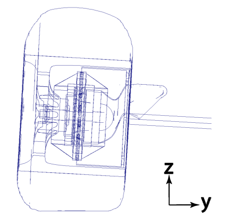
</td></tr>
<tr><td colspan="2">Description:
Stationary brake rotor</td><td colspan="2">Baseline Case: 13</td></tr>
<tr><td colspan="2">Aerodynamic Forces:</td><td colspan="2">(Case - Baseline) Force Deltas:</td></tr>
<tr><td>$C_{D,axial} = 0.488$</td><td>$C_L = 0.450$</td><td>$\Delta C_{D,axial} =$ -0.065</td><td>$\Delta C_L = +0.028$</td><td></td></tr>
</table>

Table 5.30: *Aerodynamic force breakdown (absolute & baseline deltas) of yaw simulation Case 14.*

Component	**Absolute Forces**			**(Case - Baseline) Force Deltas**		
	$C_{D,axial}$	C_{side}	C_L	$\Delta C_{D,axial}$	ΔC_{side}	ΔC_L
Wheel (Rim and Tyre)	0.451	0.044	0.045	0.000	-0.001	+0.011
Brake Scoop and Ducting	0.063	0.235	-0.005	-0.005	-0.004	+0.002
Brake Disc	-0.012	-0.045	+0.001	-0.054	+0.007	+0.013
Barrel / Shroud	-0.014	-0.114	+0.008	-0.006	-0.006	+0.006
Wheel Nut	0.000	-0.006	0.000	0.000	0.000	0.000

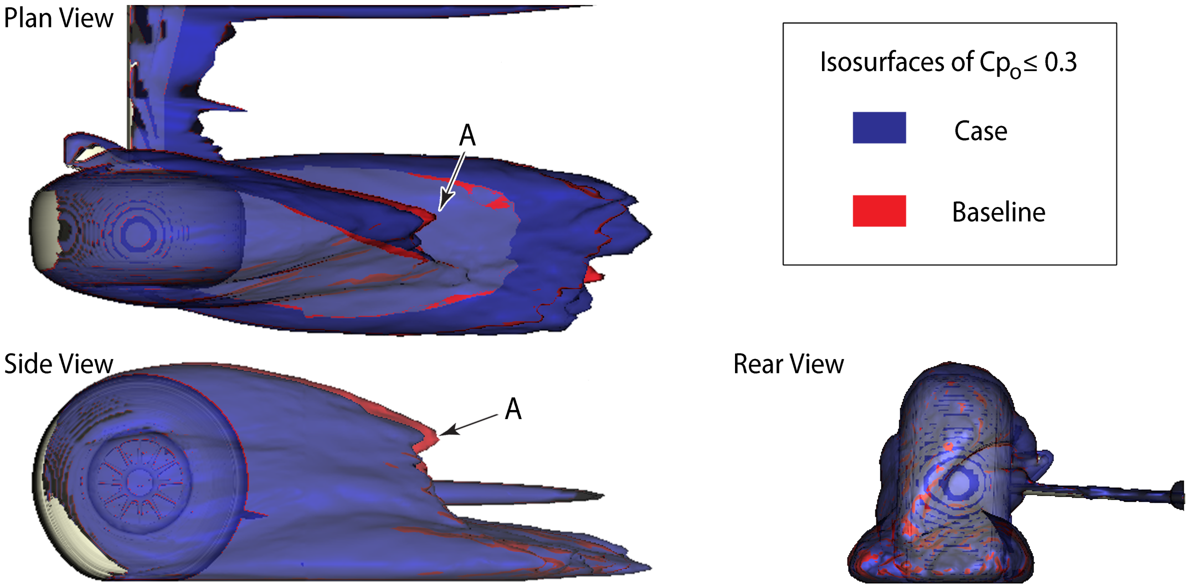

Figure 5.48: *Isosurface plots of $Cp_o \leq 0.3$, comparing Case 14 (blue) with its associated baseline (red).*

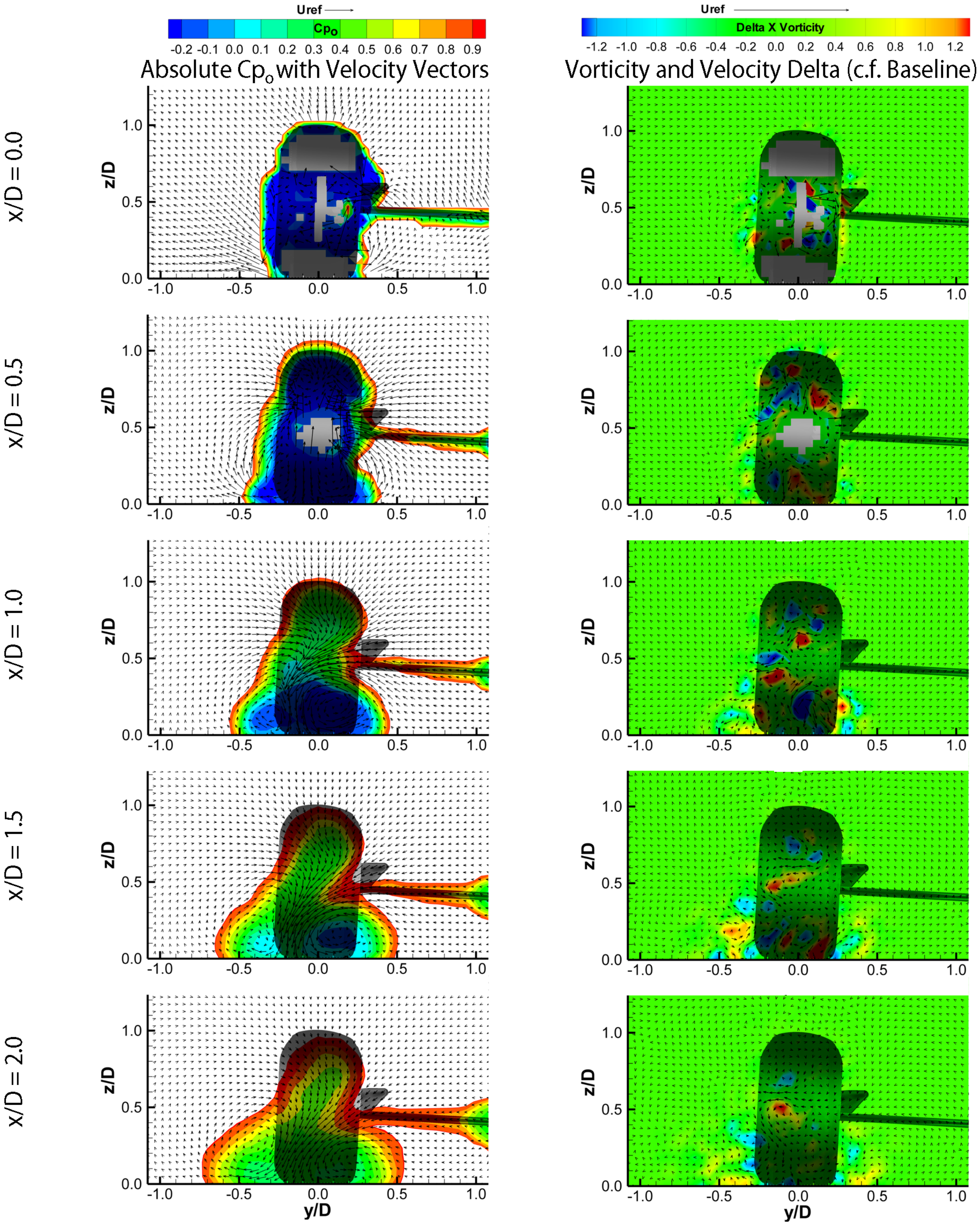

Figure 5.49: *Case 14: Y-Z crossplanes of: Absolute stagnation pressure and velocity vectors (left); Vorticity and velocity vector baseline deltas (right).*

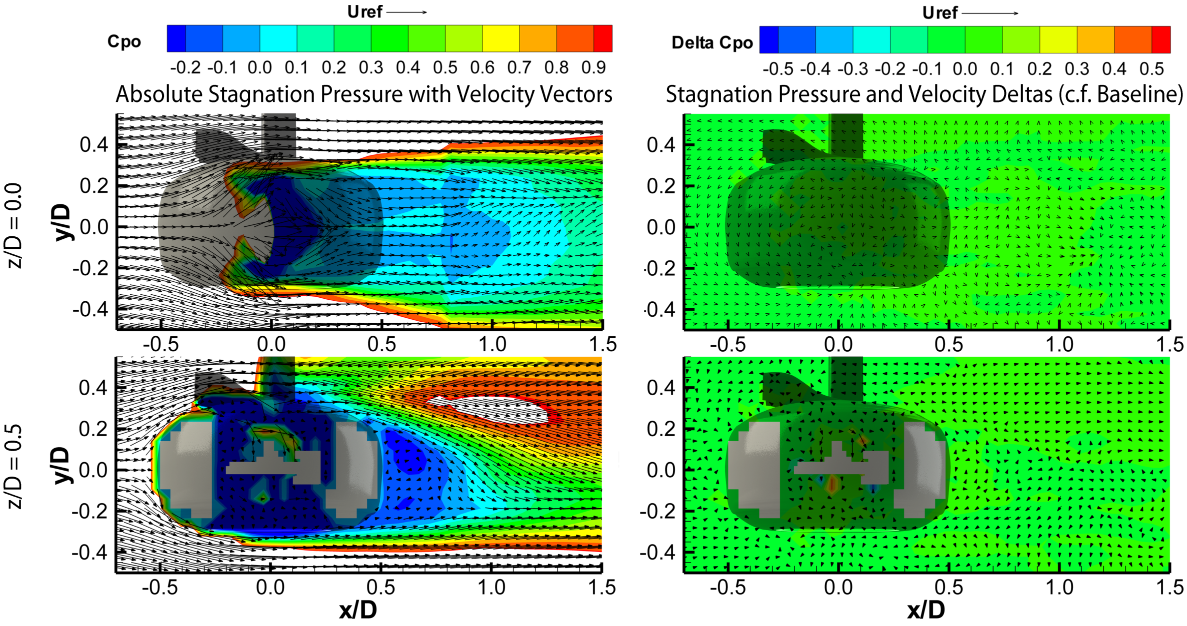

Figure 5.50: *Case 14: X-Y horizontal planes of stagnation pressure with velocity vectors. Absolute values (left) and baseline deltas (right).*

The case for the stationary brake rotor shows a significant reduction in drag compared to the baseline case with rotating internal geometry. Table 5.29 highlights the 65 count reduction in drag which is described in Table 5.30 as being almost wholly due to the contribution to the drag of the brake rotor. The remaining smaller contributions are due to other internal components such as the ducting from the scoop and the shrouding barrel. The change in lift is due to a combination of the brake rotor and the wheel (tyre and rim) components.

With regard to the flow-field, the only observable change to the global features from the iso-surface plots (Figure 5.48) is a slightly shorter and faster decaying (in height) upper wake. The wake development in Figure 5.49 shows negligible change on the left-hand side and only minor changes in vorticity for the ground lobes with a small spot at the axle height on the wheel centreline showing evidence of a slightly higher inboard feature (red spot at the upper extreme of the feature). These changes are minor, however, and therefore the effect of rotating the disc (or rotor) in the geometry appears to have minimal effect on the global flow-field. The horizontal planes in Figure 5.50 show almost identical pressures and velocity vectors to the baseline case.

Quantifying the pumping effect of the brake rotor, the measured HFN was 0.0139 which is only 0.7% lower than the rotating case (which is 27.3% itself lower than the case with the simplified internal geometry). This suggests, providing the CFD model has accurately predicted the rotating passages within the brake rotor, that the ram induced internal flow dominates the through-hub flow rate and that the internal blockage is in fact more significant than the centrifugal rotor pumping.

Chapter 6

Further Discussion

This chapter brings together the contents of chapters 3 and 5 to produce an overview of the aerodynamic sensitivities exposed by experimental and computational simulation techniques. Whilst individual results have been described on a test-by-test basis in the aforementioned chapters, the summaries in this chapter are intended to be more qualitative in terms of defining the aerodynamic behaviour for differing levels of modelling detail. The chapter begins with the most significant changes and simplifications utilised (through-hub flow) during wind tunnel or CFD testing and works towards the more detailed and subtle parameters (tyre profiles).

6.1 Modelling Through-Hub Flow

The effect of through-hub flow on the local and global flow-field is a significant detail which is often excluded from the usual isolated wheel testing methodology. Through-hub flows exist in race car wheel assemblies to cool the brake components (Chapter 1). Therefore, the transverse flow induced by the flow structure has to be quantified to determine the level of simulation detail that is required in order to achieve a sufficient test whether it be experimental or computational.

6.1.1 Effect of Through-Hub Flow (Simplified Internal Geometry)

The effect of through-hub flow variation was isolated by eliminating the complex internal geometry within the wheel. Where most cases in the literature apply a solid divider either in the centre of the rim or 'rim fairing' on both the inboard and outboard face to prevent through-hub flow, the approach here allowed a clear passage through the hub with the exception of the influence from the 12-spoke rim. The through-hub flow was introduced to the rim by an inlet scoop and the empirical rate of through-hub flow was then varied by the use of meshes in-between the scoop and the inboard face of the rim. For CFD simulations, the use of porous media was employed to achieve the same objective.

One of the main questions to be answered was whether the pumping effect of the brake rotor was more or less significant than the high loss flow trajectory through the hub. It was found that the benefit gained from the centrifugal pumping mechanism was around 40 times smaller than the losses introduced with a highly restrictive internal flow trajectory. This shows that the expected through-hub flow rate of an F1 car in the absence of upstream wing effects is exactly in the middle of the full range tested by means of introducing mesh screens.

6.1.2 Inlet Spillage Dominance

Traditionally, increasing through-body flow rate results in an increase in drag, referred to as ram drag. This is the drag induced by a combination of internal restrictions and non-axial momentum losses. For the geometry described here the internal flow undergoes a perpendicular change in direction resulting in a total loss of scoop inlet streamtube momentum.

What was observed was actually a reduction in drag between the extreme HFN values (Figure 3.26). The effect of inlet spillage drag, as studied by Williams [81] and Minto [73] was investigated and determined to be dominant on the change to the flow-field and forces at low through-hub flow rates. CFD simulations replicated this empirically observed effect very well with a reduction of drag by 2.7% (tunnel observed reduction of 2.9%). Further CFD simulations highlighted that the contribution of the scoop drag comprised 8% of the overall drag of the wheel assembly, albeit for a slightly different aspect ratio wheel to the through-hub flow experiments. This confirms that the local contribution to the drag is significant enough to dominate over any expected ram drag increase.

Inlet spillage occurs when internal passages are restricted to the point of causing a large separation over the leading edges of the inlet. This separation was observed in the wind tunnel by means of PIV (Figure 3.2) and by surface flow visualisation (Figure 3.3). Figure 6.1 shows this concept pictorially.

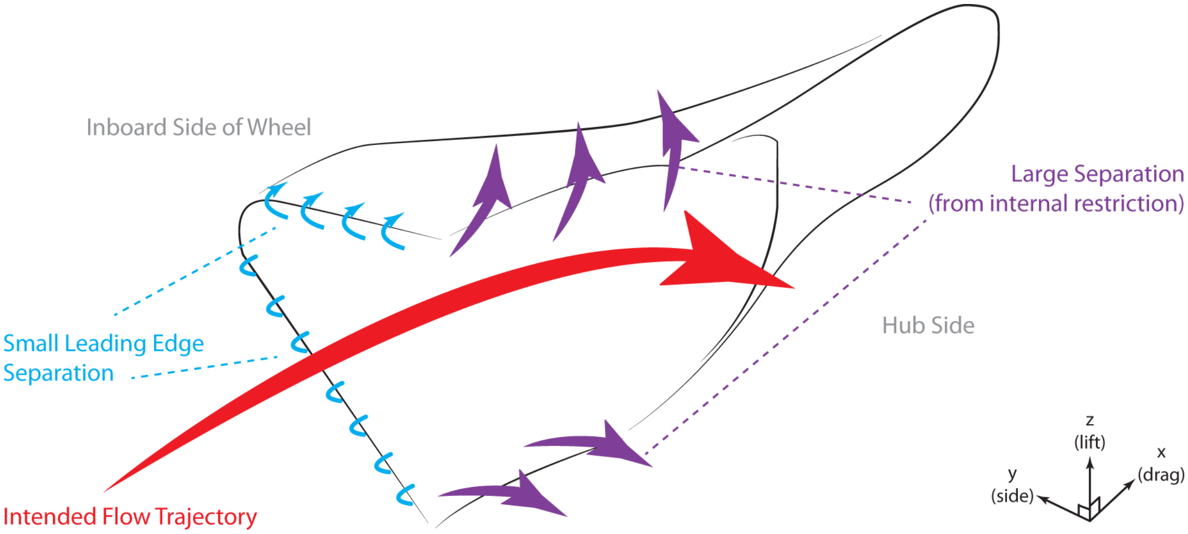

Figure 6.1: *Pictorial representation of inlet spillage at the scoop inlet.*

The spillage at the scoop causes a dominant local drag which overrides the traditional positive velocity-squared ram drag trend. Applying the mathematical model of Williams [81] to these data allowed theoretical quantification of this effect. A combination of known flow-physics could be plotted (Figure 3.14) to explain the drag trend across the HFN range.

As well as considering the drag, the overall lift was found to change more significantly by almost a factor of three larger than seen in the drag forces. This is consistent with the spillage observations as the localised low-pressure region caused above and below the scoop has more of an effect on the horizontal surfaces due to the larger surface area. The lower spillage effect was less significant than the upper due to the shorter leading edge, presence of the support sting and with the adjacent surfaces being at an angle rather than perpendicular to the lift measurement axis. For this reason, it is likely that the lower spillage separation contributed more to a sideways force than a lift force.

6.1.3 Inlet Scoop Design Sensitivity

Changes to the geometry of the baseline scoop exhibited a great deal of aerodynamic sensitivity in terms of the maximum achievable through-hub flow rate in addition to the associated absolute drag level throughout the hub-flow number range.

The spillage effect was found to be present for the whole range, even for the fully open ducting. Therefore, by introducing adaptations to the geometry to induce large separations at the leading edges of the scoop at all through-hub flow rates, the dominance of the spillage could be suppressed. This was indeed the case, resulting in a much flatter drag relationship to through-hub flow rate, although the resulting drag was considerably higher than the baseline case due to the increased frontal area.

By smoothing the leading edges of the scoop, the effect of spillage could also be reduced, though in this instance less so, due to simply suppressing the effect rather than masking it with another flow feature. The overall drag of the scoop was lower than the baseline case and the maximum through-hub flow rate achievable was higher.

6.1.4 Global Flow-Field Effects of Through-Hub Flow

The spillage on the lower edge of the scoop also resulted in a change of effective attack angle for the otherwise neutrally faired sting. This changed the size of the wake generated by the sting.

The straight-ahead cases are dominated by the inboard vortex feature which is elliptical in shape, of the order of 0.3D high by 0.5D wide at the x/D = 2.0 location. It is also more persistent than the outboard equivalent ground level feature. Therefore, the local effect of inlet spillage translates downstream to provide a change to the flow vectors near ground level, particularly in the downwash (Figure 3.9).

The longitudinal PIV measurements (x-z planes) for through-hub flow resulted in visible progressive changes when observing from the extreme inboard to outboard planes. For the open ducting there is a much smaller lower recirculation lobe than for the closed case. The closing of the duct results in a much longer recirculation lobe on the inboard side, extending 30% further downstream than the high flow case. The centreline is unaffected for both cases and the outboard plane observes the opposite trend to the inboard. When the ducting is open, a recirculation lobe appears at the axle height which represents the flow passing through the rim. This is much smaller in the case with closed ducting. It is thought that there will be some contribution to the wake in this region even in the absence of through-hub flow due to the turbulent flow around the spokes.

For full-car development purposes, the effect of through-hub flow is significant enough to make noticeable changes to the global flow-field which is therefore crucial for development and location of vortices.

6.1.5 Through-Hub Flow for Detailed Internal Geometry

Whilst the global effects were the primary concern, the exit flow condition for through-hub flow is often significant to the interaction with the wake. For the case of internal geometry such as a brake rotor and caliper, connected to the scoop inlet via a duct feeding an annulus, the exit flow condition is significantly different.

Figure 5.47 showed streamlines calculated in two directions from the plane intersecting the brake rotor. This was also done for the simplified geometry. The resulting conclusion was that the swirl induced by the intake angle was reversed by the forward rotation of the brake rotor. The simplified geometry with its much higher hub-flow number swirls the full diameter of the rim internal in the opposing direction to the wheel rotation. The flow exiting the brake rotor for the detailed internal geometry shows discrete swirls which wrap tightly around the stub-axle of the wheel. This results in a much more concentrated and central outflow than the simplified internal geometries which instead have a larger distribution but biased rearward. The simplified internal geometries illustrate evidence of having much more influence on the trailing wake than the realistic internal geometry.

The drag measurements for the detailed internal geometry cases show an increase in the drag of the overall system, contrary to that expected by the negative cooling drag trend seen by the simplified internals case. The drag for the brake rotor alone, in this case, comprised 7.6% of the overall drag which is of similar magnitude to the scoop contribution (8.0%). This increase to the drag due to a new component has overpowered the spillage effect. This is not to say that the spillage is not present, and indeed this is not the case as the surface streamlines on the scoop in Figure 4.10 showed that spillage is occurring. This shows that the introduction of a restriction is not sufficient to reproduce the correct flow features or force measurements in a car development environment. However, without making such a simplification, the effect of inlet spillage may not have been successfully isolated.

The downstream flow-field studies show that there is a severe shortening of the wake with the introduction of internal geometries and that the outboard vortex has been strengthened to the same proportion as the inboard vortex.

The flow-field of a stationary brake rotor was observed to be almost identical to that of the rotating case with only a negligible reduction in corrected through-hub flow rate and changes to the forces. For a full-car bodywork development programme, focusing on flow-field and tyre wake manipulation both upstream and downstream of the wheel, this appears to be an inconsequential simplification to make.

6.2 Modelling Tyre Deformation

This section is focused on the subtle details of the tyre itself which deforms due to both steady-state and dynamic loads whilst on-track. The high sidewalls of an F1 tyre are often considered part of the suspension and therefore, in addition to compression of the suspension geometry springs and dampers, the profile of the tyre sidewalls change regularly. This can be as a result of the velocity-squared dependent downforce, the non-symmetrical shape due to the camber of the wheel (used for mechanical benefit), lower profile dragging due to the yawing of the wheel or even unpredictable bumps in the track surface or riding kerbs. The latter was not considered within the scope of this work.

6.2.1 Effect of Axle Height

The axle height parameter defines and controls the level of the deformation applied. In this case, the maximum axle height representing the smallest vertical load, therefore representative of corner-exit or early-straight conditions was equal to 159mm (free standing wheel diameter (D) of 320mm - model-scale). The lowest axle height, representing the end-of-straight condition was 150mm, a reduction by 5.7% in height and from the CAD generated from the scanned profiles, a reduction in projected frontal area (including scoop) of 2.0% (in the highest inflation pressure case).

The axle height is a parameter which is often compromised on in order to increase the longevity of the equipment in the wind tunnel. High temperatures on thin-walled rubber are severely detrimental to the lifespan of the equipment and visible changes could be observed to the texture of the tread at the lower axle heights. The aerodynamic sensitivity of varying the axle height therefore needed to be quantified as methods of applying vertical loads in wind tunnels are limited due to the 'wheels-on' techniques used. A known technique for applying the vertical deformation load is to employ a heavy rim with internal ballast. This does not approach the levels of force being applied in this study which exceeded 30kg of load (334N) at times.

6.2.1.1 Geometrical Profile Changes

The rotation of the wheel resulted in a rise in axle height of between 2-3mm compared to the stationary case. This is as a result of the reaction force to the ground from the centrifugal 'ballooning' of the tread surface.

The sidewall and upper shoulder profiles were observed to change in shape as well as being offset by the distance change in axle height. The most sensitive profile sections appear to be the lower inboard and the upper outboard. The lower inboard is the most heavily deformed section and as such a change by 9mm vertically leads to horizontal displacements of up to 20mm, as well as the vertical offset in the sidewall. The tread section then merges with the ground plane with varying levels of severity due to the abrupt step between the sidewall and tread.

The shape of the tyre itself described a more conical structure than cylindrical. This is as a result of the tread surface not recovering from the deformation at camber. The conical nature of a rigid tyre, in order to simulate camber, was thought to be a concern (Section 1.2.2.3) but this observation in the deformable studies proves that this may not be detrimental to the flow development.

6.2.1.2 Geometrical Contact Patch Changes

The size and shape of the contact patch changes significantly with changes in axle height of just 5.7%. In all cases for this study, the contact patch shape was approximated to an ellipse although this is not strictly the true shape as there is more inboard loading due to camber. Defining the contact patch width as the y-axis measurement and the length as the x-axis measurement, the definitions of the major and minor axes of the ellipse swapped as vertical load was applied. By this, the contact patch is initially wider than the length but as a threshold axle height is reached, in the middle of the range, the length becomes the more sensitive parameter and becomes longer. This non-linear response to the measurements was combined to produce a plot of the elliptical contact patch area (Figure 3.16) and the resulting areas were found to have a linear relationship. As axle height increases, the contact patch area decreases and this occurs at a different rate depending upon the tyre inflation pressure.

6.2.1.3 Variable Axle Height Aerodynamics at Zero Yaw

For the straight-ahead case the performance of the aerodynamic system reacts with an increase in drag with axle height. The maximum change in drag was 19.0% which is significantly greater than the change in frontal area which is of the order of 2.0%. Therefore, the change in drag is an order of magnitude larger than the expected change due to increased frontal area alone. Indeed the outboard wake increases in magnitude resulting in a lower base pressure.

The increase in the outboard vortex size is also a concern for full-car development as this affects the trajectory of the wake and the impact on the downstream components. CFD simulations displayed evidence that the overall wake drifts outboard as the axle height lowers which is representative of the transition that occurs as the car accelerates down a straight. This means that the high-speed aerodynamic performance is very different from low-speed. Arguably there are other factors as well as the deflection of the tyre rubber which will cause significant aerodynamic system changes too, such as the front and rear ride heights of the car. However, this is further justification for modelling the tyre deformation correctly as any discrepancy will then cascade further downstream under the floor of the vehicle and over the sidepods.

6.2.1.4 Transience of the Wake

Frequency spectra were produced from empirical data of the non-yawed wheels at the lowest axle height with wind both on and off. Most significantly, there was a peak around 36Hz which was present with both wind on and off. The wind off magnitude was significantly lower than that of the wind-on. This suggests that there was both a mechanical and aerodynamic effect occurring at this frequency. The frequency of the rolling road rollers was known to be exactly 36.0Hz. However, the wind-on case also exhibited a peak but closer to 37Hz. Calculating the wheel-specific wake oscillation frequency from the non-dimensionalised value quoted by Axerio et al. [57], the theoretical frequency expected was 39Hz. Therefore it was postulated that the significant dominance of the wind-on spike around 37Hz could be wake oscillation.

6.2.1.5 Variable Axle Height Aerodynamics at Yaw

The significant differences to both forces and wake with axle height as shown distinctly by both the wind tunnel and CFD methodologies become a greater concern when at yaw.

The measurements of drag and lift forces both show a change in sensitivity at yaw depending upon the axle height. In the case of drag, the lower axle height appears to be the most sensitive, resulting in a crossover in absolute values with the higher axle height. This means that the trend showing the drag of the lower axle height being much lower than the higher axle height are in fact reversed above ±(3-4)° yaw (based upon interpolation).

In the case of lift, the higher axle height becomes more sensitive showing equal or lower lift measurements at positive and neutral yaw. At negative yaw, the higher axle height exhibits much higher lift than the lower axle height. The higher axle height responds generally symmetrically with positive and negative yaw angles but the lower axle height seems much less sensitive to both, and in particular negative yaw.

Quantifying this, the positive yaw case for the low axle height (Case 4) resulted in a rise in drag by 9.8% with an increase in frontal area of 6.5%. The higher axle height resulted in a change in drag of only 0.6% with a change in area of 6.0%. In terms of lift, the lower axle height responded with an increase by 19.0% and the higher axle height by 32.4% for the same angles. It therefore seems that the lift is very sensitive to the axle height when at yaw. The response to drag and lift for the change in axle height is greater for yaw than straight-ahead.

From a flow-field perspective, as summarised by Figure 6.2, the change in axle height at yaw is significant. The wake is more inclined to be outboard biased for a lower axle height. The change is of similar scale to the straight-ahead case when observing positive yaw (cases 4 and 7) but when observing negative yaw (cases 9 and 11) the differences become extreme. Whilst at the low axle height there was a complete suppression of the inboard vortex, the high axle height contained a feature of size 0.7D x 0.5D in width (y-axis) and height (z-axis) respectively. This complete change in flow structure for only a 5.6% change in axle height has dramatic consequences for full-car development when yaw.

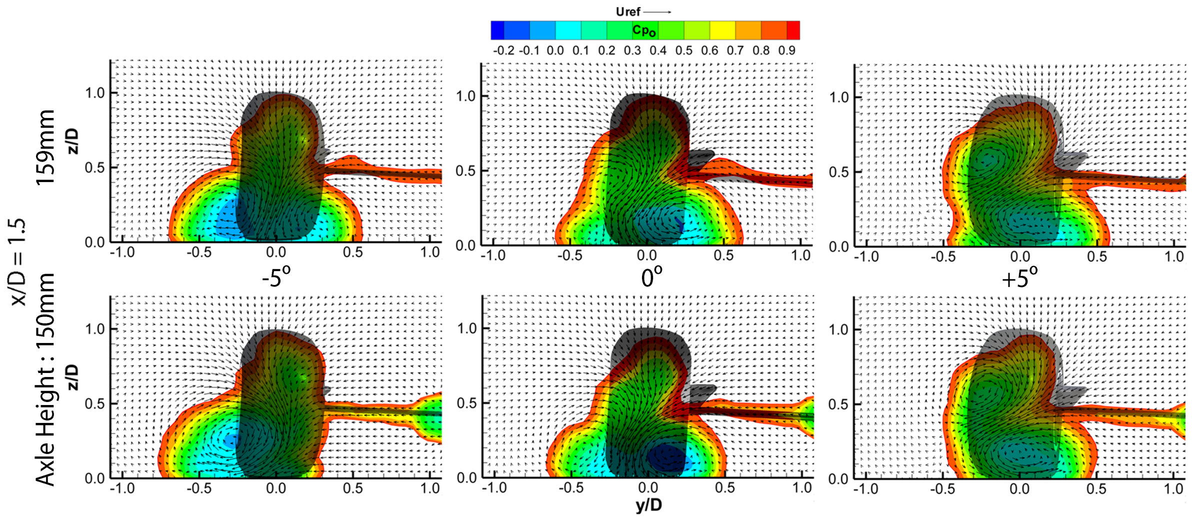

Figure 6.2: *A summary of the flow-field at x/D = 1.5 for 0° and ±5° yaw at axle height extremes.*

The surface static pressure distributions, which agree well with the much earlier work of Fackrell [23], Mears [3] and Hinson [32] show that there is an earlier separation for the lower axle height case by 8° (separating 1° forward of top dead centre). Earlier separation is responsible for lower drag for the comparison between rotating and stationary wheels and this conclusion is consistent here.

6.2.2 Effect of Tyre Inflation Pressure

Tyre inflation pressure is a parameter which is compromised in testing environments in order to increase the longevity of the equipment. This allows direct control of how much vertical load is required in order to achieve the axle heights representative of those on-track. In order to achieve the range of axle heights in the wind tunnel the nominal forces required were 46-240N for the 3.4kPa (0.5psi) inflation pressure case, and 175-334N for the 20.7kPa (3.0psi) case. These forces are extreme when considering model scale components and the friction generated between the rubber of the tyre, the rolling road belt and the platen, most significantly at yaw. As such, it is often the case that only the highest axle heights are tested in the industrial environment. The heavy rim technique described earlier is insufficient to achieve full deformation levels even at the extremely low inflation pressure.

6.2.2.1 Geometrical Sensitivity to Tyre Inflation Pressure

The linear relationship of the contact patch area against the axle height parameter shows two different gradients for the two inflation pressures (Figure 3.16). It is not surprising to find that the higher inflation pressure reacts less to a change in axle height than the lower tyre pressure. With a higher internal pressure, the resistance of the tread to vertical load becomes greater. The sidewalls also exhibit stiffening and hold their curved shape more than for a lower inflation pressure.

In observing the tyre profiles for the differing axle heights it is apparent that the lower inflation pressure always exhibits less curvature continuity where the sidewalls have appeared to begin folding as opposed to curving or bulging. The sections close to the rim, known as the bead of the tyre, are very similar in both cases due to the substantial reinforcement that exists there (see Chapter 1). As the observation point gets closer to the tread surface, the differences get larger. The contact patch is observed to be wider for the lower inflation pressure.

6.2.2.2 Aerodynamic Sensitivity to Tyre Inflation Pressure

The change between maximum and minimum axle heights for the lowest inflation pressure has already been presented to have exhibited an increase in drag almost three times larger than that of the highest inflation pressure. The intermediate tyre pressure held values which lay between these two extremes showing that there is a tight correlation between drag force (local static pressures and immediate wake) and inflation pressure. At higher axle heights, representative of low vertical loading and therefore early-straight conditions, the three tested tyre pressures converge. The cases with high levels of deformation at low axle heights show a large disparity depending upon the inflation pressure. The behaviour at the lower axle heights appears to show evidence of levelling off for the high inflation pressures whereas the lower ones continue to follow the near-linear trend. This is consistent with the behaviour of the tyre profile characteristics in Section 6.2.2.1.

The presence of sharper edged profiles in close proximity to the ground are usually conducive to stronger vortex structures, due to more aggressive pressure gradients. The main differences in tyre profiles due to inflation pressure are much higher than the observed sensitive region of within 2-10 mm of the ground plane. In fact this is more generally of the order of twice that distance. This is thought to be the explanation for a reduced impact on the formation of the vortices making inflation pressure have localised effects only.

It has been concluded that the flow-field is largely unaffected by the change in tyre inflation pressure. Aside from the local effects, of which the force measurements are the most significant, the downstream wake appears insensitive. This is an important result as the conclusion from the axle height experiments showed that it was not a parameter that should be compromised. Therefore, reducing the inflation pressure in order to ensure a correct axle height would be the least detrimental methodology of achieving accurate far-field wake for full-car development whilst maximising the longevity of the equipment within the wind tunnel.

6.3 Modelling Tyre Setup and Realistic Conditions

This section tackles the discussion of the major movements and setup parameters which are commonplace on a competition vehicle. The front wheels of a racing car are very rarely, if at all, desired mechanically to be run straight-up and straight-ahead. Therefore understanding of the aerodynamic consequences of this was important to the scope of this work.

6.3.1 Effect of Camber

Camber is a setup parameter and therefore not likely to change significantly on-track, due in part to the nature of double wishbone suspension geometry. Therefore characterising the aerodynamic performance of a cambered wheel is as significant as yaw.

6.3.1.1 Geometrical Sensitivity to Camber

The nature of camber means that there is unequal loading on the inboard and outboard tyre sidewalls and the contact patch is not centred or symmetrical about the tyre's centreline. Geometrical scans in the wind tunnel have shown this well (Section 3.18). The same scans also displayed a conical nature to the overall shape including the upper tread. This shows that there is a slow response in the rubber of the tyre which does not allow full recovery of its natural shape even by the top of the rotation.

Camber has a further idiosyncrasy when turned to yaw. Because of the uneven loading on the sidewalls, the width of the contact patch and therefore extent of the sidewall dragging due to the friction with the road when at yaw are both much more sensitive to one yaw direction than the other. In the case of the wheel used here, set up as a front-left wheel assembly with negative camber (as is typical of a racing car) the inboard sidewall is more heavily loaded. Therefore by turning to positive yaw, thus representing the outside wheel of a turn, the contact patch widens significantly due to relieving the heavily loaded sidewall and the full potential of the tyre is delivered. Here, an increase in contact patch width of 31.6% was observed at the low axle height. This compares to an increase in contact patch width of only 16.6% for the same tyre at negative yaw. This difference is in fact even larger when the fact that the inside wheel is usually unloaded when traversing a corner and therefore would observe a higher axle height reducing the 16.6% even further.

6.3.1.2 Aerodynamic Sensitivity to Camber

The effect of the drag force over a range of camber angles was investigated and found to be in close agreement to those of Whitbread [5]. A minimum drag value was measured to be at -3°, this is different to the trough found by Whitbread at -2°. In order to establish whether the effect was due to the dominance of an over-designed brake scoop component, which would have been optimised in CFD and a wind tunnel for this sort of level of camber, a sweep of drag measurements were taken without this component. Despite the lower resolution of the sweep, the same trend was discovered and the effect of diminishing drag followed by a slight increase with camber angle is therefore considered an effect of the geometry of the tyre itself. Since the same trend was observed between the work performed here and that of Whitbread, who did not make use of a deformable tyre (only a 3mm thick rubber coating on the tread), the effect is considered to be dominated by the global movement of the bluff body and not a detail of the sidewall bulge.

The flow-field studies showed a similar observation whereby the structure and the size of the wake seemed largely unchanged, only with a movement of features consistent with the additional angle of the wheel. With negative camber the upper features were moved inboard and the lower features moved further outboard giving a higher angle of lean to the central downwash.

6.3.2 Effect of Yaw

Yaw is a parameter which can either be permanently present, in the case of toe, or induced by driver operation in the form of an applied steering angle or due to effects taking place around the vehicle due to the dynamics of cornering. As such, over the course of a lap, there will be very little chance of ever observing a wheel directly in line with the axis of the vehicle (and freestream). Therefore, understanding the nature of the flow-field at positive and negative yaw is essential to developing a car which has low sensitivity to yawed wheel wake. Essentially, downforce is wasteful if it only occurs in a straight line and the most successful cars retain downforce in the most critical situation, when cornering.

6.3.2.1 Geometrical Sensitivity to Yaw

Aside from the obvious increase in projected frontal area of the wheel, the majority of interest originates from the lower sidewalls of the tyre. When turning to yaw the friction between the road and the tyre results in a deformation or dragging. There was also a change in behaviour of the step from the sidewall to the tread due to this lateral deformation.

6.3.2.2 Aerodynamic Sensitivity to Yaw

The drag and lift forces are both observed to increase when the wheel is turned to yaw. Whilst this is expected for drag due to the increased frontal area, although not responsible for the entire change to the forces, the lift is less obvious. The wake for a yawed wheel is also observed to be much narrower as presented earlier. In some cases the change in axle height can be greater than the effect of changing yaw.

The positive yaw case shows evidence of much larger leading edge separation over the tyre due to the presence of the scoop on the inboard side. In fact, the scoop had a much larger than normal influence on the aerodynamic performance. The lift and drag of the positive yaw case both increased as expected but 37% of the change in drag was due to the scoop and a larger than usual contribution to the lift of 6% was also observed. This confirms that not only is ±5° yaw sufficient to cause leading edge separation over the tyre, but that this is a highly sensitive region from a global perspective.

In order to understand the behavioural changes to the primary vortex structures, Table 6.1 has been prepared to compare the qualitative change to the step between the tread and sidewall and the change that occurred to the resulting vortex feature. Cases with ‘N/A’ describe cases where this is an inappropriate comparison due to a much bigger effect being responsible for the flow-field change, such as axle height or yaw angle. Nevertheless, it was apparent that even some of these cases exhibited the trends described.

Figure 6.3 describes pictorially the point made by Table 6.1. The general observation is that the sharper or more aggressive the step is, the more inclined it is to form a stronger (and in many cases more tightly wound) vortex. This is highly dependent upon the ground clearance. In some cases, the condition of the vortex could be described as being the same despite a change to the aggressiveness of the step. This is because the step that is present is approximately 11mm off the ground. In most cases, even minor changes are more influential when of the order of 2mm off the ground plane.

In addition to the changes to the profile shape and the presence and aggressiveness of the sidewall to tread transition, there are notable changes to the contact patch shape. The lift measurements observed

Table 6.1: *Comparison of qualitative tread-to-sidewall transition severity and its height off the floor with the aerodynamic change in the resulting vortex structure.*

Case	BL	Inboard			Outboard		
		Step Type	Step z (mm)	Vortex	Step Type	Step z (mm)	Vortex
1	N/A	Medium	2	N/A	Aggressive	5	N/A
2	1	Sharp	7	N/A	Medium	10	N/A
3	1	Medium	2	N/A	Aggressive	5	N/A
4	1	None	0	N/A	Sharp	2	N/A
5	4	Medium	2	Stronger	Aggressive	5	Stronger
6	4	Sharp	2	Stronger	Medium	4	Weaker
7	2	Smooth	3	N/A	Medium	7	N/A
8	7	Sharp	7	Stronger	Medium	10	No Change
9	1	None	0	N/A	Smooth	3	N/A
10	9	Medium	2	Stronger	Aggressive	5	Stronger
11	2	None	0	N/A	Smooth	10	N/A
12	11	Sharp	7	No Change	Medium	10	No Change

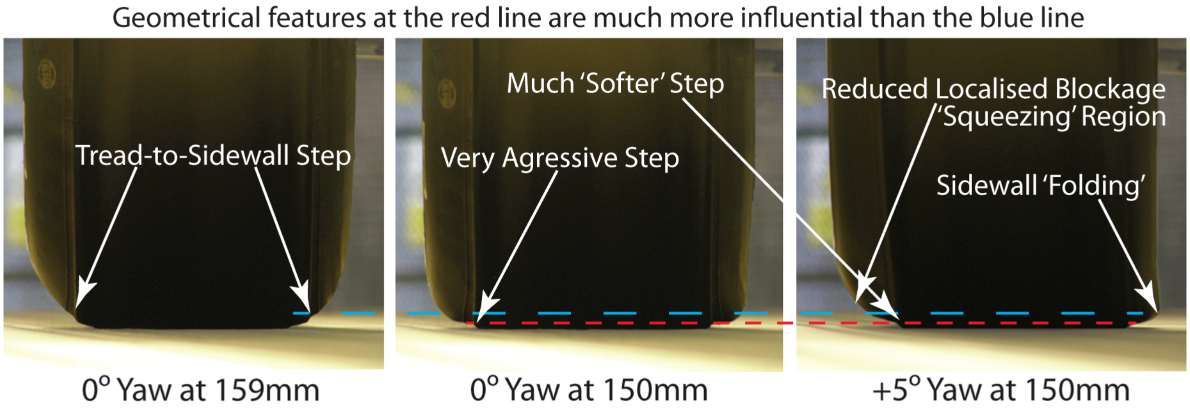

Figure 6.3: *Pictorial illustration of the squeezing effect at the transition from the tread to the sidewall conducive of producing larger vortex structures.*

significant changes, of up to 26% at times which appeared between cases where only the lower sidewalls and contact patch region changed.

The behaviour of the flow-field at the contact patch is sensitive to extreme changes in pressure which are responsible for such big changes in lift. Figure 6.4 shows the types of contact patch present in these simulations and the behaviour of the local flow-field.

It is clear to see that the cases with favourable ellipses, longer (in wheel centreline) with less blockage (blockage denoted by the white ellipses in the figure), are responsible for high flow-rate underneath the tyre and therefore a lower pressure than the other cases resulting in lower lift. There is also a

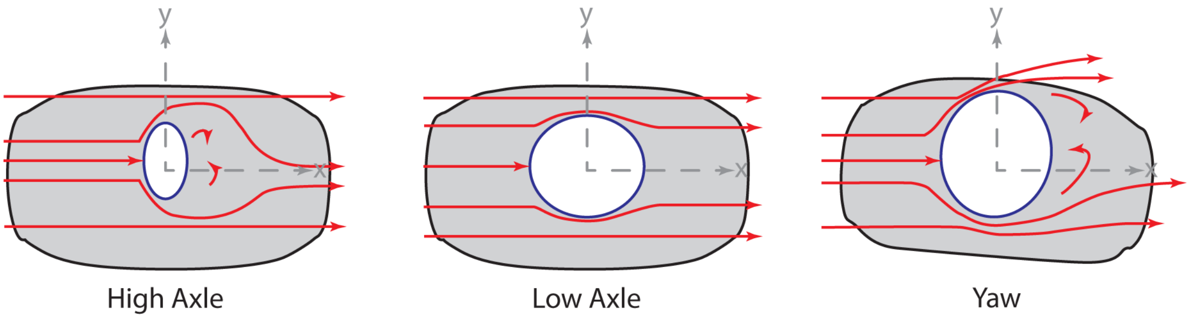

Figure 6.4: *Illustrative diagram showing the local flow behaviour, contact patch orientation and size for the extreme axle heights at zero yaw and a typical example at yaw.*

much larger surface area of the tyre under which the air flow is travelling. This is the reason why the non-yawed tyre profiles produced a far lower coefficient of lift than the measured realistic profiles when at yaw. Higher blockage and wider contact patches due to yaw or high deformation are conducive to high frontal contact patch pressures which result in high values of lift.

6.4 Modelling Simplifications for Wind Tunnel and CFD

The remaining section of this summarising discussion presents compromises and simplifications often made in wind tunnel and computational settings which have not been adequately quantified in the literature in terms of their aerodynamic consequences. These compromises are either made to preserve equipment and increase longevity of the consumables within a wind tunnel or in the case of CFD, purely through lack of available data or resources.

6.4.1 CFD: Effect of the Straight-Ahead Profiles Turned to Yaw

Often when performing yaw studies in a CFD environment the wheel used for straight-ahead studies is simply rotated to the yaw angle. The results within this work have exposed that this is not sufficient for simulating the correct flow-field or achieving the correct forces as the geometrical sidewall dragging results in a major change to the local flow-field under the contact patch, which in turn changes the lift force generated and the wake. Specifically, the biased loading introduced with camber means the flow-field is affected differently at positive or negative yaw. For positive yaw the entire contact patch becomes loaded (the outside wheel when cornering) and the flow-field is dominated more by the physical turning than by the subtleties of the axle height and profile. The opposite is true for the case where the wheel is at negative yaw, in this case, the unloaded wheel when cornering.

The dragging of the sidewall introduces a blockage bias near the ground plane toward one side depending upon which way the wheel has been turned. This blockage affects the wake development and the formation of the sidewall to tread step and therefore the trailing vortex structures as described in Section 6.3.2.2. A similar scenario for wind tunnel applications would be in the use of a rigid tyre with a fixed profile. This would, however, not simulate changes to a contact patch and so the effect on the wake may not be as severe.

As most studies do not have the availability of deformable tyres or have any means of acquiring data for yawed profiles, this consequence is difficult to avoid. As a result, the measured profiles used within this study have been tabulated in Appendix B for use in further computational studies where a realistic geometry is desired.

6.4.2 CFD: Effect of the Inclusion of the Support Sting

The presence of the support sting appears to have conflicting influences on the wake. The intersection between the main strut and the reinforcement bar both in close proximity to the ground builds up a vortex due to the camber angle and ground effect although this feature does not appear to influence the vortices from the tyre. This is visible in both the wind tunnel and CFD environments.

A CFD simulation with the sting removed resulted in a surprise increase to the drag by 8%. This was despite the removal of the vortex as described above and a reduced overall wake. The removal of the sting, however, resulted in an increase in the lift of the scoop (although the overall lift was unchanged) due to a removed accelerated region below the scoop. Most significantly, the formation of the inboard vortex from the sidewall had been increased dramatically which is not only consistent with the drag increase but also a large deviation from the flow-field of the baseline case with the sting.

It is obvious that no realistic experimental case could exist without a sting. Likewise, the presence of full suspension geometry is too specific to a manufacturer to justify a generic isolated study. However, the differences observed are sufficient to prove that any computational simulations to be performed must simulate the sting or suspension of the reference case in order to achieve a realistic aerodynamic performance.

6.4.3 Wind Tunnel: Effect of the use of Glycerol

The use of glycerol on a rolling road system is often employed to reduce the friction between the tyre and the belt of the moving ground plane. Whilst this results in lower temperatures and less abrasion, the deformation level achievable with the deformable tyre does not exhibit a true yawed profile.

Scanned profile measurements show evidence of three major areas for concern. Firstly, the inboard contact patch location is only 28% of the way towards being a true yawed profile. This was matched with a reduction in lift of 26%. The drag, however, did not intersect the two measurements of the true yawed profile against the non-yawed profile, at yaw. This resulted instead in an increase in drag. There are many factors that could cause this due to such a large change in the local geometry of the sidewall to contact patch region.

The use of glycerol resulted in a build-up on the surface of the wheel and belt and most significantly in the step between the sidewall and the tread. This resulted in a smoother scanned outboard profile which translated to the CFD and resulted in a smaller outboard vortex. This effect was not as severe on the inboard side due to the level of deformation on the case used. A similar study of a glycerol coated tyre at a higher axle height may result in an even further reduced total wake due to the same build up on the inboard step. Since there has been an established relationship between the apparent severity of the sidewall to tread transition step with the size of the resulting vortex, the use of glycerol compromises the wake development in this small detail alone.

The third concern is the most obvious. The shape of the sidewall itself has changed to accompany the change in contact patch width. However, as shown by the studies of inflation pressure, which resulted in similar changes in the curvature of the sidewall, this did not seem to be consequential to the far-field wake. Therefore the primary concerns for full-car development purposes are the first two points which have led to reduced vorticity and a less persistent faster decaying wake. Given the limited alternatives to achieving a more realistic tyre profile on a day-to-day process, it is important to understand these limitations and the changes that are brought about by the use of such a methodology in order to design and iterate downstream components for a successful full-car F1 aerodynamic system.

Chapter 7

Conclusions

The work presented here has investigated the aerodynamic sensitivities to key test parameters applicable to the investigation of an isolated wheel. This has been done both empirically in a wind tunnel and theoretically via CFD simulations. Techniques used included a rotating tyre sidewall scanning methodology, static contact patch size measurements, five-hole pressure probe wake measurements, particle image velocimetry (PIV) and load-cell drag measurements. CFD simulations utilising two popular industrial codes, based on RANS and Lattice-Boltzmann techniques respectively, were also performed to support the experimental work.

It has long been established in the literature that the aerodynamic characteristics of the wheel itself, and in turn their interaction with those of other components, are a crucial area of understanding for high-performance race and production car technology. The highly tuned aerodynamic system of vortices and pressure gradients built into modern vehicles for high downforce, or low drag, can be deteriorated by interaction with the low pressure wake from the front wheels in particular. The purpose of this thesis was to investigate details of the testing process in order to establish an order of aerodynamic sensitivity to allow prioritisation of simplifications, or even compromises, in future testing regimes.

7.1 Scope of Investigation

Several test parameters were considered and the following objectives, split into two areas for desired improved understanding, were set:

Use of Deformable Tyres:

- Identify the exact nature of geometrical changes to the sidewalls under varying load conditions.
- Determine the significance of their effects on the aerodynamic flow-field and force measurements.
- Use a deformable tyre to study the properties of yaw (steer, slip and toe) and camber.

Through-Hub Flow:

- Identify the external flow-field influences from through-hub flows.
- Experiment with scoop/brake duct inlet conditions.
- Determine the necessity for detailed internal geometry in model-scale testing.

The scope and objectives of the work have been met and the key findings are concluded in the remaining sections.

7.2 Effect of Tyre Deformation

The work undertaken made use of up-to-date technology in terms of the deformable slick tyre which was manufactured by the official F1 tyre supplier of its year. There is little presented in the literature regarding the usage of fully deformable tyres and indeed most published studies still make use of rigid conical tyres which have long been the standard. The effects of the changes in the contact patch region as well as the tyre sidewall bulge as a result of tyre deformation, which are even more apparent at yaw, are contained within this work.

7.2.1 Geometrical Effects Under Load

This study tested far more realistic conditions than are known to be executed within the motorsport industry. In particular, axle height, which directly characterises the level of vertical deflection the tyre experiences, is a parameter which is often compromised in favour of improving equipment longevity. Likewise the use of glycerol on the belt of a rolling road system is known to be used for reducing friction at yaw at the expense of an under-representation in the deformed tyre profile.

When experiencing vertical load of any form, the tyre's profile deforms and becomes non axially symmetric. A change of axle height by only 0.03D, equating to the difference between corner-exit and end-of-straight downforce levels resulted in significant changes in the contact patch width and the form of the sidewall of the tyre. The latter changed from a smooth curvature to a profile that was 'folded' in appearance. The changes were again emphasised at yaw where lateral sidewall dragging was observed. This was biased dependent upon the camber angle of the wheel. For the case of negative camber on a left hand side wheel, as in this research, positive yaw (clockwise from plan view) resulted in a full utilisation of the contact patch, twice the increase when compared to the negative yaw case which would describe the unloaded inside wheel when cornering.

7.2.2 Aerodynamic Effects Under Load

The local flow effects at the contact patch perimeter are significant in terms of how they dictate the global flow-field. The 'squeezing' regions either side of the contact patch determine the strength of the vortex structures produced and, in general, sharper geometrical profiles result in more aggressive vortex features and a higher-loss wake. Geometrical features within the first few millimetres of the moving ground plane are much more influential to the global flow-field than those higher up. It was observed that the 'sharp' step between the slick tread and the sidewall led to larger areas of lower stagnation pressure in the wake. In addition to the detail of the step between the tread and the sidewall, the opening up of the air channel below the tyre at a higher axle height, due to the camber angle, also had a large effect on the vorticity and form of the wake.

Yawing the wheel fundamentally changes the characteristic structure of the downstream wake to a point of non-recognition compared to the straight-ahead case, when turned to positive yaw (loaded outside wheel). When turning to negative yaw, the unloaded inside wheel when cornering, the axle height is a much more dominant parameter. Because the front wheels yaw frequently in either direction, this means the two parameters are effectively of equal importance when simulating cornering effects.

7.3 Effect of Through-Hub Flow

Academic studies often simplify further by restricting or completely removing the effect of through-hub flow, often present particularly in race cars for brake cooling purposes. This flow condition has been investigated in some depth in terms of inlet flow conditions, the through-hub flow nature with and without cooling components, and the exit flow influence on the global wake.

7.3.1 External Aerodynamic Effects of the Scoop Inlet

The external wake of the isolated wheel was largely changed by the varying level of restriction introduced into the interface between the scoop inlet and the hub of the wheel. This restriction resulted in an effect known as inlet spillage and induced a negative cooling drag trend, whereby the drag of the whole system decreased with increasing through-hub flow, contrary to traditional cooling flow theory.

7.3.2 Internal Aerodynamic Effects of Brake Cooling

Detailed internal geometry was simulated in CFD in order to assess the effect of the through-hub flow with the rotation of the brake rotor and the centrifugal pumping effect which takes place in its internal channels. The pumping effect was found to be negligible compared to the restrictive effect of introducing more complex internal geometry and the complexity of the geometry was found to result in a very different exit flow condition compared to the simplified internals.

7.4 Key Parameters for a Development Environment

Summarising the above, the following list ranks these test parameters starting with the most sensitive variable from an aerodynamic perspective. In conclusion, it is considered fundamental to a full-car or isolated wheel experiment to ensure the correct:

- Axle height
- Yawed sidewall profile *(no use of glycerol or CFD simplification at yaw)*
- Camber angle
- Presence of internals *(brake ducting and rotor)*
- High inflation pressure *(contact patch is more sensitive than sidewall curvature)*
- Through-hub flow rate
- Rotation of internal components *(the brake rotor)*

For full-car development it is essential to set geometrical variables relating to the typical setup parameters of a race car (such as axle height, toe and camber) as accurately as possible. It is essential when performing work at yaw to steer the wheels to a representative yaw angle relative to the vehicle axis in order to represent slip. It is also important to ensure the correct mass-flow through the hub. There is, however, scope for simplifications to be made in terms of internal geometry detail. For example, there is little need for rotation of internal components which adds both mechanical complication as well as question over repeatability of results by adding another variable.

These conclusions should assist any relevant study within the field in order to either further this work or to be used to hone the development of a full-car aerodynamic system. With improved understanding of the individual aerodynamic characteristics of the tyre, the flow-field (local details and global effects) and their effect on aerodynamic loading, this should allow more efficient development of other vehicle components. In the case of F1 in particular, this applies to front wing end-plates, bargeboards, turning vanes, brake cooling components and suspension geometry. More efficient design of these components allows for better quality and higher energy airflow to the sensitive underfloor region and ultimately the rear of the car, which in turn results in increased competitiveness of the vehicle.

Chapter 8

Recommendations for Future Work

The following suggestions are intended as a guide for any reader considering carrying out extended investigations based upon this work. During this research several areas of study have emerged as being far too extensive for the scope of this work alone. In addition to this, the investigations contained within this thesis have shed light on new problems which may indeed become research topics in their own right.

8.1 Measurement of Wheel Lift

A long-standing issue with experimental rotating wheel aerodynamics has been due to the lack of ability to reliably resolve the aerodynamic lift of the wheel due to varying reaction forces (Mears [3], Whitbread [5], Fackrell [23], Hinson [32] and McManus & Zhang [33]). Some studies covered within Chapter 1 present the findings of an experiment with an under-belt (moving ground plane) load-cell [45] but this again suffers a similar issue. Other methods involve the integration of surface static pressure distributions which are ultimately considered the most reliable.

Measuring the rotating wheel lift is a crucial parameter to know due to the fact that full-car development wind tunnels may only get a reading of the 'car-load' and have no direct reference to the amount of unsprung loading being generated on the wheel, particularly in the case of a 'wheels-on' model. An aerodynamic component placed on the wheel, such as a brake duct, may have an undesirable positive lift effect which would not be detected in such a wind tunnel and therefore a positive downforce effect on the rest of the car may be cancelled or even less significant. This is a long-standing problem which although outside of the scope of this work, was found to be an inconvenient fact as CFD lift forces have no form of validation other than the work by other authors on differing geometries.

8.2 Unsteady Flow Investigation

The transience or unsteadiness of flow-fields is becoming an increasingly researched topic in the field of vehicle aerodynamics. Indeed suggestions as to the developing understanding of the unsteady nature of the flow-field of an isolated wheel were suggested by Axerio et al. [57] who postulated that the vortex core centres in the trailing wake of the isolated wheel were in fact oscillating with a frequency related directly to the wheel diameter and rotational frequency. Further effects such as 'chopping' from the spokes and cumulative shedding frequencies from adjacent components lead to additions to what is already an unsteady wake. Whilst most studies, including this one, focus primarily on the time-averaged flow-field, there is an increasing requirement to understand the underlying flow-physics behind the oscillation of the wake and the unsteadiness of the trailing vortex structures. Knowing more about these unsteady characteristics and being able to predict them is the next stage in developing downstream components which benefit from increased understanding of wheel aerodynamic flows.

8.3 Thermal Internal Flow Simulations and Experimentation

The high-temperature nature of the components in the wheel assembly presented here raises a question of thermal effects on the internal fluid-flow. Indeed, the internal fluid-flow is intended primarily to remove this heat from the components and therefore a significant amount of thermal energy is transferred to the air in the process. Parameters in the air such as density and viscosity change significantly, which in turn affect the air density, momentum, Reynolds number and the characteristic aerodynamic behaviour. In addition to heat-transfer effectiveness of internal flows, the global flow-field effect is an unknown due to the nature of the exit flow and potential change to the mass-flow within the ducting due to differing flow-regimes. Particular local interest lies within the channels of the brake rotor in addition to the global flow-field.

8.4 Rim Designs to Draw Increased Through-Hub Flow

As a conclusion of this work it was found that increasing the rate of through-hub flow, as well as having potential improvements in brake component cooling, can lead to more outboard biased flow which provides cleaner airflow to the sensitive regions of an F1 car in particular. In addition to this, the reduced drag from cleaner inlet flow (reduced spillage separation due to internal restriction) provides a less wasteful aerodynamic system around the wheel assembly.

Over recent years many attempts have been employed within F1 to increase through-hub flow rate or reduce the drag of the wheel assembly (or both) by placing devices on the rim of the wheel. The photographs in Figure 1.28 reproduced below as Figure 8.1 show some of these devices.

Figure 8.1: *Left: Standard rim, spokes only with glowing brake rotor. Centre: Rim fairing characteristic of the 2008 and 2009 F1 season. Right: A Post 2009 wheel cover ban solution incorporating the "fairing" into the rim itself.*

The full wheel fairing with exit hole allows a more controlled exit of the through-hub flow into a region which maximises the thrust recovery. In the case of the latest options, it is proposed that their performance increase is in fact due to creating a low pressure on the outboard side of the rim which assists the draw of through-hub flow.

A detailed study into the vast array of modern devices which are appearing on race car wheel rims and the exact aerodynamic reasoning would be of useful benefit particularly in lower formulae where such extreme levels of research and development are not available. An investigation into the techniques of measuring through-hub flow should also be included to determine if a single point measurement is sufficient to describe the through-hub flow rate.

8.5 Dynamic Contact Patch Measurement

Whilst it was not a common technique in the literature before this research to measure the dynamic rotating sidewalls of a pneumatic tyre, the other key variable highlighted within this thesis, the contact patch size and shape, remains purely a qualitative study.

The primary issue regarding measurement of a rotating wheel is due to the necessity for a moving ground plane. An investigation would be proposed whereby a fine grid of pressure sensitive cells (or even micro-switches) were to be placed underneath the wheel's contact patch. The issues with this experimental methodology are due to having a high velocity moving surface between the proposed matrix of sensors and the tyre which has a significant amount of load applied through it. Given the requirement for such high load (in excess of 300N for an end-of-straight deformation condition), the equipment could be made quite robust and require in itself a significant amount of pressure before being activated. The surface would in all likelihood require some form of low-friction coating such as Teflon or equivalent. In addition, the thickness of a rolling road belt is often significant preventing the exact structure of the tyre to be represented in the sensor array.

An alternative to the above suggestion would be to make use of a row of sensors as used by Mágori et al. [14] or Brandt et al. [15]. Applying a row of their single distance sensors mounted inside the tyre to measure the distance from the axle to the tread surface would allow a full description of the tread shape under rotation to be measured. In conjunction with the laser scanning technique used within this work a full description of a deformable tyre would be achievable.

Knowing the exact shape and size of the contact patch would be a key asset to any team or individual wishing to perform CFD studies on a car under stressed conditions such as those experienced under heavy cornering, when essentially the car requires its highest level of aerodynamic performance.

8.6 Wheels-On Application of Deformation

The method in which deformation was applied in this research was by the use of a wheels-off sting, mounted to the side of the wind tunnel. The amount of vertical force which could be applied was therefore limited only to the physical capabilities of the pneumatic system in place.

Wheels-on models are favourable due to their lower blockage and realistic mounting methods to the hub. These methods present their own problems, particularly during the process of taking a mechanical tare. However, this is the mechanism favoured by F1 and as such a method of applying deformation via a wheels-on model would be desirable. The main considerations are the stresses which the main support beam (or sting) would experience as well as the structural integrity of the model car. A design of a 'bare-bones' system with a sting mounting and a rigid backbone comprising active axle height adjustment would be a significant area of research in order to highlight and solve some of the technical difficulties which lie within such a system.

There are many conditions under which an F1 car is required to be tested aerodynamically. Parameters such as yaw, roll, pitch, ride heights and steering angle are just some of the variables which change the aerodynamic flow-field of a car significantly. The work presented within this thesis has shown that the change in flow-field by changing axle height by only around 3% of the wheel diameter is significant. The addition of the yaw variable into this axle height change makes this much more dramatic. Therefore in the endeavour to measure the aerodynamics of the full-car system as accurately as possible under varying conditions would benefit largely by the research suggested within this section.

8.7 Isolated Effects of Contact Patch and Sidewall Deformation

Demanding a realistic deformable tyre requires a model which changes both in sidewall and contact patch shape. Both parameters have been observed to be vastly linked to the global aerodynamic flow-field of a wheel assembly. It has been postulated that the more significant variable is the contact patch. However, it is not possible to fully isolate this variable from the data collected here.

A series of CFD simulations would be proposed whereby the effect of sidewall shape and contact patch could be varied under a controlled manner, thus eliminating the realism from the model but allowing vital information as to what has the larger effect and where. Parameters to investigate would be size, major-to-minor axis ratio of the contact patch shape, orientation, severity of the step between the tread and the sidewall, amount of bulge in the sidewall and location of the sidewall bulge (close to the ground or further up near the rim bead). Such an investigation would perhaps allow simplified and more repeatable wind tunnel tyres to be produced for academic settings, more likely to capture the realistic flow-field than a rigid tyre and with a predetermined idea as to the limitations and sensitivities of the geometry to the aerodynamic flow-field.

References

[1] Smith, C., *Tune to Win : The Art and Science of Race Car Tuning and Development* (Aero Publishers Inc., 1978) pp13-18, 60-62

[2] Katz, J., *New Directions in Race Car Aerodynamics: Designing for Speed* p54 (Robert Bentley Publishers, 1995)

[3] Mears, A. P., *The Aerodynamic Characteristics of an Exposed Racing Car Wheel* (PhD Thesis, University of Durham, 2004)

[4] Kellar, W. P., Pearse, S. R. G., & Savill, A. M., *Formula 1 Car Wheel Aerodynamics* (J. Sports Engineering, ISEA, 1999) 2:203-212

[5] Whitbread, L., *Measurement of the Lift Distribution on a Rotating Wheel* (M.Sc. Thesis, Cranfield University, 2000)

[6] Dominy, R. G., *Aerodynamics of Grand Prix Cars* (Proc. Inst. Mech. Eng., 1992) 206D:267-274

[7] Dominy, J. A. & Dominy, R. G., *Aerodynamic Influences on the Performance of the Grand Prix Racing Car* (Proc. Inst. Mech. Eng, Part D, J. Automobile Eng., Inst. Mech. Eng., 1984)

[8] Velenis, E. & Tsiotras, P., *Minimum Time vs. Maximum Exit Velocity Path Optimization During Cornering* (Proc. IEEE Int. Symp. Ind. Elec., IEEE, 2005) 1:355-360

[9] Yang, X. & Olatunbosun, O. A., *Optimization of reinforcement turn-up effect on tyre durability and operating characteristics for racing tyre design* (J. Materials and Design, Elsevier Ltd., 2011) 35:798-709

[10] Clark, S. K., *The Rolling Tire Under Load* (SAE Inc., 1965) SAE Technical Paper 650493

[11] Ridha, R. A. & Theves, M., *Advances in Tyre Mechanics* (Rapra Technology Ltd, 1994) Rapra Review Reports 7(5):Rpt77

[12] Ghoreishy, M. H. R., *Finite Element Analysis of the Steel-Belted Radial Tyre with Tread Pattern under Contact Load* (Iranian Polymer Journal, IPPI, 2006) 15(8):667-674

[13] Sabey, B. E. & Lupton, G. N., *Photography of the real contact area of tyres during motion* (Road Research Laboratory RRL Report LR64, Ministry of Transport, 1967)

[14] Mágori, V., Mágori, V. R. & Seitz, N., *On-Line Determination of Tyre Deformation , a Novel Sensor Principle* (IEEE Ultrasonics Symposium, IEEE, 1998) 0-7803-4095-7/98

[15] Brandt, M., Bachmann, V., Vogt, A., Fach, M., Mayer, K., Breuer, B. & Hartnagel, H. L., *Highly Sensitive AlGaAs/GaAs position sensors for measurement of tyre tread deformation* (Electronics Letters, IEE, 1998) 34(8):760-762

[16] Dixon, J. C., *Tyres, Suspension and Handling* (Cambridge University Press, 1991) pp66-68, 75, 86-87, 127-128, 240 - 241, 267-273

[17] Bastow, D., *Car Suspension and Handling* (Pentech, London, 1987) pp85-95

[18] Jones, B., *60 Years of the Formula One Championship* (Carlton Books Ltd., 2009) p11

[19] Bearman, P. W., *REVIEW - Bluff Body Flows Applicable to Vehicle Aerodynamics* (J. Fluids Eng., ASME, 1980) 102:265-274.

[20] Park, C. W. & Lee, S. J., *Free End Effects on the Near Wake Flow Structure Behind a Finite Circular Cylinder* (J. Wind Eng. & Ind. Aero., 2000) 88:231-246

[21] Park, C. W., & Lee, S. J., *Effects of Free-End Corner Shape on Flow Structures Around a Finite Cylinder* (J. Fluids & Struct., 2004) 19:141-158

[22] Massey, B. S. & Ward-Smith, A. J., *Mechanics of Fluids* 8^{th} *Edition* (Taylor and Francis, London and New York, 2006) pp415, 195-201, 339-350

[23] Fackrell, J. E., *The Aerodynamics of an Isolated Wheel Rotating in Contact with the ground* (PhD Thesis - University of London 1974)

[24] Fail, R., Lawford, J. A. & Eyre, R. C. W., *Low-Speed Experiments on the Wake Characteristics of Flat Plates normal to an Air Stream (London: HM Stationery Office, 1959)*

[25] http://www.fia.com/en-GB/sport/regulations/Pages/FIAFormulaOneWorldChampionship.aspx (Cited January 2013)

[26] Bearman, P. W. & Zdravkovich, M. M., *Flow around a circular cylinder near a plane boundary* (J. Fluid Mech., Cambridge University Press, 1978) 89:33-47

[27] Cooper, K. R., *Bluff-Body Aerodynamics as Applied to Vehicles*, (J. Wind Eng. & Ind. Aero., Elsevier Ltd., 1993) 49:1-21

[28] Cogotti, A., *Aerodynamic Characteristics of Car Wheels* (Int. J. Vehicle Design, 1983) SP3(1983):173-196

[29] Clarke, S. C., *An Investigation of the Flow Around a Rotating Cylinder Near the Critical Reynolds Number* (MSc Thesis, Cranfield University, 1975)

[30] Swanson, W. M., *The Magnus Effect: A Summary of Investigations to Date* (J. Basic Eng., 1961) Sept 1961:461-470

[31] Morelli, A., *Aerodynamic Actions on an Automobile Wheel* (First Symp. Road Vehicle Aero., City University, 1969) Paper 5

[32] Hinson, M., *Measurement of the Lift Produced by an Isolated, Rotating Formula One Wheel Using a New Pressure Measurement System* (M.Sc. Thesis, Cranfield University: College of Aeronautics, 1999)

[33] McManus, J. & Zhang, X., *A Computational Study of the Flow Around an Isolated Wheel in Contact With the Ground* (Transactions of the ASME, ASME, 2006) 128:520-530

[34] Stapleford, W. R. & Carr, G. W., *Aerodynamic Characteristics of Exposed Rotating Wheels* (Technical Report MIRA, 1970) 1970/2

[35] Regert, T. & Lajos, T., *Investigation of Flow Field Past Rotating Wheels of Cars* (Proceedings of CMFF, Budapest, September 3 - 6, 2003)

[36] Gaylard, A. P. & Duncan, B, *Simulation of Rear Glass and Body Side Vehicle Soiling by Road Sprays* (J. of Passeng. Cars - Mech. Syst., SAE Int., 2011) 4(1):184-196, SAE Technical Paper 2011-01-0173

[37] Bearman., P. W., De Beer, D., Hamidy, E. & Harvey, J. K., *The Effects of a Moving Floor on Wind Tunnel Simulation of Road Vehicles* (SAE Inc., 1988) SAE Technical Paper 880245

[38] Wiedemann, J., *The Influence of Ground Simulation and Wheel Rotation on Aerodynamic Drag Optimization - Potential for Reducing Fuel Consumption* (SAE Inc., 1996) SAE Technical Paper 960672

[39] Mercker, E., Breuer, N., Berneberg H. & Emmelmann, H. J., *On the Aerodynamic Interference Due to The Rolling Wheels of Passenger Cars* (SAE Inc., 1991) SAE Technical Paper 910311

[40] Axon, L., Garry, K. & Howell, J., *The Influence of Ground Condition on the Flow Around a Wheel Located Within a Wheelhouse Cavity* (SAE Int., 1999) SAE Technical Paper 1999-01-0806

[41] Wickern, G., Zwicker, K. & Pfadenhauer, M., *Rotating Wheels - Their Impact on Wind Tunnel Test Techniques and on Vehicle Drag Results* (SAE Inc., 1997) SAE Technical Paper 970133

[42] Regert, T. & Lajos, T., *Description of Flow Field in the Wheelhouses of Cars* (Int. J. Heat & Fluid Flow, Elsevier Ltd., 2007) 28:616-629.

[43] Elofsson, P. & Bannister, M., *Drag Reduction Mechanisms Due to Moving Ground and Wheel Rotation in Passenger Cars* (SAE Int., 2002) SAE Technical Paper 2002-01-0531

[44] Ahmed, S. R., Ramm, G. & Faltin, G., *Some Salient Features of the Time Averaged Ground Vehicle Wake* (SAE Inc., 1984) SAE Technical Paper 840300

[45] Dimitriou, I. & Klussmann, S., *Aerodynamic Forces of Exposed and Enclosed Rotating Wheels as an Example of the Synergy in the Development of Racing and Passenger Cars* (SAE Int., 2006) 2006-01-0805

[46] http://www.pirelli.com/tyre/ww/en/f1/tyre-range.html
(Cited January 2013)

[47] http://www.mts.com/en/products/industry/ground-vehicles/index.htm
(Cited January 2013)

[48] Fackrell, J. E. & Harvey, J. K., *The Flow Field and Pressure Distribution of an Isolated Road Wheel* (Advances in Road Vehicle Aero., BHRA Fluid Eng. Conference, BHRA, 1973) Paper 10 - Stephens, H.S

[49] Mears, A. P., Dominy, R. G. & Sims-Williams, D. B., *The Flow About an Isolated Rotating Wheel - Effects of Yaw on Lift, Drag and Flow Structure* (4th MIRA International Vehicle Aerodynamics Conference : Warwick - UK, MIRA, 2002)

[50] Mears, A. P., Dominy, R. G. & Sims-Williams, D. B., *The Air Flow About an Exposed Racing Wheel* (SAE Int., 2002) SAE Technical Paper 2002-01-3290

[51] Mears, A. P., Crossland S. C., & Dominy, R. G.*An Investigation into the Flow-Field About an Exposed Racing Wheel* (SAE Int. 2004) 04ANNUAL-453

[52] Purvis, A. R., *The Wake Behind a Deformable Racing Tyre* (MSc Thesis, Cranfield University, 2003)

[53] Uawithya, C., *Aerodynamic Measurements on Rotating Racing Car Wheels* (Technical Report, University of Durham, 1994)

[54] Mowatt, P., *A new telemetry system for the transmission of signals from rotating machines* (Technical Report, University of Durham, 1993)

[55] Wäschle, A., Cyr, S., Kuthada, T. & Wiedemann, J., *Flow Around an Isolated Wheel - Experimental and Numberical Comparison of Two CFD Codes* (SAE Int., 2004) SAE Technical Paper 2004-01-0445

[56] Saddlington, A. J., Knowles, R. D. & Knowles, K., *Laser Doppler Anemometry Measurements in the Near-Wake of an Isolated Formula One Wheel* (J. Exp. Fluids, Springer-Verlag, 2007) 42:671-681

[57] Axerio, J., Iaccarino, G., Issakhanian, E., Lo, K., Elkins, C. & Eaton, J., *Computational and Experimental Investigation of the Flow Structure and Vortex Dynamics in the Wake of a Formula 1 Tire* (SAE Int., 2009) SAE Technical Paper 2009-01-0775

[58] Landstrom, C., Josefsson, L., Walker, T., & Lofdahl, L., *Aerodynamic Effects of Different Tire Models on a Sedan Type Passenger Car* (SAE Int. 2012) SAE Technical Paper 2012-01-0169

[59] Knowles, R. D., *Monoposto Racecar Wheel Aerodynamics: Investigation of Near-Wake Structure & Support-Sting Interference* (PhD Thesis, Cranfield University, 2005)

[60] Knowles, R. D., Saddlington, A. J. & Knowles, K., *On the Near Wake of Rotating, 40%-Scale Champ Car Wheels* (Proceedings of the 2002 SAE Motorsports Engineering Conference, 2002)

[61] Knowles, R., Saddlington, A. & Knowles, K., *Simulation and Experiments on an Isolated Racecar Wheel Rotating in Ground Contact* (MIRA Conference, MIRA, 2002) Session 7A

[62] Hetherington, B. & Sims-Williams, D. B., *Wind Tunnel Model Support Strut Interference* (SAE Inc., 2004) SAE Technical Paper 2004-01-0806

[63] Hetherington, B. & Sims-Williams, D. B., *Support Strut Interference effects on Passenger and Racing car Wind Tunnel Models* (SAE Int., 2006) SAE Technical Paper 2006-01-0565

[64] Hetherington, B., *Interference of Supports used for Ground Vehicle Wind Tunnel Testing* (PhD Thesis, Durham, University, 2007)

[65] http://formula1.brembo.com (Cited January 2013)

[66] http://www.hitcoracing.com/formula1.htm (Cited January 2013)

[67] http://www.f1technical.net/articles/2 (Cited January 2013)

[68] McPhee, A. D., & Johnson, D. A., *Experimental Heat Transfer and Flow Analysis of a Vented Brake Rotor* (Int. J. Thermal Sciences, 2008) 47:458-467

[69] Charlesworth A. *Vehicle Drag Reduction through the use of Boat Tailing and Vented Base Cavities* (M.Eng. Thesis, Durham University, 2012)

[70] Johnson, D. A., Sperandei, B. A. & Gilbert, R. *Analysis of turbulent flow and separation in a vented rotor* (J. Fluids Eng., ASME, 2003) 125:979-986

[71] Parish, D. & MacManus, D. G., *Aerodynamic investigations of ventilated brake discs* (Proc. IMechE. Automobile Eng., IMechE, 2005) 219(D):471-486

[72] Fackrell, J. E. & Harvey, J. K., *The Aerodynamics of an Isolated Road Wheel* (Proc. 2^{nd} AIAA Symp. Aero. of Sports & Comp. Vehicles, 1975) Vol. 16

[73] Minto, J., *Investigation into the Effects of Varying Through-Hub Flow on the Aerodynamics of Exposed Racing Car Wheels* (M.Eng. Thesis, Durham University, 2010)

[74] Sprot, A. J., Minto, J. B., Sims-Williams, D. B. & Dominy, R. G., *Aerodynamic Investigation on the Effect of Varying Through-Hub Flow on a Formula One Front Wheel Assembly* (J. of Passeng. Cars - Mech. Syst., SAE Int., 2011) 4(1):929-944. SAE Technical Paper 2011-01-1431

[75] Barnard, R. H., *Theoretical and Experimental Investigation of the Aerodynamic Drag due to Automotive Cooling Systems* (Proc. Instn. Mech. Engrs., 2000) 214D:919-927

[76] Hucho, W. H., *Aerodynamics of Road Vehicles 4th Edition* (SAE Int., Warrendale, PA, 1998) ISBN:978-0-7680-0029-0 pp197-201

[77] Seddon, J. & Goldsmith, E. L., *Intake Aerodynamics* (AIAA Education Series, 1985) pp 217-220

[78] Oler, J. W., Roseberry, C. M., Jordan, D. P. & Williams, J. E., *Ram-Recovery Coefficient Correlations for Automotive Cooling Airflows* (SAE Inc., 1991) SAE Technical Paper 910309

[79] Gilliéron, P. & Chometon, F., *Reduction of Cooling Air Drag of Road Vehicles: An Analytical Approach* (SAE Int., 2001) SAE Technical Paper 2001-01-1266

[80] Williams, J., Karanth, D. & Oler, W., *Cooling Inlet Aerodynamic Performance and System Resistance* (SAE Inc., 2002) SAE Technical Paper 2002-01-0256

[81] Williams, J. E., *Aerodynamic Drag of Engine-Cooling Airflow With External Interference* (SP-1786, SAE Int., 2003) SAE Technical Paper 2003-01-0996

[82] Sims-Williams, D. B. & Dominy, R. G., *The Design of a New Wind Tunnel for Vehicle Aerodynamics Research* (4th MIRA International Vehicle Aerodynamics Conference, Warwick, UK, 2002)

[83] Sims-Williams, D. B. & Dominy, R. G., *The Design of an Open-Jet Wind Tunnel for Model Testing* (SAE Int., 2002) SAE Technical Paper 2002-01-3340

[84] Johnson, R. W., *The Handbook of Fluid Dynamics* (CRC Press, 1998)

[85] Barlow, J. B. ,Rae Jr, W. H. & Pope, A., *Low Speed Wind Tunnel Testing, 3rd Edition* (John Wiley & Sons, 1999)

[86] http://en.espnf1.com/mclaren/motorsport/story/58215.html (Cited January 2013)

[87] Hughes, I. G. & Hase, T. P. A, *Measurements and their Uncertainties : A Practical Guide to Modern Error Analysis* (OUP Oxford, 2010)

[88] Oettle, N. R., Sims-Williams, D. B., Dominy, R. G., Darlington, C., Freeman, C & Tindall, P. *The Effects of Unsteady On-Road Flow Conditions on Cabin Noise* (SAE Int., 2011) SAE Technical Paper 2010-01-0289

[89] Oettle, N. R., Sims-Williams, D. B., Dominy, R. G., Darlington, C. & Freeman, C, *The Effects of Unsteady On-Road Flow Conditions on Cabin Noise: Spectral and Geometric Dependence* (J. of Passeng. Cars - Mech. Syst., SAE Int., 2011) 4(1):120-130, SAE Technical Paper 2011-01-0159

[90] Oettle, N. R., Mankowski, O. A., Sims-Williams, D. B., Dominy, Freeman, C & Gaylard, A. *Assessment of a Vehicle's Transient Aerodynamic Response* (SAE Int., 2012) SAE Technical Paper 2012-01-0449

[91] Sims-Williams, D. B. & Dominy, R. G., *The Validation and Application of a 5-hole Pressure Probe with Tubing Transfer Function Correction for Time-Accurate Measurements in Unsteady Flows* (2nd MIRA Int. Conf. Vehicle Aerodynamics, 1998)

[92] Bryer, D. W. & Pankhurst, R. C., *Pressure-Probe Methods for Determining Wind Speed and Flow Direction* (Her Majesty's Stationary Office, St. Albans, 1971)

[93] http://www.ila.de (Cited January 2013)

[94] http://www.esi.com/Products/NewWaveResearch.aspx (Cited January 2013)

[95] Riethmuller, M. L, *Particle Image Velocimetry - Lecture Series 1996-2003* (Von Karman Institute for Fluid Dynamics)

[96] Silfvast, W. T., *Laser Fundamentals : 2nd Edition* (Cambridge University Press, 2008)

[97] http://www.edmundoptics.com/optics/optical-mirrors/flat-mirrors/nd-yag-laser-line-mirrors/2765 (Cited January 2013)

[98] Howell, J., Sims-Williams, D. B., Sprot, A. J. & Hamlin, F., *Bluff Body Drag Reduction with Ventilated Base Cavities* (SAE Int., 2012) SAE Technical Paper 2012-01-0171

[99] Newnham, P. S., *The Influence of Turbulence on the Aerodynamic Optimisation of Bluff Body Road Vehicles* (Ph.D. Thesis, Loughborough University, 2007)

[100] Thivolle-Cazat, E. & Gilliéron, P., *Flow Analysis Around a Rotating Wheel* (13th Int. Symp. on Applications of Laser Techniques to Fluid Mechanics, Lisbon, Potugal, 26 - 29 June, 2006)

[101] http://www.tecplot.com (Cited January 2013)

[102] Brizzi, L., Noel, A. & Herbert, V., *Phase Average Velocity Field in the Vicinity of an Isolated Wheel Model* (Technical Report, Université Poitiers, 2004)

[103] Ferziger, J. H. & Perić, M., *Computational Methods for Fluid Dynamics 3rd Edition* (Springer-Verlag, 2002)

[104] Mears, A. P. & Dominy, R. G., *Racing Car Wheel Aerodynamics - Comparisons Between Experimental and CFD Derived Flow-Field Data* (SAE. Int., 2004) SAE Technical Paper 2004-01-3555.

[105] Axon, L., Garry, K. & Howell, J., *An Evaluation of CFD for Modelling the Flow Around Stationary and Rotating Isolated Wheels* (SAE Inc., 1998) SAE Technical Paper 980032

[106] Axon, L., *The Aerodynamic Characteristics of Automobile Wheels - CFD Prediction and Wind Tunnel Experiment* (Ph.D. Thesis, Cranfield University: College of Aeronautics, 1999)

[107] Skea, A. F., Bullen, P. R., & Qiao, J., *The Use of CFD to Predict the Air Flow Around a Rotating Wheel* (2nd MIRA Int. Conf. Vehicle Aerodynamics, 1998)

[108] Skea, A. F., Bullen, P. R., & Qiao, J., *CFD Simulations and Experimental Measurements of the Flow Over a Rotating Wheel in a Wheel Arch* (SAE Int., 2000) SAE Technical Paper 2000-01-0487

[109] http://www.exa.com/powerflow.html (Cited January 2013)

[110] Bienz, C., Larsson, T., Sato, T. & Ullbrand, B., *In Front of the Grid - CFD at SAUBER PETRONAS F1 Leading the Aerodynamic Development* (1st European Automotive CFD Conference, Bingen, Germany - June 2003, EACC, 2003)

Publications and Conferences

The work contained within this thesis has appeared in the following conferences and publications to-date:

Conference Inclusions

IMechE - Enhancing Car Design Through Aerodynamics - MIRA - October 2012

SAE World Congress - Detroit - April 2012

SAE World Congress - Detroit - April 2011

Publications

Sprot, A. J., Sims-Williams, D. B. & Dominy, R. G., *The Aerodynamic Characteristics of a Fully Deformable Formula One Wind Tunnel Tyre* (J. of Passeng. Cars - Mech. Syst., SAE Int., 2012) 5(2):1026-1041

SAE Technical Paper 2012-01-1166

Sprot, A. J., Minto, J. B., Sims-Williams, D. B. & Dominy, R. G., *Aerodynamic Investigation on the Effect of Varying Through-Hub Flow on a Formula One Front Wheel Assembly* (J. of Passeng. Cars - Mech. Syst., SAE Int., 2011) 4(1):929-944

SAE Technical Paper 2011-01-1431

Appendices

Appendix A: Calibrations

Various calibrations are presented here, either for the reader's reference or for validation purposes.

Load-Cell Calibration

The load-cell calibration (Figure A.1) was achieved by applying known masses to the load-cell attached to a fixed mounting and the associated voltages recorded.

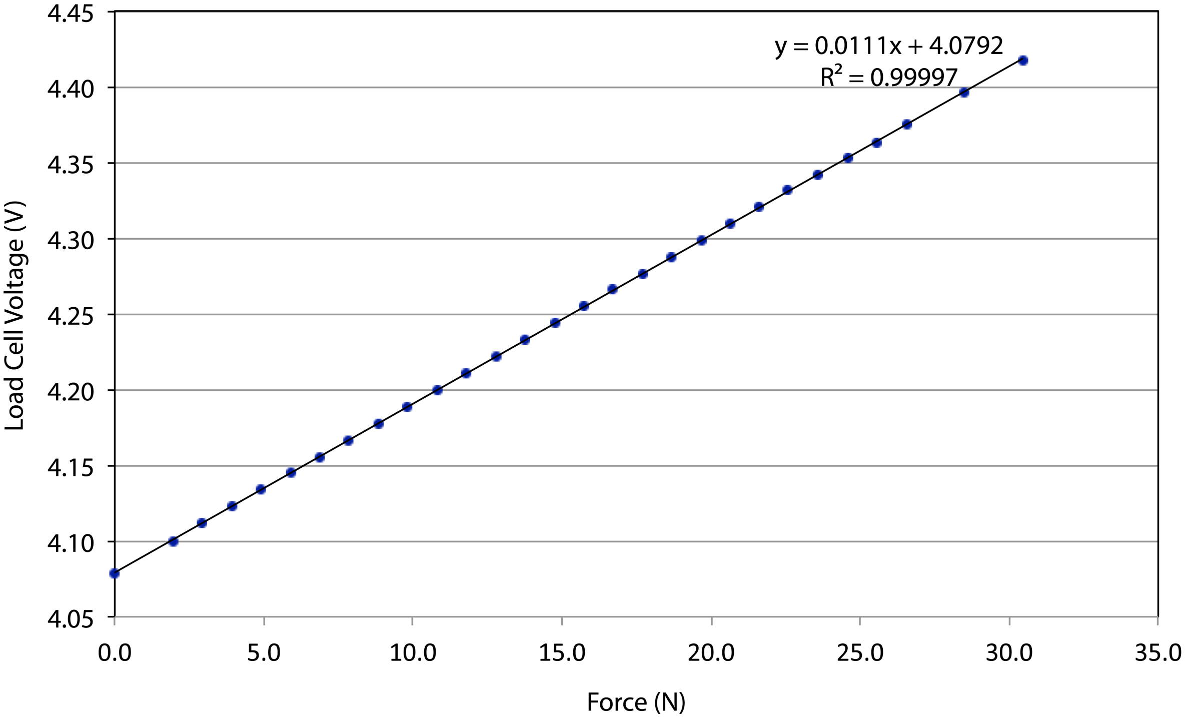

Figure A.1: *Load-cell calibration.*

Laser Distance Meter Calibration

The calibration of the laser distance meter was required to be more thorough in order to assess the repeatability and sensitivity to different surface finishes and curvatures. The device was used for measuring real-time axle height for the axle-rise experiments (the rise due to the wheel's rotation) and for measuring the sidewall profiles of the tyre. Figure A.2 shows the calibration for the device for three surfaces. The response and repeatability for all three surfaces (shiny and rough, white (reflective) and black) was within the scatter of the device. In reality, the changes in the surface of the tyre due to the elastic and deformable nature of the tyre were much more significant than this and therefore the calibration confirms it was suitable to be used for the intended experiments.

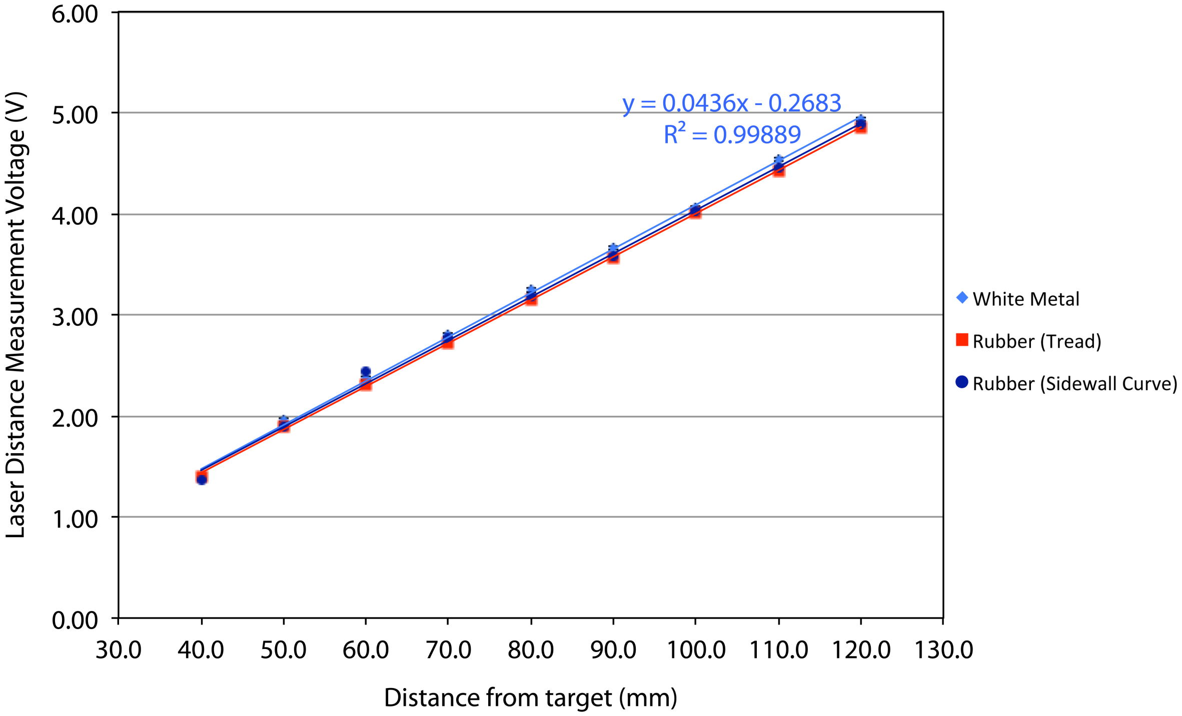

Figure A.2: *Laser distance meter calibration.*

Tyre Inflation Pressure - Transducer Calibration

The pressure transducer used to accurately measure the inflation pressure of the tyre is presented in Figure A.3. The amplified transducer allowed a low voltage sensitivity to the small inflation pressures used, therefore giving confidence in the setup process (a reliably measurable 0.6V between both the two most commonly used tyre pressure cases), ensuring the correct tyre pressure was set.

1psi = 6.89kPa = 0.0689bar

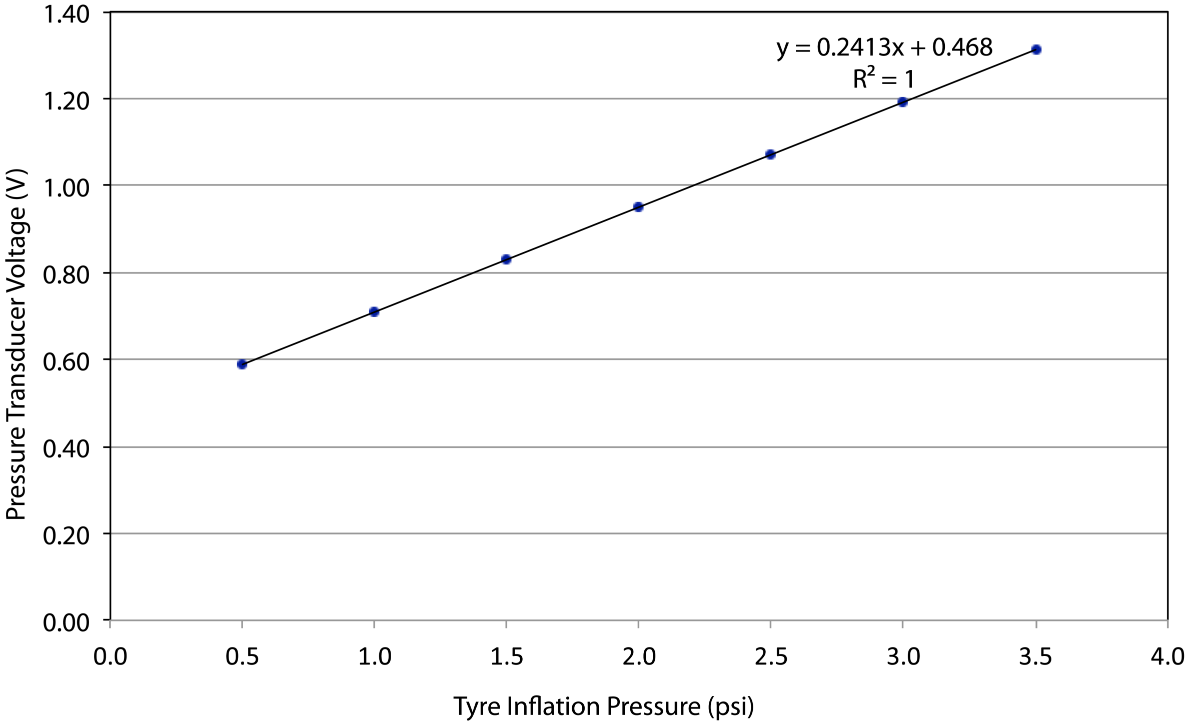

Figure A.3: *Tyre Inflation Pressure - Transducer Calibration.*

Five-Hole Pressure Probe Calibration

The pressure probe calibration as described in Chapter 2 was calibrated between ±60° although it is sensitive only to ±45° before going 'out-of-range' (DataStatus non-zero (green in A.4)). The below plots in Figure A.4 show the relationship for the four coefficients with their associated physical angles. Producing these calibration maps allows the reverse process to be applied (automated with software within DSW) to extract the exact angle of the local flow at the probe-tip location. Details of the equations used to obtain the coefficients can also be found in Chapter 2, specifically Section 2.2.3.

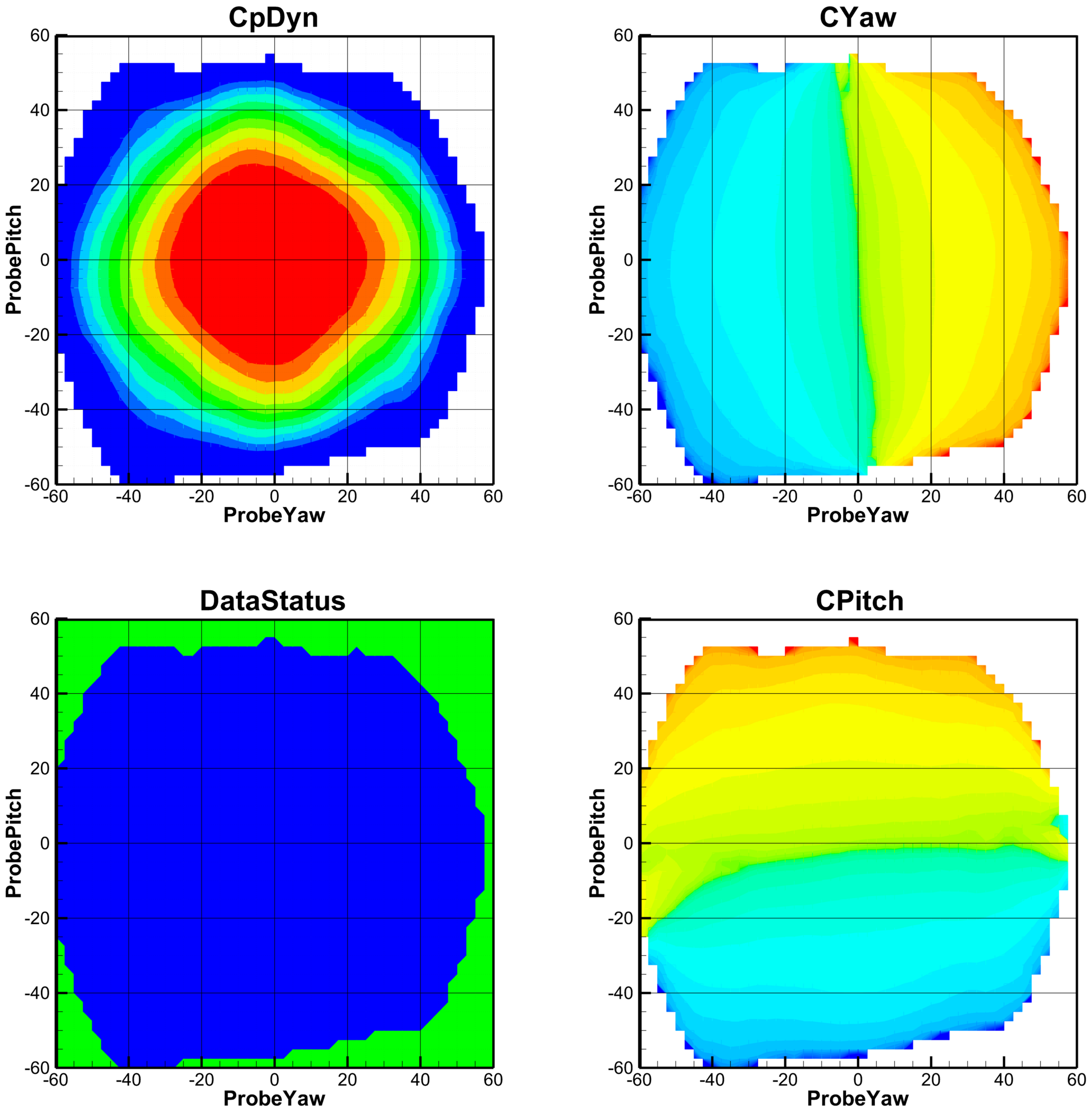

Figure A.4: *Five-hole pressure probe calibration.*

Appendix B:

Tyre Profile Measurements

The data contained within this appendix is provided for those who wish to perform CFD simulations based on deformed tyre profiles. The tyre profiles contained within this appendix are a reduced resolution version of the scans used to produce the profile figures within this document although enough points have been included to provide a smooth profile with all of the important features of the sidewall shape.

All measurements are model-scale and specific to the wheel assembly geometry as outlined in the methodology section.

APPENDIX B

0° Yaw - High Deformation (150mm) - 3.0psi (20.7kPa) - ROTATING

Lower Inboard (x = 0)		Upper Inboard (x = 0)		Upper Outboard (x = 0)		Lower Outboard (x = 0)		Horizontal Inboard (z = 150)		Horizontal Outboard (z = 150)	
y (mm)	**z (mm)**	**y (mm)**	**z (mm)**	**y (mm)**	**z (mm)**	**y (mm)**	**z (mm)**	**± x (mm)**	**y (mm)**	**± x (mm)**	**y (mm)**
50.00	0.00	89.97	236.61	-79.77	246.10	-50.00	0.00	88.00	84.87	88.00	-84.87
57.42	1.00	91.67	247.00	-79.73	254.00	-59.76	1.00	92.00	85.71	92.00	-84.93
59.39	2.00	91.35	259.00	-78.86	262.00	-61.49	2.00	96.00	85.74	102.00	-84.62
62.00	3.00	89.33	267.00	-77.00	270.00	-67.04	3.00	108.00	84.32	108.00	-83.93
68.10	6.00	88.56	271.00	-73.89	278.00	-69.58	4.00	116.00	82.20	114.00	-82.32
71.82	10.00	87.72	273.00	-69.45	286.00	-70.72	5.00	124.00	78.99	120.00	-80.13
75.22	18.00	85.55	277.00	-64.46	294.00	-71.55	7.00	132.00	74.80	126.00	-77.42
77.23	26.00	84.20	281.00	-58.93	300.00	-73.58	9.00	140.00	69.44	132.00	-73.88
78.04	30.00	78.92	289.00	-58.23	302.00	-80.20	15.00	148.00	63.17	138.00	-69.81
78.81	34.00	76.73	293.00	-54.56	306.00	-84.52	23.00	154.00	58.17	144.00	-65.71
78.99	38.00	76.12	295.00	-53.89	308.00	-87.95	31.00	156.00	54.52	150.00	-61.54
79.28	42.00	74.26	297.00	-51.72	310.00	-90.26	39.00	158.00	50.14	154.00	-56.34
79.87	46.00	72.53	299.00	-47.78	312.00	-90.92	47.00	160.00	43.99	156.00	-52.06
79.67	50.00	66.69	304.00	-43.06	315.00	-91.27	55.00	162.00	32.17	158.00	-45.67
79.77	53.90	62.81	306.00	-41.47	316.00	-89.97	63.39	163.00	20.64	160.00	-30.96

0° Yaw - Low Deformation (159mm) - 3.0psi (20.7kPa) - ROTATING

Lower Inboard (x = 0)		Upper Inboard (x = 0)		Upper Outboard (x = 0)		Lower Outboard (x = 0)		Horizontal Inboard (z = 159)		Horizontal Outboard (z = 159)	
y (mm)	**z (mm)**	**y (mm)**	**z (mm)**	**y (mm)**	**z (mm)**	**y (mm)**	**z (mm)**	**± x (mm)**	**y (mm)**	**± x (mm)**	**y (mm)**
44.00	0.00	90.34	245.22	-79.35	255.45	-44.00	0.00	88.00	84.86	88.00	-84.87
54.45	6.00	91.55	247.00	-80.28	259.00	-62.11	7.00	96.00	84.88	92.00	-84.55
57.30	8.00	92.08	251.00	-79.74	267.00	-66.00	8.00	104.00	83.98	98.00	-84.54
61.21	10.00	92.10	265.00	-78.62	275.00	-68.81	9.00	112.00	82.11	104.00	-84.05
64.05	12.00	91.32	269.00	-77.73	279.00	-72.21	12.00	120.00	79.43	110.00	-83.20
66.52	14.00	90.75	273.00	-76.17	283.00	-76.16	16.00	124.00	77.66	116.00	-81.33
69.16	18.00	89.64	277.00	-73.23	291.00	-81.63	24.00	132.00	73.21	122.00	-78.90
71.47	22.00	87.17	283.00	-70.62	295.00	-84.21	28.00	136.00	70.76	134.00	-72.16
73.67	26.00	85.91	287.00	-65.93	303.00	-86.39	32.00	144.00	65.31	140.00	-67.88
74.94	30.00	84.97	289.00	-62.66	307.00	-89.23	40.00	148.00	61.28	146.00	-62.88
77.55	38.00	81.85	293.00	-59.72	311.00	-91.25	48.00	152.00	58.69	150.00	-60.98
78.68	46.00	79.83	297.00	-56.60	315.00	-91.63	52.00	154.00	54.96	152.00	-58.79
79.49	51.00	77.12	302.00	-53.69	319.00	-92.04	60.00	156.00	50.95	154.00	-55.62
79.49	55.00	74.16	304.00	-49.39	323.00	-91.65	64.00	158.00	45.68	156.00	-51.10
79.80	59.00	72.85	308.00	-46.03	325.00	-90.92	70.00	160.00	36.38	158.00	-43.33
79.35	62.55	70.09	310.00	-41.99	327.00	-90.34	72.78	162.00	18.12	160.00	-24.08

APPENDIX B

0° Yaw - High Deformation (150mm) - 3.0psi (20.7kPa) - STATIONARY											
Lower Inboard (x = 0)		**Upper Inboard (x = 0)**		**Upper Outboard (x = 0)**		**Lower Outboard (x = 0)**		**Horizontal Inboard (z = 150)**		**Horizontal Outboard (z = 150)**	
y (mm)	**z (mm)**	**y (mm)**	**z (mm)**	**y (mm)**	**z (mm)**	**y (mm)**	**z (mm)**	**± x (mm)**	**y (mm)**	**± x (mm)**	**y (mm)**
53.00	0.00	89.97	234.61	-77.77	244.10	-61.64	0.00	88.00	84.87	88.00	-84.87
56.68	1.00	91.17	247.00	-81.32	247.00	-68.01	1.00	92.00	85.71	92.00	-84.93
61.14	2.00	90.71	259.00	-81.26	254.00	-70.72	2.00	96.00	85.74	102.00	-84.62
64.65	3.00	88.30	267.00	-80.71	260.00	-71.63	3.00	108.00	84.32	108.00	-83.93
69.87	6.00	87.30	271.00	-79.92	265.00	-72.21	4.00	116.00	82.20	114.00	-82.32
73.62	10.00	86.11	273.00	-78.54	270.00	-72.79	5.00	124.00	78.99	120.00	-80.13
77.30	18.00	83.48	277.00	-75.14	278.00	-74.20	7.00	132.00	74.80	126.00	-77.42
78.94	26.00	81.66	281.00	-70.38	286.00	-78.16	9.00	140.00	69.44	132.00	-73.88
79.50	30.00	80.84	283.00	-62.85	296.00	-83.93	15.00	148.00	63.17	138.00	-69.81
79.79	34.00	79.44	285.00	-58.84	300.00	-88.30	23.00	154.00	58.17	144.00	-65.71
79.55	38.00	77.01	287.00	-55.25	304.00	-90.92	31.00	156.00	54.52	150.00	-61.54
79.61	42.00	75.33	289.00	-52.87	308.00	-92.50	39.00	158.00	50.14	154.00	-56.34
79.66	46.00	72.94	292.00	-50.25	310.00	-92.36	47.00	160.00	43.99	156.00	-52.06
79.16	50.00	71.78	295.00	-45.15	312.00	-91.91	55.00	162.00	32.17	158.00	-45.67
79.77	51.90	64.40	300.00	-42.43	313.00	-89.97	61.39	163.00	20.64	160.00	-30.96

APPENDIX B

+5° Yaw - High Deformation (150mm) - 3.0psi (20.7kPa) - ROTATING

Lower Inboard (x = 0)		Upper Inboard (x = 0)		Upper Outboard (x = 0)		Lower Outboard (x = 0)		Horizontal Inboard (z = 150)		Horizontal Outboard (z = 150)	
y (mm)	z (mm)	y (mm)	z (mm)	y (mm)	z (mm)	y (mm)	z (mm)	± x (mm)	y (mm)	± x (mm)	y (mm)
67.24	0.00	89.97	236.61	-79.77	246.10	-57.50	0.00	88.00	84.87	88.00	-84.87
73.47	2.00	91.67	247.00	-79.73	254.00	-58.86	2.00	92.00	85.71	92.00	-84.93
76.89	4.00	91.35	259.00	-78.86	262.00	-63.17	4.00	96.00	85.74	102.00	-84.62
78.68	6.00	89.33	267.00	-77.00	270.00	-70.74	6.00	108.00	84.32	108.00	-83.93
79.39	8.00	88.56	271.00	-73.89	278.00	-74.58	8.00	116.00	82.20	114.00	-82.32
80.01	10.00	87.72	273.00	-69.45	286.00	-76.33	10.00	124.00	78.99	120.00	-80.13
81.15	18.00	85.55	277.00	-64.46	294.00	-84.28	18.00	132.00	74.80	126.00	-77.42
81.39	26.00	84.20	281.00	-58.93	300.00	-88.00	26.00	140.00	69.44	132.00	-73.88
81.25	30.00	78.92	289.00	-58.23	302.00	-89.67	30.00	148.00	63.17	138.00	-69.81
81.02	34.00	76.73	293.00	-54.56	306.00	-90.94	36.00	154.00	58.17	144.00	-65.71
80.90	38.00	76.12	295.00	-53.89	308.00	-91.20	40.00	156.00	54.52	150.00	-61.54
80.70	42.00	74.26	297.00	-51.72	310.00	-91.26	46.00	158.00	50.14	154.00	-56.34
80.38	46.00	72.53	299.00	-47.78	312.00	-91.43	56.00	160.00	43.99	156.00	-52.06
80.34	50.00	66.69	304.00	-43.06	315.00	-89.60	62.00	162.00	32.17	158.00	-45.67
79.77	53.90	62.81	306.00	-41.47	316.00	-89.97	63.39	163.00	20.64	160.00	-30.96

-5° Yaw - High Deformation (150mm) - 3.0psi (20.7kPa) - ROTATING

Lower Inboard (x = 0)		Upper Inboard (x = 0)		Upper Outboard (x = 0)		Lower Outboard (x = 0)		Horizontal Inboard (z = 150)		Horizontal Outboard (z = 150)	
y (mm)	z (mm)	y (mm)	z (mm)	y (mm)	z (mm)	y (mm)	z (mm)	± x (mm)	y (mm)	± x (mm)	y (mm)
52.56	0.00	89.97	236.61	-79.77	246.10	-58.11	0.00	88.00	84.87	88.00	-84.87
58.57	2.00	91.67	247.00	-79.73	254.00	-73.41	2.00	92.00	85.71	92.00	-84.93
62.06	4.00	91.35	259.00	-78.86	262.00	-76.52	4.00	96.00	85.74	102.00	-84.62
64.73	6.00	89.33	267.00	-77.00	270.00	-77.28	6.00	108.00	84.32	108.00	-83.93
66.96	8.00	88.56	271.00	-73.89	278.00	-78.91	8.00	116.00	82.20	114.00	-82.32
68.94	10.00	87.72	273.00	-69.45	286.00	-81.04	10.00	124.00	78.99	120.00	-80.13
74.42	18.00	85.55	277.00	-64.46	294.00	-86.78	18.00	132.00	74.80	126.00	-77.42
78.12	26.00	84.20	281.00	-58.93	300.00	-89.52	26.00	140.00	69.44	132.00	-73.88
78.76	30.00	78.92	289.00	-58.23	302.00	-90.50	30.00	148.00	63.17	138.00	-69.81
79.45	34.00	76.73	293.00	-54.56	306.00	-91.08	36.00	154.00	58.17	144.00	-65.71
80.05	38.00	76.12	295.00	-53.89	308.00	-91.56	40.00	156.00	54.52	150.00	-61.54
80.00	42.00	74.26	297.00	-51.72	310.00	-91.54	46.00	158.00	50.14	154.00	-56.34
80.09	46.00	72.53	299.00	-47.78	312.00	-91.11	56.00	160.00	43.99	156.00	-52.06
79.77	50.00	66.69	304.00	-43.06	315.00	-90.55	62.00	162.00	32.17	158.00	-45.67
79.77	53.90	62.81	306.00	-41.47	316.00	-89.97	63.39	163.00	20.64	160.00	-30.96

APPENDIX B

+5° Yaw - Low Deformation (159mm) - 3.0psi (20.7kPa) - ROTATING

Lower Inboard (x = 0)		**Upper Inboard (x = 0)**		**Upper Outboard (x = 0)**		**Lower Outboard (x = 0)**		**Horizontal Inboard (z = 159)**		**Horizontal Outboard (z = 159)**	
y (mm)	**z (mm)**	**y (mm)**	**z (mm)**	**y (mm)**	**z (mm)**	**y (mm)**	**z (mm)**	**± x (mm)**	**y (mm)**	**± x (mm)**	**y (mm)**
54.36	0.00	90.34	245.22	-79.35	255.45	-51.00	0.00	88.00	84.86	88.00	-84.87
61.98	2.00	91.55	247.00	-80.28	259.00	-55.50	2.00	96.00	84.88	92.00	-84.55
64.14	4.00	92.08	251.00	-79.74	267.00	-58.73	4.00	104.00	83.98	98.00	-84.54
68.65	6.00	92.10	265.00	-78.62	275.00	-60.05	6.00	112.00	82.11	104.00	-84.05
70.69	8.00	91.32	269.00	-77.73	279.00	-65.97	8.00	120.00	79.43	110.00	-83.20
73.61	12.00	90.75	273.00	-76.17	283.00	-68.82	10.00	124.00	77.66	116.00	-81.33
75.66	16.00	89.64	277.00	-73.23	291.00	-71.32	12.00	132.00	73.21	122.00	-78.90
76.95	20.00	87.17	283.00	-70.62	295.00	-76.87	18.00	136.00	70.76	134.00	-72.16
78.23	26.00	85.91	287.00	-65.93	303.00	-82.92	24.00	144.00	65.31	140.00	-67.88
79.20	30.00	84.97	289.00	-62.66	307.00	-87.02	32.00	148.00	61.28	146.00	-62.88
79.62	38.00	81.85	293.00	-59.72	311.00	-90.81	42.00	152.00	58.69	150.00	-60.98
79.91	46.00	79.83	297.00	-56.60	315.00	-92.14	52.00	154.00	54.96	152.00	-58.79
79.94	52.00	77.12	302.00	-53.69	319.00	-92.22	64.00	156.00	50.95	154.00	-55.62
80.25	56.00	74.16	304.00	-49.39	323.00	-91.95	68.00	158.00	45.68	156.00	-51.10
79.96	60.00	72.85	308.00	-46.03	325.00	-91.56	70.00	160.00	36.38	158.00	-43.33
79.35	62.55	70.09	310.00	-41.99	327.00	-90.34	72.78	162.00	18.12	160.00	-24.08

-5° Yaw - Low Deformation (159mm) - 3.0psi (20.7kPa) - ROTATING

Lower Inboard (x = 0)		**Upper Inboard (x = 0)**		**Upper Outboard (x = 0)**		**Lower Outboard (x = 0)**		**Horizontal Inboard (z = 159)**		**Horizontal Outboard (z = 159)**	
y (mm)	**z (mm)**	**y (mm)**	**z (mm)**	**y (mm)**	**z (mm)**	**y (mm)**	**z (mm)**	**± x (mm)**	**y (mm)**	**± x (mm)**	**y (mm)**
42.29	0.00	90.34	245.22	-79.35	255.45	-61.34	0.00	88.00	84.86	88.00	-84.87
47.57	2.00	91.55	247.00	-80.28	259.00	-70.24	4.00	96.00	84.88	92.00	-84.55
52.04	4.00	92.08	251.00	-79.74	267.00	-74.15	6.00	104.00	83.98	98.00	-84.54
53.97	6.00	92.10	265.00	-78.62	275.00	-75.99	8.00	112.00	82.11	104.00	-84.05
56.66	8.00	91.32	269.00	-77.73	279.00	-76.52	10.00	120.00	79.43	110.00	-83.20
61.06	12.00	90.75	273.00	-76.17	283.00	-78.70	12.00	124.00	77.66	116.00	-81.33
65.01	16.00	89.64	277.00	-73.23	291.00	-80.81	14.00	132.00	73.21	122.00	-78.90
67.50	20.00	87.17	283.00	-70.62	295.00	-83.68	18.00	136.00	70.76	134.00	-72.16
71.34	26.00	85.91	287.00	-65.93	303.00	-86.62	24.00	144.00	65.31	140.00	-67.88
73.46	30.00	84.97	289.00	-62.66	307.00	-89.71	32.00	148.00	61.28	146.00	-62.88
75.86	38.00	81.85	293.00	-59.72	311.00	-91.85	42.00	152.00	58.69	150.00	-60.98
76.57	42.00	79.83	297.00	-56.60	315.00	-92.38	52.00	154.00	54.96	152.00	-58.79
78.89	54.00	77.12	302.00	-53.69	319.00	-91.93	62.00	156.00	50.95	154.00	-55.62
78.95	56.00	74.16	304.00	-49.39	323.00	-91.85	64.00	158.00	45.68	156.00	-51.10
79.12	60.00	72.85	308.00	-46.03	325.00	-91.50	68.00	160.00	36.38	158.00	-43.33
79.35	62.55	70.09	310.00	-41.99	327.00	-90.34	72.78	162.00	18.12	160.00	-24.08

APPENDIX B

+5° Yaw - High Deformation (150mm) - 3.0psi (20.7kPa) – ROTATING - GLYCEROL

Lower Inboard (x = 0)		Upper Inboard (x = 0)		Upper Outboard (x = 0)		Lower Outboard (x = 0)		Horizontal Inboard (z = 150)		Horizontal Outboard (z = 150)	
y (mm)	**z (mm)**	**y (mm)**	**z (mm)**	**y (mm)**	**z (mm)**	**y (mm)**	**z (mm)**	**± x (mm)**	**y (mm)**	**± x (mm)**	**y (mm)**
64.17	0.00	89.97	236.61	-79.77	246.10	-53.00	0.00	88.00	84.87	88.00	-84.87
71.10	2.00	91.67	247.00	-79.73	254.00	-57.50	2.00	92.00	85.71	92.00	-84.93
72.81	4.00	91.35	259.00	-78.86	262.00	-61.00	4.00	96.00	85.74	102.00	-84.62
74.15	6.00	89.33	267.00	-77.00	270.00	-63.08	6.00	108.00	84.32	108.00	-83.93
75.07	8.00	88.56	271.00	-73.89	278.00	-68.05	8.00	116.00	82.20	114.00	-82.32
75.91	10.00	87.72	273.00	-69.45	286.00	-74.83	10.00	124.00	78.99	120.00	-80.13
77.53	18.00	85.55	277.00	-64.46	294.00	-81.79	18.00	132.00	74.80	126.00	-77.42
78.79	26.00	84.20	281.00	-58.93	300.00	-86.46	26.00	140.00	69.44	132.00	-73.88
78.86	30.00	78.92	289.00	-58.23	302.00	-87.73	30.00	148.00	63.17	138.00	-69.81
79.38	34.00	76.73	293.00	-54.56	306.00	-90.39	36.00	154.00	58.17	144.00	-65.71
79.68	38.00	76.12	295.00	-53.89	308.00	-90.88	40.00	156.00	54.52	150.00	-61.54
79.58	42.00	74.26	297.00	-51.72	310.00	-91.56	46.00	158.00	50.14	154.00	-56.34
79.73	46.00	72.53	299.00	-47.78	312.00	-91.37	56.00	160.00	43.99	156.00	-52.06
80.04	50.00	66.69	304.00	-43.06	315.00	-89.97	60.00	162.00	32.17	158.00	-45.67
79.77	53.90	62.81	306.00	-41.47	316.00	-89.97	63.39	163.00	20.64	160.00	-30.96

+5° Yaw - Low Deformation (159mm) - 3.0psi (20.7kPa) – ROTATING - GLYCEROL

Lower Inboard (x = 0)		Upper Inboard (x = 0)		Upper Outboard (x = 0)		Lower Outboard (x = 0)		Horizontal Inboard (z = 159)		Horizontal Outboard (z = 159)	
y (mm)	**z (mm)**	**y (mm)**	**z (mm)**	**y (mm)**	**z (mm)**	**y (mm)**	**z (mm)**	**± x (mm)**	**y (mm)**	**± x (mm)**	**y (mm)**
50.95	0.00	90.34	245.22	-79.35	255.45	-54.29	0.00	88.00	84.86	88.00	-84.87
57.43	2.00	91.55	247.00	-80.28	259.00	-67.81	4.00	96.00	84.88	92.00	-84.55
57.95	4.00	92.08	251.00	-79.74	267.00	-68.82	6.00	104.00	83.98	98.00	-84.54
60.88	6.00	92.10	265.00	-78.62	275.00	-70.61	8.00	112.00	82.11	104.00	-84.05
62.91	8.00	91.32	269.00	-77.73	279.00	-72.67	10.00	120.00	79.43	110.00	-83.20
69.27	16.00	90.75	273.00	-76.17	283.00	-74.18	12.00	124.00	77.66	116.00	-81.33
70.28	18.00	89.64	277.00	-73.23	291.00	-76.25	14.00	132.00	73.21	122.00	-78.90
71.29	20.00	87.17	283.00	-70.62	295.00	-79.84	18.00	136.00	70.76	134.00	-72.16
74.78	26.00	85.91	287.00	-65.93	303.00	-82.94	24.00	144.00	65.31	140.00	-67.88
76.08	30.00	84.97	289.00	-62.66	307.00	-87.62	32.00	148.00	61.28	146.00	-62.88
78.62	38.00	81.85	293.00	-59.72	311.00	-90.82	42.00	152.00	58.69	150.00	-60.98
79.45	46.00	79.83	297.00	-56.60	315.00	-91.75	52.00	154.00	54.96	152.00	-58.79
79.83	52.00	77.12	302.00	-53.69	319.00	-91.89	60.00	156.00	50.95	154.00	-55.62
79.71	56.00	74.16	304.00	-49.39	323.00	-91.83	64.00	158.00	45.68	156.00	-51.10
79.35	60.00	72.85	308.00	-46.03	325.00	-91.44	68.00	160.00	36.38	158.00	-43.33
79.35	62.55	70.09	310.00	-41.99	327.00	-90.34	72.78	162.00	18.12	160.00	-24.08